Table of Contents

Abstract ii

Acknowledgements iv

List of Figures xii

List of Tables xxiii

Nomenclature xxvi

1 Introduction 1

1.1 Project Objectives 2

1.2 Outline of Thesis 3

2 Literature Review 4

2.1 Wastewater Treatment and Advanced Oxidation 4

2.2 Photocatalysis 4

2.2.1 Introduction to Photocatalysis 4

2.2.2 Advantages of Photocatalysis 6

2.2.3 Disadvantages of Photocatalysis 7

2.3 Homogeneous vs. Heterogeneous Photocatalysis 7

2.3.1 Homogeneous Photocatalysis 7

2.3.2 Heterogeneous Photocatalysis 7

2.4 The Conventional Mechanism of Photocatalysis 8

2.5 Photocatalytic Properties of Semiconductors 14

2.6 ZnO as Photocatalyst 15

2.7 Factors Affecting Photocatalysis 16

2.7.1 Suspended Versus Supported (Immobilised) Photocatalysts 16

2.7.2 Catalyst Concentration/Catalyst Loading 17

2.7.3 Effect of pH 18

2.7.4 Effect of UV Light Intensity and Wavelength 21
2.7.4.1 Effect of light intensity 23
2.7.4.2 Effect of UV wavelength 24
2.7.4.3 Overall implications of intensity and wavelength on photocatalytic activity/reaction rate 24
2.7.5 The Effect of Photocatalyst Type: Preparation Technique/Method 25
2.7.6 The effect of Surface Morphology 27
2.7.6.1 ZnO (Powder) as photocatalyst 27
2.7.6.2 ZnO thin films 28
2.7.7 Effect of Crystallinity 29
2.7.8 Effect of Dissolved Oxidant 30
2.7.8.1 Effect of dissolved oxygen 30
2.7.8.2 Effect of H_2O_2 31
2.7.8.3 Effect of ozone 32
2.7.8.4 Overall effect of oxidant 32
2.7.9 The Effect of Mass Transfer 32
2.8 Photocatalytic Reactors 35
2.8.1 Classification of Photoreactor on the Basis of the State of the Catalyst 35
2.8.1.1 Slurry reactor 36
2.8.1.2 Immobilised reactor 39
2.8.2 Classification of Photoreactor on the Basis of Type of Illumination 43
2.8.3 Classification of Photoreactors on the Basis of Position of the Irradiation Source 44
2.9 Increasing Photocatalytic Activity – the Effect of Doping 46
2.9.1 Types of Dopant: 46
2.9.1.1 Cationic doping 46
2.9.1.2 Anionic doping 46
2.9.2 Impact of Dopant on the Semiconductors 47

2.9.3 Doped ZnO Photocatalytic Materials....48
2.9.4 Nitrogen-doped ZnO (N:ZnO)....49
2.9.4.1 Nitrogen doping methods....49
2.9.4.2 Effect of N_2 dopant on band gap and photocatalysis....50
2.9.4.3 Effect of doped nitrogen concentration on photocatalysis....50
2.9.4.4 Effect of N_2 doping on morphology....51
2.9.4.5 Effect of N_2 doping on crystallinity....51
2.9.5 Cobalt-doped ZnO (Co:ZnO)....51
2.9.5.1 Methods used for Co:ZnO....52
2.9.5.2 Effect of Co dopant on band gap and photocatalysis....52
2.9.5.3 Effect of Co dopant type and concentration on Co:ZnO....52
2.9.5.4 Effect of Co dopant on surface morphology....53
2.9.5.5 Effect of Co doping on crystallinity....53
2.10 Kinetic Modelling....54
2.11 Implications of the Literature....56
3 Materials and Methods....58
3.1 Materials....58
3.2 Photocatalytic Experiments....58
3.2.1 Photocatalytic Reaction Vessel....58
3.2.2 Reaction Conditions for Initial Trial Experiments....59
3.2.3 Reaction Conditions for Second, Third, and Last Phase of Experiments....60
3.2.3.1 Reaction conditions for experiments under both oxygen-limited and rich conditions 60
3.2.3.1.1 Reaction under oxygen-limited conditions....60
3.2.3.1.2 Reaction under oxygen-rich conditions....61
3.3 Preparation of Undoped and Doped ZnO Nanostructured Thin Films....62
3.3.1 Preparation of Undoped Nanostructured Zno Thin Films....62

3.3.2 Nitrogen-doped ZnO (N:ZnO) Thin Films 63
3.3.2.1 N:ZnO thin films preparation using dopant N_2 gas 63
3.3.2.2 N:ZnO thin films preparation using TEA as nitrogen source 64
3.3.3 Preparation of Cobalt-Doped Nano Structure Zinc Oxide Thin Films (Co:ZnO). 67
3.4 Analytical Techniques 68
3.4.1 UV-Visible Spectrophotometer (UV-Vis) 68
3.4.2 High Performance Liquid Chromatography (HPLC) 69
3.4.3 Liquid Chromatography and Mass Spectroscopy (LC-MS) 69
3.4.4 Scanning Electron Microscopy 70
3.4.5 X-ray Diffractometer 70
3.4.6 Atomic Absorption Spectroscopy 70
4 The Effect of Morphology on Undoped ZnO Photocatalysed Reaction Rate, Film Stability and Implications to the Photocatalytic Mechanism 72
4.1 Introduction 72
4.2 Data Treatment and Kinetic Analysis 73
4.3 Relationships with Surface Morphologies and Thin Film Preparations 74
4.3.1 Morphology Before Reaction 74
4.3.2 Morphology after Reaction under Limited Oxygen Conditions 77
4.3.3 Morphology after Reaction under Oxygen-rich Conditions 82
4.4 Mass Transfer Limitation Studies 86
4.5 Relationships with Photocatalytic Activity (Reaction Rate) 89
4.5.1 Reaction Kinetics 89
4.5.2 Oxygen-limited Conditions 89
4.5.3 Oxygen-rich Conditions 91
4.6 Reuseability of the Thin Films 93
4.6.1 Oxygen-limited Conditions 94
4.6.2 Oxygen-rich Conditions 99

4.7 Comparison between S2-MS, ZnO MS films and ZnO Powder 103
4.8 Effect of Model compound MB Concentration on Photocatalytic Activity 105
4.9 Summary 111
5 A More Detailed Investigation of Conventional versus Lattice Photocatalysed Reactions at both 254nm and 340nm 112
5.1 Introduction 112
5.2 Morphologies before Reaction 112
5.2.1 Morphologies after Reaction upon UV Irradiation of 254nm 114
5.2.1.1 Morphologies after reaction under oxygen-limited conditions 114
5.2.1.2 Morphologies after reaction under oxygen-rich conditions 116
5.2.2 Morphologies after Reaction upon UV Irradiation of 340nm 117
5.3 Reaction Intermediates and Product Analysis. 120
5.3.1 Species Identification 120
5.3.2 Reactions with Irradiation at 254nm 120
5.3.3 Reactions with Irradiation at 340nm 124
5.4 Proposed Reaction Mechanism 128
5.5 Summary 133
6 Doped Nanostructured ZnO Thin Films: Impact Of Dopant On Photocatalytic Activity, Reaction Mechanism and Stability 135
6.1 Introduction 135
6.2 Impact of Dopant on Surface Morphologies 135
6.2.1 Nitrogen-doped Zinc Oxide (N:ZnO) Nanostructured Thin Films 135
6.2.1.1 N:ZnO thin film morphologies obtained by using N_2 gas as nitrogen source 136
6.2.1.2 N:ZnO thin films morphologies obtained by using TEA as an N_2 source 138
6.2.1.2.1 Morphologies obtained at high concentration of TEA with pH control 139
6.2.1.2.2 Morphologies obtained at low concentration of TEA with pH control 142

6.2.1.2.3 Morphologies obtained at high and low concentrations of TEA without pH control 144

6.2.2 Cobalt-doped Nanostructured ZnO (Co:ZnO) Thin Films 146

6.2.2.1 Comparison of cobalt-doped and undoped ZnO nanostructure 146

6.2.2.1.1 Variation of Co:S1-MS morphology with Co concentration 147

6.2.2.1.2 Variation of Co:S1-CG morphology with Co concentration 148

6.2.2.1.3 Variation of Co:S2-MS and Co:S2-CG morphology with Co concentration 150

6.2.2.1.4 Overall morphology comparison between all doped and undoped films 152

6.2.2.2 Comparison of crystal planes and dopant concentration 153

6.2.2.2.1 Comparison of XRD analysis between doped and undoped films 153

6.2.2.2.1 Comparison of dopant concentration 155

6.2.2.3 Cobalt-doped ZnO nanostructure and pH 158

6.2.2.3.1 Effect of pH on the morphologies of Co:S1-MS and Co:S1-CG 158

6.2.2.3.2 Effect of pH on the morphologies of Co:S2-MS and Co:S2-CG 159

6.3 Impact of Photocatalytic Reactions on Cobalt-Doped Nanostructured Zinc Oxide (Co:ZnO) Thin Films 160

6.3.1 Morphologies after Reaction upon UV Irradiation at 254nm 161

6.3.1.1 Under oxygen-limited conditions 161

6.3.1.2 Under oxygen-rich conditions 162

6.3.2 Morphologies after Reaction upon UV Irradiation at 340nm 167

6.3.3 XRD Analysis of All Cobalt-Doped Thin Films 167

6.4 Doped Surface Morphologies and Photocatalytic Activity Relationship 170

6.4.1 Photocatalytic Activity, Reaction Rate and Reaction Kinetics 170

6.4.2 Photocatalytic Activity and Reaction Intermediate Kinetics under UV Irradiation of 254nm 170

6.4.2.1 Oxygen-limited conditions 170

6.4.2.2 Oxygen-rich conditions 179
6.4.2.3 Overall implications of Co doping on the photocatalytic reaction mechanism at 254nm 183
6.4.3 Photocatalytic Activity and Reaction Intermediate Kinetics under UV irradiation 340nm 186
6.5 Impact of Dopant on Reaction Mechanism(S) 189
6.6 Summary 191
7 Conclusions and Future Work 194
7.1 Conclusions 194
7.1.1 Undoped Nanostructured ZnO Thin Films, Photocatalytic Activity and Reaction Mechanism 194
7.1.2 Impact of Dopant on Nanostructured ZnO Thin Films, Photocatalytic Activity and Reaction Mechanism 195
7.2 Implications for Industrial Applications 197
7.3 Future Work 197
Appendix A: Control Experiments 199
Appendix B: Reproducibility and effect on of nanostructured ZnO thin films morphologies under UV irradiation of 340nm 205
Appendix C: Reaction Intermediate analysis by using LC-MS. 207
Appendix D: Band Gap Calculations 221
Appendix E 223
References 250

List of Figures

Figure 2.1: The general conventional mechanism of the photocatalysis. [Reproduced from N. Daneshvar *et al*. 2004]. 9
Figure 2.2: Secondary reactions with activated oxygen species in the photo-electrochemical mechanism. [Reproduced from Hoffmann *et al.* [45]]. 13
Figure 2.3: Pourbaix diagram for Zn .[Reproduced from [78]]. 19
Figure 2.4: Dissolution of ZnO films in aqueous solutions at different pH level: (a) within 24 h; (b) after 24 h and 1 week. [Taken from Han *et al.* [83]]. 21
Figure 2.5: Explanation of mass transfer in supported metal oxide photocatalyst. 33
Figure 2.6: Schematic diagram of the integrated photo-reactor-membrane UF system. [Reproduced from Lasa *et al.* [138]].....36
Figure 2.7: Taylor vortex reactor in operation. [Reproduced from Lasa *et al.* [138]]....36
Figure 2.8: Plug flow annular reactor. [Reproduced from Biard *et al.* [139]]. 37
Figure 2.9: Experimental Up-Flow system; 1: glass jacket reactor; 2: UV lamp; 3: tank; 4: solution; 5: centrifugal pump; 6: cryostat of circulation water; 7: quartz jacket; 8: water inlet;9: water outlet; 10: flow meter; 11: valve; 12: bypass; 13: air pump. [Reproduced from Merabet *et al.* [140]]. 37
Figure 2.10: Swirl Flow Reactor. [Reproduced from Ray *et al.* [141]]. 38
Figure 2.11: Turbulent slurry photocatalytic reactor for hydrogen production. [Reproduced from Xiaowei *et al.* [142]].....38
Figure 2.12: Open dish illumination arrangement. A, Pyrex glass dish; B, TiO_2 coated sand; C, solution; D, peristaltic pump; E, 100 W medium pressure mercury lamp. [Reproduced from Matthews *et al.* [149]] 39
Figure 2.13: Schematic representation of the Falling Film Reactor. [Reproduced from Lasa *et al.* [138]] 40
Figure 2.14: Schematic representation of the optical-fibre bundled array photocatalytic reactor system. [Reproduced from Lasa *et al.* [138]] 41
Figure 2.15: Schematic representation of a multiple tube reactor. [Reproduced from Lasa *et al.* [138]] 41
Figure 2.16: Annular packed-bed reactor. [Reproduced from Lasa *et al.* [138]] 42

Figure 2.17: Rotating disk reactor, (a) variable speed motor, (b) Pyrex reactor wall, (c) support disk,.....42
Figure 2.18: Tube light Reactor (TLR). [Reproduced from Lasa *et al.* [138]].....42
Figure 2.19: Various schemes illustrating the possible changes that might occur to the band gap electronic structure of anatase TiO_2 on doping with various nonmetals: (a) band gap of pristine TiO_2; (b) doped TiO_2 with localized dopant levels near the VB and the CB; (c) band gap narrowing resulting from broadening of the VB; (d) localized dopant levels and electronic transitions to the CB; and (e) electronic transitions from localized levels near the VB to their corresponding excited states for Ti^{3+} and F^{+} centers. [Reproduced from Serpone [191]].....48
Figure 3.1: Photo of the photo reactor illustrating the photoreactor set-up, showing the stainless steel enclosure with its concave reflector for the UV lamp, power supplies and magnetic stirrers.....58
Figure 3.2: Schematic of the photoreactor set-up for experiments under oxygen-limited conditions.....61
Figure 3.3: Schematic of the photoreactor set-up for experiments under oxygen-rich conditions.....61
Figure 3.4: Preparation N:ZnO by using N_2 gas as nitrogen dopant source: (A) N_2 saturated $Zn(NO)_3.6H_2O$; (B) N_2 saturated HMT; (C) Mixing of N_2 saturated $Zn(NO)_3.6H_2O$ and HMT under extensive supply of N_2; (D) Magnified view of sealable glass jar. 64
Figure 3.5: Sealable glass jar. 68
Figure 4.1: Cross-sectional view of the surface morphologies of the different ZnO thin films before photocatalysis: (A) S1-MS; (B) S1-CG; (C) S2-MS (inset, an example of the large crystals that were sporadically present on the surface of the main structure); (D) S2-CG; (E) S3-MS; (F) S3-CG. 75
Figure 4.2: XRD analysis of all thin film morphologies after reaction under both oxygen-limited and rich conditions: (A) S1-MS; (B) S1-CG; (C) S2-MS; (D) S2-CG. 76
Figure 4.3: Comparison of the solution 1 (S1) derived ZnO thin film surface morphologies using SEM imaging before and after Methylene Blue photocatalysed degradation: (A)S1-MS (un-reacted); (B) S1-MS (reacted with limited O_2); (C) S1-MS (reacted under O_2 rich conditions); (D) S1-CG (un-reacted); (E) S1-CG (reacted with limited O_2); (F)S1-CG (reacted under O_2 rich conditions). 80

Figure 4.4: Concentration of Zn metal in the final reaction liquid as measured by atomic absorption spectroscopy (AAS) for the reactions photocatalysed by the ZnO thin film derived from solutions S1 and S2 on both clean glass slides (CG) and magnetron sputtered templates (MS). 81
Figure 4.5: Comparison of the solution 2 (S2) derived ZnO thin film surface morphologies using SEM imaging before and after Methylene Blue photocatalysed degradation: (A) S2-MS (un-reacted); (B) S2-MS (reacted with limited O_2); (C) S2-MS (reacted under O_2 rich conditions); (D) S2-CG (un-reacted); (E) S2-CG (reacted with limited O_2); (F) S2-CG (reacted under O_2 rich conditions). 82
Figure 4.6: Comparison of the solution 3 (S3) derived ZnO thin film surface morphologies from SEM imaging before and after Methylene Blue photocatalysed degradation: (A) S3-MS (un-reacted); (B) S3-MS (reacted with limited O_2); (C) S3-MS (reacted under O_2 rich conditions); (D) S3-CG (un-reacted); (E) S3-CG (reacted with limited O_2); (F)S3-CG (reacted under O_2 rich conditions). 84
Figure 4.7: Comparison of photocatalytic degradation of Methylene Blue solution at different mechanical stirring speeds. 88
Figure 4.8: Comparison of surface morphology of S1-MS under same reaction conditions at various mixing speeds. (A) 100rpm; (B) 200rpm; (C) 300rpm; (D) 400rpm. 88
Figure 4.9: Comparison of the degradation of Methylene Blue by the ZnO thin films derived from solutions S1, S2 and S3 under oxygen-limited conditions.....90
Figure 4.10: Comparison of the degradation of Methylene Blue by the ZnO thin films derived from solutions S1, S2 and S3 under oxygen-rich conditions.....91
Figure 4.11: XRD analysis of thin flm S2-MS. 93
Figure 4.12: Reusability and reproducibility of the ZnO thin films in the photocatalysed degradation of 5mg L^{-1} Methylene Blue under O_2 limited conditions. (A) S1-MS; (B) S1-CG; (C) S2-MS; (D) S2-CG; (E) S3-MS; (F) S3-CG, where 1R denotes initial use of a film, and 2R and 3R denote the first and second reuse of the same film respectively.95
Figure 4.13: SEM images of morphology S1-MS after first (1R) and second run (2R); reproducibility and effect on morphology.(A) S1-MS first run (top view); (B) S1-MS first run (cross-sectional view); (C) S1-MS second run (top view); (D) S1-MS second run (cross-sectional view) under oxygen-limited conditions.....96
Figure 4.14: SEM images of morphology S1-CG after first (1R) and second (2R) run; reproducibility and effect on morphology.(A) S1-CG first run (top view); (B) S1-CG

first run (cross-sectional view); (C) S1-CG second run (top view); (D) S1-CG second run (cross-sectional view) under oxygen-limited conditions. 96
Figure 4.15: SEM images of morphology S2-MS after first (1R) and second run (2R); reproducibility and effect on morphology.(A) S2-MS first run (top view); (B) S2-MS first run (cross-sectional view); (C) S2-MS second run (top view); (D) S2-MS second run (cross-sectional view) under oxygen-limited conditions. 97
Figure 4.16: SEM images of morphology S2-CG after first (1R) and second run (2R); reproducibility and effect on morphology.(A) S2-CG first run (top view); (B) S2-CG first run (cross-sectional view); (C) S2-CG second run (top view); (D) S2-CG second run (cross-sectional view) under oxygen-limited conditions. 97
Figure 4.17: Concentration of Zn metal in the final reaction liquid for the first run (1R) as measured by atomic absorption spectroscopy (AAS) for the reactions photocatalysed by the ZnO thin films derived fromsolutions S1 and S2 on both clean glass slides (CG) and magnetron sputtered templates (MS). 98
Figure 4.18: Concentration of Zn metal in the final reaction liquid for the second run (2R) as measured by atomic absorption spectroscopy (AAS) for the reactions photocatalysed by the ZnO thin films derived from solutions S1 and S2 on both clean glass slides (CG) and magnetron sputtered templates (MS). 98
Figure 4.19: Reusability and reproducibility of the ZnO thin films in the photocatalysed degradation of 5mg L^{-1} Methylene Blue under O_2 rich conditions, A) S1-MS; (B) S1-CG; (C) S2-MS; (D) S2-CG; (E) S3-MS; (F) S3-CG, where 1R denotes initial use of a film, and 2R and 3R denote the first and second reuse of the same film respectively. 100
Figure 4.20: SEM images of morphology S1-MS after first (1R) and second run (2R); reproducibility and effect on morphology.(A) S1-MS first run (top view); (B) S1-MS first run (cross-sectional view); (C) S1-MS second run (top view); (D) S1-MS second run (cross-sectional view) under oxygen-rich conditions. 101
Figure 4.21: SEM images of morphology S1-CG after first (1R) and second run (2R); reproducibility and effect on morphology.(A) S1-CG first run (top view); (B) S1-CG first run (cross-sectional view); (C) S1-CG second run (top view); (D) S1-CG second run (cross-sectional view) under oxygen-rich conditions. 101
Figure 4.22: SEM images of morphology S2-MS after first (1R) and second run (2R); reproducibility and effect on morphology.(A) S2-MS first run (top view); (B) S2-MS first run (cross-sectional view); (C) S2-MS second run (top view); (D) S2-MS second run (cross-sectional view) under oxygen-rich conditions. 102

Figure 4.23: SEM images of morphology S2-CG after first (1R) and second run (2R); reproducibility and effect on morphology.(A) S2-CG first run (top view); (B) S2-CG first run (cross sectional view); (C) S2-CG second run (top view); (D) S2-CG second run (cross sectional view) under oxygen-rich conditions. 102
Figure 4.24: Comparison between photocatalytic activity of MS films (S2-MS, ZnO MS) to ZnO powder under both oxygen-limited and oxygen-rich conditions.....103
Figure 4.25: The effect of photocatalytic reaction of Methylene Blue on the top surface morphology of the MS films using SEM imaging: (A) MS only; (B) MS film reacted under oxygen-limited conditions O2; (C) MS film reacted under oxygen-rich conditions.....104
Figure 4.26: Overall comparison of degradation of MB (5 and 10 mgL^{-1}) for the thin films derived from solution S1 and S2 under both oxygen-limited and oxygen-rich conditions.....109
Figure 4.27: Concentration of Zn metal in the final reaction liquid as measured by atomic absorption spectroscopy (AAS) for the reactions($5mgL^{-1}$ MB) photocatalysed by the ZnO thin film derived from solutions S1 and S2 on both clean glass slides (CG) and magnetron sputtered templates (MS).....110
Figure 4.28: Concentration of Zn metal in the final reaction liquid as measured by atomic absorption spectroscopy (AAS) for the reactions($10mgL^{-1}$ MB) photocatalysed by the ZnO thin film derived from solutions S1 and S2 on both clean glass slides (CG) and magnetron sputtered templates (MS). 110
Figure 5.1: SEM cross-sectional views of surface morphologies of the different ZnO thin films on glass substrate before photocatalysis: A, S1-MS; B, S1-CG; C, S2-MS; D, S2-CG. 113
Figure 5.2: HPLC Chromatograms and SEM cross-sectional views of the thin films after the photocatalytic degradation of MB with UV irradiation of 254nm under oxygen-limited conditions: A, reaction intermediates from thin film S1-MS; B, reaction intermediates from thin film S1-CG; C, reaction intermediates from thin film S2-MS; D, reaction intermediates from thin film S2-CG; E, cross-sectional view of thin film S1-MS after reaction; F, cross-sectional view of thin film S1-CG after reaction; G, cross-sectional view of thin film S2-MS after reaction; H, cross-sectional view of thin film S2-CG after reaction. 115
Figure 5.3: HPLC Chromatograms and SEM cross-sectional views of the thin films after the photocatalytic degradation of MB with UV irradiation of 254nm under

oxygen-rich conditions: A, reaction intermediates from thin film S1-MS; B, reaction intermediates from thin film S1-CG; C, reaction intermediates from thin film S2-MS; D, reaction intermediates from thin film S2-CG; E, cross-sectional view of thin film S1-MS after reaction; F, cross-sectional view of thin film S1-CG after reaction; G, cross-sectional view of thin film S2-MS after reaction; H, cross-sectional view of thin film S2-CG after reaction. 116
Figure 5.4: HPLC Chromatograms and SEM cross-sectional views of the thin films after the photocatalytic degradation of MB with UV irradiation of 340nm under oxygen-rich conditions: A, reaction intermediates from thin film S1-MS; B, reaction intermediates from thin film S1-CG; C, reaction intermediates from thin film S2-MS; D, reaction intermediates from thin film S2-CG; E, cross-sectional view of thin film S1-MS after reaction; F, cross-sectional view of thin film S1-CG after reaction; G, cross-sectional view of thin film S2-MS after reaction; H, cross-sectional view of thin film S2-CG after reaction. 118
Figure 5.5: Comparison of the concentration of Zn metal in the final reaction liquid as measured by atomic absorption spectroscopy (AAS) for the reaction photocatalysed by the ZnO thin films under oxygen-rich conditions upon UV irradiation 254 and 340nm. 119
Figure 5.6: Reaction profile comparison of the reaction intermediates from methylene blue photocatalysed by four different ZnO thin films upon UV irradiation at 254nm under oxygen-limited and oxygen-rich conditions, obtained by HPLC: A, S1-MS: oxygen-limited; B, S1-CG: oxygen-limited; C, S2-MS: oxygen-limited; D, S2-CG: oxygen-limited; E, S1-MS: oxygen-rich; F, S1-CG: oxygen-rich; G, S2-MS: oxygen-rich; H, S2-CG: oxygen-rich.....122
Figure 5.7: Reaction profile comparison of the reaction intermediates from methylene blue photocatalysed by four different ZnO thin films upon UV irradiation at 340nm under oxygen-rich conditions only, obtained by HPLC: A, S1-MS; B, S1-CG; C, S2-MS; D, S2-CG.....125
Figure 5.8: Proposed methylene blue ZnO photocatalysed reaction mechanism for the thin films studied based on the identified intermediates and reaction profiles in this work. 130
Figure 5.9: Overall reaction mechanism for the photocatalytic degradation of methylene blue based on this work and literature. 131

Figure 5.10: Schematic representation of the initial stages of the proposed Mars Van Krevelen type ZnO photocatalysed methylene blue reaction mechanism: (a) under oxygen-limited conditions, (b) under oxygen-rich conditions.....132
Figure 6.1: A: SEM image (top view) of nitrogen-doped nanostructured ZnO thin films N:S1-MS; B:EDX analysis at position P1(ZnO single crystal).....136
Figure 6.2: A: SEM image (top view) of N:S1-CG; B:EDX analysis at position P1(ZnO single crystal).....137
Figure 6.3: A: SEM image (top view) of N:S2-MS; B: EDX analysis at position P1(complex ZnO single crystal).....138
Figure 6.4: A: SEM image (top view) of N:S2-CG; B: EDX analysis at position P1(complex ZnO single crystal).....138
Figure 6.5: A: SEM image (top view) of N1:S1-MS; B: EDX analysis at position P1 (X-shaped ZnO crystal); C: EDX analysis at position P2 (layer upon magnetron sputtered coating and small ZnO crystal) at high concentration of TEA with pH control.....139
Figure 6.6: A:SEM image (top view) of N1:S1-CG; B:EDX analysis at position P1(regular ZnO crystal); C:EDX analysis at position P2(layer upon magnetron sputtered coating) at high concentration of TEA with pH control.....140
Figure 6.7: A: SEM image (top view) of N2:S2-MS; B: EDX analysis at position P1(cluster of ZnO crystal); C: EDX analysis at position P2(ZnO single crystal); D: EDX analysis of at position P3 (layer upon magnetron sputtered coating).....141
Figure 6.8: A: SEM image (cross-sectional) of N2:S2-MS; B: EDX analysis at position P1 (cluster of ZnO crystal); C: EDX analysis at position P2(complex ZnO single crystal).....141
Figure 6.9: A: SEM image (top view) of N3:S1-MS; B: EDX analysis at position P1 (cluster of small ZnO crystals); C: EDX analysis at position P2 (large ZnO crystal); D: EDX analysis at position (layer upon magnetron sputtered coating) at low concentration of TEA with pH control.....142
Figure 6.10: A: SEM image (top view) of N4:S2-MS; B: EDX analysis at position P1(cluster of ZnO crystal); C: EDX analysis at position P2(layer upon magnetron sputtered coating).....143
Figure 6.11: A: SEM image (top view) of N4:S2-CG; B: EDX analysis at position P1(ZnO jointed crystal); C: EDX analysis at position P2 (layer upon magnetron sputtered coating) at low concentration of TEA with pH control.....143

Figure 6.12: A:SEM image (top view) of N5:S2-MS; B:EDX analysis at position P1(cluster of ZnO crystal); C:EDX analysis at position P2(layer upon magnetron sputtered coating) at high concentration of TEA without pH control. 144
Figure 6.13: A:SEM image (top view) of N5:S2-CG; B:EDX analysis at position P1(edged ZnO crystal); C:EDX analysis at position P2(layer upon magnetron sputtered coating) at high concentration of TEA without pH control. 145
Figure 6.14: A:SEM image (top view) of N6:S2-MS; B:EDX analysis at position P1(cluster of ZnO crystal); C:EDX analysis at position P2(flowery layer upon magnetron sputtered coating) at low concentration of TEA without pH control. 145
Figure 6.15: Cross-sectional SEM images of cobalt doped and un-doped ZnO nanostructured thin films. A: Un-doped S1-MS; B: Co5%:S1-MS, C: Co10%:S1-MS, D: Co15%:S1-MS and E: Co25%:S1-MS. 148
Figure 6.16: Cross-sectional SEM images of cobalt doped and un-doped ZnO nanostructured thin films. A: Un-doped S1-CG; B: Co5%:S1-CG, C: Co10%:S1-CG, D: Co15%:S1-CG and E: Co25%:S1-CG.....150
Figure 6.17: Cross-sectional SEM images of cobalt doped and undoped ZnO nanostructured thin films. A: Undoped S2-MS; B: Co5%:S2-MS, C: Co10%:S2-MS, D: Co15%:S2-MS and E: Co25%:S2-MS. 151
Figure 6.18: Cross-sectional SEM images of cobalt doped and undoped ZnO nanostructured thin films. A: Undoped S2-CG; B: Co5%:S2-CG, C: Co10%:S2-CG, D: Co15%:S2-CG. 152
Figure 6.19: XRD comparison of undoped and cobalt-doped ZnO nanostructured thin films. 154
Figure 6.20: Cross-sectional SEM images of the cobalt doped ZnO nanostructured thin films. A: Co5%:S1-MS at pH=4, B: Co5%:S1-MS at pH=5, C: Co5%:S1-CG at pH=4 and D: Co5%:S1-CG at pH=5. 159
Figure 6.21: Cross-sectional SEM images of cobalt doped ZnO nanostructured thin films. A: Co5%:S2-MS at pH=6.5, B: Co5%:S2-MS at pH=7.5, C: Co5%:S2-CG at pH=6.5 and D: Co5%:S2-CG at pH=7.5. 160
Figure 6.22: Cross-sectional SEM images of cobalt-doped nanostructured ZnO thin films surface morphologies before and after reaction under oxygen-limited and rich conditions upon UV irradiation of 254nm. A: Co15%:S1-MS unreacted, B: Co15%:S1-MS reacted under O_2 limited conditions, C: Co15%:S1-MS reacted under O_2 rich conditions, D: Co10%:S1-MS unreacted, E: Co10%:S1-MS reacted under O_2 limited

conditions, F: Co10%:S1-MS reacted under O_2 rich conditions, G: Co5%:S1-MS unreacted, H: Co5%:S1-MS reacted under O_2 limited conditions, I: Co5%:S1-MS reacted under O_2 rich conditions.....163
Figure 6.23: Cross-sectional SEM images of cobalt-doped nanostructured ZnO thin films surface morphologies before and after reaction under oxygen-limited and rich conditions upon UV irradiation of 254nm. A: Co15%:S1-CG unreacted, B: Co15%:S1-CG reacted under O_2 limited conditions, C: Co15%:S1-CG reacted under O_2 rich conditions, D: Co10%:S1-CG unreacted, E: Co10%:S1-CG reacted under O_2 limited conditions, F: Co10%:S1-CG reacted under O_2 rich conditions, G: Co5%:S1-CG unreacted, H: Co5%:S1-CG reacted under O_2 limited conditions, I: Co5%:S1-CG reacted under O_2 rich conditions.....164
Figure 6.24: Cross-sectional SEM images of cobalt-doped nanostructured ZnO thin films surface morphologies before and after reaction under oxygen-limited and rich conditions upon UV irradiation of 254nm. A: Co25%:S2-MS unreacted, B: Co25%:S2-MS reacted under O_2 limited conditions, C: Co25%:S2-MS reacted under O_2 rich conditions, D: Co15%:S2-MS unreacted, E: Co15%:S2-MS reacted under O_2 limited conditions, F: Co15%:S2-MS reacted under O_2 rich conditions, G: Co10%:S2-MS unreacted, H: Co Co10%:S2-MS reacted under O_2 limited conditions, I: Co Co10%:S2-MS reacted under O_2 rich conditions, J: Co5%:S2-MS unreacted, K: Co5%:S2-MS reacted under O_2 limited conditions, L: Co5%:S2-MS reacted under O_2 rich conditions. 165
Figure 6.25: Cross-sectional SEM images of cobalt-doped nanostructured ZnO thin films surface morphologies before and after reaction under oxygen-limited and rich conditions upon UV irradiation of 254nm. A: Co15%:S2-CG unreacted, B: Co15%:S2-CG reacted under O_2 limited conditions, C: Co15%:S2-CG reacted under O_2 rich conditions, D: Co10%:S2-CG unreacted, E: Co10%:S2-CG reacted under O_2 limited conditions, F: Co10%:S2-CG reacted under O_2 rich conditions, G: Co5%:S2-CG unreacted, H: Co5%:S2-CG reacted under O_2 limited conditions, I: Co5%:S2-CG reacted under O_2 rich conditions.....166
Figure 6.26: Cross-sectional SEM images of cobalt-doped and undoped nanostructured ZnO thin films surface morphologies before and after reaction under oxygen-limited and rich conditions upon UV irradiation of 340nm. A: Co:S1-MS(15wt%) unreacted, B: Co:S1-MS(15wt%) reacted under O_2 limited conditions, C: Co:S1-MS(15wt%) reacted under O_2 rich conditions, D: Co:S2-MS(25wt%) unreacted, E: Co:S2-MS(25wt%)

reacted under O_2 limited conditions, F: Co:S2-MS(25wt%) reacted under O_2 rich conditions, G: Co:S2-MS(15wt%) unreacted, H: Co:S2-MS(15wt%) reacted under O_2 limited conditions, I: Co:S2-MS(15wt%) reacted under O_2 rich conditions. 168
Figure 6.27: Comparison of XRD analysis of photocatalytically reacted cobalt doped nanostrcutred ZnO thin films upon UV irradition of 254nm and 340nm under both oxygen-limited and oxygen-rich conditions. 169
Figure 6.28: Overall comparison of photocatalytic degradation profiles of MB by using nanostructured Co:ZnO thin films under oxygen-limited conditions upon UV irradiation of 254nm. A: Co5%:ZnO thin films; B: Co10%:ZnO thin films; C: Co15%:ZnO thin films; D: Co25%:ZnO thin films. 173
Figure 6.29: Overall comparison of photocatalytic degradation profiles of MB by using undoped nanostructured Co:ZnO thin films under oxygen-limited and rich conditions upon UV irradiation of 254nm. A: undoped ZnO thin films under oxygen-limited conditions; B: undoped ZnO thin films under oxygen-rich conditions. 174
Figure 6.30: Reaction profile comparison of the reaction intermediates from methylene blue photocatalysed by three different Co:S1-MS thin films upon UV irradiation at 254nm under both oxygen-limited and oxygen-rich conditions. A: Co5%:S1-MS under O_2 limited conditions, B: Co5%:S1-MS under O_2 rich conditions, C: Co10%:S1-MS under O_2 limited conditions, D: Co10%:S1-MS under O_2 rich conditions, E: Co15%:S1-MS under O_2 limited conditions, F: Co15%:S1-MS under O_2 rich conditions. 175
Figure 6.31: Reaction profile comparison of the reaction intermediates from methylene blue photocatalysed by three different Co:S1-CG thin films upon UV irradiation at 254nm under both oxygen-limited and oxygen-rich conditions. A: Co5%:S1-CG under O_2 limited conditions, B: Co5%:S1-CG under O_2 rich conditions, C: Co10%:S1-CG under O_2 limited conditions, D: Co10%:S1-CG under O_2 rich conditions, E: Co15%:S1-CG under O_2 limited conditions, F: Co15%:S1-CG under O_2 rich conditions. 176
Figure 6.32: Reaction profile comparison of the reaction intermediates from methylene blue photocatalysed by four different Co:S2-MS thin films upon UV irradiation at 254nm under both oxygen-limited and oxygen-rich conditions. A: Co5%:S2-MS under O_2 limited conditions, B: Co5%:S2-MS under O_2 rich conditions, C: Co10%:S2-MS under O_2 limited conditions, D: Co10%:S2-MS under O_2 rich conditions, E: Co15%:S2-MS under O_2 limited conditions, F: Co15%:S2-MS under O_2 rich conditions, G: Co25%:S2-MS under O_2 limited conditions, H: Co25%:S2-MS under O_2 rich conditions. 177

Figure 6.33: Reaction profile comparison of the reaction intermediates from methylene blue photocatalysed by three different Co:S2-CG thin films upon UV irradiation at 254nm under both oxygen-limited and oxygen-rich conditions. A: Co5%:S2-CG under O_2 limited conditions, B: Co5%:S2-CG under O_2 rich conditions, C: Co10%:S2-CG under O_2 limited conditions, D: Co10%:S2-CG under O_2 rich conditions, E: Co15%:S2-CG under O_2 limited conditions, F: Co15%:S2-CG under O_2 rich conditions.....178
Figure 6.34: Over all comparison of photocatalytic degradation profiles of MB by using nanostructured Co:ZnO thin films under oxygen-rich conditions upon UV irradiation of 254nm. A: Co:ZnO thin films at 5wt%; B: Co:ZnO thin films at 10wt%; C: Co:ZnO thin films at 15wt%; D: Co:ZnO thin films at 25wt%. 180
Figure 6.35: Overall comparison of photocatalytic degradation profiles of MB by using nanostructured Co:ZnO thin films under oxygen-limited and rich conditions upon UV irradiation of 340nm. A: Co:ZnO thin films (Co15%:S1-MS, Co15%:S2-MS and Co25%:S2-MS) under oxygen-limited conditions; B: Co:ZnO thin films (Co15%:S1-MS, Co15%:S2-MS and Co25%:S2-MS) under oxygen-rich conditions.....188
Figure 6.36: Reaction profile comparison of the reaction intermediates from methylene blue photocatalysed by Co:S1-MS thin films upon UV irradiation at 340nm under both oxygen-limited and oxygen-rich conditions. A: Co15%:S1-MS under O_2 limited conditions, B: Co15%:S1-MS under O_2 rich conditions. 188
Figure 6.37: Reaction profile comparison of the reaction intermediates from methylene blue photocatalysed by two different Co:S2-MS thin films upon UV irradiation at 340nm under both oxygen-limited and oxygen-rich conditions. A: Co15%:S2-MS under O_2 limited conditions, B: Co15%:S2-MS under O_2 rich conditions, C: Co25%:S2-MS under O_2 limited conditions, D: Co25%:S2-MS under O_2 rich conditions.....189

List of Tables

Table 2.1: Band-Gap energies of semiconductors used for photocatalytic processes reproduced from Bhatkhande *et al.* 2002. 15
Table 2.2: Types of UV radiation 22
Table 2.3: Comparison of slurry and immobilised photo-reactors reproduced from [138]. 43
Table 3.1: Summary of the initial parameters to study the photocatalytic activity. .. 59
Table 3.2: Reaction conditions for experiments under both oxygen-limited and rich conditions. 60
Table 3.3: Un-doped ZnO thin film preparation conditions 63
Table 3.4: Nitrogen-doped nanostructure ZnO thin film (N:ZnO) preparation conditions by using N_2 gas as nitrogen dopant source. 64
Table 3.5: Nitrogen doped nanostructured ZnO thin film (N:ZnO) preparation conditions by using TEA as Nitrogen dopant source. 66
Table 3.6: Cobalt-doped ZnO thin film preparation conditions. 67
Table 3.7: Summary of nanostructured ZnO thin films morphologies obtained at different cobalt (as dopant) concentration. 68
Table 3.8: HPLC gradient method used to resolve methylene blue and its reaction products. 69
Table 4.1: Concentration of zinc in reaction solutions as determined by atomic absorption spectroscopy (AAS), summarised as total zinc concentration (Zn; ppb) and zinc concentration normalised by the original surface area of the thin film catalyst (Zn/*S*; ppb/m^2). 78
Table 4.2: pH of the reaction fluid throughout the reaction under oxygen-limited and rich conditions. 83
Table 4.3: Summary of Reynold's Number and reaction rate constant(s) on a liquid volume basis (k_{app} ; s^{-1}) and a UV exposed surface area (*S*) basis (k''_{app} , $m^3\ m^{-2}\ s^{-1}$) for the photocatalysed degradation of methylene blue. 87

Table 4.4: Summary of the 1st order reaction rate constants on a liquid volume basis (k_{app} ; s^{-1}) and a UV exposed surface area (S) basis (k''_{app} , m^3 m^{-2} s^{-1}) for the photocatalysed degradation of 5 mg L^{-1} methylene blue. 90
Table 4.5: Summary of 1st order reaction rate constants on liquid volume basis (k_{app} ; s^{-1}), UV exposed surface area (S) basis (k''_{app} , m^3 m^{-2} s^{-1}) and mass of the catalyst basis (k''_{app} , m^3 kg^{-1} s^{-1}) for the photocatalysed degradation of 5 mg L^{-1} methylene blue..... 106
Table 4.6: Summary of Ist order reaction rate constants on liquid volume basis (k_{app} ; s^{-1}), UV exposed surface area (S) basis (k''_{app} , m^3 m^{-2} s^{-1}) and mass of the catalyst basis (k''_{app} , m^3 kg^{-1} s^{-1}) for the photocatalysed degradation of 10 mg L^{-1} methylene blue..... 106
Table 4.7: Summary of % photocatalytic degradation for the photocatalysed degradation of 5 and 10 mg L^{-1} methylene blue under oxygen-limited conditions. 107
Table 4.8: Summary of % photocatalytic degradation for the photocatalysed degradation of 5 and 10 mg L^{-1} methylene blue under oxygen-rich conditions. 107
Table 5.1: Summary of 1st order reaction rate constant on liquid volume basis (k_{app}: s^{-1}), catalyst mass basis (k'_{app}: $m^3kg^{-1}s^{-1}$) and a UV exposed surface area (S) basis (k''_{app}: m^3 m^{-2} s^{-1}) for the photocatalysed degrdation of 10 mg L^{-1} Methylene Blue under UV irradiation of 254nm..... 123
Table 5.2: Summary of 1st order reaction rate constant on liquid volume basis (k_{app}: s^{-1}), catalyst mass basis (k'_{app}: $m^3kg^{-1}s^{-1}$) and a UV exposed surface area (S) basis (k''_{app}: m^3 m^{-2} s^{-1}) for the photocatalysed degradation of 10 mg L^{-1} Methylene Blue under UV irradiation of 340nm..... 126
Table 6.1: Comparison of Cobalt content in the Co:ZnO thin films at two different concentration of $Co(NO)_3.6H_2O$, derived from EDX analysis. 156
Table 6.2: Comparison of Cobalt content in the Co:ZnO thin films at two different concentration of $Co(NO)_3.6H_2O$, derived from EDX analysis. 157
Table 6.3: Summary of the 1st order reaction rate constants on mass of the catalyst (k'_{app}), UV exposed catalyst surface area (k''_{app}) and volume of the catalysts (k'''_{app}) basis for the photodegradation of 10 mg L^{-1} methylene blue by using cobalt-doped ZnO thin films under oxygen-limited conditions upon UV irradiation of 254nm... 184
Table 6.4: Summary of the Ist order reaction rate constants on mass of the catalyst (k'_{app}), UV exposed catalyst surface area (k''_{app}) and volume of the catalysts (k'''_{app})

basis for the photodegradation of 10 mg L^{-1} methylene blue by using cobalt-doped ZnO thin films under oxygen-rich conditions upon UV irradiation of 254nm. 184
Table 6.5: Summary of the 1st order reaction rate constants on mass of the catalyst (k'_{app}), UV exposed catalyst surface area (k''_{app}) and volume of the catalysts (k'''_{app}) basis for the photodegradation of 10 mg L^{-1} methylene blue by using cobalt doped ZnO thin films under both oxygen-limited and rich conditions upon UV irradiation of 340nm. 185

Nomenclature

ZnO	Zinc Oxide
N:ZnO	Nitrogen Doped Zinc Oxide
Co:ZnO	Cobalt Doped Zinc Oxide
MB	Methylene Blue
AB	Azure B
AC	Azure C
TH	Thionin
R , $R'^{\bullet}$	Alkyl radicals
TEA	Triethyleneamine
HMT	Hexamethylenetetramine
TFA	Trifluoro Acetic Acid
MO	Metal Oxide
UV	Ultra Violet
HPLC	High Performance Liquid Chromatography
UV-Vis	Ultra Violet Visible Spectrophotometer
AAS	Atomic Absorption Spectroscopy
XRD	X-ray Diffraction
LC-MS	Liquid Chromatography-Mass Spectrometry
EDX	Energy Dispersive X-ray Spectroscopy
µmol/L	Micro Mole per Litre

mg L^{-1}	Milligram per Litre
Wt%	Weight per Cent
rpm	Revolution per Minute
mL	Millilitre
mm	Millimetre
µm	Micrometer
S	Exposed Surface Area
t	Time
N	Number of Moles
K	Adsorption Equilibrium Constant
V	Liquid Volume (m^3)
W	Mass of the Solid Catalyst (kg)
V_s	Volume of the solid catalyst (m^3)
k'_{app}	Apparent Reaction Rate Constant on Mass Basis ($m^3kg^{-1}s^{-1}$)
k''_{app}	Apparent Reaction Rate Constant on Area Basis ($m^3m^{-2}s^{-1}$)
k'''_{app}	Apparent Reaction Rate Constant on Volume Basis ($m^3m^{-3}s^{-1}$)

1 Introduction

Photocatalysis: the acceleration of a photoreaction in the presence of a catalyst, a form of advanced oxidation, is one of the emerging tools that can be used to oxidise a wide range of bio-recalcitrant waste compounds because of its efficiency in the total destruction of pollutants, non-selectivity, and the formation of congenial products [1].

Most chemical industries, for example the pharmaceutical, petrochemical and especially the chemical industries, use a wide variety of catalysts. It is well known that catalysts increase overall process efficiency generally by speeding up a reaction without being consumed. However, the important issue in catalytic reactions is the possibility of recycling and removing the catalyst at the end of the reaction. Presently, many solid catalysts are used as powders. However, powder catalysts may cause serious problems when used, as they are difficult to completely separate and recover, can cause health problems and environmental uncertainties if not well contained, and have low reaction efficiencies [2]. To minimise the above problems, catalysts are immobilised onto solid supports. Attempts to immobilise film deposition onto rigid supports have shown low efficiencies due to their smaller surface area in comparison to powders [3]. Much research has been focused on the design of these materials, to improve their effectiveness, stereo-specificity and yield. Coherent and comprehensive treatment of the subject is still under tight scrutiny to address unanswerable questions, and to unveil new horizons in photocatalytic reaction engineering.

Supported semi-conductor metal oxide nanostructures are a promising candidate in addressing the aforementioned issues because of the structure, porosity and properties of a wide range of oxides including ZnO, TiO_2, Al_2O_3 and SiO_2. Nano-sized catalysts are, however, not widely used, despite their potential to improve the efficiency of chemical reactions. Nanostructured thin films with high porosity have a very extensive surface area, with microstructures such as whiskers, rods or ribbons which would make them ideal for catalytic reactions – doubling the surface area typically doubles the reaction rate [4]. Furthermore, immobilisation allows for easy removal of the catalyst from the reaction mixture in one step, enabling the nano-sized catalysts to be cleaned, reused, and to yield catalyst-free products.

Understanding of both the theoretical and experimental aspects of nanostructured metal oxides is crucial in their synthesis, fabrication, processing and overall characterisation in the field of chemical and materials engineering [5]. The surface morphologies of a wide range of oxides including ZnO, TiO_2, Al_2O_3 and SiO_2 can be controlled by processing and composition. Thin films are coated onto a range of substrates, the most common being glass and stainless steel [6-8]. Among other methods of nanostructured oxide thin film preparation, hydrothermal solution deposition [7, 9] is a cheap and easy technique to prepare a large variety of nanostructure ZnO thin films by using the combination of both magnetron sputtered coated ZnO (ZnO seed on glass substrate) and clean glass substrates [7, 9, 10]. These nanostructured ZnO thin films have enormous potential to be used as photocatalysts for commercial advantage because of their high surface to volume ratio [4]. Further details of the background and uses of these films can be found in Chapter 2.

This project is an extensive study of these nanostructured ZnO thin films as photocatalysts, including the study of the reaction kinetics, accessibility of the supported catalyst to UV irradiation, both internal and external mass transfer limitations, reusability, reproducibility, possible implication of the availability of the source of the oxidant in liquid phase photocatalytic oxidation, interaction of the supported catalyst with the reaction intermediates species, and the impact of dopant on the catalyst surface morphology, and the overall efficiency of the photocatalytic reaction.

1.1 Project Objectives

The objective of this project was to study the suitability of nanostructured ZnO thin films as efficient photocatalysts, and to characterise any issues that may be involved in the scale-up of photocatalytic systems based on these types of immobilised nanostructured ZnO thin films.

To achieve this, the specific objectives of this project were:

A. To characterise the use of these nanostructured oxide films as photocatalysts in terms of reaction rate, solution and solid reaction mechanisms, and stability (leaching, mechanical durability) both under oxygen-limited and rich conditions at two different UV irradiation wavelengths.
B. To relate the surface morphology of the thin films (based on microstructure, porosity and chemical composition) to photocatalytic activity and reaction mechanism(s).

Based on these results, the characteristics of nanostructured oxides with the best catalytic properties are to be identified.

C. To study the effect of doping on the surface morphology of the previously characterised nanostructured ZnO thin films and to determine the effect of this doping on the relationship between photocatalytic activity, reaction mechanism and stability of the thin films.

ZnO had been used extensively as a photocatalyst for the degradation of bio-recalcitrant compounds. Methylene Blue (MB) was chosen as the model compound as it is well studied for ZnO (powder) and is non-toxic. MB is also appropriate for kinetic studies since it does not directly mineralise and therefore has intermediates that can be measured [11, 12]. Another advantage is that no stable intermediates are formed that are more toxic than the original dye [13, 14], indicating that photocatalytic oxidation is a valid method for the complete elimination of dyes in waste streams without causing secondary pollution.

A full analysis of the reactions was used to achieve these objectives, including: UV-Vis analysis coupled with high performance liquid chromatography (HPLC), liquid chromatography mass spectroscopy (LC-MS), scanning electron microscopy (SEM), X-ray diffractometer (XRD) and atomic absorption spectroscopy (AAS). By applying this methodology, important reaction characteristics such as reaction rate, reaction mechanism and their correlation with surface morphologies could be established.

1.2 Outline of Thesis

The work presented in this thesis is composed of seven chapters and five appendices. Chapter 2 present a systematic literature review. All the materials, experimental and analytical methods used, are outlined in Chapter 3. Thereafter, this thesis represents the systematic and detailed study of each objective in detail. Chapter 4 details the effect of morphology on undoped ZnO photocatalysed reaction rate, film stability and the implications to the photocatalytic mechanism. Detailed reaction mechanism type and parameters that may govern it are summarised in Chapter 5. Therefore, Chapter 6 is focused to address the main issues highlighted in Chapter 4 and 5 by using doped ZnO. Overall, Chapter 6 described the impact of dopant on photocatalytic activity, reaction mechanism and stability. On the basis of, the conclusions and finding, from the preceding chapters, future work are outlined in Chapter 7.

2 Literature Review

2.1 Wastewater Treatment and Advanced Oxidation

Global attention has been paid to the management, treatment and ultimate eradication of hazardous materials from wastewater effluents [1]. Conventional treatment methods (sedimentation, coagulation, adsorption etc.) have low capability in meeting stringent environmental quality standards. Generation of high oxidising species/radicals makes advanced oxidation techniques (AOT) such as photolysis, photo-fenton, sonolysis, photocatalysis, supercritical water oxidation, sonochemical oxidation [15], electrochemical oxidation [16], electrolytic beam oxidation [17], and wet air oxidation [18, 19] more attractive in almost all water and wastewater treatments for solids, gaseous and liquid streams. Selection of a treatment method/process depends heavily upon such diverse factors as the nature of the waste streams, concentration of the effluents, the volume and their toxicity [18]. Among AOTs, heterogeneous photocatalysis is at the forefront of much of the research activity due to its efficiency in the total destruction of pollutants, non-selectivity and the formation of congenial products [1]. Photocatalytic processes are most economically and practically useful for treating bio-recalcitrant wastewater components. They are therefore best applied as either a point-source wastewater pre-treatment unit for a biological wastewater treatment facility (to make one or more streams more biodegradable before aggregated treatment) or as a polishing step for an aggregated wastewater stream from a wastewater treatment plant.

2.2 Photocatalysis

2.2.1 Introduction to Photocatalysis

Photocatalysis is the acceleration of a photoreaction in the presence of a catalyst [20]. A photoreaction is induced by a photon having energy greater than the band gap of the substance used as photocatalyst. ‘Photocatalytic activity’ is a term used to gauge the extent of the efficiency of a photocatalyst [20]. It depends on the ability of the catalyst to create a UV-induced electron-hole pair, which further generates free radicals able to undergo secondary reactions. These free radicals are very efficient in oxidising a wide range of pollutant waste and the overall behaviour of the photocatalyst depends on how these free radicals trigger reactions (i.e. the reaction mechanism) and mass transfer limitations (if there are any).

In general, the quantum efficiency (a ratio of UV-induced electrons per second to the number of photons hitting a photosensitised surface per second), quantum yield (a ratio of the number of molecules decomposed to the number of photons being absorbed) and turnover frequency (molecules reacting per active site in the unit area) are used to study the photocatalytic activity of a photocatalytic process. These parameters usually do not provide sufficient information to characterise a photocatalyst in terms of reaction rate (slow or fast), extent and kinetics of the reaction. Therefore, to have in-depth study of the behaviour of the supported catalyst, interaction of the catalyst to the secondary or tertiary (and so on) reaction intermediate species, more precise terms such as 'reaction rate constants', and 'reaction kinetics' should be employed. Thus in this work, the photocatalytic activity will be benchmarked by measuring both the true and apparent reaction rates, the reaction intermediates species and their possible further degradation into less harmful products.

In the last two decades, photocatalysts have been the subject of intense and vigorous academic research [21]. Photocatalytic oxidation, photocatalytic reduction, dehydrogenation, hydrogen transfer, water detoxification, and gas-phase pollutants removal are some of the main applications of semiconductor photocatalysis [22]. In particular, photocatalysis has been vigorously employed to degrade bio-recalcitrant organic compounds in both aqueous and gases phases, much work being done on the colour removal of stringent dyes, with MB being one of the prime azo dye compounds studied. Much is consequently known about the photocatalytic reactions of MB and because of this it has been used in this study as the model compound to compare the reaction rate and photocatalytic reaction mechanisms of different catalysts so that the differences between the catalytic materials can be the main unknown factors to be characterised and hypothesised on.

In addition to the above, major applications investigated for this technology are as follows [23-30]:

- Destruction of dyes and colour removal.
- Removal of chemical oxygen demand (COD).
- Mineralisation of potentially hazardous organic and inorganic waste.
- Treatment of heavy metals.
- Destruction of cancer cells and viruses.
- Decontamination of indoor air and malodorous compounds.
- Killing of harmful fungicide and herbicides.

- Water splitting in order to produce hydrogen fuel.
- Removal of NO_x.
- Indoor air treatment; especially the decomposition of dioxins and other volatile organic compounds.
- Drinking water disinfection.
- Plant protection, especially in the control and inactivation of pathogen species present in nutrient solutions.
- Elimination of unwanted micro-organisms, especially in areas where chemicals or biocides are less effective or are due to regulatory restrictions such as those of the pharmaceutical and food industries.
- Control/removal of infections associated with biomedical implants.

Commercial applications of photocatalysts [31, 32] are few; for instance:

- Sterilisation of surgical instruments.
- Removal of unwanted fingerprints from optical and sensitive electrical components.
- Self-cleaning of glass and side-view mirror coating

The main focus of the research has been the oxidation of organic compounds and the development and characterisation of new photocatalytic materials with enhanced photocatalytic properties.

There are many reasons to explain why photocatalytic materials have been the subject of this intense study, but have not been widely applied in industry and commercially. These are as follows:

2.2.2 Advantages of Photocatalysis

The major advantages of photocatalysis [33] are:

- Photocatalytic reactions are not specific, can be easily applied, and are capable of destroying a wide spectrum of organic pollutants.
- The high immunity of the process to organic toxicity makes the photocatalytic process very attractive for the destruction of bio-recalcitrant and toxic compounds. In addition, photocatalytic processes are usually very efficient in achieving the complete mineralisation of bio-recalcitrant and/or toxic waste.

- Both liquid and gaseous waste streams can be easily treated in photocatalytic reactors.
- The potential use of solar light in photocatalysis makes the process potentially more economically viable in situations and applications requiring low operating costs, or where electricity is expensive and/or scarce.
- The reaction conditions for the process are very mild, requiring a lesser reaction time and fewer chemical inputs compared to other waste degradation processes [24].

2.2.3 Disadvantages of Photocatalysis

The major disadvantages are as follows [24]:

- Can be expensive if the photocatalyst is not reusable or recycled.
- Optimum catalyst loading is important for the efficiency of the photocatalytic process. Low and high catalyst loading are discouraging parameters in photocatalysis (see Section 2.7.2 for a more complete coverage of this).
- Current photocatalysts have low overall energy efficiency [34].

2.3 Homogeneous vs. Heterogeneous Photocatalysis

Photocatalysis is generally divided into two main categories: homogeneous and heterogeneous photocatalysis.

2.3.1 Homogeneous Photocatalysis

Photocatalysis in which the catalyst used is in the same phase as that of the reactant(s) is a homogeneous photocatalysis; such as (O_3/UV/H_2O_2/Fe^{+2} and O/UV/Fe^{+2}) [35, 36]. Homogenous photocatalysis usually have high efficiency and high reaction rates owing to low (or non-existant) mass transfer resistances due to the reactant and catalyst being in the same phase. However, because of their high cost; the huge technological challenges of separating dissolved (same phase) catalytic components from the reactants and products so that the catalyst can be reused and the complex modelling involved [37]; this type of photocatalysis is currently the least suitable for a wide range of applications.

2.3.2 Heterogeneous Photocatalysis

'Heterogeneous' is used to describe a system composed of multiple phases. Hence heterogeneous photocatalysis is the catalysis in which the photocatalyst has a different phase from that of the reactant species. Usually the catalyst is in a solid phase and the reactant(s)/pollutant(s) is in a liquid phase. Generally semiconductor metal oxides are used as

photocatalysts, and the overall mechanism of semiconductor mediated photocatalysis is usually summarised as follows [38]:

- Mass transfer of liquid/gas (fluid) phase reactants to the catalytic surface from the bulk fluid
- Adsorption of reactants to the surface of the catalyst
- Interplay between photon (or photo-excited catalyst surface) oxidant and reactant at the catalyst surface
- Formation of free radicals (oxidising species) from the oxidant at the catalyst surface
- Photoreaction with fluid or surface adsorbed phase
- Desorption of the obtained products from the surface of the catalyst
- Mass transfer of the product from the catalyst surface.

In semiconductor photocatalysis, conventional thermal activation of the catalyst is usually replaced by photonic activation (though thermal activation can have a role). The mechanism of photocatalysis has been widely studied and is summarised next.

2.4 The Conventional Mechanism of Photocatalysis

UV irradiation of light having photonic energy greater than band gap (the energy difference between a top-filled valence band [VB] to the bottom of the vacant conduction band [CB]) of a semiconductor metal oxide (used as photocatalyst) can excite an electron from the filled valance band to the empty conduction band. This excitation of electrons from VB to CB results in the formation of an excited electron (e^-) - positive hole (h^+) pair. In terms of a consequent redox reaction, the photogenerated electrons (e^-) and holes (h^+) are the reducing agent and oxidising agent respectively. Consequently, these e^- and h^+ can either reduce or oxidise a variety of organic compounds on the surface of the photocatalyst or can recombine to generate heat with no net chemical reaction. The original chemical composition and/or structure of the mother semiconductor metal oxide remains unchanged if an equal number of (e^-) and (h^+) are consumed during a chemical reaction and/or recombination [39].

Usually the life\time of an e^-- h^+ pair is nanoseconds [40]; however, this is sufficient time to initiate redox reactions in a photocatalytic system. Unlike metals, which have a continuum of electronic states, a semiconductor is composed of energy regions which do not have any

continuous energy levels, a lack which assist in preventing the recombination [41] of photo-induced (e^-) and (h^+).

The participation of a photo-induced electron-hole pair in redox reactions is shown in Figure 2.1(reproduced from N. Daneshvar *et al.* [42]).

Figure 2.1: The general conventional mechanism of the photocatalysis. [Reproduced from N. Daneshvar *et al*. 2004].

While different fluids can be used in a photocatalytic reaction, this thesis is concerned with aqueous photocatalytic reactions. In an aqueous photocatalytic system, the induced hole is used: to oxidise the water to a powerful oxidising radical species, typically the hydroxyl radical (however, other radical species are formed depending on the pH of the system) which further helps in the oxidisation of an organic/model compound; or to combine with an electron donor species. Similarly, the electron produced upon UV irradiation is usually either taken up by an electron acceptor such an oxygen molecule (O_2) or by a metal ion. If the pH is greater than a point zero charge, a superoxide radical is formed when it is taken up by the O_2, which reacts with water to form hydrogen peroxide (H_2O_2) − which on further oxidation generates $OH^{\bullet}$ radicals.

These $OH^{\bullet}$ radicals further attack the reactant species to degrade them into carbon dioxide (CO_2), water and minerals (i.e. mineralisation). The metal ion (if any) can be reduced to its lower valence state and be deposited on the surface of the catalyst if the induced electron is taken by a metal ion having a redox potential more than the band gap of the photocatalyst. Because of the preferential ability of oxygen with other reacting species, oxidation of metal ions are rare Overall, the electron process becomes more efficient if the reaction species are pre-adsorbed on the surface of the catalyst [24]. In short, the induced electron-hole pair helps in the formation of hydroxyl radicals (a primary oxidant) which are ultimately used in oxidising organic and inorganic species present in the reaction system [43-45]. A more detailed division of the stages in the conventional photocatalytic reaction mechanism can be summarised as follows ([45-47]):

- *Excitation.* Production of an electron-hole pair upon UV irradiation on semiconductor metal oxide.

$$MO + UV \rightarrow e^-_{cb} + h^+_{vb}$$

- *Trapping.* Photo-generated charges are trapped either by oxygen available in the bulk of the fluid or adsorbed to the surface of metal oxide or anywhere within the reaction system.

$$e^-_{cb} + O_{2,ads} \rightarrow O^-_{2,ads}$$

or

$$h^+_{vb} + H_2O_{ads} \rightarrow OH^{\bullet}_{ads}$$

- *Radical Reactions.* Various radical reactions are reported after the electron-hole trap, such as:

$$O^{-}_2 + H^+ \rightarrow HO_2^{\bullet}$$

$$HO_2^{\bullet} + e^- \rightarrow HO^{-}_2$$

$$HO^{-}_2 + H^+ \rightarrow H_2O_2$$

$$2HO_2^{\bullet} \rightarrow H_2O_2 + O_2$$

$$O^{-}_2 + HO_2^{\bullet} \rightarrow O_2 + HO^{-}_2$$

$$H_2O_2 + e^{-} \rightarrow \cdot OH + OH^{-}$$

$$H_2O_2 + OH \rightarrow H_2O + HO_2^{\bullet}$$

$$2OH \rightarrow H_2O_2$$

- *Reaction with organic and inorganic species.* Both radicals obtained through radical reaction and photo-generated charges are reported [24, 38] to react with organic (known as 'photo-oxidation') and inorganic (called 'photo-reduction') species such as;

$$HO^{\bullet}_2 + R\text{-}H \rightarrow H_2O_2 + R^{\bullet}$$

$$HO^{\bullet}_2 + R\text{-}H \rightarrow H_2O + R'^{\bullet}$$

Both liquid-gas and liquid-solid based reactions may occur simultaneously. For example, in a liquid-gas system the presence of dioxygen, and adsorbed oxygen species are the most probable electron acceptors [38]. Un-dissociated oxygen leads to the superoxide radical ion $O_2^{\cdot -}$

$$e^{-} + O_2 \rightarrow O_2^{\cdot -} \qquad \text{---------- Eq. [1]}$$

$$O_2^{\cdot -} + H^{+} \rightarrow HO^{\bullet} \qquad \text{---------- Eq. [2]}$$

In liquid water, two $HO^{\bullet}_2$ radicals can combine, yielding H_2O_2 and O_2 (called a 'dis-proportionate' reaction).

$$HO^{\bullet}_2 + HO^{\bullet}_2 \rightarrow H_2O_2 + O_2 \qquad \text{---------- Eq. [3]}$$

In turn, H_2O_2 can scavenge an electron from the conduction band to form the superoxide and accordingly be reduced to a hydroxyl radical $OH^{\bullet}$ and/or a hydroxide ion OH^{-}.

$$H_2O_2 + e^- \rightarrow OH^{\bullet} + OH^- \text{----------Eq. [4]}$$

$$H_2O_2 + O_2^{\bullet -} \rightarrow OH^{\bullet} + OH^- + O_2 \text{----------Eq. [5]}$$

If the following reactions are added with the stated stoichiometry:

$$5[1] + 4[2] + 2[3] + 1[4] + 1[5]$$

The following balanced reaction system is obtained:

$$5e^- + 5O_2 \rightarrow 5O_2^{\bullet -}$$

$$4O_2^{\bullet -} + 4\,H^+ \rightarrow 4HO_2^{\bullet}$$

$$2HO_2^{\bullet} + 2\,HO_2^{\bullet} \rightarrow 2H_2O_2 + 2O_2$$

$$H_2O_2 + e^- \rightarrow OH^{\bullet} + OH^-$$

$$H_2O_2 + O_2^{\bullet -} \rightarrow OH^{\bullet} + OH^- + O_2$$

$$2O_2 + 6e^- + 4H^+ \rightarrow 2OH^{\bullet} + 2OH^-$$

Which can be simplified to:

$$O_2 + 3e^- + 2H^+ \rightarrow OH^{\bullet} + OH^- \text{----------Eq. [6]}$$

These radicals then further attack organic and/or inorganic species present in the reaction system.

In a review by Hoffmann *et al.* [45] hydrogen peroxoide is formed upon UV-illuminated TiO_2 in the presence of air. Additional H_2O_2 and organic peroxide is also formed in the presence of organic scavengers such as:

$$TiOH^+ + RCH_2R`` \rightarrow TiOH_2^+ + RR``CH^{\bullet}$$

$$RR``CH^{\bullet} + O_2 \rightarrow RR``CHO_2^{\bullet}$$

$$RR``CHO_2^{\bullet} + R`H \rightarrow RR``CHOOH + R`^{\bullet}$$

$$R`^{\bullet} + O_2 \rightarrow R`O_2^{\bullet}$$

$$R`O_2^{\bullet} + HO_2^{\bullet} \rightarrow R`O_2H + O_2$$

Where

$RCH_2R``$ = organic electron donor with an abstract-able hydrogen

$RR``CH^{\bullet}$ = free radical intermediate produced by oxidation of $RCH_2R``$

Figure 2.2: Secondary reactions with activated oxygen species in the photo-electrochemical mechanism. [Reproduced from Hoffmann *et al.* [45]].

In most photocatalytic experiments, oxygen acts a primary electron acceptor. The formation of H_2O_2 (via two electron reductions of oxygen) and hydroxyl radicals on the surface of metal oxide (via reaction of h^+_{vb} with adsorbed H_2O, hydroxide or TiOH- surface titanol group) as shown in Fig. 2.2 is mainly responsible for the photocatalytic reaction propagation [45].

In short, the chemistry occurring at the surface of the photo-excited semiconductor in liquid-gas based photocatalysis depends on the radicals formed from O_2, H_2O and electron-rich organic compounds.

2.5 Photocatalytic Properties of Semiconductors

The photocatalytic properties of semiconductors play a very important role in overall photocatalytic activity. Many semiconductor materials such as TiO_2, ZnO, ZrO_2, CdS, MoS_2, Fe_2O_3, WO_3, and their various combinations have been examined as photocatalysts for the degradation of organic and inorganic pollutants. They all possess certain properties, which can be summarised as follows:

A semiconductor photocatalytic material:

- Should be capable of reversible change in its valance state to accommodate a hole without decomposing the semiconductor [48].
- Should have more than one stable valence state[48].
- Must be stable towards photo-corrosion [24].
- Must have suitable band gaps [24]. A list of the band gaps of some of the semiconductors used as photocatalysts is summarised in Table 2.1 (which is reproduced from [49]).
- Should be non-toxic [24].
- Must be cheap and easily available [24]
- Must be stable [50].
- Must have high photosensitivity [50].
- Must be easily deposited/grown onto an inexpensive substrate such as glass at a relatively low temperature [51].
- Must be able to display various formations of structure such as nano belts, nano wires, nano cages, nano combs, nano springs, nano rings, nano halides [52], and nano rods [8].

Zinc oxide, with valence state 2^+, was chosen for this study because it fulfils all of the requirements above.

Table 2.1: Band-Gap energies of semiconductors used for photocatalytic processes reproduced from Bhatkhande *et al.* 2002.

Photocatalyst	Band gap energy (eV)	Photocatalyst	Band gap energy (eV)
Si	1.1	TiO_2 rutile	3.0
WSe_2	1.2	Fe_2O_3	2.2
α-Fe_2O_3	3.1	TiO_2 anatase	3.2
CdS	2.4	ZnO	3.2
V_2O_5	2.7	$SrTiO_3$	3.4
WO_3	2.7	SnO_2	3.5
SiC	3.0	ZnS	3.7

2.6 ZnO as Photocatalyst

The most widely used and studied photocatalyst is currently titanium dioxide (TiO_2), of which most commercial use is from P25, manufactured by Degussa. However, many studies have reported that ZnO appears to be a suitable alternative to TiO_2 [42, 44, 50, 53-55]. Some of the most important reasons for this are as follows:

- ZnO has high photosensitivity, is stable and has a wide band gap [34, 53, 56, 57].
- It has high surface volume and quanta dimensions [58].
- Shao *et al.* [55, 58, 59] found that ZnO nano powder was photocatalytically very efficient in degrading MB and concluded that it could decompose a wide range of tough organic compounds.
- ZnO is widely available and nontoxic [14, 50].
- ZnO is available at low cost [44].
- ZnO can efficiently act as sensitiser for light-induced redox processes because of its favourable behaviour of filled valence band and empty conduction band upon UV/solar irradiation [60]. Other semiconductors such as TiO_2, Fe_2O_3, CdS and ZnS are also prone to similar characteristics [60].
- ZnO has been shown to be an economical alternative to the most commonly used TiO_2, especially in large water treatments [14, 59].
- ZnO has the ability to absorb a large fraction of the solar spectrum (because of its threshold value) than TiO_2 [55, 56, 61, 62], and its conventional photocatalytic reaction mechanism is found to be similar to TiO_2 [42].

- ZnO was found to be the most active under solar light in the photocatalytic degradation of phenol, compared to TiO_2 powder.[59].
- ZnO has been found to be more photocatalytically active than TiO_2 for a number of different compounds. For example, Sakthivel *et al.* [55] found it to be most active in the photocatalytic degradation of acid brown14 compared to other semiconductor metal oxides such as TiO_2, α-Fe_2O_3, ZrO_2, CdS, WO_3, and SnO_2. The order of photocatalytic activity was $ZnO > TiO_2 > \alpha\text{-}Fe_2O_3 > ZrO_2 > CdS > WO_3 > SnO_2$.
- Ullah *et al.* [63] concluded that a semiconductor with tailored optical absorption characteristics such as ZnO is capable of operating effectively and efficiently under UV irradiation to decontaminate wastewater.
- Above all, ZnO has the ability to demonstrate a multifaceted nature that has a diverse group of growth morphologies such as nano belts, nano wires, nano cages, nano combs, nano springs, nano rings, nano helix and nano rods [54].

In short, many studies [1, 62, 64-71] have successfully used ZnO (powder) as a photocatalyst to degrade harmful and toxic-compound streams, with many finding it to be superior to other photocatalysts.

2.7 Factors Affecting Photocatalysis

The photocatalytic activity of a heterogeneous photocatalytic process depends upon on a vast array of different factors, some having more impact than others. Some of the main parameters that may affect the reactions and engineering involved in heterogeneous photocatalysis are summarised below:

2.7.1 Suspended Versus Supported (Immobilised) Photocatalysts

Choosing whether the heterogeneous photocatalyst should be either suspended or supported, and how this is done, is one of the major challenges in the optimum design of a photocatalytic reactor. The methods of suspension and support within a reactor are addressed in Section 2.8.1. Here the issue of choosing between the two methods will be more fully addressed, since both suspended and supported photocatalysts have been employed in many studies: each has its merits and demerits.

A majority of studies have used the suspended form of photocatalyst to evaluate the effectiveness of the photocatalytic process in degrading typically recalcitrant and/or toxic

compounds present in wastewater streams. Suspended photocatalysts typically show a higher photocatalytic activity compared to supported catalysts because of an efficient mass transfer and better reactor design. The major disadvantage, however, is that suspended catalytic systems are extremely complicated to engineer since it is often difficult and expensive to separate the powdered catalyst from the product and/or waste streams. If this is not done, the catalyst goes to waste, unnecessarily increasing the waste disposal quantity and expense. Consequently, some researchers have attempted to recover the powdered catalyst but only at the expense of the process which usually did not remain economically viable [24, 72]. On the other hand, supported photocatalysts have had few issues of recovery at the end of the photocatalytic reaction, so long as the photocatalytic material remains intact and active throughout its lifetime (making lifetime mechanical strength and integrity, and photocatalytic activity with reuse two of the most important factors in evaluating supported/immobilised photocatalysts). In the supported format, the photocatalyst is usually anchored or fixed on a stable support such as fibre glass, metal fibres, steel mesh, steel plates, aluminium, plastics, silica [24] and zeolites [73]. Some of the major demerits of supported photocatalysts are the low surface to volume ratios, fouling and light scattering, and that they are usually less photocatalytically active compared to powdered catalysts [74, 75]. This problem can be overcome by preparing photocatalysts with high surface to volume ratios, such as nanostructured ZnO thin films. This work will characterise different nanostructured ZnO thin films under true and tough photocatalytic reaction conditions to address their stability, light scattering effect and fouling of the photocatalyst. Section 2.7.6.2 covers more on the known properties and characteristics of nanostructured thin films used as photocatalysts.

2.7.2 Catalyst Concentration/Catalyst Loading

Many studies have shown that the photocatalytic activity of the photocatalytic process depends on the amount/quantity of the catalyst used, which is normally given in terms of either concentration or catalyst loading. All studies have been for suspended catalysts and a summary of more important is shown below:

- Kabra *et al.* [24] determined that for an optimum photocatalytic activity, the optimal catalyst loading depends entirely on the type and dimensions of the reactor as well as the type and concentration of the oxidised compound.
- Daneshvar *et al.* [42] and Behnajadey *et al.* [61] found that photodegradation efficiency of Acid Red 14 and Acid Yellow 23 respectively increases with an increase in ZnO concentration, and then decreases. This decrease was due to the non-

availability of active sites on the catalyst surface and the penetration of UV light into the suspension. Total active surface area available for photocatalysis is directly proportional to the amount of catalyst powder.

- Deneshvar *et al.* [76] observed less penetration (due to scattering effects) of UV light due increased turbidity of suspension, which ultimately decreases the photo-activated volume of suspension. Sakthivel *et al.* [51] concluded that the photocatalytic reaction rate was decreased for the same reasons.
- Chiing-chang Chen [44] observed that the photocatalytic activity of ethyl violet first increased with an increase in ZnO concentration and then started decreasing when the catalyst loading was varied between 0.1 and 2 g/L under the same reaction conditions. He was of the view that aggregation may cause this decrease along with a decrease in the number of active surface sites, as well as a decrease in photonic flux within the irradiated solution.
- Koyal *et al.* [14] varied catalyst concentration from 0.5 to 3.5 g/L and showed that at higher loading levels, the irradiation field inside the reaction medium is reduced because of the light scattering by catalyst particles. He noticed a sharp increase in photocatalytic activity for Remazol Red PR, with the increase in catalyst loading up to 1.5 to 2g/L, decreasing beyond this limit.

From the above summary, it can be seen that for suspended photocatalysts, photocatalytic activity increases with the increase in the photocatalyst amount and then starts decreasing at high catalyst loading due to the following factors related to an increased turbidity:

- An aggregation of photocatalyst particles at high concentrations, causing a decrease in the number of surface active sites.
- An increase in opacity and light scattering of photocatalyst particles at high concentrations, leading to the decreased passage of photons through the system.

2.7.3 Effect of pH

The pH of the photocatalytic system plays a significant role in photocatalyst stability, photocatalytic activity and reaction mechanism. Many studies have been reported describing the impact of pH on the photocatalytic reaction solution. For ZnO this is particularly important, since it is amphoteric, and so can dissolve in both acidic and alkaline

environments [54, 77]. The Zn-pourbaix diagram (see Fig. 2.3) shows clearly the range of pH and voltage in which ZnO remains stable

Figure 2.3: Pourbaix diagram for Zn .[Reproduced from [78]].

The above described being one of the main disadvantages precluding the wider use of ZnO as a photocatalyst, it is addressed in this thesis work. There have been many other studies of the effect of pH on ZnO photocatalysts; selected studies and their important results are outlined below.

Daneshvar *et al.* [42] found that pH affects the photocatalytic degradation rate of colour removal efficiency of acid red 14 solution using ZnO (powder) as a photocatalyst. Khodja *et al.* [79] observed increased photodegradation efficiency in acidic compared to basic conditions. This increased photodegradation efficiency was due to photodecomposition of ZnO powder at a pH lower than 4 (acidic conditions). The photodegradation was due to the attack of photocatalytic induced holes (h^+) on ZnO as shown in equation 7:

$$ZnO + 2h^+ \rightarrow Zn^{+2} + O^* \qquad \text{----------Eq. [7]}$$

Whereas under basic conditions (pH=10) no photo-corrosion of ZnO took place and the formation of hydroxyl radical is favoured under basic conditions:

$$h^+ + OH^- \rightarrow OH^{\cdot}$$

However, overall Khodja *et al.* [79] found almost neutral conditions to be best for photocatalytic degradation because of the more efficient formation of a hydroxyl radical from hydroxyl ion than from water itself, or the higher oxidability of the anionic form of the model compound (2-phenylphenol) in comparison with the molecular form.

Chakrabarti *et al.* [70] studied the photocatalytic degradation of MB by using ZnO (powder). They noted decreased photocatalytic activity under acidic pH, attributed to high adsorption at low pH. The dissolution of ZnO under low pH has also been reported by Wang *et al.* [54]. Chakrabarti *et al.* [70] however also found that an excess of OH anions, under basic conditions, facilitated the photodegradation of hydroxyl radicals. They concluded that change in pH shifts the redox potentials of the valence and conduction band, which may affect the interfacial charge transfer.

Huihu *et al.* [54] and G Parks *et al.* [80] described a different perspective of the pH effect on photocatalytic activity associated with the zero point charge of a semiconductor photocatalyst for the degradation of solid hydroxide and aqueous hydroxo complex systems. The zero point charge (isoelectric point) of ZnO is 9. A pH greater than the zero point charge (ZPC) favours the formation of a hydroxyl radical and preferential cover of a negatively charged dye molecule (methyl orange) under a pH less than the zero point charge. Therefore an increased photocatalytic activity was observed at a pH higher than the zero point charge.

Poulios *et al.* [81] found an increased pH reduced the overall adsorption of pyridinyl oxyacetic on the oxide surface, and a gradual increase in electrostatic repulsion between pyridinyl oxyacetic anion and the oxide surface ultimately reduced the overall photocatalytic actvity.

Zouaghi *et al.* [82] showed that overall photocatalytic activity of Monolinuron and Linuron decreases because of the decrease in the rate of formation of an OH radical due to decreased OH ions concentration at a low pH. At a higher pH near to ZPC, an increased photocatalytic activity was noticed because of the increased rate of formation of the OH radical up to a certain pH closely associated with the zero point charge. With further increase in pH beyond the zero point charge the photocatalytic activity decreases because of the retardation in the rate of formation of the OH radical at the higher pH.

Han *et al.* [83] studied the dissolution of ZnO under various pH values for 24 hours and found dissolution of ZnO films to be highest at low pH values (3-5). The least dissolution of

ZnO was found to be at pH 10 and beyond this the pH dissolution rate was found to be increased, .as shown in Fig. 2.4.

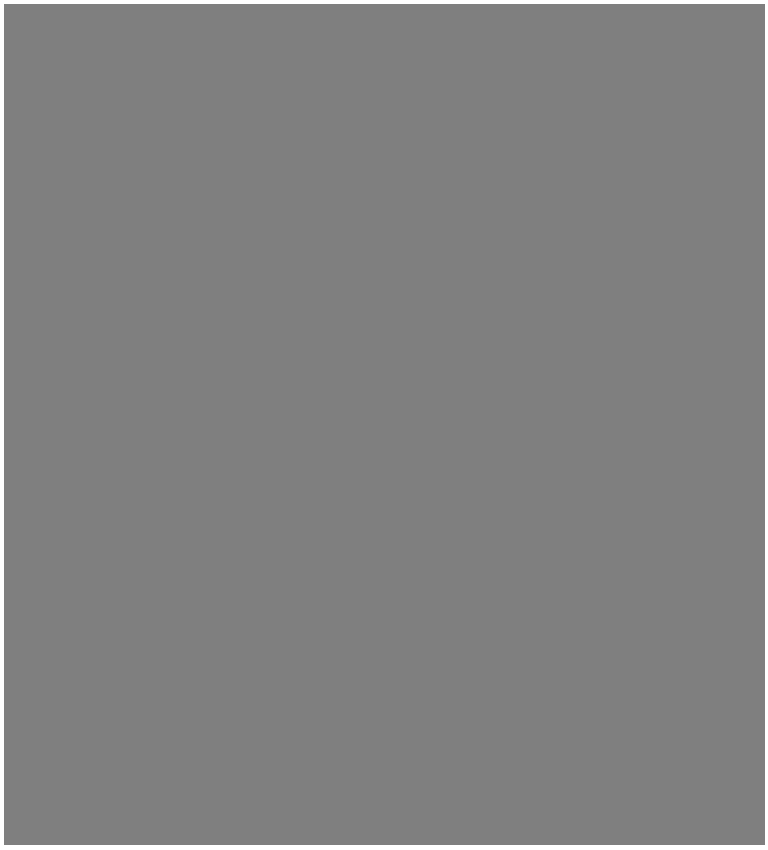

Figure 2.4: Dissolution of ZnO films in aqueous solutions at different pH level: (a) within 24 h; (b) after 24 h and 1 week. [Taken from Han *et al.* [83]].

The above studies do not clarify whether or not acidic or basic and/or neutral conditions are favourable to photocatalytic activity, but do establish that acidic conditions are detrimental to catalyst stability (since it dissolves). Consequently the monitoring and control of pH so that the solution does not become too acidic are important facets of photocatalytic work with ZnO.

2.7.4 Effect of UV Light Intensity and Wavelength

Ultra violet (UV) is a type of electromagnetic radiation having a wavelength higher than X-rays and lower than visible light. Its wavelength ranges from 10nm to 400nm and is composed of energies from 3eV to 124eV. It is known as ultraviolet because it has a frequency higher than that of the colour violet, the shortest wavelength band of visible light.

The source of UV is either from sunlight or a man-made UV source (ultra violet fluorescent lamps, black lights, ultra violet LEDS, ultra violet lasers, gas discharge lamps). Further categories of UV light are summarised in the table below, reproduced from Standard ISO 21348:2007E.[84]

Table 2.2: Types of UV radiation

Name	Abbreviation	Wavelength range in nanometres	Energy per photon
Ultraviolet A, long wave, or black light	UVA	400 nm–315 nm	3.10–3.94 eV
Near	NUV	400 nm–300 nm	3.10–4.13 eV
Ultraviolet B or medium wave	UVB	315 nm–280 nm	3.94–4.43 eV
Middle	MUV	300 nm–200 nm	4.13–6.20 eV
Ultraviolet C, short wave, or germicidal	UVC	280 nm–100 nm	4.43–12.4 eV
Far	FUV	200 nm–122 nm	6.20–10.2 eV
Vacuum	VUV	200 nm–100 nm	6.20–12.4 eV
Low	LUV	100 nm–88 nm	12.4–14.1 eV
Super	SUV	150 nm–10 nm	8.28–124 eV
Extreme	EUV	121 nm–10 nm	10.2–124 eV

UV radiation has wide applications, including security, forensics, astronomy, spectro-photometry, food processing, lasers, catalysis and many more [84]. The Beer-Lambert Law (also known as Beer's Law) is used to describe a relationship between absorption of light to the properties of material through which the light passes as absorption of UV induced photons by metal oxide is required to initiate UV induced electron-hole pair rather than to be absorbed by the bulk of the reaction fluid. Generally it is written as:

$$A = \varepsilon cl$$

Where:

A = absorbance of light

ε = molar absorptivity

c = concentration of the compound in the sample

l = sample path length

Photocatalysis needs irradiation of suitable photons, usually acquired from UV light. Suitable photons must have sufficient energy to excite the production of electron-hole pairs (as

described in Section 2.2.1). This depends on the wavelength of UV light and the nature of the photo-material. The overall energy applied during photocatalysis depends upon the light intensity (higher intensities give more energy) and wavelength (smaller wavelengths have more energy). Therefore, both intensity and wavelength are crucial to the photocatalytic processes.

2.7.4.1 Effect of light intensity

Ollis *et al.* [85] reviewed the impact of light intensity on photocatalytic decomposition and categorically stated that:

- Under low UV intensities the rate is linearly proportional to light intensity.
- For intermediate light intensities, the reaction rate depends on the square root of light intensity.
- For high light intensities, the reaction rate is independent of light intensity.
- A similar conclusion was confirmed by Yawalkar *et al.* [86]. Crittenden *et al.* [87] found that increased reaction rate was dependent on both light intensity and catalyst loading. However, the increased rate with light intensity depends on the catalyst dosage.

Moreover, boundaries between the relationships most likely depend on the catalyst and compounds being degraded. For example, Okamoto *et al.* [88] studied the photocatalytic decomposition of phenol by using anatase powder, concluding that both the initial reaction rate and the apparent rate constant depend upon the intensity of the light (I) of the UV irradiation. They observed a linear relationship between the reaction rate constant (k) and light intensity for reaction rates below 1×10^{-5}mol $m^{-2}s^{-1}$ and a relationship of k to $I^{1/2}$ if the reaction rate equals to 2×10^{-5}mol $m^{-2}s^{-1}$. Mehos *et al.* [89] reached a similar conclusion when studying the photocatalytic decomposition of trichloroethylene. They concluded that the phenomenon was due to the increased intensity of UV irradiation, which causes a greater generation of holes and a lesser chance of electron-hole pair recombination.

These relationships also affect photocatalysis with natural sunlight. For example, Ahmed *et al.* [90] studied the photocatalytic decomposition of trichloroethylene and chloroform over anatase TiO_2 with natural sunlight and found the initial reaction rate to be constant over the central period of the day. The variation of the total scattered sunlight was 10% over the central six hours of the day.

2.7.4.2 Effect of UV wavelength

Metal oxides (both doped and undoped) as photocatalysts can be conducted with different wavelengths, depending on the lamp employed. A wide range of wavelengths has been studied, mostly in the UV-A (320-380nm), UV-B (315-280nm) and UV-C(280-100nm) regions of electromagnetic spectrum supplied either by low, medium or high pressure mercury lamps. Few researchers have studied the effect of wavelengths in detail, however.

Puma *et al.* [91] studied the effect of the radiation wavelength on the degradation and reaction rate of organic pollutant 2-Chlorophenol over TiO_2 by using UV-A alone and a concomitant supply of UV-A, UV-B and UV-C radiations. They concluded that both rate of mineralisation and degradation were significantly increased under the combined supply of UV-ABC. They attributed this increased rate to the combined effect of photolysis, photocatalysis and synergistic effects.

Matthews *et al.* [92] observed that shorter wavelengths (254nm) are more effective for photocatalytic degradations than longer (350nm). This was because the optimum rate occurred with a lower catalyst loading than was required when using 350nm. Hofstadler *et al.* [93] reached the same conclusion: since a shorter wavelength has higher photocatalytic activity compared to a higher wavelength they suggested that this higher photocatalytic activity was because shorter wavelengths carry a higher photon energy. Similar results were also presented by Yue *et al.* [94] on the photocatalytic degradation of salicylic acid in an annular reactor. Bayarri *et al.* [95] used an annular reactor to study the effect of UV-A and UV-ABC radiations on two different model compounds, 2,4-dichlorophenol and sulfamethoxazole. They concluded that not only the wavelengths but also the properties of individual pollutants play a very important role in the photocatalytic activity of the system.

2.7.4.3 Overall implications of intensity and wavelength on photocatalytic activity/reaction rate

It has been observed that the photocatalytic reaction rate depends upon UV light intensity and wavelength. However, because of the gaps in literature such as behavior of a metal oxide - in particular supported ZnO – to UV light penetration path which presumably strongly depends on surface morphology, crystal alignment and mass transfer limitations, no specific model or study has yet characterised the effect of UV wavelength on photocatalytic reactions with metal oxide thin films, in particular for both doped and undoped ZnO nanostructures. Consequently, this will be studied in this work.

2.7.5 The Effect of Photocatalyst Type: Preparation Technique/Method

Thin film metal oxide photocatalysts can be prepared using a range of different methods, each of which affects the resulting morphology, composition, crystallinity and mechanical properties (amongst other properties). The methods usually used to prepare thin films can be classified into two main categories: physical deposition techniques and chemical deposition techniques.

Some of the physical deposition techniques are as follows:

- Physical vapour deposition [34]
- Magnetron sputter deposition [10, 96-99]
- Pulsed laser deposition [100]
- Wet impregnation deposition [101]
- Thermal evaporation deposition [34]
- Physical dip coating deposition [102]

Similarly, some of the chemical deposition techniques are as follows:

- Chemical vapour deposition [103, 104]
- Molecular beam epitaxy deposition [105]
- Anodising [106]
- Sol-Gel [107, 108]
- Atomic layer deposition [109]
- Micro-emulsion deposition [110]
- Chemical dip coating deposition [111]
- Spray pyrolysis [53]

Chemical deposition techniques are usually harder to employ compared to physical deposition techniques because of their inherent complexity involved in a chemical reaction. Another drawback is the film thickness quality, usually that of non-uniformity. Chemical deposition processes usually take much longer to generate film thickness (to some microns) because of the post treatment involved. On the other hand, physical deposition techniques are easy to manipulate to obtain more desired thin film. For the physical deposition techniques, the sputtering method is most favoured and widely used in the preparation of nanostructure thin films because of the ease with which one can control the film-forming parameters. It is however, difficult to scale up. Overall, oxygen concentration, pressure, and flow rate play

significant roles in obtaining various types of thin films, each having a different nature of microstructure and surface morphology. Prof Wei Gao and his research group have produced a novel approach to preparing nanostructure semiconductor metal oxide based on a combination of both physical and chemical deposition. i.e: sputter coating and hydrothermal deposition [7, 8, 10, 112]. The application of different ZnO nanostructured films fabricated by this method will be studied in this work for the first time.

It has been found that the preparation technique directly affects the photocatalytic nature of supported or suspended photocatalysts. For example, Li *et al.* [113] found that a change in the crystallinity of the ZnO, prepared under two methods under equal conditions (apart from calcination temperature), affects the photocatalytic activity of ZnO more than the surface area of the same original ZnO powder. Wang *et al.* [54] prepared ZnO nano-powder by two different methods: chemical deposition and thermal evaporation. The photocatalytic activity of ZnO (10nm) powder obtained through chemical deposition was lower than the ZnO powder (200nm) obtained by thermal evaporation. Eufinger *et al.* [98] prepared TiO_2 thin films deposited by D.C. magnetron sputtering. The chemical activity of the catalyst depended on the active sites and total available surface area, which could be controlled by varying argon gas pressure within the same preparation technique.

The reagents employed to prepare ZnO nanostructure thin films, particularly via the hydrothermal deposition technique [7, 8, 10, 112], also have much significance on the final thin film type and morphology. For example, an additional reagent's nature and its concentration in the preparation of ZnO thin films play a pivotal role in the thin film formation mechanism. Take for example hexamethylenetetramine (HMT) [114]:

- The HMT molecule acts as a template for nucleation of ZnO because of its similarity to the ZnO crystal along the direction [0, 0, 1].
- It acts as a surfactant and gives passivity to the surface of ZnO particles against excessive growth and further reaction by reducing the surface tension of ZnO particles.
- It is a source of NH_4OH (generated by the decomposition of HMT in water), which is useful in the formation of $Zn(OH)_2$.
- It acts as a condensation agent to produce ZnO.
- The increased ratio of HMT to $Zn(NO)_3$ presses down the formation of $Zn(OH)_2$, which ultimately causes less production of ZnO via condensation.

Similarly, the aspect ratio of ZnO crystals can be controlled by regulating their nucleation and growth through the use of organic molecules such as citrate [115].

Overall, the type of preparation technique, reagent(s) and parameters used within ZnO can dramatically affect the nature of the obtained photocatalyst. Even a small change in one of the parameters may lead to new photocatalytic characteristics (such as morphology, composition, crystallinity and/or mechanical properties). Therefore one has to be very careful in selecting a suitable technique to produce a photocatalyst with the desired properties and then to achieve a reproducible uniform photocatalyst; huge attention must be paid to keep exactly the same working parameters.

In this work, hydrothermal growth combined with a magnetron sputtered template was chosen since it generates highly porous metal oxide films with a large surface area.

2.7.6 The effect of Surface Morphology

'Morphology' is a term used to study the form and nature of the structure and its arrangement. Many researches (the more important of which are summarised below) show that it plays a crucial role in determining an efficient and effective catalyst and photocatalyst. For semiconductor ZnO, the two major forms are either powder or ZnO thin film on a substrate, both of which can have a wide variety of surface morphologies. ZnO has been widely prepared as nano wires, nano cages, nano belts, nano combs, nano springs, nano helix, nano powder, nano fibre, nano crystal, nano particles and nano flowers [52, 66, 116-120]. However, not all morphologies of ZnO have been tested as a photocatalyst.

2.7.6.1 ZnO (Powder) as photocatalyst

Most of the available photocatalytic studies have used ZnO in the form of nano powder, nano crystalline powder, nano flowers and micro rods. It has been found that the particle morphology of ZnO powder does affect the photocatalytic activity of a ZnO as a photocatalyst:

Li *et al.* [113] prepared different samples of ZnO powders (mono-dispersed spherical particles, intertwined ellipsoidal aggregates, rod-like and intertwined needle aggregates) obtained from three different preparation methods. He concluded that the particle morphology has a very close association with increased photocatalytic activity along with other parameters such as crystallinity and/or surface area.

Wang *et al.* [54] prepared two different morphologies (tetra-pod and irregular) composed of four different sizes of ZnO nano powders (mean diameter size: 10, 50, 200 and 1000 nm) by using two different preparation methods: chemical deposition and the thermal evaporation (or evaporation condensation) method. Irregular ZnO nano particles were obtained from the evaporation-condensation method, whereas chemical deposition produced ZnO nano-colloidal particles composed of rods and hexangular shapes. He observed that the smallest ZnO nano powders (10nm) did not show the highest photocatalytic activity; instead, 50nm ZnO nano powders had the highest (compared to their counterpart 10, 200 and 1000 nm ZnO nano particles). He also noticed that tetra-pod morphology obtained from thermal evaporation is more photocatalytically active compared to irregular ZnO nano powders.

Jang *et.al* [121] prepared two different morphologies of ZnO (nano particles and nano crystalline particles) having the same size (20nm) by using the same technique (spray pyrolysis) under two different conditions. ZnO nano particles were more photocatalytically active compared to nano crystalline particles.

Moghaddam *et al.* [122] prepared 30nm spherical ZnO nano powders by using microwave assisted solution growth. He found that the ZnO nano powder was 24 times more photocatalytically active compared to the larger ZnO bulk powder. A similar conclusion was made by Hariharan [119] during photocatalysis of a waste composed of several organic contaminants in water.

Finally, Jimin *et al.* [120] obtained ZnO micro flowers (1.7μm) and micro rods by using the thermal decomposition technique using two reagents under different modes. Micro flowers proved to be more photocatalytically active compared to nano rods for a Friedel-Craft acylation of anisole and benzoyl chloride.

2.7.6.2 ZnO thin films

There has been little literature cited on using ZnO as a photocatalyst in the form of a supported ZnO thin film. Of those attempted, the usual support/ substrates were glass or pure silicon.

Fouad *et al.* [34] prepared needle-like (10-80nm) ZnO thin films on a silicon substrate by using thermal physical vapour deposition. He found these film morphologies to show high photocatalytic activity at low pH (=2). However, he did not mention/study anything on the effects of surface morphology after photocatalysis.

C.Hariharan [119] prepared 'ZnO nano' (both nano powder having size of 39nm and thin films on quartz substrate). He concluded ZnO nano was more photocatalytically active compared to bulk ZnO and commercially available Degussa (P25). However, he did not correlate the stability, reproducibility and effects of surface morphology after photocatalysis.

Jun *et al.* [123] tested the photocatalytic activity of ZnO thin films (floccule-like ZnO) obtained from two-step thermal oxidation of dc-magnetron sputtered Zn films on a glass substrate and found the photocatalytic activity of these films to depend on the temperature of the photocatalytic reaction liquid.

Thus, as far as this author can tell from the available literature, there is little information on the effect of surface morphologies on the photocatalytic characteristics of supported ZnO thin films. There have been a few studies studying just one type of morphology, researchers which have found these films to be photocatalytically active [66, 116-120]. However the effect of surface morphologies obtained under different parameters using the same techniques has not been studied, until now. Similarly, the relationship between photocatalytic activity and surface morphologies before and after photocatalysis, reusability and reproducibility of the reaction rates, and the photocatalytic reaction mechanism of nanostructured ZnO thin films, has not been studied yet to establish that ZnO thin films (supported) could be strong and efficient candidates as photocatalysts.

Overall, since morphology is related to both UV-exposed surface area, crystallinity and other effects such as shadowing, mass transfer, porosity and conductivity, all of which affect photocatalytic activity, it will always have a significant effect on photocatalytic activity.

2.7.7 Effect of Crystallinity

Crystallinity is also one of the most important parameters that may affect the photocatalytic activity of the photocatalyst. Eufinger *et al.* [98], Yubuta *et al.* [124] and Tavares *et al.* [97] found that photocatalytic activity increased with increased crystallinity of the semiconductor metal oxides tested (TiO_2 and ZnO). Similarly Li *et al.* [113] concluded that the photocatalytic activity of various ZnO powders depends on crystallinity rather than a surface area; however, he was unable to predict a specific relationship between photocatalytic activity, crystallinity and surface area. However, increased crystal structure may not necessarily improve photocatalysis as pointed out by Jang *et al.* [121] who found that nano-particles of ZnO were more photocatalytically active than nano-crystalline ZnO particles. This was in fact due to a difference in the surface area (58 m^2/g and 15 m^2/g for nano-

particles and nano-crystalline particles respectively), which is well known to increase the photocatalytic activity in heterogeneous photocatalysis.

2.7.8 Effect of Dissolved Oxidant

In the conventional mechanism of photocatalysis (see Section 2.4), both the electron and hole play an important role in the initiation of a photocatalytic reaction. Beyond this, the oxidant plays a vital role in the propagation of the reaction, and it is the electron that is usually taken up by the oxidant molecule present in the bulk fluid. Three major sources of dissolved oxidant are mentioned in the literature [38]:

- Oxygen gas (O_2)
- Hydrogen peroxide (H_2O_2)
- Ozone (O_3)

Each source of oxidant plays a particular role in the photocatalytic oxidation, as summarised in the next subsections:

2.7.8.1 Effect of dissolved oxygen

The most favourable source of oxidant is dissolved oxygen, the presence of which plays an important role in the photocatalytic degradation of the molecules under consideration. Dissolved oxygen usually participates in three ways in the overall degradation of a model compound:

- Dissolved oxygen can easily scavenge an electron at the surface of a UV-irradiated semiconductor metal oxide, which aids in the separation of photo-generated charges; this decreases the recombination of generated electron-hole pairs.
- Dissolved oxygen present in the bulk of the reaction fluid can also react with alkyl radicals (usually from organic pollutants), yielding peroxyl radicals, which are very helpful in the overall mineralisation of an organic molecule.
- The radical anion superoxide can easily react with an organic radical cation (obtained through the possible reaction of a hole with electron-rich organic pollutant) to initiate one of the primary steps in the overall degradation of organic pollutants.

Due to the multiple roles of oxygen, photocatalytic reactors used in the waste treatment process should always allow air or O_2 gas to be easily accessible to the semi-conductor metal oxide surface: i.e., rates of gas (O_2) to liquid (aqueous solution of pollutant) and from liquid

to solid (catalyst) should be maximised [125]. The maximum availability of O_2 can be achieved by:

- Supplying/bubbling of O_2 gas into the photocatalytic reaction vessel.
- Bubbling air into the photocatalytic reaction system.
- Generating a turbulent flow of the aqueous solution into the air in order to entrain/capture oxygen.

Kara *et al.* [24] showed that dissolved oxygen either supported or hindered the photocatalytic reaction, depending on the degradation pathway/mechanism of the photocatalytic process. Peterson *et al.* [126] suggested that one of the primary roles of dissolved oxygen is to act as an electron sink for the photo-generated carriers. Shirayama *et al.* [127], calculating the degradation rates both under dissolved oxygen and without the presence of oxygen, found elevated rates in the absence of oxygen. The decreased rate under dissolved oxygen was due to reduced UV light intensity in the photoreactor as molecular oxygen has a tendency to absorb light. In contrast, Wang *et al.* [128] confirmed an increased photocatalytic reaction rate under dissolved oxygen as it plays a pivotal role in the photocatalytic degradation rate of 2-chlorobiphenyl (which was used as the model compound).

Oxygen was used as the oxidant in this work because of the multiple potential benefits outlined above.

2.7.8.2 Effect of H_2O_2

Another oxidant is hydrogen peroxide H_2O_2, which can both dissociate directly to hydroxyl radicals and also release oxygen molecules during its disproportionation. The use of H_2O_2 may increase or decrease the photocatalytic activity of a photo-degradation process, because despite the fact that it can produce oxidising radicals, the hydroxyl radical may also react with added H_2O_2 instead of reacting with pollutants/organic compounds [38]:

$$OH^{\cdot} + H_2O_2 \rightarrow H_2O + HO^{\cdot}_2 \qquad (8)$$

One must therefore be careful in employing H_2O_2 as the oxidant source, since the total impact of H_2O_2 on photocatalysis is not clear. Consequently it was not used in this work.

2.7.8.3 Effect of ozone

Ozone has more electron affinity (2.1eV) compared to oxygen (0.44eV). Therefore, the presence of ozone is usually assumed to be favourable in capturing photo-generated electrons directly (as shown in equation 9a) or indirectly (as shown in equation 9b) during a photocatalytic process.

$$e^- + O_3 \rightarrow O_2 + O^{\bullet -} \qquad (9a)$$

Or

$$O_2^{\bullet -} + O_3 \rightarrow O_2 + O_3^{\bullet -} \qquad (9b)$$

Due to the highly unstable nature of $O_3^{\bullet -}$, it presumably splits on the catalyst surface and generates $O^{\bullet -}$ radicals, which increase the photocatalytic activity of the photocatalyst. Ozone was not used in this work, however, due to the added complexity and expense of generating and storing this unstable compound.

2.7.8.4 Overall effect of oxidant

Overall, the presence of oxidant is generally favourable in enhancing the photocatalytic activity of the photocatalytic system. However, the above literature shows the care that must be taken when selecting the source of oxidant.

2.7.9 The Effect of Mass Transfer

The interaction of the reagent as well as the intermediate and product mass, with the catalyst, in a photocatalytic system plays a significant role in determining the overall photocatalytic activity of a photoreactor. Usually two modes (suspended and immobilised form) of catalyst are employed to degrade a model pollutant in a photoreactor (see Section 2.8 for further details). Due to the size of the catalysts used (usually ultra fine) minimal or no internal mass transfer limitations exist for a suspended system as the maximum diffusion distance is very small [129]. Significant external mass transfer limitations can occur if the system is not well mixed or the catalyst loading is too high (making the system difficult to mix). Suspended catalysts are not favourable because of the aforementioned complications in the post reaction separation of the suspended catalyst from the reaction product. As also mentioned, this

problem can be eliminated by using the catalyst in an immobilised form. However, catalyst immobilisation can cause the following issues, as summarised by Ding *et al.* [130]:

- There is lower accessibility of the catalyst surface to the irradiated photons and various reaction intermediates produced during the photocatalysis.
- The influence of external mass transfer (i.e. transfer of fluid from the bulk solution to the surface of the catalyst) becomes significant especially at very low flow rates, due to the increased diffusional length of the reactant from the bulk solution to the catalyst surface.
- With an increase in catalyst film thickness, internal mass transfer (transfer of the fluid present in the vicinity of the support-catalyst interface) may play a dominant role in photocatalytically active efficiency by limiting the utilisation of the catalyst near the support-catalyst interface.

Fig. 2.5 shows a schematic representation of both internal and external mass transfer issues in the immobilised form of a catalyst.

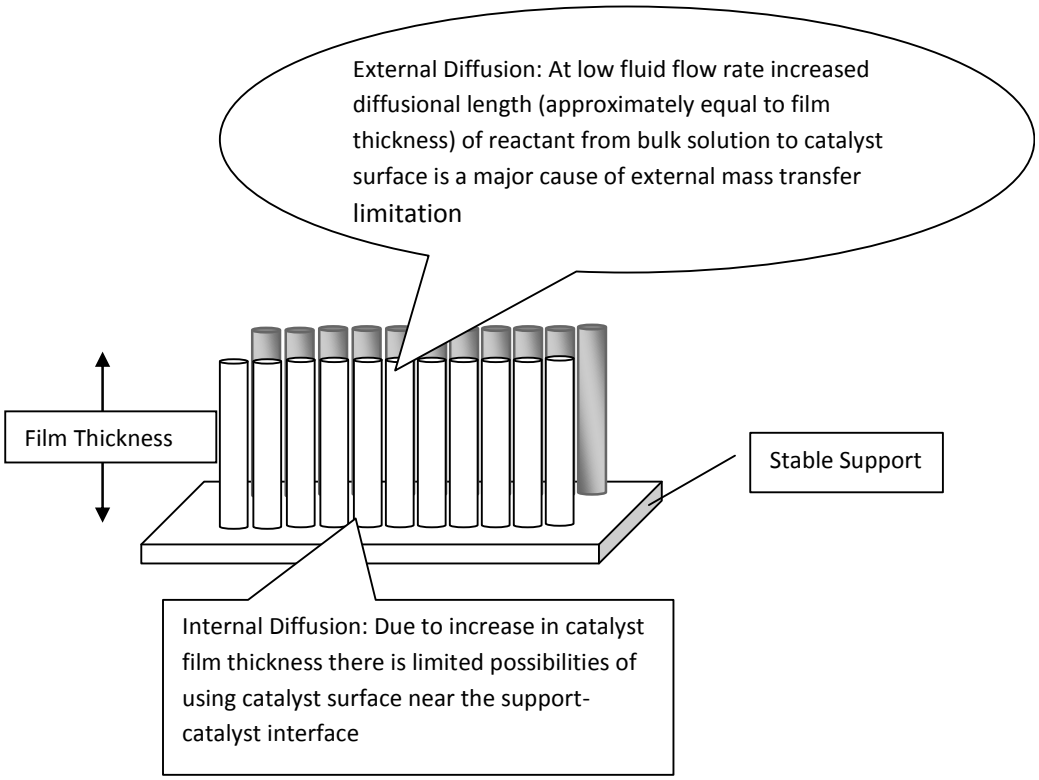

Figure 2.5: Explanation of mass transfer in supported metal oxide photocatalyst.

Some studies have tried to model the above mentioned mass transfer issues:

Goetz *et al.* [131] investigated a possible relationship between mass transfer and irradiated photonic flux at the surface of the semiconductor metal oxide by deploying immobilised TiO_2 under sunlight using Atrazine (a herbicide). He concluded that the apparent rate constant depends on both the mass transfer coefficient (directly linked to the flow conditions inside the photoreactor) and photon flux. Dingwang *et al.* [130] studied some important modelling parameters such as both external and internal mass transfer coefficients, dynamic adsorption equilibrium constant, adsorption rate constant, and effective diffusivity, both experimentally, and by fitting realistic models to the data obtained from the photocatalytic decomposition of benzoic acid as a model compound; they found that the reaction rate was controlled by internal mass transfer resistance. Similar parameters were also studied by Chang *et al.* [33]. Dijkstra *et al.* [132] used modelling to try to determine how to overcome the mass transfer issues in immobilised photocatalyst systems and found that the adsorption of the model compound (formic acid) and the oxidant source (oxygen) on the catalyst layer appeared to play an important role in the photocatalytic activity. A mixing phenomenon was used to overcome the external mass transfer limitations. They observed increased reaction rate, because of the increased mass transfer coefficient, with the increase in Reynold's number at increased mixing of the fluid. This increase in reaction rate was due entirely to the increased external mass transfer coefficient, as the supply of oxygen remained constant at saturation level.

In general, the literature shows that the models used to quantify both internal and external mass transfer issues are complex and difficult to apply to the data obtained from the photocatalytic reactions and reactors studied. Usually, these models require multiple data sets obtained under many different sets of conditions. Consequently, the easiest possible solution to overcoming the problem of mass transfer related issues is to eliminate it. To do this, a parameter such as Reynold's number (ratio of inertial forces to the viscous forces, e.g. for a magnetically stirred tank reactor, such as that used in this study: $N_{Re} = \frac{D^2}{\mu} N \rho$ [133-137]) can be evaluated in order to determine if the reactor is mixed well enough to eliminate (or at least minimise) mass transfer limitations. This approach was taken in this work.

2.8 Photocatalytic Reactors

Both suspended (free) and supported/immobilised catalyst photo-reactors have been developed to accommodate the use of these two different modes of catalyst. Each has its own advantages and disadvantages. In the present study, the aim is to use glass-supported nanostructured ZnO thin films, to permit the continuous use of the photocatalyst, eliminating the need for post-process filtration coupled with particle recovery and catalyst regeneration. ZnO can be grown on inexpensive substrates, such as glass, at relatively low temperatures in a variety of nanostructures. These structures are ideal for photocatalytic applications due to their large surface area to volume ratio [7, 51, 112]. In this study, the reaction rate, reaction mechanism, deactivation, stability and reusability of these nanostructured ZnO thin films are to be evaluated in order to propose a relationship between photocatalytic activity, surface morphology and reaction mechanism. The types of reactors and fixed parameters used in doing this are crucial.

It has been well documented [138] that many types of reactors have been employed to study the photocatalytic degradation rate of both organic as well as inorganic compounds. Photocatalytic reactors for various studies can be classified into three main categories, owing to their design characteristics:

- State of the photocatalyst
- Type of illumination
- Position of irradiation source

2.8.1 Classification of Photoreactor on the Basis of the State of the Catalyst

As mentioned previously in Section 2.7.1, metal oxides used as photocatalysts are used either suspended or attached/grown to a stable support. Based on this, the category can be further divided into two main types:

a. Slurry reactor
b. Immobilised/supported photocatalytic reactor

Details are described in the following sections.

2.8.1.1 Slurry reactor

In slurry type photocatalytic reactors, the photocatalysts are usually well mixed in an aqueous solution of the model compound or pollutant.

Several different types of slurry reactors [138-142] are employed to study the photocatalytic reaction systems of various metal oxides with different reactants, including: Integrated Flow Reactor Membrane with Filtration System (Fig. 2.6), Taylor Vortex Reactor (Fig. 2.7), Plug Flow Annular Reactors (Fig. 2.8), Open Up-flow Reactor (Fig. 2.9), Swirl Flow Reactor (Fig. 2.10), and Turbulent Slurry Reactor (Fig. 2.11).

Figure 2.6: Schematic diagram of the integrated photo-reactor-membrane UF system. [Reproduced from Lasa *et al.* [138]].

Figure 2.7: Taylor vortex reactor in operation. [Reproduced from Lasa *et al.* [138]].

Figure 2.8: Plug flow annular reactor. [Reproduced from Biard *et al.* [139]].

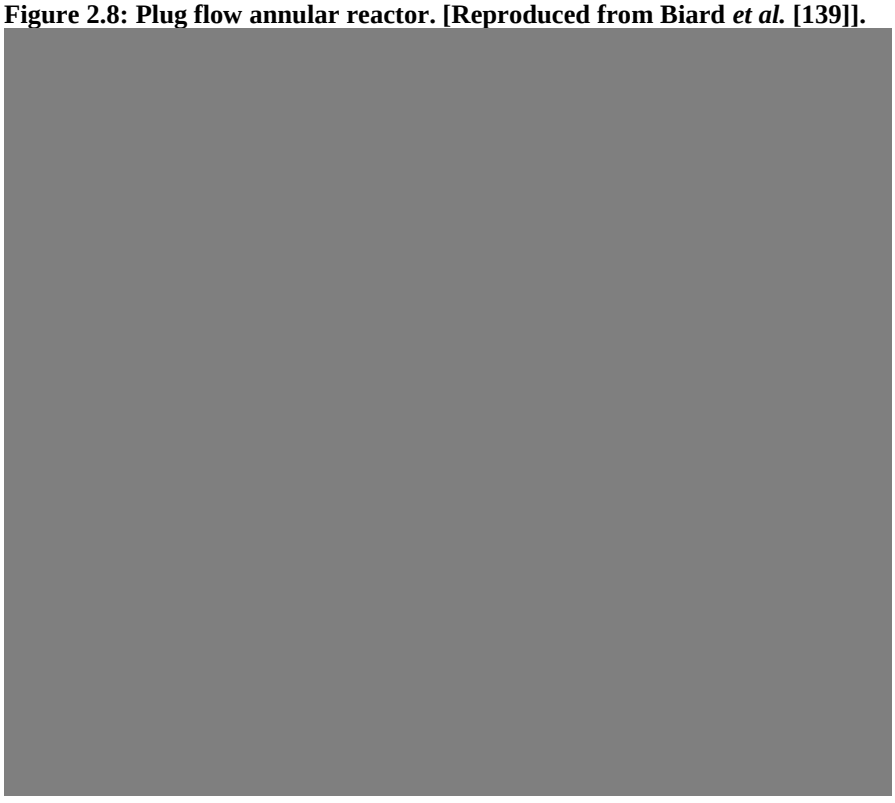

Figure 2.9: Experimental Up-Flow system; 1: glass jacket reactor; 2: UV lamp; 3: tank; 4: solution; 5: centrifugal pump; 6: cryostat of circulation water; 7: quartz jacket; 8: water inlet;9: water outlet; 10: flow meter; 11: valve; 12: bypass; 13: air pump. [Reproduced from Merabet *et al.* [140]].

Figure 2.10: Swirl Flow Reactor. [Reproduced from Ray *et al.* [141]].

Figure 2.11: Turbulent slurry photocatalytic reactor for hydrogen production. [Reproduced from Xiaowei *et al.* [142]]

Most studies [1, 59, 64, 67, 143-146] have used slurry-type reactors to characterise the photocatalytic nature of metal oxide solids. This type of reactor usually gives a high photocatalytic activity compared to a photocatalytic reactor with an immobilised photocatalyst because of mass transfer limitations, poisoning, and deactivation with the immobilised photocatalyst [147].

Matthews *et al.* [148] performed a comparative study of the photocatalytic activity of TiO_2 for both slurry and solid immobilised reactor types (as shown in Fig. 2.12). The reactor

configurations for different modes (suspended and slurry) were the same, except for the catalyst mode used: TiO_2 coated sand and TiO_2 powder. They found that the slurry type photocatalytic reactor had a three times greater photocatalytic activity compared to the reactions with the immobilised catalytic reactor, mainly because of the mass transfer limitations, low concentration driving force between the solution, and the catalyst surface.

Figure 2.12: Open dish illumination arrangement. A, Pyrex glass dish; B, TiO_2 coated sand; C, solution; D, peristaltic pump; E, 100 W medium pressure mercury lamp. [Reproduced from Matthews *et al.* [149]]

In spite of the fact that the slurry-type photoreactor has a high photocatalytic activity, its greatest disadvantage is the separation of the powdered catalyst from the reaction products and photocatalytically treated compounds(s). This separation step is usually highly complicated because of the very small size of the powder (usually in microns), and increased capital cost of the treatment process. Secondly, one needs to carefully consider complications in the total adsorbed amount of radiation at higher catalyst loading (i.e. increased shadowing) decreasing the efficiency of a photocatalytic system, this because of the decreased UV light penetration due to higher turbidity [150].

2.8.1.2 Immobilised reactor

A reactor in which the photocatalyst is fixed (usually the outer surface of the UV source casing), or anchored on a stable support via various physical or chemical deposition techniques, is an immobilised photoreactor. Some of the main types of immobilised photoreactor [138] are: Falling Film Reactor (Fig. 2.13), Fibre Optic Cable Reactor (Fig. 2.14), Multiple Tube Reactor (Fig. 2.15), Packed Bed Reactor (Fig. 2.16), Rotating Disk

Reactor with Controlled Periodic Illumination (Fig. 2.17), and the Tube Light Reactor (Fig. 2.18). This type of reactor has an intrinsic advantage over slurry photoreactors, as it does not require any separation of the photocatalyst, the catalyst not being present in the aqueous stream of pollutant(s) or model compound. Secondly, immobilised photocatalyst photoreactor systems allow the researcher to use the catalyst continuously, without any need for post − reaction filtration coupled with particle recovery and catalyst regeneration. The usual problems with immobilised photoreactors are summarised below [138]:

- Low surface area to volume ratios
- Catalyst fouling or catalyst wash out
- Difficult ‘in situ’ catalyst regeneration
- Significant pressure drop
- Light scattering
- Poor mass transfer

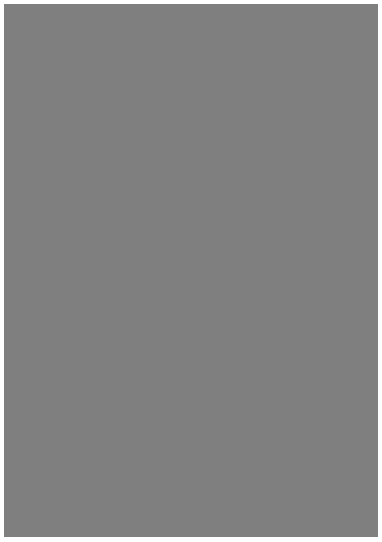

Figure 2.13: Schematic representation of the Falling Film Reactor. [Reproduced from Lasa *et al.* [138]]

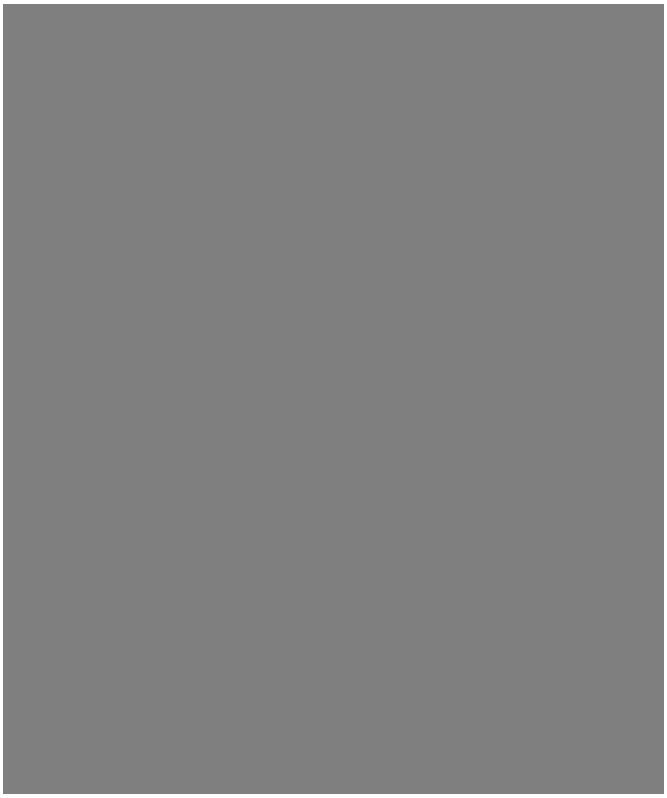

Figure 2.14: Schematic representation of the optical-fibre bundled array photocatalytic reactor system. [Reproduced from Lasa *et al.* [138]]

Figure 2.15: Schematic representation of a multiple tube reactor. [Reproduced from Lasa *et al.* [138]]

Figure 2.16: Annular packed-bed reactor. [Reproduced from Lasa *et al.* [138]]

Figure 2.17: Rotating disk reactor, (a) variable speed motor, (b) Pyrex reactor wall, (c) support disk, (d) TiO_2 catalyst coating, and (e) quartz base plate. [Reproduced from Lasa *et al.* [138]]

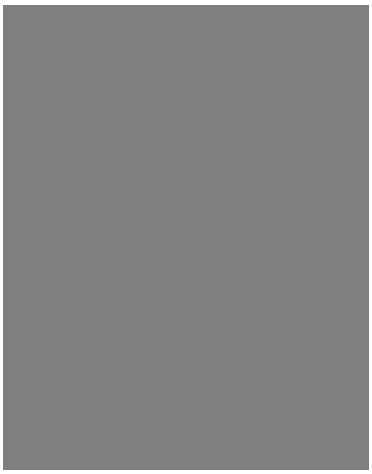

Figure 2.18: Tube light Reactor (TLR). [Reproduced from Lasa *et al.* [138]]

Many researchers have attempted to study the photocatalytic activity of a photocatalyst by using one that has been immobilised [3, 34, 45, 119, 151]. Advantages and disadvantages of both slurry and immobilised photoreactors are summarised in Table 2.3, reproduced from [138].

Table 2.3: Comparison of slurry and immobilised photo-reactors reproduced from [138].

Slurry Reactors	Immobilized Reactors
Advantages • Fairly uniform catalyst distribution • High photocatalytic surface area to reactor volume ratio • Limited mass transfer • Minimum catalyst fouling aspects • Low pressure drop Disadvantages • Requires post-process filtration • Important light scattering and adsorption in the particle suspended medium	Advantages • Continuous operation • Improved removal of organic material from water phase while using a support with adsorption properties • No need for an additional catalyst separation Disadvantages • Low light utilisation efficiencies due to light scattering by immobilised photocatalyst. • Restricted processing capacities due to possible mass transfer limitations • Possible catalyst deactivation and catalyst wash out.

2.8.2 Classification of Photoreactor on the Basis of Type of Illumination

Another category in which a photo-reactor can be classified is on the basis of type of illumination [138]. Both artificial UV light source and natural UV light source (sunlight) are employed to study the photocatalytic activity of a photocatalyst. On this basis the reactor can be classified into:

- Artificial UV light sources.
- Natural UV light sources (i.e. sunlight)

Artificial UV light source photoreactors can be further divided into two types:

- Monochromatic UV lamp Photoreactor
- Polychromatic UV lamp Photoreactor

High, medium and low pressure mercury lamps, either monochromatic or polychromatic, were employed to examine various photocatalytic studies. High to medium pressure lamps usually provide non-uniform photon flux compared to low pressure mercury lamps with more consistent and uniform photon flux [152].

On the basis of this, a low pressure mercury lamp was used as an artificial UV light source.

Similarly, photoreactors based on solar light can be further categorised into two types:

- Non-concentrated photoreactor (one in which irradiation intensities are equal to or less than natural solar irradiation).
- Concentrated photoreactor (one in which irradiation intensities surpass the irradiations equivalent to one sun).

Both non-concentrated and concentrated photoreactors have their merits and demerits. The merits are negligible optical loss, direct and diffuse light utilisation (for non-concentrated reactors), and small reactor volume and harvesting area (for the concentrated reactor). However, the demerits are considerable, such as high frictional losses (for non-concentrated reactors), and high investment cost, square root dependence between efficiency and radiation intensity (for concentrated reactors), making them less favourable to use at laboratory scale [138].

2.8.3 Classification of Photoreactors on the Basis of Position of the Irradiation Source

The third category of photoreactors is based on the position of the irradiation source. On this basis, the photoreactor is further divided into three types:

- Photoreactor with immersed light source
- Photoreactor with external light source
- Photoreactor with distributed light source.

For the immersed type of photoreactors, the UV light source/lamp is placed within the reaction vessel. On the other hand, for photoreactors with an external light source, the UV lamp/source is located outside the reaction vessel. In distributed/divided photo-reactors, UV

light is usually transported from the UV source by optical means, such as reflectors or light guides etc.

Many researchers had attempted both solar as well as artificial UV light sources:

Kabra *et al.* [24] showed that the overall cost of a photocatalytic reactor can be minimised by using sunlight as the UV light source for many applications. Both concentrated and non-concentrated types of photoreactors can use solar light; each has its own benefits and demerits. The concentrated photoreactors were easy to use because of their small reactor tube area whereas non-concentrated systems can easily collect and use both diffused and direct light. Kabra *et al.* [24] also reviewed and compared the advantages and disadvantages of two different photo-reactor designs: a low concentrated radiation system (with a compound parabolic concentrator reactor) and medium–concentrated radiation system (with a parabolic trough collector reactor), for the photocatalytic oxidation of 2,4-dichlorophenol (DCP) using TiO_2 suspensions at pilot plant scale. The compound parabolic-concentrated reactor showed higher efficiency compared to the medium-concentrated reactor under cloudy conditions, whereas little difference was noticed on a clear day. Kabra *et al.* [24] had also reviewed the economics of three different reactors: a parabolic trough (PTR) collector, a plexi glass double skin sheet (PDSS) reactor, and a thin-film fixed-bed (TFF) reactor. Both the PDSS and TFF reactors were extremely useful in using total global UV irradiation, with simple construction and low investment, whereas the PTR needs high investment and can absorb only direct UV irradiation, which is 50% of global UV sunlight.

Zhang *et al.* [153] studied phenol degradation using a rotating drum coated with Pt-loaded TiO_2 on the outer surface, under solar light and utilising oxygen from the atmosphere. The reactor was found to be very efficient, degrading phenol along with its complete mineralisation through reaction intermediates within 100 minutes. Xi *et al.* [154] used an aerated cascade photoreactor for the degradation of dicholoro acetic acid and compared the results with a thin-film fixed-bed reactor. The aerated cascade photoreactor was found to be 3 to 13 times more efficient than the thin-film fixed bed reactor because of the increased mass transfer and use of oxygen from the air as an oxidising agent. Ray *et al.* [155] used a new reactor composed of hollow tubes coated with TiO_2 as a catalyst to achieve better light distribution and greater specific surface area, showing promising results for the photocatalytic degradation of an acid dye: special brilliant blue. Dionysiou *et al.* [156] used a continuous-flow TiO_2 rotating-disk photocatalytic reactor to evaluate the photocatalytic degradation of

phenols, chlorinated phenols and lindane. The highest removal efficiencies were noted at low molar feed concentration.

Only very few studies have used a distributed light source photoreactor (e.g. [75]); most have used Pyrex glass beakers as a reaction vessel within a UV impermeable enclosure containing the UV lamp [34, 50, 54, 58, 70, 157-159]. This is the easiest and cheapest possible configuration for a photoreactor, allowing the researcher to simply manipulate the parameters necessary to characterise a photoreaction.

2.9 Increasing Photocatalytic Activity – the Effect of Doping

The addition of a very small amount of a foreign substance (impurity) to a very pure substance is known as 'doping' (one dopant atom per 100 million atoms to one dopant atom per ten thousand). The addition of these impurities serves different purposes under different needs. For example, the addition of nitrogen or any other metal as an impurity to pure ZnO may affect its physical and chemical properties. In particular, doping to ZnO allows researchers to tailor its structural, morphological, optical, magnetic and electrical properties.

2.9.1 Types of Dopant:

Doping to semiconductor metal oxides (e.g. TiO_2 and ZnO) can be divided into two categories as described below:

2.9.1.1 Cationic doping

The doping of a cation to metal oxide is known as cationic doping; e.g. Al, V, Cr, Mn, Fe, Ni [160-164], Co[165-170] were used as cationic dopant(s) to ZnO and/or TiO_2.

2.9.1.2 Anionic doping

The doping of an anion to metal oxide is known as anionic doping; e.g. N, C, and S [103, 146, 171-185] were used as anionic dopant(s) to ZnO/TiO_2

To observe the impact of doping on photocatalytic activity, surface morphology and reaction mechanism both anionic (nitrogen) and cationic (cobalt) doped nanostructure thin films were prepared and analysed (see Appendix I for further details).

Cationic doping leads to localised d-states in the band gap of TiO_2, which usually act as recombination centres for photoexcited electrons, and holes leading to lower photocatalytic activity [161, 162]. It might also unfavourably shift the conduction band below the redox potential of adsorbates, rendering the material inactive for photocatalysis. In contrast, anionic doping results in p-states near the valence band similar to other deep donor levels in the semiconductor [173-176] .

2.9.2 Impact of Dopant on the Semiconductors

Nearly 5% of the incoming solar energy is the UV part of the solar spectrum, while the rest is visible light [186]. It is therefore of great significance to develop a material that can absorb both UV irradiation and visible light to widen the range of a photocatalyst. In almost all photocatalytic materials, the band gap (for further details see Appendix F) of the semiconductor metal oxide plays a pivotal role in triggering the photoreaction after UV-induced electron-hole pair (as outlined in Section 2.4). In undoped TiO_2 and ZnO materials, the energy associated with visible light is not enough to initiate the photoreaction. Many studies have been cited showing that doping of a metal or transition element can cause a hyper-chromic shift in the optical absorption of semiconductor metal oxide [187-189]. Usually doping is done to create tail states within the band gap [188]; to increase surface defects [189, 190] which ultimately increase the surface area (a mandatory aspect if there is to be a significant increase in photocatalytic activity); and/or to alter the electrical properties [187] of the semiconductor metal oxide (such ZnO and TiO_2). The doped metal or transition element causes the following changes in the electrical structure as shown in Fig. 2.19 summarised by Serpone [191]:

- Incorporation of localised dopant levels near the valence band and the conduction band
- Band gap narrowing resulting from the broadening of the valance band
- Localised dopant levels and electronic changes to the conduction band
- Electronic transition from localised levels near the valence band to their corresponding excited states.

Another aspect of doping to semiconductor metal oxides is the thermal instability and its tendency towards charge-carrier recombination centers [192] that could reduce the overall UV-induced electron and/or hole taken up by their respective accepting species.

Figure 2.19: Various schemes illustrating the possible changes that might occur to the band gap electronic structure of anatase TiO_2 on doping with various nonmetals: (a) band gap of pristine TiO_2; (b) doped TiO_2 with localized dopant levels near the VB and the CB; (c) band gap narrowing resulting from broadening of the VB; (d) localized dopant levels and electronic transitions to the CB; and (e) electronic transitions from localized levels near the VB to their corresponding excited states for Ti^{3+} and F^+ centers. [Reproduced from Serpone [191]].

Overall, the dopant is favourable in imparting electrical changes, narrowing of band gap, and increased optical adsorption range.

2.9.3 Doped ZnO Photocatalytic Materials

To this author's knowledge, Ag^{+2}, Mn^{+2}, Pb^{+2}, Co^{+2}, N, Ag, Cu, Sb, Au, As, In, Li, [103, 146, 165, 166, 168, 170, 171, 180, 181, 183, 184, 187, 188, 190, 193-199] metal or transition elements ions have been used to create doped ZnO semiconductors. Most of the studies attempted to describe the photoluminescence, optical activity, and magnetic properties of the doped ZnO semiconductor metal oxide. Only a few conducted photocatalytic studies, such as Xu *et al.* [166], Wang *et al.* [190], summarised below:

- Wang *et al.* [190] concluded that silver ion doping to ZnO (silver doped ZnO powder) greatly improved the photocatalytic efficiency of MB and phenol in aqueous suspension because of the improved surface properties of the silver-doped ZnO such as O vacancies, crystal deficiencies, and increased specific surface area.
- Xu *et al.* [166] studied the photocatalytic degradation of basic organic dye Methyl Orange by using cobalt-doped ZnO and found it to be more photocatalytically active

than undoped ZnO because of the absorption edge shift towards the longer wavelength.

Based on the findings of Li *et al.*, [200] and noting the importance of controlling surface morphology within this project, a cobalt dopant was chosen to produce cationic-doped ZnO, since this should give nearly the same morphology as that of the undoped ZnO.

2.9.4 Nitrogen-doped ZnO (N:ZnO)

2.9.4.1 Nitrogen doping methods

Various sources of nitrogen [183] such as N_2, N_2O, NO and NH_3 gases can be used to prepare N:ZnO and N:TiO_2 thin films. The methods used are summarised as follows:

- Ion implantation transition metal (V or Cr ions) to TiO_2 – to increase photocatalysis [180].
- Group I, V elements - to increase the photocatalysis and p-type ZnO [201]. DC thermal plasma technique [202], hydrogen plasma technology [180] and magnetron sputtering technology [172, 201] were used to dope these elements.
- Surface sensitisation of the metal oxide (TiO_2) photocatalyst via chemisorbed or physioabsorbed dyes [180].
- Coupling TiO_2 with other semiconductor oxides [180] (such as Cds, WO_3, V_2O_5), as these can absorb lights in a visible region.
- Decomposition of zinc nitrate under different heat treatment conditions.[146]
- Radical beam gettering epitaxy [183] on a ZnSe substrate by using NO gas as the oxygen precursor and nitrogen dopant source.
- Hydrothermal method [184], to obtained dense and vertically aligned ZnO nano wires.
- Low pressure chemical vapour deposition [171] to obtained nitrogen doped ZnO.
- Sol-gel method [186, 203-217] to produce TiO_2 nanoparticles.

Overall, thermal stability, an increase of charge carrier recombination centres, and high cost, have limited the performance of transition metal doped TiO_2 [161, 218, 219].

2.9.4.2 Effect of N dopant on band gap and photocatalysis

In 2003, Futsuhara *et al.* [179] observed that the optical band gap of ZnO decreases from 3.26 to 2.30eV when doped with N. This doping was carried out using a ZnO target in an N_2-Ar mixture using magnetron sputter. It shifts the doping absorption edge from 380nm (UV region) to 539nm (visible region). The same visible absorption feature in nitrogen-doped ZnO was also noted by Wang *et al.* in 2001 [103].

Wang *et al.* [178] prepared nitrogen-doped titania nanobelts and concluded that the absorption range extended from 380nm to 580nm, decreased in photocatalytic activity under UV irradiation and increased under visible light. This visible light-responsive photocatalytic activity of N-doped titania originated from the excited electrons from N 2p states on the edge of the valence band maximum (VBM) and the local N 2p levels above the VBM. The decrease response to ultra violet irradiation photocatalytic activity was caused by 3d states of Ti^{+3} below the conduction band, which were associated with the oxygen vacancies that acted as electron-hole pair recombination centres. Wong *et al.* [172] suggested that the shift in nitrogen-doped TiO_2 from UV to visible light is due to the N 2p state contribute to the band-gap narrowing by mixing with O 2p states. Yang *et al.* [184] suggested that the introduction of N in the crystal lattice of ZnO will result in an intermediate energy level in the band gap, and reduce the absorption energy. Kerr *et al.* [171] concluded that increase of carbon content in nitrogen doped zinc oxide (ZnO:N) may affect the donor behaviour of the film.

2.9.4.3 Effect of doped nitrogen concentration on photocatalysis

Two different opinions were apparent on the effect of nitrogen-doped concentration. Asahi *et al.* [174] observed that band gap narrowing occurs when a high concentration (6-12.5%) of oxygen sites was substituted by nitrogen, Whereas Okato *et al.* [220] claimed no band gap narrowing at a high concentration of nitrogen atoms. Wong *et al.* [172] suggested that an increase in doped nitrogen concentration makes the thin film opaque, ultimately

reducingd/destroying the photocatalytic activity of N-doped TiO_2. Chen-shifu *et al.* [146] concluded that an N-containing ZnO photocatalyst prepared by decomposition of zinc nitrate has a higher level of visible light photocatalytic activity. However, under UV irradiation, a decrease in photocatalytic oxidation (Methyl Orange) and an increase in photocatalytic reduction (potassium dichromate) as compared to pure ZnO, was observed. Chen-Shfiu *et al.* [146] also proposed an energy band structure model of N-containing ZnO, suggesting that electrons generated in the valence band could have been first excited to AL (localised band near to valence band), and further transferred to the conduction band of ZnO.

2.9.4.4 Effect of N_2 doping on morphology

The effect of N_2 doping on ZnO morphology has not been well studied. To this author's knowledge, only Lin *et al.* [202] have concluded that under illumination of both UV and visible light, ZnO spherical particles had better anti-microbial ability, while particles with tetra-pod and rod-like shapes were more effective at decomposing MB.

2.9.4.5 Effect of N_2 doping on crystallinity

Torbjorn *et al.* [182] show that doping not only alters the charge transfer properties but also affects the crystallinity and optical properties of the material. They suggested that crystal structure of nitrogen doped TiO_2 was prone to the preparation environment such as the gas mixture in the sputter plasma. Alves *et al.* [185] concluded that both substrate and RF power play an important role in determining crystalline quality. Wang *et al.* [103] have compared the doped and undoped ZnO crystal planes, concluding that N-doped ZnO thin films are of better crystal quality with smaller mosaicity than non-doped samples.

2.9.5 Cobalt-doped ZnO (Co:ZnO)

Cobalt doping to ZnO has primarily been used in past studies to characterise the changes this dopant imparts on the structural, electrical and magnetic (spintronics) properties of the ZnO. Little attention has been paid to the characterisation of the effect of this dopant on surface morphology − a crucial aspect which contributes to the reaction mechanism and governs the

overall reaction rate. The Co:ZnO structure is a hexagonal wurtzite crystal [165, 166, 168, 169], the same as undoped ZnO .

2.9.5.1 Methods used for Co:ZnO

Different sources like cobalt acetate [$Co(CH_3COO)_2$], cobalt nitrate [$Co(NO_3)_2\ 6H_2O$], cobalt oxide [CoO], pure cobalt oxide (Co_3O_4) [165-169, 193, 199] were used to prepare nano particles, nano rods and/or thin films of Co:ZnO. Methods used to obtain these nano rods and/or thin films are summarised as follows:

- Hydrothermal solution deposition [166, 167, 200].
- Sol-Gel [168, 198].
- Wet chemical method combined with an electro deposition process [165, 169].
- Magnetic sputtered technique [199].

The Co:ZnO obtained by using the hydrothermal deposition technique is strongly dependant on experimental conditions [9], such as temperature, concentration and substance/substrate preparation. The hydrothermal growth method is a more convenient, low temperature and low cost method [9, 221, 222]. Moreover, doping during the hydrothermal synthesis is simple and typically involves merely mixing the precursors in an appropriate ratio [200].

2.9.5.2 Effect of Co dopant on band gap and photocatalysis

Huaming *et al.* [170] found that the band gap decreases with the increasing concentration of cobalt. Cobalt-doped ZnO spherical nanostructures have a 2.83 eV band gap compared to an undoped ZnO band gap of 3.11 eV. This decrease in band gap may be helpful in expanding the use of Co:ZnO under both UV and visible light degradation of recalcitrant and toxic organic waste. Co:ZnO powder [166] has shown increased photocatalysis of methyl orange compared to undoped ZnO. Dan *et al.* [200] also concluded that band gap depends upon the type of dopant and its effect on optical properties (the ratio of UV to detect emission as well as the position of the UV emission peak).

2.9.5.3 Effect of Co dopant type and concentration on Co:ZnO

Dopant type and dopant concentration are crucial to obtaining a desired Co:ZnO. Dan *et al.* [200] concluded that the incorporation of a dopant element depends on its nature, and its ability to become incorporated in the pure substance. They concluded that the Cobalt (Co), Manganese (Mn) incorporate better than Chromium (Cr). Ling *et al.* [168] noticed that the crystal size of Co:ZnO nano powder decreases with the increase in the concentration of cobalt

as dopant. Chao [166] *et al.* prepared Co:ZnO by using a different composition of cobalt (0, 1.5, 3, 5 molar %) and found that a 3% molar composition of cobalt as dopant shows a high photocatalytic activity to degrade Methyl Orange as a model compound. Similarly, Aihua *et al.* [165] made Co:ZnO nanostructured thin films by using three different molar compositions of cobalt as dopant (0, 15, 30 molar %). He found that a 15% molar composition produced a morphology nearly the same as undoped ZnO. Neogi *et al.* [198] also concluded that concentration of dopant severely affected the structural, morphological and transport properties of Co:ZnO. A similar conclusion was also reached by Huaming *et al.* [170] for the Co:ZnO nanostructure.

2.9.5.4 Effect of Co dopant on surface morphology

Very little literature is available on the impact of a dopant source and its nature on surface morphology. So far, nano rods, nano particles, spherical powder and polycrystalline structures have been tried. Only a few studies indicate what each type of dopant does to the surface morphology. These include the following:

Aihua *et al.* [165] prepared nano rods of Co:ZnO using a wet chemical method combined with an electro-deposition process onto an ITO (Indium Tin Oxide) substrate. Pandiyarajan *et al.* [169] developed Co:ZnO nano particles by using a simple wet chemical method. Huaming *et al.* [170] obtained a nano-spherical morphology of Co:ZnO from zinc acetate and cobalt acetate by using a novel freeze-drying route. Similarly Neogi *et al.* [198] observed the polycrystalline wurtizite structure of Co:ZnO by using the same sources used by Huaming *et al.* [170]. Dan *et al.* [200] found that the Co:ZnO morphology was much closer to that of the undoped ZnO compared to Cr and Mn doping. Therefore in order to test the effect of doping, rather than morphology change, on the photocatalytic properties of ZnO thin films, Co is the best choice for the dopant.

2.9.5.5 Effect of Co doping on crystallinity

Source, nature of dopant, and the method used to prepare the Co:ZnO, do affect the preferred crystal orientation of cobalt-doped ZnO. Most researchers have obtained (1,0,0), (0,0,2), (1,0,1) plane orientations for Co:ZnO [166, 167, 198, 199]. However, Huaming *et al.* [170] and Pandiyarajan *et al.* [169] obtained (1,1,1), (1,0,1) crystal planes only. More work is thus required to properly determine this effect, and is done in this study.

2.10 Kinetic Modelling

Kinetic modelling will be used to compare the reaction rates and mechanisms in this work. In the field of photocatalysis or photocatalytic reaction engineering, many different kinetic models are available to describe the reaction. The choice depends on the reaction mechanism present in a particular reaction system. Some of the more common models include:

- Langmuir kinetic model [88, 223-225]
- Freundlich kinetic model [226]
- Langmuir-Hinshelwood kinetic model [42, 50, 70, 157, 227-230]
- Parallel series kinetic model approximation [138]

The Langmuir isotherm is used in adsorption studies based on four assumptions: (1) surfaces are uniform; (2) the adsorbed molecules form a monolayer; (3) adsorbed molecules do not interact; (4) the adsorption and de-sorption should be comparable to that of the vaporisation of a liquid [231]. Later, Freundlich derived another isotherm based on Langmuir's model by adding a corrected assumption (i.e. the lateral interaction between chemisorbed atoms and/or molecules should be considered). Overall, the Freundlich isotherm is a relationship between the concentration of the solute on the surface of the adsorbent and the concentration of the solute in the fluid with which it is in contact [232].

The Langmuir-Hinshelwood kinetic model is an improved version of the Langmuir kinetic model. It involves the adsorbed molecules undergoing a bimolecular reaction at the surface of the catalyst, providing a better insight to the overall reaction via adsorption [231]. This model is subject to the assumption that the *"sorption of both the reductant and the oxidant is a rapid equilibrium process in both forward and reverse direction and the rate determining step of the reaction involves both species present in a monolayer at the solid-liquid interface"*[233].

The parallel series kinetic model approximation can be used to model a series of multiple and complex reactions that involve both partial and total oxidation: such as the photocatalytic oxidation of phenol [138]. Lumped kinetic modelling [234], the simplest form of parallel series kinetic model, was also used to model the kinetics of the photocatalytic reaction(s).

Most heterogeneous photocatalysis studies use a Langmuir-Hinshelwood kinetic model to model the photocatalytic reaction of a model compound because it accounts for the reaction [231] occurring between the reactant(s) involving surface adsorption. Assuming a batch reactor, simplified form of the Langmuir-Hinshelwood kinetic model is shown in equation

(1):

$$r = -\frac{d[C]}{dt} = -\frac{kK[C]}{1+K[C]} \qquad (10)$$

Where

r = degradation rate or rate of disappearance of the reagent (g/L.s or mol/L.s)

C = concentration of the model compound (g/L or mol/L)

t = irradiation or illumination time (s)

k = rate constant

K = adsorption coefficient

At very low concentrations (milli-moles) of model compound $K[C]$=0 i.e. pseudo first order reaction, equation 10 can be rewritten as

$$r = -\frac{d[C]}{dt} = k^{*}[C] = kK[C] \qquad (11)$$

Where k^{*} = the apparent first order rate constant

The apparent rate constant generally incorporates multiple rate constants: such as reaction rate constant, adsorption rate constant and the reaction rate constant on the basis of surface area, mass or weight of the photocatalysts. In photocatalytic reactions, surface area, mass and volume of the catalyst play a crucial role in determining the overall photocatalytic activity. Ideally, all these parameters should be incorporated, to achieve a better understanding of the overall reaction. Consequently, rate constants on a mass and surface area basis (defined as $k^{'}$ and $k^{'''}$ respectively) are used as standard in heterogeneous catalyst reaction and reactor engineering.

A more simplified form of equation 10 can be expressed as:

$$[C] = [C]_o e^{-k^{*}t} \qquad (12)$$

$$\ln\left(\frac{[C]_0}{[C]}\right) = -kKt = -k^{*}t \qquad (13)$$

Or

$$\ln\left(\frac{[C]}{[C]_0}\right) = kKt = k^* t \qquad (14)$$

Some of the most significant studies (in relation to this thesis) that have used the Langmuir-Hinshelwood kinetic model are summarised below:

Mohamed *et al.* [227] used the Langmuir-Hinshelwood kinetic model to study the photocatalytic degradation of MB by using vanadium-doped TiO_2 and sulphated TiO_2 (rutile) and concluded that photocatalytic reaction follows first order reaction kinetics on the assumption that hydroxyl radical is a primary oxidant for the degradation of MB. Similarly, Muruganandham *et al.* [228] used the Langmuir-Hinshelwood kinetic model to describe the pseudo first order reaction kinetics of the photocatalytic degradation of azo dye Reactive Orange 4 by using H_2O_2 upon UV-A irradiation. Kinetic analysis of photodegradation of azo dyes performed by Konstantinou [229] follows approximately pseudo first order kinetics based on the Langmuir-Hinshelwood model. Later, Zhang [230] also concluded that TiO_2-assisted photodegradation kinetics of Eosin follow the Langmuir-Hinshelwood type equation. Similarly, Daneshvar *et al.* [157], Height *et al.* [50], Chakrabarti *et al.* [70] and Daneshvar *et al.* [42] used Langmuir-Hinshelwood kinetics and concluded that the photocatalytic reaction rates, at the low concentrations used, follow pseudo first order reaction kinetics.

Messina *et al.* [158] applied both Langmuir and Freundlich isotherm equations to the experimental data obtained from the adsorption of two basic dyes MB and Rhodamine B, finding that the Langmuir type model equation fits better and follows a first order reaction kinetics.

Consequently, the Langmuir-Hinshelwood kinetic model will be used in this work.

2.11 Implications of the Literature

The literature has shown that suspended photocatalytic reaction systems are complicated to engineer because of the complexity and economics involved in the separation of powder catalyst from treated waste streams. Preparation of low cost and highly active supported photocatalysts for a wide range of bio-recalcitrant and toxic waste is the most preferred way to address this issue. However, because of the associated (both internal and external) mass

transfer limitations; low accessibility of the catalyst surface to UV irradiation; reaction mechanism(s); and interaction of the catalyst with the secondary, tertiary, or more reaction intermediate species; the reaction kinetics of supported photocatalysts, such as ZnO, are not widely studied.

The literature reviewed previously has indicated that new and innovative techniques to produce supported nanostructured photocatalysts via easy and cheap methods are needed to make photocatalysis an economical, feasible, robust and reliable process option, and to give photocatalysts the widest possible application range. Thus reusability and stability of the photocatalyst under the toughest reaction conditions is an outstanding issue. Furthermore, the surface morphology of the supported photocatalyst and its effects on reaction rate, reaction kinetics and reaction mechanism(s) have not been fully explored. The impact of UV irradiation energy/wavelength on reaction mechanism(s), reaction rate and kinetics, especially for supported ZnO photocatalysts, is rarely studied. The implication of the source of the oxidant, if any, on the liquid phase photocatalytic oxidation by a supported photocatalyst has not been fully studied; in particular, its effect on photocatalytic activity, reaction mechanism(s) and kinetics, as well as surface morphology, has not been studied at all.

The preceding literature review also showed that the following aspects of increasing the photocatalytic activity via doping (either cationic or anionic) have not been studied: the impact of dopant(s) in ZnO – such as nitrogen and cobalt – on the reaction rate and mechanism, and the possible correlation between doped and undoped micro/nanostructure ZnO.

Consequently, to address the aforementioned implications, a detailed research was conducted by studying nanostructured oxide films as photocatalysts in terms of reaction rate, solution and solid reaction mechanisms, and stability (leaching, mechanical durability), both under oxidant – limited and rich conditions at two different UV irradiation wavelengths. An attempt was made to correlate the surface morphology of the thin films (based on microstructure, porosity and chemical composition) to photocatalytic activity and reaction mechanism. The effect of doping on the surface morphology nanostructured ZnO thin films and its effect on the relationship between photocatalytic activity, reaction mechanism and stability of the thin films, was also studied.

3 Materials and Methods

3.1 Materials

The following chemicals were obtained from Sigma Aldrich (New Zealand): zinc nitrate hexahydrate ($Zn(NO_3)_2.6H_2O$) 98%, polyethyleneimine (PEI) 50wt % solution in water, cobalt nitrate hexahydrate ($Co(NO)_3$. $6H_2O$) 97.8%, triethyleneamine (TEA) 98.5% , 10% diluted ammonia solution (69%), 4% diluted nitric acid (70% purity), pure zinc metal and methylene blue (regent grade), hexamethylenetetramine (HMT) synthesis grade, acetonitrile (HPLC grade), trifluoroacetic acid (reagent grade), potassium hydrogen phthalate (reagent grade), sodium hydrogen carbonate (reagent grade), Azure B (regent grade), Azure A (regent grade), zinc nitrate AAS standard, formic acid (HPLC grade) and microscope glass slides (7105 WT). Deionised water (Millipore Milli Q A10) was used in all work. Zinc oxide powder was obtained in-house (originally obtained from Beijing Mountain Technical Development Centre for Non Ferrous Metals-China).

3.2 Photocatalytic Experiments

Photocatalytic experiments were performed in a specially-designed photocatalytic reaction vessel under the specific reaction conditions described below.

3.2.1 Photocatalytic Reaction Vessel

Photocatalytic degradation experiments were performed in a custom-made stainless steel UV reaction enclosure shown in Fig. 3.1. Its removable lid was equipped with changeable low pressure UV lamps (254nm and 340nm) connected to a power supply (Davey Water Products, NZ). The enclosure was placed on top of two magnetic stirrers and had side ports for both in situ liquid sample removal and oxygen pipe entry. Two 100mL glass beakers were used as reaction vessels, and two reactions were run in parallel.

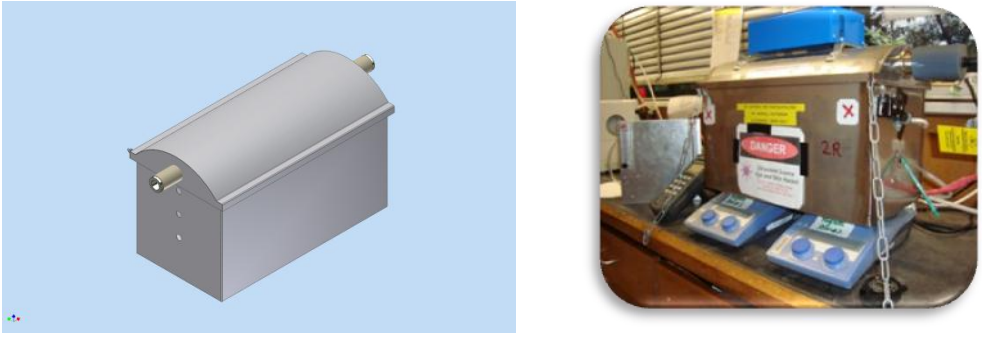

Figure 3.1: Photo of the photo reactor illustrating the photoreactor set-up, showing the stainless steel enclosure with its concave reflector for the UV lamp, power supplies and magnetic stirrers.

The ZnO films were mounted horizontally inside 100mL beakers with the film side facing upwards. The films were secured in the centre of each beaker with Kanthal D wire. In experiments with ZnO powder, a measured amount of this powder (catalyst loading) was dispersed into the Methylene Blue solution. 40mL of $10mgL^{-1}$or $5mgL^{-1}$ Methylene Blue solution was then poured into each beaker. A magnetic stirrer was used to stir the solutions by placing a magnetic bar in a beaker, which weas then placed inside the stainless steel enclosure.

3.2.2 Reaction Conditions for Initial Trial Experiments

To study the photocatalytic degradation of the model compound, reaction kinetics, reusability and reproducibility of undoped nanostructured ZnO thin films and ZnO powder experiments were performed under the following reaction conditions Table 3.1.

Table 3.1: Summary of the initial parameters to study the photocatalytic activity.

Parameter(s)	***Amount Selected***
Concentration of Stock Solution	5, 10, 25 and 50 mgL^{-1} Methylene Blue
Dark Adsorption Equilibrium Time Interval "UV Lamp OFF"	30minutes
Total Reaction Time	6hr (360minutes)
Sample Size	1mL
Total Reaction Volume	40mL
Stirring Speed	300rpm
Temperature (Degree Celsius)	Ambient temperature
Pressure	Atmospheric air (78%N_2, 21%O_2 and trace element) at room pressure (not monitored)
Sampling Time Interval(s) for UV-Vis analysis	0, 15, 30, 45, 60, 75, 90, 105, 120, 135, 150, 165, 180, 210, 240, 270,300, 330, 360 minutes
Sampling Time Interval(s) for HPLC analysis	1hr, 2hr, 3hr, 4hr, 5hr, 6hr
Sampling Time Interval(s) for AAS analysis	6hr

3.2.3 Reaction Conditions for Second, Third, and Last Phase of Experiments

The second, third and last phases of the reactions were performed under both oxygen-limited and rich conditions using both undoped and doped nanostructured ZnO thin films.

3.2.3.1 Reaction conditions for experiments under both oxygen-limited and rich conditions

The reaction conditions for oxygen-limited conditions are summarised in Table 3.2.

Table 3.2: Reaction conditions for experiments under both oxygen-limited and rich conditions.

Parameter(s)	***Amount Selected***
Concentration of Stock Solution	10 and 5 mgL^{-1} Methylene Blue
Dark Adsorption Equilibrium Time Interval "UV Lamp OFF"	30 minutes
Total Reaction Time	24hr for 10 mgL^{-1} and 6hr for 5 mgL^{-1}
Sample Size	0.8mL
Total Reaction Volume	40mL
Stirring Speed	300rpm
Temperature (Degree Celsius)	Ambient temperature
Pressure	Atmospheric air (78%N_2, 21%O_2 and trace element) at room pressure (not monitored)
Sampling Time Interval(s) for UV-Vis analysis	0, 1hr, 2hr, 3hr, 4hr, 6hr, 8hr, 10hr, 12hr and 24hr
Sampling Time Interval(s) for HPLC analysis	0hr, 4hr, 8hr, 12hr, 24hr
Sampling Time Interval(s) for AAS analysis	24 hr

3.2.3.1.1 Reaction under oxygen-limited conditions

Experiments under oxygen-limited conditions were performed using horizontally mounted nanostructure ZnO films in 100mL beakers with the film side facing upwards. The film was secured in the centre of each beaker with Kanthal D wire. The beaker was placed inside the reaction vessel as shown in Fig. 3.2. In each beaker, a magnetic stirrer was place to stir the

reaction mixture at 300rpm. Reaction containers were then exposed to UV light of wavelength (254 or 340nm) supplied by low pressure mercury lamps after adsorption in the dark (for 30 minutes).

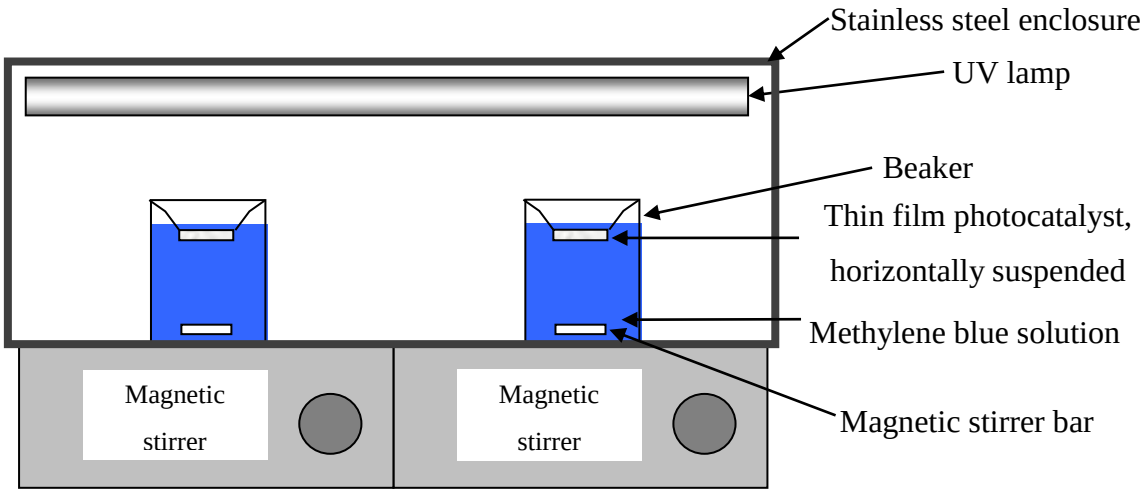

Figure 3.2: Schematic of the photoreactor set-up for experiments under oxygen-limited conditions.

3.2.3.1.2 Reaction under oxygen-rich conditions

Experiment under oxygen-rich conditions were performed under the same reaction conditions as to oxygen-limited, except for the additional source of oxygen. Oxygen from a cylinder (BOC, New Zealand, 99.5%) was added at a flow rate of 250 cc/min O_2 (measured by using RAM-12-SSV rotameter, Dwyer Instruments Inc., USA) into the reaction beaker, as shown in Fig 3.3. This ensured that the reaction solution was kept saturated by the continuous supply of diatomic oxygen at a constant flow rate.

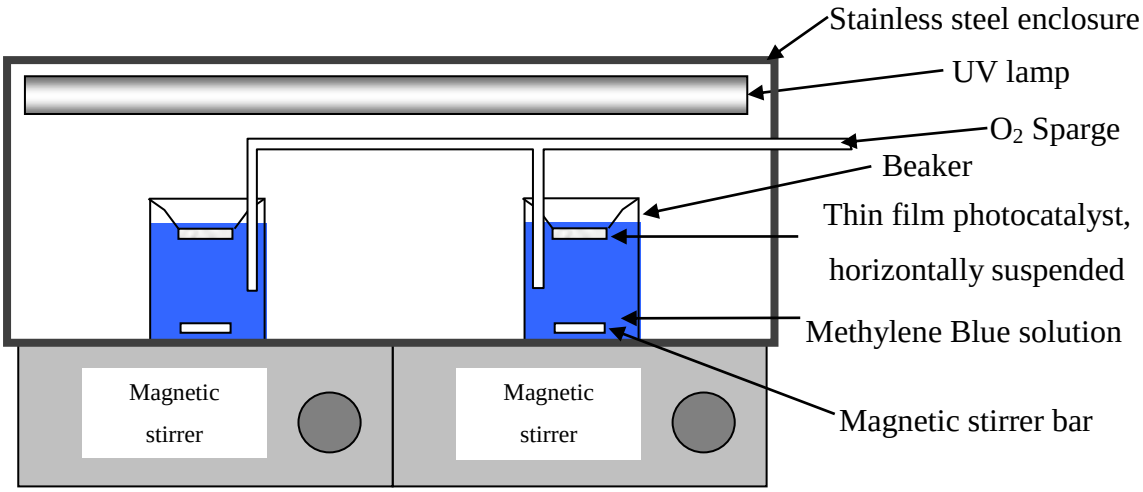

Figure 3.3: Schematic of the photoreactor set-up for experiments under oxygen-rich conditions.

Two repeats were conducted for each experiment and data are presented with error bars ± 1.88 standard deviation. Prior to irradiation, MB and ZnO films were allowed to equilibrate in the dark for 30 minutes. UV irradiation (254nm or 340nm) was then carried out, having light intensity of approximately 0.83 and 0.81 $mWcm^{-2}$ respectively (measured by using an IL 1700 Radiometer) for 24 hours at a constant stirring speed.

3.3 Preparation of Undoped and Doped ZnO Nanostructured Thin Films

3.3.1 Preparation of Undoped Nanostructured Zno Thin Films

Six different ZnO morphologies were prepared using a hydrothermal chemical deposition technique. The substrate was either clean glass slides (henceforth referred to as 'clean glass film growth' or CG) or glass slides with an under-layer of magnetron sputtered ZnO (henceforth referred to as 'magnetron sputtered template growth' or MS) with an approximate substrate top surface area of 2×1 cm^2.

Magnetron sputtered template: For the magnetron sputtered template growth films, the clean glass substrate was loaded into the chamber of a custom made magnetron sputter film depositor [10]. When the deposition chamber was evacuated down to $\sim5.3\times10^{-4}$ Pa, high purity argon was introduced into the chamber. Radio-frequency (13.56 MHz) power of 500 W was forwarded to the substrates to initialise plasma for surface cleaning. Direct-current power was then forwarded to a ZnO target (99.99%). Deposition was conducted for 30 minutes to establish a thin ZnO film on the glass substrate. This established a ZnO film template onto which further ZnO was deposited by solution growth.

Solution growth: Aqueous solutions for the growth of ZnO nano/microrods were prepared by mixing 80mL each of 0.025mol L^{-1} zinc nitrate and 0.025 mol L^{-1} hexamethylenetetramine (HMT) and 0.3mL of 100% polyethyleneimine (PEI). Diluted nitric acid (4%) or diluted ammonium hydroxide solution (10%) was used to adjust the pH value to 5 or 7.5 to give a clear, colourless solution. The solution was then transferred into a sealable glass jar, in which the glass substrates were suspended vertically using a corrugated Teflon support, to achieve chemical deposition growth on one side of the substrate. The sealed jar was then put into an oven at 95°C for 4 hours, after which the glass substrates were withdrawn from the solution, rinsed and wiped on the underside with deionised water, and then dried at room temperature [235]. Three different reaction conditions were used, summarised in Table 3.3. The films obtained from solution 1 (S1) having composition $Zn(NO_3)_2$ + HMT on magnetron sputtered

template growth and clean glass slides were called S1-MS and S1-CG. Similarly, the films obtained from solution 2 (S2) with $Zn(NO_3)_2$ + HMT + PEI on magnetron sputtered template growth and clean glass slides were called S2-MS and S2-CG; and those obtained from solution 3 (S3) with $Zn(NO_3)_2$ + HMT + Citrate on magnetron sputtered template growth and clean glass slides were called S3-MS and S3-CG respectively.

Table 3.3: Un-doped ZnO thin film preparation conditions

	S1-MS	S1-CG	S2-MS	S2-CG	S3-MS	S3-CG
pH	5	5	7.5	7.5	5	5
Solution composition	$Zn(NO_3)_2$ + HMT	$Zn(NO_3)_2$ + HMT	$Zn(NO_3)_2$ + HMT + PEI	$Zn(NO_3)_2$ + HMT + PEI	$Zn(NO_3)_2$ + HMT + Citrate	$Zn(NO_3)_2$ + HMT + Citrate

Three different batches of the above mentioned nanostructured ZnO thin films were prepared.

3.3.2 Nitrogen-doped ZnO (N:ZnO) Thin Films

Nitrogen-doped nanostructure ZnO (N:ZnO) thin films were prepared using two different dopant sources: N_2 gas and TEA.

3.3.2.1 N:ZnO thin films preparation using dopant N_2 gas

Freshly prepared nitrogen-saturated solutions of the reactants $Zn(NO)_3.6H_2O$ and HMT, each having a molar composition of $0.025 molL^{-1}$, were mixed in a sealable glass jar containing a vertically suspended glass substrate (CG and MS) on a custom-made Teflon support under an extensive supply of N_2 gas (to keep the N_2 saturation intact) using an N_2 gas sparger as shown in Fig. 3.4. The pH of the solutions was adjusted to a value of 5 or 7.5 by using diluted nitric acid (15%) or diluted ammonium hydroxide solution (28%). The sealed jar was then put into an oven at 95°C for 4 hours, after which the glass substrates were withdrawn from the solution, rinsed, wiped on the underside with deionised water and dried at 100 ^oC [165] in the oven. The two different reaction conditions used are summarised in Table 3.4. The films obtained from the new solution N:S1 [$Zn(NO_3)_2.6H_2O$ + HMT+ (saturated with N_2 gas) and pH 5 on magnetron sputtered template growth and clean glass substrate] were called N:S1-MS and N:S1-CG. Similarly, the films obtained from the new solution N:S2 [$Zn(NO_3)_2\,6H_2O$ + HMT + PEI+ (saturated with N_2 gas) and pH 7.5 on magnetron sputtered template growth and clean glass substrate] were called N:S2-MS and N:S2-CG respectively.

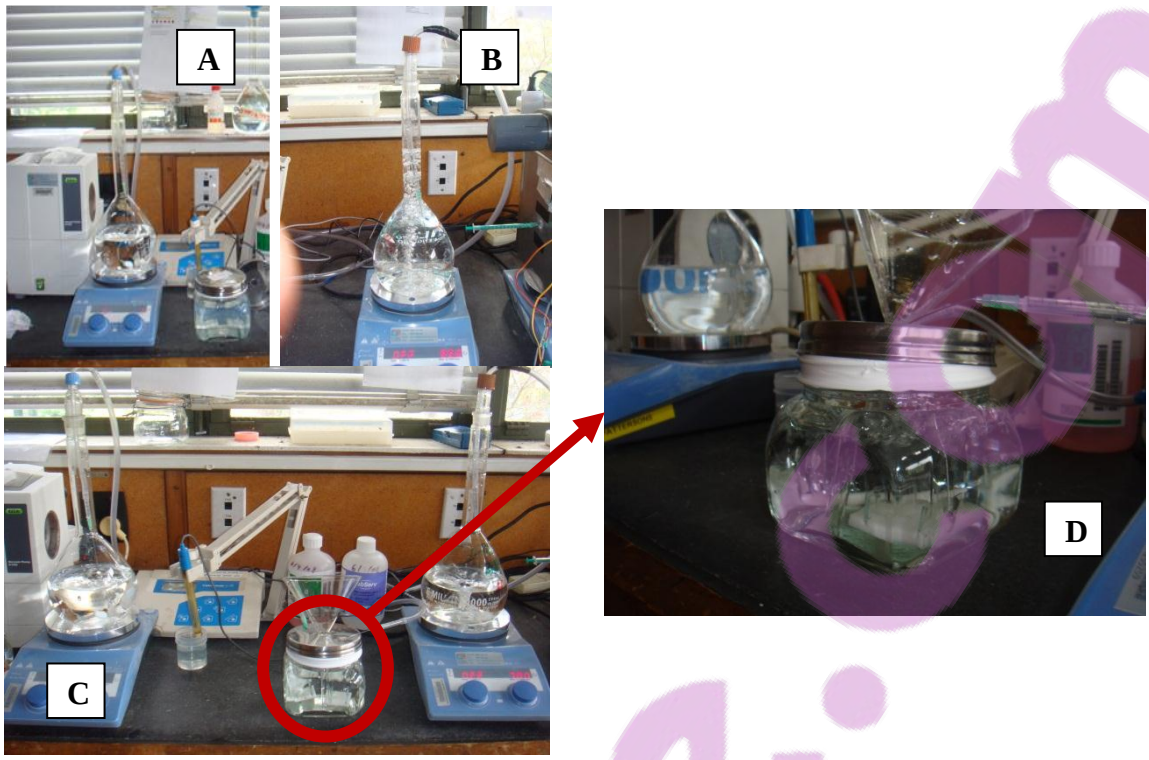

Figure 3.4: Preparation N:ZnO by using N_2 gas as nitrogen dopant source: (A) N_2 saturated $Zn(NO)_3.6H_2O$; (B) N_2 saturated HMT; (C) Mixing of N_2 saturated $Zn(NO)_3.6H_2O$ and HMT under extensive supply of N_2; (D) Magnified view of sealable glass jar.

Table 3.4: Nitrogen-doped nanostructure ZnO thin film (N:ZnO) preparation conditions by using N_2 gas as nitrogen dopant source.

	N:S1-MS	N:S1-CG	N:S2-MS	N:S2-CG
pH	5	5	7.5	7.5
Solution composition	$Zn(NO_3)_2$ + HMT + N_2 gas	$Zn(NO_3)_2$ + HMT + N_2 gas	$Zn(NO_3)_2$ + HMT + PEI + N_2 gas	$Zn(NO_3)_2$ + HMT + PEI + N_2 gas

3.3.2.2 N:ZnO thin films preparation using TEA as nitrogen source

Table.3.5 summarised the six batches of N:ZnO thin films obtained by using TEA as a nitrogen source. Freshly prepared stock solutions of SA (TEA), (SB) $Zn(NO)_3.6H_2O$ and SC (HMT), each $0.025 molL^{-1}$, were mixed in either ratio 1.2:1:1 or 0.4:1:1, in a sealable glass jar containing vertically suspended glass substrate (CG and MS) on a custom-made Teflon support. The pH of the solutions was adjusted to a value of 5 or 7.5 by using diluted nitric acid (15%) or diluted ammonium hydroxide solution (28%). The sealed jar was then put into an oven at 95°C for 4 hours, after which the glass substrates were withdrawn from the

solution, rinsed, wiped on the underside with deionised water, and dried at room temperature. The films obtained from different batches 1-2 (Table 3.5) on magnetron sputtered template growth were called N1:S2-MS, N2:S2-MS respectively; batches 3-4 (Table 3.5) on magnetron sputtered template growth and clean glass slides were called N3:S2-MS , N4:S2-MS, N3:S2-CG and N4:S2-CG respectively; batch 5 (Table 3.5) on magnetron sputtered template growth, and clean glass slides, were called N5:S1-MS and N5:S1-CG respectively; and those from batch 6 (Table 3.5) on magnetron sputtered template growth were called N6:S1-MS

Table 3.5: Nitrogen doped nanostructured ZnO thin film (N:ZnO) preparation conditions by using TEA as Nitrogen dopant source.

Source of N_2 : Tri-ethyl-amine (TEA)				
		Composition of Reaction Mixture	**Substrate**	**Morphology**
Batch 1:		N′:S1 = SA:SB:SC = 1.2:1:1 15% HNO_3 to maintain pH 5.0	Template: MS and CG	N1:S1-MS N1:S1-CG
SA: 0.025 mol L-1TEA	***37.5%***			
SB:0.025 mol $L^{-1}Zn(NO_3)_2.6H_2O$	***31.5%***			
SC: 0.025 mol $L^{-1}HMT$	***31.5%***			
pH = 5				
Batch 2:		N′:S2 = SA:SB:SC = 1.2:1:1 0.3mL PEI 28% NaOH to maintain pH 7.5	Template: MS	N2:S2-MS
SA: 0.025 mol L-1TEA	***37.5%***			
SB:0.025 mol $L^{-1}Zn(NO_3)_2.6H_2O$	***31.5%***			
SC: 0.025 mol $L^{-1}HMT$	***31.5%***			
pH = 7.5				
Batch 3:		N″:S1 = SA:SB:SC = 0.4:1:1 15% HNO_3 to maintain pH 5.0	Template: MS	N3:S1-MS
SA: 0.025 mol L-1TEA	***16.67%***			
SB:0.025 mol $L^{-1}Zn(NO_3)_2.6H_2O$	***41.67%***			
SC: 0.025 mol $L^{-1}HMT$	***41.67%***			
pH = 5				
Batch 4:		N″:S2 = SA:SB:SC = 0.4:1:1 0.3mL PEI 28% NaOH to maintain pH 7.5	Template: MS and CG	N4:S2-MS N4:S2-CG
SA: 0.025 mol L-1TEA	***16.67%***			
SB:0.025 mol $L^{-1}Zn(NO_3)_2.6H_2O$	***41.67%***			
SC: 0.025 mol $L^{-1}HMT$	***41.67%***			
pH = 7.5				
Batch 5:		N‴:S2 = SA:SB:SC = 1.2:1:1 0.3mL PEI	Template: MS and CG	N5:S2-MS N5:S2-CG
SA: 0.025 mol L-1TEA	***37.5%***			
SB:0.025 mol $L^{-1}Zn(NO_3)_2.6H_2O$	***31.5%***			
SC: 0.025 mol $L^{-1}HMT$	***31.5%***			
Without pH Control				
Batch 6:		N‴:S2 = SA:SB:SC = 0.4:1:1 0.3mL PEI	Template: MS	N6:S2-MS
SA: 0.025 mol L-1TEA	***16.67%***			
SB:0.025 mol $L^{-1}Zn(NO_3)_2.6H_2O$	***41.67%***			
SC: 0.025 mol $L^{-1}HMT$	***41.67%***			
Without pH Control				

3.3.3 Preparation of Cobalt-Doped Nano Structure Zinc Oxide Thin Films (Co:ZnO).

To study the effect of dopant on photocatalytic activity, surface morphology and reaction mechanism, cobalt-doped nanostructured ZnO thin films (Co:ZnO) were also prepared by using a modified form of the method used by Aihu Wang *et al.* [165] 'the low temperature hydrothermal solution doping technique'. The same two (different) glass substrates (CG and MS) were used to prepare the four different surface morphologies. Molar compositions of the reactants $Zn(NO)_3.6H_2O$ (0.425moles), HMT (0.425moles) and $Co(NO)_3.6H_2O$ (0.15moles) were mixed in a sealable glass jar (Fig. 3.5) in which the glass substrates (CG and MS) were suspended vertically by using a corrugated Teflon support, to achieve chemical deposition growth on one side of the substrate. The pH of the solutions was adjusted by using diluted nitric acid (4%) or diluted ammonium hydroxide solution (10%) to a pH value of 5 or 7.5 to give a clear, colourless solution. The sealed jar was then put into an oven at 95°C for 15 hours, after which the glass substrates were withdrawn from the solution, rinsed and wiped on the underside with deionised water, and then dried at 100^{o}C [165]. Two different reaction conditions were used, as summarised in Table 3.6. The films obtained from solution 1 (Co:S1) having composition $Zn(NO_3)_2.6H_2O$ + HMT+ $Co(NO)_3.6H_2O$ on magnetron sputtered template growth and clean glass slides were called as Co:S1-MS and Co:S1-CG. Similarly the films obtained from solution 2 (Co:S2) with $Zn(NO_3)_2$ $6H_2O$ + HMT + PEI+ $Co(NO)_3.6H_2O$ on magnetron sputtered template growth and clean glass slides were called as Co:S2-MS and Co:S2-CG respectively. Nomenclature of obtained morphology (Cox%:Sy-Z: x = wt% Co, y = solution (S1 or S2), Z = MS or CG) is summarised in Table 3.7.

Table 3.6: Cobalt-doped ZnO thin film preparation conditions.

	Co:S1-MS	Co:S1-CG	Co:S2-MS	Co:S2-CG
pH	5	5	7.5	7.5
Solution composition	$Zn(NO_3)_2$ + HMT + $Co(NO)_3.6H_2O$	$Zn(NO_3)_2$ + HMT + $Co(NO)_3.6H_2O$	$Zn(NO_3)_2$ + HMT + PEI + $Co(NO)_3.6H_2O$	$Zn(NO_3)_2$ + HMT + PEI + $Co(NO)_3.6H_2O$

Table 3.7: Summary of nanostructured ZnO thin films morphologies obtained at different cobalt (as dopant) concentration.

Co0%:S1-MS =undoped S1-MS	Co0%:S1-CG =undoped S1-CG	Co0%:S2-MS =undoped S2-MS	Co0%:S2-CG =undoped S2-CG
Co5%:S1-MS	Co5%:S1-CG	Co5%:S2-MS	Co5%:S2-CG
Co10%:S1-MS	Co10%:S1-CG	Co10%:S2-MS	Co10%:S2-CG
Co15%:S1-MS	Co15%:S1-CG	Co15%:S2-MS	Co15%:S2-CG
Co25%:S1-MS	Co25%:S1-CG	Co25%:S2-MS	Co25%:S2-CG

Figure 3.5: Sealable glass jar.

3.4 Analytical Techniques

3.4.1 UV-Visible Spectrophotometer (UV-Vis)

A Lambda 35 UV-Visible Spectrophotometer (Perkin Elmer) was used for the quantification of the concentration of unreacted MB. This instrument allows the measurement of the relative absorbance of the sample. UV-visible spectrophotometer incorporates a dual halogen and deuterium flashing tube with a maximum scan wavelength range of 190-1100nm, 0 nm for alignment purposes and minimum radiation effect on a photosensitive sample. A 1.0ml polystyrene cuvette was used to analyse the unreacted MB quantity, placing it inside the cell holder compartment which was fully closed before starting the analysis. The sample was scanned in the wavelength range 250nm-900nm. Two repeats were conducted and the average value of the two was recorded. Maximum absorbance was recorded at 662nm. Before each analysis the instrument had been zeroed at a wavelength 662nm with de-ionized water. A linear relationship was then also established for the Methylene Blue concentration at 662nm.

3.4.2 High Performance Liquid Chromatography (HPLC)

An Agilent 1100 high performance liquid chromatography (HPLC) instrument was used to analyse different reaction intermediates and product characterisations. Species are separated in the column on the basis of their affinity to the non polar stationary and mobile phases. The system had an 1100 quaternary high-pressure mixing pump, a 1200 autosampler, the thermostated column, and an Agilent 1100 variable wavelength detector (set at 600nm). The data peaks were recorded using HP chemstation® software. An Agilent Zorbax® Eclipse XDB C-18 (5µm, 4.6 × 150mm) was used, maintained at room temperature (25^{o}C). 100µL of sample at 1.00ml/L were injected using the autosampler, and eluted under the gradient method shown in Table 3.8, which varied the volume percent of two solutions: mobile phase A (0.07% Trifluoroacetic acid (TFA) in 80% acetonitrile) and mobile phase B (0.1% TFA in deionised water) V/V, a modified form of the method described by Viridiana *et al.* [236]. Peak area was converted into a concentration by using external calibration from the known standards of both Methylene Blue and the identified reaction species.

Table 3.8: HPLC gradient method used to resolve methylene blue and its reaction products.

Time(minutes)	*Deionised water with 0.1% TFA*	*80% Acetonitrile + 20% Deionised water with 0.07% TFA*
0	95%	5%
5	90%	10%
40	10%	90%
45	95%	5%

3.4.3 Liquid Chromatography and Mass Spectroscopy (LC-MS)

To identify all peaks in the chromatograms, both external standards and liquid chromatography-mass spectrometry (LC-MS) analysis were performed. LC-MS analysis was conducted on a Dionex UltiMate3000 system with a binary high-pressure mixing pump, thermostatted autosampler, thermostatted column oven, a variable-wavelength UV-Vis detector and a Bruker MicrOTOF Q-II Quadrupole/Time-of-Flight Mass Spectrometer run in 'MS' Scan Mode. A Gemini 5 µm C6-Phenyl 110 Å 150 x 3.0 mm ID HPLC column was used. Calibration was carried out with sodium formate clusters from dilute sodium formate. The mass range was set to 50-1000 m/z; Ion transfer capillary: 3500V; Nebulizer: 2.0Bar;

Drying Gas: 5.0 L/min; Drying Gas Temp: 190 degree Celsius; Quadrupole Ion Energy: 3.0eV (low mass set here to 100); Collision Cell Energy: 8.0eV; Collision RF: 150V; InSource Collision Energy: 0.0eV; Funnel RF (1&2): 200V; Hexapole RF: 100V; Summation: 5000pulses/spectrum. For the analysis, the mobile phase (the 'carrier', as it is in, Flow-Injection Analysis [FIA] mode) consisted of 50% of 0.1% formic acid in water and 50% acetonitrile with 0.1% formic acid, run isocratically at a flow rate of 0.1mL/min. Sample injection volume is 10uL. Samples were diluted by 50% with acetonitrile to enable them to be filtered through 4mm diameter 0.45um PTFE filters without loss of sample, and to enhance spray (hence ion) formation.

3.4.4 Scanning Electron Microscopy

The surface and cross-sectional morphologies of ZnO thin films before and after photocatalytic reaction were characterised by scanning electron microscopy (SEM) using a Philips XL-30s operating at 5kV. This characterisation involved measuring the thin film thickness, the effect of reaction on morphology, and attrition/stress on the surface caused by UV irradiation. Both top surface and cross-sections were imaged. Cross-sectioning was carried out by cutting the thin film sample into two parts using wire cutters whilst holding it with pliers. Polaron SC 7640 Sputter Coater was used to give a very thin, minimal Pt coating (600 seconds) suitable for SEM viewing.

3.4.5 X-ray Diffractometer

The crystallinity and the phases present in both undoped and doped nanostructure ZnO thin films were characterised by using an X-ray diffractometer (XRD) with Cu-Kα radiation (Bruker D8). This characterisation involves the study of any effect/change in the crystal and number of phases after photocatalytic reaction. Undoped and doped nanostructure ZnO thin films, before and after reaction, were glued horizontally to the base of the sample holder in such a way that the top surface of both the unreacted and reacted ZnO thin films faced upward. Angle of incident (2θ) range were adjusted to 30-65 and 30-70 for undoped and doped ZnO thin films respectively. Bruker AXS: EVA software was used to study the change in crystallinity and number of phases before and after reaction.

3.4.6 Atomic Absorption Spectroscopy

In order to quantify the stability of ZnO nanostructure thin films, the presence of Zn metal was studied using atomic absorption spectroscopy (AAS) coupled with GTA 1110 Varian

graphite furnace and autosampler. Unreacted and reacted samples were collected at the end of each reaction, and analysed using AAS under the following adjusted analytical parameters:

Matrix: 0.01% Nitric Acid; Lamp Current: 5mA; Wavelength: 213.9nm; Ash Temperature: 400^{o}C; Characteristic mass: (Oxygen-free N_2): 0.15pg. By using three point (20ppb, 50ppb and 100ppb) and a quadratic through origin algorithm calibration curve, the presence of Zn metal was quantified.

4 The Effect of Morphology on Undoped ZnO Photocatalysed Reaction Rate, Film Stability and Implications to the Photocatalytic Mechanism

4.1 Introduction

The objective of this chapter is to determine a relationship between initial and reacted catalyst morphology (such as irradiated surface area and structure) and photocatalytic activity (reaction rate) for a range of ZnO thin films prepared by magnetron sputtering; hydrothermal solution deposition; and a combination of the two and their reusability (both photocatalytic activity and stability of nanostructured thin films) under both limited and rich oxygen conditions. The thin films were produced using an innovative combination of magnetron sputtered surfaces and hydrothermal solution deposition that allows the morphology, porosity and thickness to be controlled by varying the composition and processing conditions (preparation method is outlined in Section 3.3.1).

Experiments were performed as described in Section 3.2.3. Comparison experiments with ZnO powder were also performed at catalyst loading of 50mgL^{-1} (since this was the lowest catalyst mass that could be accurately measured). The following control experiments were performed to determine the baseline MB degradation in the absence of UV and photocatalysts and to determine the effect of water and UV alone on the ZnO thin films:

a) Methylene Blue solution in the dark

b) Methylene Blue solution irradiated with UV (photolysis)

c) ZnO thin film in deionised water in the dark

d) ZnO thin film without water irradiated by UV

e) ZnO thin films in water irradiated with UV

The results of these experiments showed no decolourisation of the irradiated solution in the absence of photocatalysts; nor was there significant change in the surface morphologies of the ZnO thin films (see Appendix A for further details).

4.2 Data Treatment and Kinetic Analysis

The Langmuir-Hinshelwood kinetic model was used to determine the reaction kinetics [237] (Eq.4.1), where C is the concentration of the reactant at any time t, N is the number of moles of reactant at any time t, k is the limiting reaction rate constant at maximum surface coverage of the reactant on the catalyst on a liquid volume basis, K is the reactant adsorption equilibrium constant, and V is the liquid volume in the reactor. At low concentrations, $KC << 1$, and the equation 1 can be simplified to equation 2, the first order rate equation, where k_{app} is the apparent first order rate constant. Since first order degradation has been seen to occur in other studies [42, 50, 70, 157, 227-230, 238], a first order kinetic analysis will be used here.

$$-\frac{dC}{dt} = -\frac{1}{V}\frac{dN}{dt} = \frac{kKC}{1+KC} \tag{4.1}$$

$$-\frac{dC}{dt} = -\frac{1}{V}\frac{dN}{dt} = k_{app}C \tag{4.2}$$

Equations (4.1) and (4.2) are in a liquid-volume basis [239]. However, since this does not account for any catalyst properties of the catalyst (such as mass, surface area and volume of the solid catalyst), the kinetic constants derived from these equations cannot be used to fairly compare the relative photoactivity of the different catalysts studied. Therefore, the kinetic parameters on the basis of mass, surface area and volume (of the solid catalyst) will also be evaluated [239]; where $k^{'}$, $k^{''}$, $k^{'''}$ are the true reaction rate constants at maximum mass, surface, volume of the catalyst; and $k^{'}_{app}$, $k^{''}_{app}$, $k^{'''}_{app}$ are the apparent first order rate constants on a catalyst mass, surface, and volume basis respectively (equations 4.3-4.5):

$$-\frac{1}{W}\frac{dN}{dt} = \frac{k^{'}KC}{1+KC} \approx k^{'}_{app}C \tag{4.3}$$

$$-\frac{1}{S}\frac{dN}{dt} = \frac{k^{''}KC}{1+KC} \approx k^{''}_{app}C \tag{4.4}$$

$$-\frac{1}{V_S}\frac{dN}{dt} = \frac{k^{'''}KC}{1+KC} \approx k^{'''}_{app}C \tag{4.5}$$

Where:

W is the mass of solid

S is the exposed surface area

V_s is the volume of the solid.

4.3 Relationships with Surface Morphologies and Thin Film Preparations

4.3.1 Morphology Before Reaction

Fig.4.1 shows the SEM images for the cross-sections of the supported catalysts produced from the different preparation methods outlined in Table 3.3 before the reaction. For the S1 films (Figs. 4.1A and 4.1B), the surface morphologies for the template and clean glass slide growth display a different growth pattern, but similar sizes of ZnO deposits. Both S1-MS (Fig. 4.1A) and S1-CG (Fig. 4.1B) growth is characterised by relatively large ZnO rods (producing a film thickness of approximately 1.5-4μm for S1-MS and 2-5μm for S1-CG). The main difference is that for the MS template growth (S1-MS), the ZnO structure was better aligned and arrayed, with single crystals (with [1,0,0], [1,0,1] and [1,1,0] prominent crystal planes: see Fig. 4.2A) growing up from the magnetron sputtered template (Fig. 4.1A). For the clean glass film growth (S1-CG), the ZnO columns aggregate in random stacks both horizontally and vertically (with [1,0,0], [0,0,2] and [1,0,1] prominent crystal planes: see Fig. 4.2B), as would be expected from growth that has no template to follow (Fig. 4.1B). For S1-MS, the magnetron sputtered underlayer for S1-MS is barely visible (0.1-0.2μm), but it is smaller than that for the S2-MS (1 μm) films (Fig. 4.1C). This is most likely because the acidic growth conditions could have caused the magnetron sputtered underlayer to partly dissolve. This means that while it can no longer function efficiently as a template for the size of growth, it still aligns its direction, which explains the similar size but different alignment of the S1 structures.

For the second solution (S2; Figs. 4.1C and 4.1D), there is a marked difference in both size and direction of the ZnO crystal growth (with [1,0,0] and [0,0,2] planes: see Fig. 4.2 C-D) between the films resulting from template and clean glass slide growth. The S2-MS (Fig. 4.1C) is characterised by rods (about 1-2 μm tall) smaller than the S1-MS. Also in Fig. 4.1C, the magnetron sputtered layer can be clearly observed, in contrast to that in Fig. 4.1A. This is because solution S2 has a neutral pH, the magnetron sputtered template hence remaining intact during the solution growth, giving rise to an orderly small structure. Note that on top of this (Fig. 4.1C), there was a sparsely distributed (~ 2-5%) large structure, similar to S2-CG.

For this structure (Fig. 4.1D), the ZnO structures are larger (2-4.5μm tall), with more random growth. Furthermore, the structure was not evenly distributed across the glass substrate.

For the third solution (S3, Figs. 4.1E and 4.1F), there is also marked difference in both size and direction of ZnO crystal growth. S3-MS (Fig. 4.1E) has a considerably smaller (0.2-0.8 μm) fine, flaky, ZnO structure on top of the magnetron sputtered layer than the others. This structure is similar to that which is expected when citrate is used in the hydrothermal solution deposition growth period [115]. In contrast, S3-CG (Fig. 4.1F) has a structure consisting of an aggregated stack of woven spheres that resemble a bunch of Genda flowers (1-3μm) upon an extremely dense three-dimensional ZnO crystal structure, and is more uniform than S3-MS.

These structures are changed by the photocatalytic reaction with MB, depending on whether the oxygen supplied is limited or rich, as shown in Figs. 4.3, 4.5 and 4.6. These two conditions and the mechanistic implications of these results will be outlined individually.

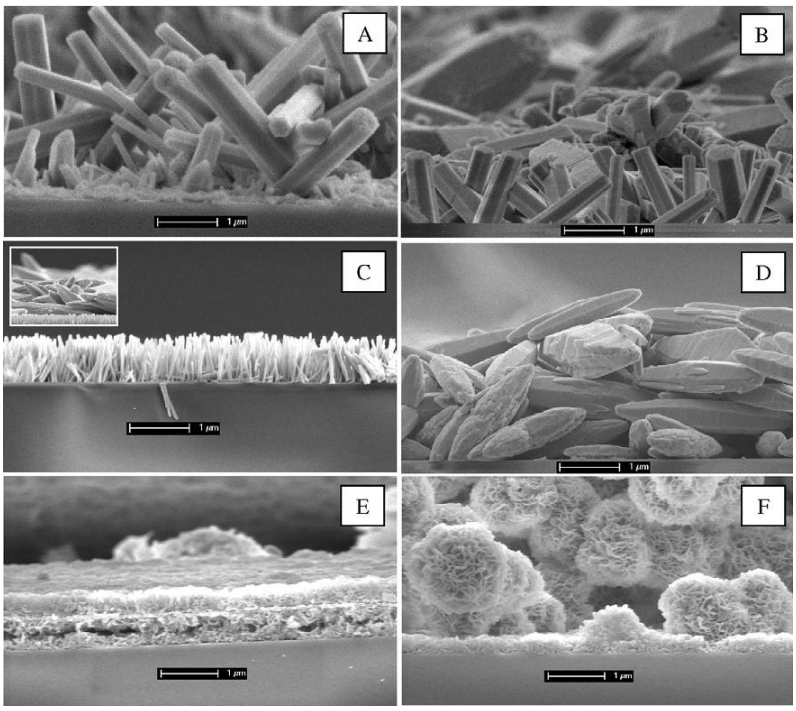

Figure 4.1: Cross-sectional view of the surface morphologies of the different ZnO thin films before photocatalysis: (A) S1-MS; (B) S1-CG; (C) S2-MS (inset, an example of the large crystals that were sporadically present on the surface of the main structure); (D) S2-CG; (E) S3-MS; (F) S3-CG.

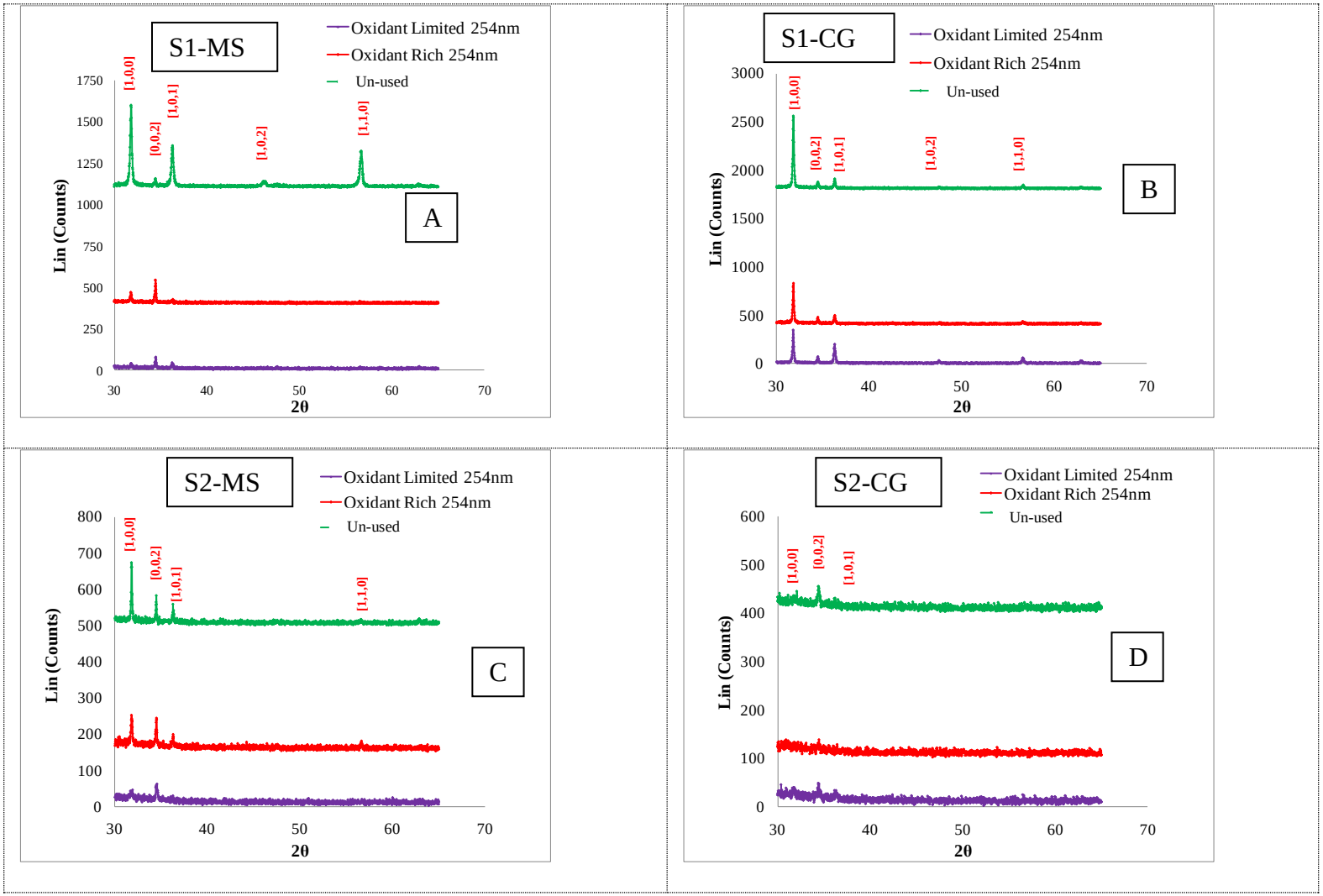

Figure 4.2: XRD analysis of all thin film morphologies after reaction under both oxygen-limited and rich conditions: (A) S1-MS; (B) S1-CG; (C) S2-MS; (D) S2-CG.

4.3.2 Morphology after Reaction under Limited Oxygen Conditions

Experiments with limited oxygen supply were initially performed to compare catalysts under the 'toughest' reaction regime – no extra source of oxidant beyond the surrounding air, where the overall reaction rate could be mass transfer limited by the supply of oxidant (See Section 4.4). In this case, the only oxidant is from the dissolved oxygen within the liquid, and additional oxygen can be provided only by mass transfer through the surface of the reaction liquid. Figs. 4.3(B and E), Figs. 4.5(B and E), and Figs. 4.6(B and E), show how the surface structures for the six different films have changed after the photocatalysed reaction in oxygen-limited conditions. Photocatalytic degradation of methylene blue did occur under these conditions at reaction rates comparable to those under oxygen-rich conditions (see Sections 4.5 and 4.6). However, it can be observed that the ZnO structures are severely affected by the photocatalytic oxidation, with significant degradation of all thin film structures in all reactions. SEM images show this very clearly. Prior to the reaction, the films (S1-MS, S1-CG, S2-MS and S2-CG) have intact solid columns of ZnO with smooth surfaces (Figs. 4.1A-D), S3-MS (Fig. 4.1E) has flaky ZnO structures and S3-CG (Fig. 4.1F) has a spherical woven structure, as previously discussed. After the reaction, the columns have a rougher surface and some appear to be hollowed out (Fig. 4.3B is an example of this), whereas S3-MS (Fig.4.6B) shows that a layer of the ZnO thin film has been eroded away leaving only the thin MS layer, thus decreasing the thin film thickness. The component ZnO columns have also increased in size, perhaps through aggregation, or a dissolution and re-crystallisation process during the reaction. This has caused an overall reduction in its surface area (see Appendix K). The spherical woven structure of S3-CG (Fig. 4.6E) is degraded into a more irregular woven structure through loss of parts of the ZnO structure.

As this degradation runs in parallel to a photocatalytic degradation of methylene blue that is comparable in terms of rate, and extent of reaction, to those in oxygen-rich conditions (see Section 4.3.3), the oxidant that is integral to the radical photocatalytic degradation mechanism must be emanating from some source within these reactions. From the erosion of the thin films (see Appendix H), it is reasonable to conclude that the oxidant is being provided by the ZnO – and therefore the oxygen within the lattice. Also the thickness of ZnO layer could play a significant role as thinner layer means less ZnO is available, which ultimately leads to overall less photocatalytic activity.

Table 4.1: Concentration of zinc in reaction solutions as determined by atomic absorption spectroscopy (AAS), summarised as total zinc concentration (Zn; ppb) and zinc concentration normalised by the original surface area of the thin film catalyst (Zn/*S*; ppb/m^2).

Thin film photo-catalyst	O_2 Limited			O_2 Excess			% Decrease Zn/*S* *
	Surface Area (*S*) m^2	Zn (ppb)	Zn/*S* (ppb/m^2)	Surface Area (*S*) m^2	Zn (ppb)	Zn/*S* (ppb/m^2)	
S1-MS	0.1296	9575	73881	0.1296	4527	34931	52.7
S1-CG	0.0599	7532	125743	0.0599	5425	90568	28.0
S2-MS	0.3427	7252	21161	0.3427	5975	17435	17.6
S2-CG	0.0445	6123	137596	0.0445	4942	111056	19.3
S3-MS	-	2131	-	-	1984	-	-
S3-CG	-	2204	-	-	2105	-	-

*This is equivalent to % increase in thin film stability.

Corroboration of the ZnO thin film erosion was made by AAS analysis of the reaction liquid (Fig.4.4),confirming, that the degradation is a result of the Zn leaching out of the ZnO lattice, Zn metal (Table 4.1 and Fig.4.4) being detected in the reaction samples taken after six hours in each case. When compared on a surface area normalised basis, both template growth films (S1-MS and S2-MS) leached the least amount of zinc, with S2-MS being the most stable by a factor of 3.5. No significant change was noticed in the solution concentration of Zn for S3-MS and S3-CG (Fig. 4.4) before and after reaction under limited O_2 conditions. This may indicate that the erosion is caused by leaching of a component other than ZnO, and, combined with the low reaction rate seen from these films (Section 4.5) corroborates the hypothesis that the oxidant is being provided by the ZnO lattice.

However, the above results show that these films are not suitable for photocatalysis under oxygen-limited conditions.

Reaction in O_2 Limited Conditions	Reaction in O_2 Rich Conditions

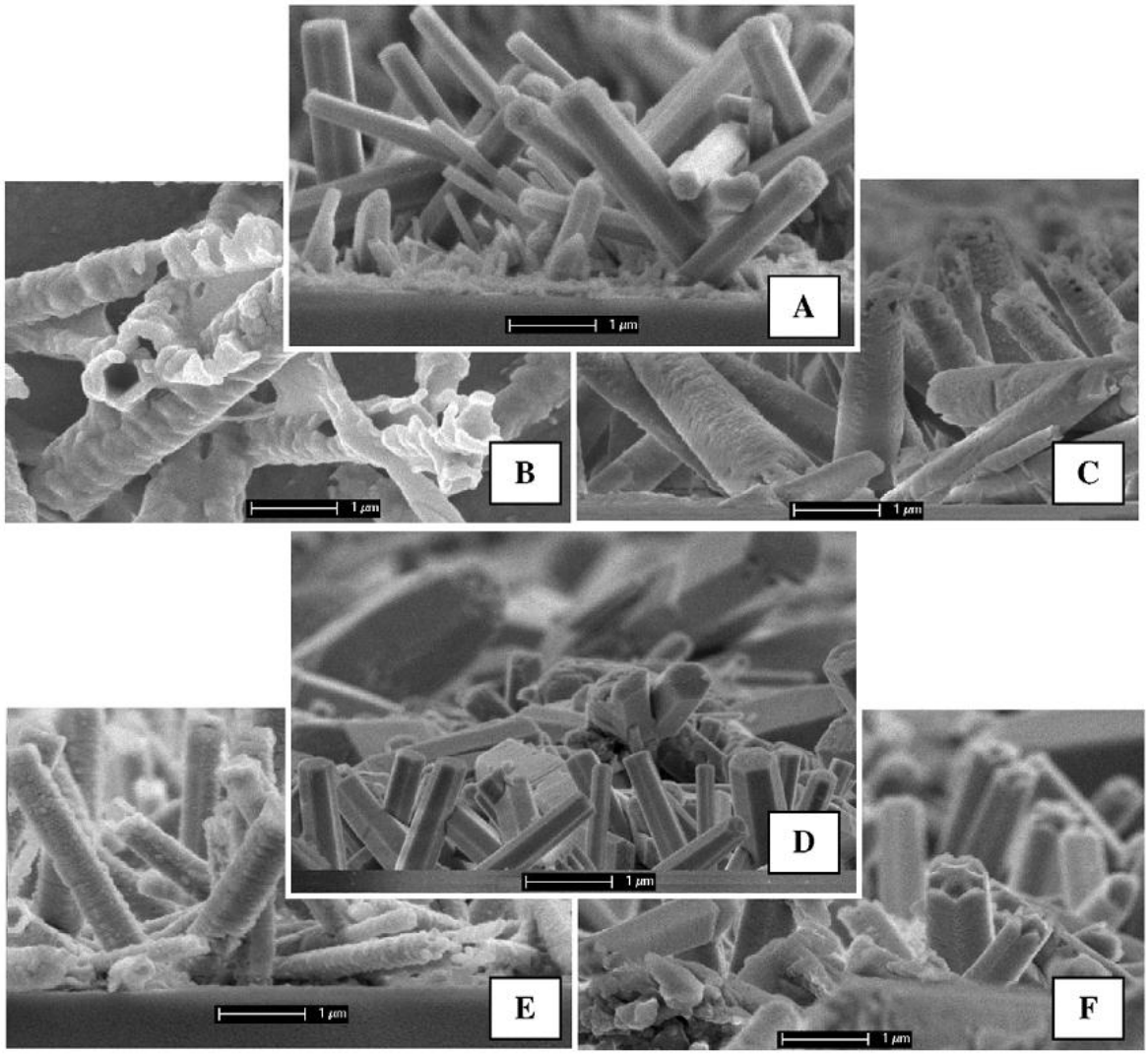

Figure 4.3: Comparison of the solution 1 (S1) derived ZnO thin film surface morphologies using SEM imaging before and after Methylene Blue photocatalysed degradation: (A)S1-MS (un-reacted); (B) S1-MS (reacted with limited O_2); (C) S1-MS (reacted under O_2 rich conditions); (D) S1-CG (un-reacted); (E) S1-CG (reacted with limited O_2); (F)S1-CG (reacted under O_2 rich conditions).

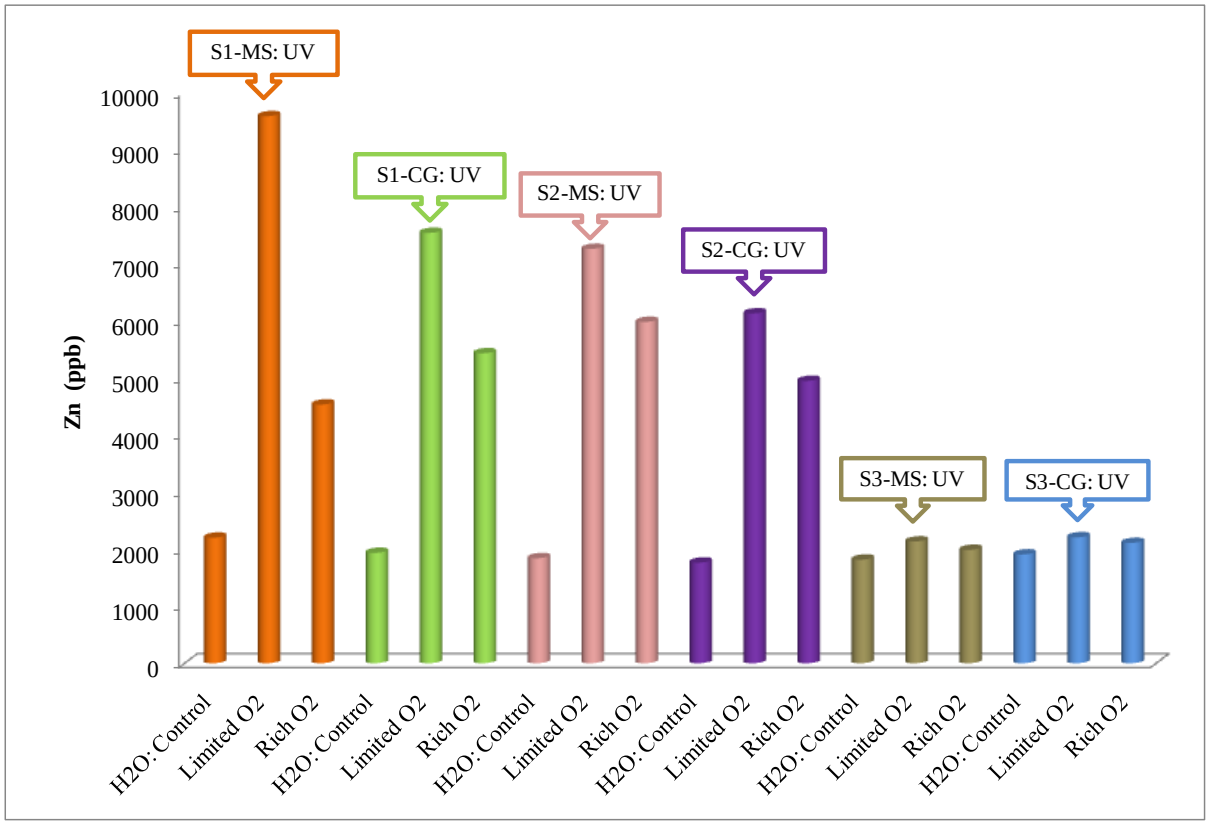

Figure 4.4: Concentration of Zn metal in the final reaction liquid as measured by atomic absorption spectroscopy (AAS) for the reactions photocatalysed by the ZnO thin film derived from solutions S1 and S2 on both clean glass slides (CG) and magnetron sputtered templates (MS).

Reaction in O_2 Limited Conditions	Reaction in O_2 Rich Conditions

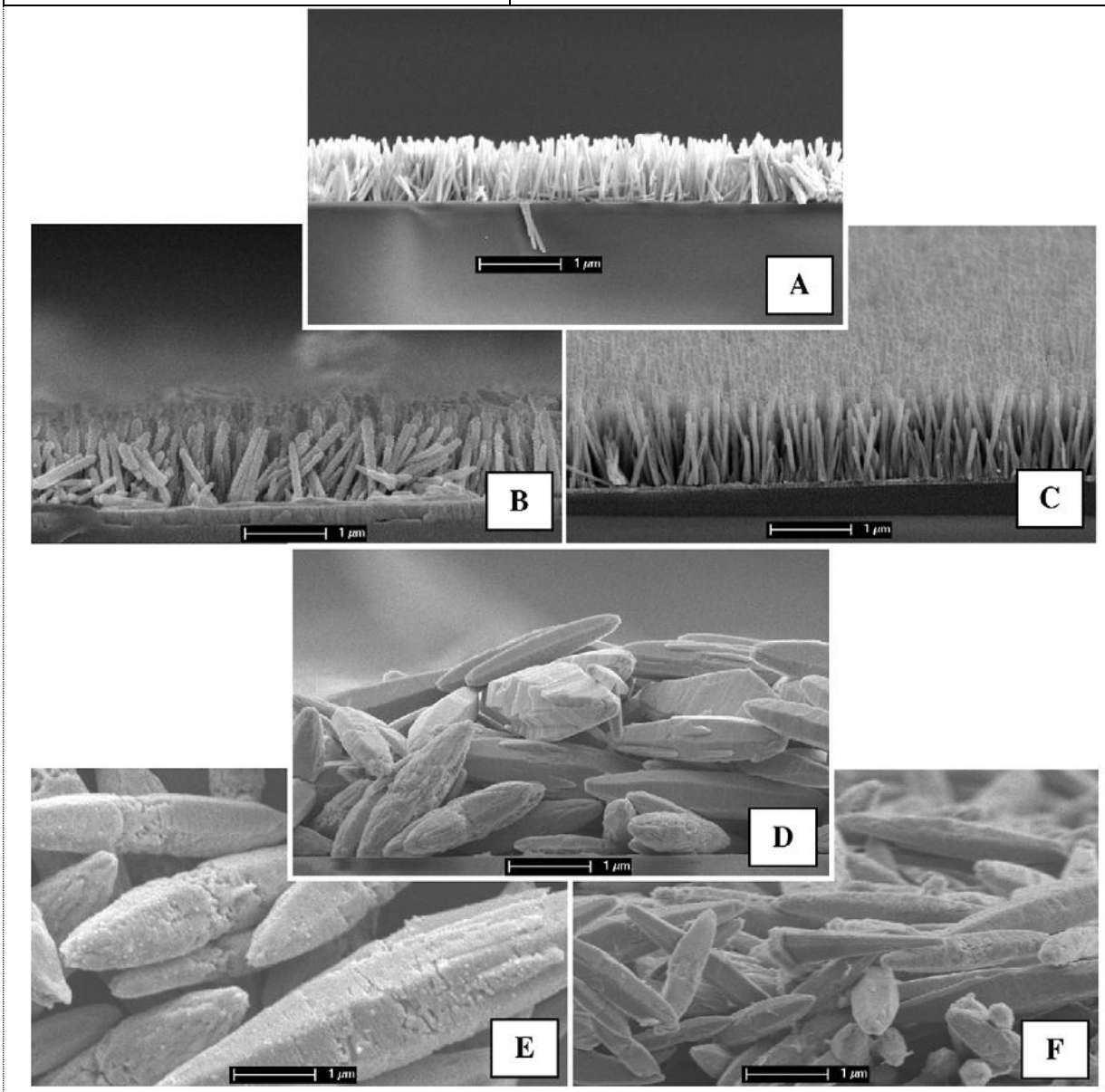

Figure 4.5: Comparison of the solution 2 (S2) derived ZnO thin film surface morphologies using SEM imaging before and after Methylene Blue photocatalysed degradation: (A) S2-MS (un-reacted); (B) S2-MS (reacted with limited O_2); (C) S2-MS (reacted under O_2 rich conditions); (D) S2-CG (un-reacted); (E) S2-CG (reacted with limited O_2); (F) S2-CG (reacted under O_2 rich conditions).

4.3.3 Morphology after Reaction under Oxygen-rich Conditions

To try to overcome the stability problem and to also determine the true reaction rate (i.e. the reaction is not mass transfer limited), experiments under oxygen-rich conditions were conducted. Four trial experiments at different oxygen flow rates (100, 150, 250 and 300 cc/min air (measured by using RAM-12-SSV, Dwyer Instrument Inc., USA) were conducted to ensure the saturation of the reaction vessel with oxygen; 250 cc/min were found to be

sufficient. Figs. 4.3(B-C and E-F), Figs. 4.5(B-C and E-F) and Figs.4.6 (B-C and E-F) show the surface of the six different thin films after the photocatalytic oxidation of methylene blue under oxygen-rich conditions. It can be observed that the structures of S1-MS, S1-CG, S2-MS and S2-CG are more intact and less hollowed out in comparison to the films used in oxygen-limited conditions, showing that the presence of readily available oxygen (dissolved in the liquid) makes the thin films more stable and robust. No prominent changes in the surface morphologies of S3-MS (Figs.4.6B and 4.6C) and S3-CG (Figs.4.6E and 4.6F) were noticed both under oxygen-limited and rich conditions, however, indicating that the chemistry and/or morphology of the films from solution 3 (S3) are unstable to any photocatalytic process. As discussed in section 4.3.2, this is most likely because something other than ZnO is leaching from the thin film lattice, causing the erosion.

Initial and final pH of the reaction fluid both under oxygen-limited and rich conditions were also monitored. Negligible changes in pH were observed during the reaction. Almost all the reactions were carried at pH out ≈ 7.0 (see Table 4.2). The negligible changes in pH indicated that variation in surface morphology, if there is any, was not due to the acidic or basic condition of the reaction fluid.

Table 4.2: pH of the reaction fluid throughout the reaction under oxygen-limited and rich conditions.

	pH Under Oxygen-limited		pH Under Oxygen-rich	
	Before Reaction	After Reaction	Before Reaction	After Reaction
S1-MS	6.75 ± 0.18	6.70 ± 0.19	6.65 ± 0.15	6.75 ± 0.12
S1-CG	6.60 ± 0.25	6.62 ± 0.20	6.65 ± 0.22	6.55 ± 0.23
S2-MS	7.10 ± 0.11	7.05 ± 0.18	7.05 ± 0.12	7.08 ± 0.19
S2-CG	7.15 ± 0.09	7.06± 0.13	7.10 ± 0.08	7.08 ± 0.10

AAS analysis of the reaction liquid (Fig. 4.4 and Table 4.1) confirms that all morphologies (S1-MS, S1-CG, S2-MS and S2-CG) show less dissolution of Zn under oxygen-rich, compared to oxygen-limited conditions.

Reaction in O_2 Limited Conditions	Reaction in O_2 Rich Conditions

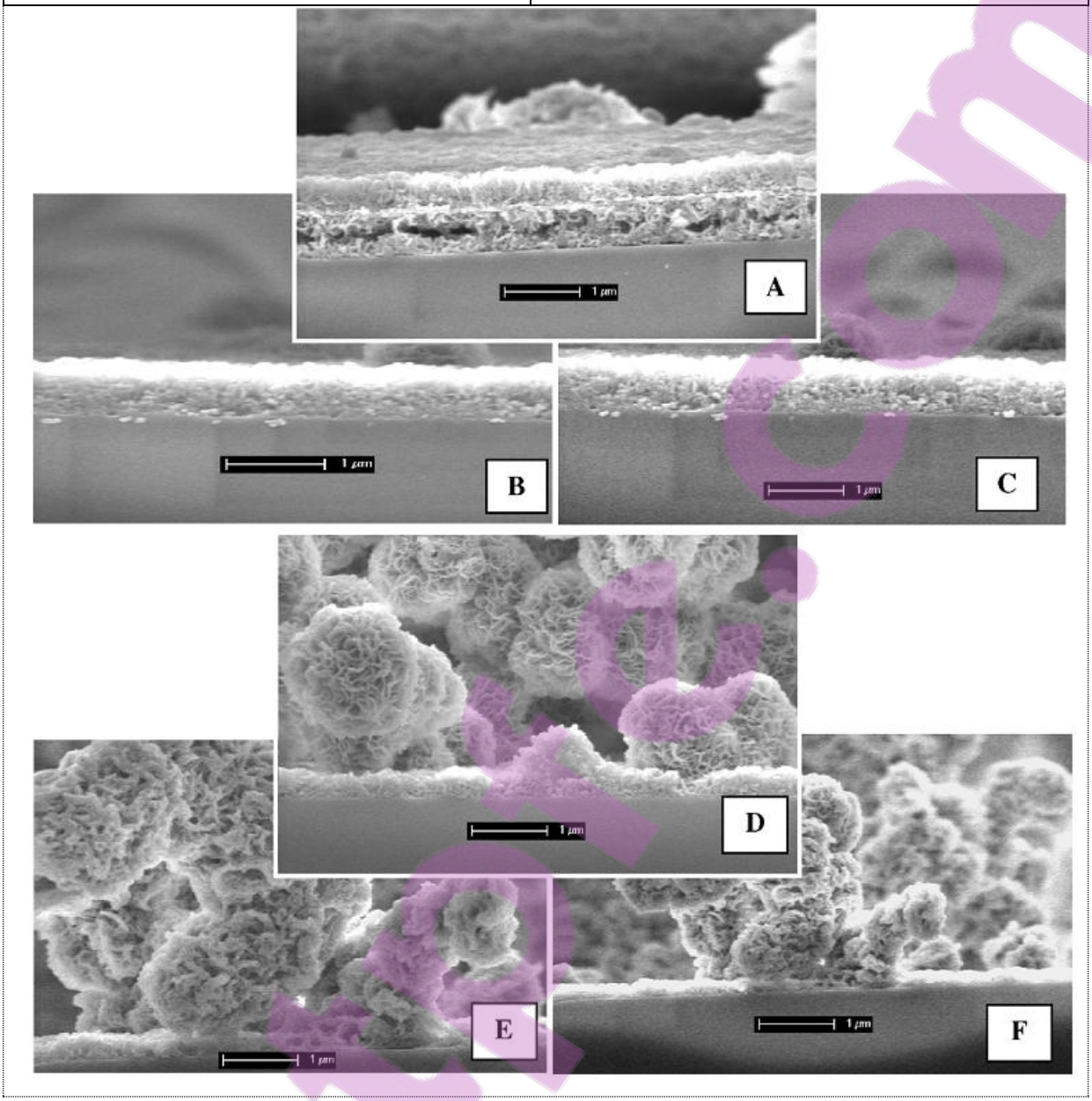

Figure 4.6: Comparison of the solution 3 (S3) derived ZnO thin film surface morphologies from SEM imaging before and after Methylene Blue photocatalysed degradation: (A) S3-MS (un-reacted); (B) S3-MS (reacted with limited O_2); (C) S3-MS (reacted under O_2 rich conditions); (D) S3-CG (un-reacted); (E) S3-CG (reacted with limited O_2); (F)S3-CG (reacted under O_2 rich conditions).

Very minute (≤ 3.51%) changes in the amount of Zn were calculated (based on AAS results) in S3-MS and S3-CG samples under oxygen-rich reaction conditions (Table 4.1, Fig. 4.4). Table 4.1 shows that on a surface area basis, the template growth films (S1-MS and S2-MS) again show the least amount of Zn leaching, (with S2-MS once more leaching the least amount of Zn) and are therefore the most stable under both oxygen-limited and oxygen-rich conditions. This perhaps indicates that the MS template (because of good interfacial adhesion

to the substrate and the high packing density of the grown film [10, 240] and ZnO bonding to ZnO is stronger than the ZnO to glass - provides a base for nucleation and suitable growth orientation for ZnO nanorods) either allows a more stable bond between the glass substrate and the ZnO film and/or the morphologies produced are less susceptible to leaching during photocatalysis. This may also indicate that PEI and deposition at pH 7.5 increases the binding of the ZnO and decreases the amount of Zn lost during reaction.

This result suggests that using oxygen-rich conditions either minimises or prevents lattice oxygens from participating in the photocatalysed oxidation reaction, or replaces those used (see Appendix H).At this stage, It was difficult to estimate the stochiometric ratio between each and every lattice oxygen participation to each Zn lost (a further work is needed to establish this fact). This could indicate that photocatalysed oxidation of methylene blue by these ZnO thin films occurs (at least partially) through a Mars van Krevelen type mechanism [241]. It is speculated that oxygen from the catalyst lattice is removed and used in the radical initiation and propagation phases of the photocatalytic reaction (this hypothesis could be tested/verified by using isotopes of oxygen).

The physical ZnO degradation observed in the oxygen-limited experiments is most likely a result of there being only a limited oxygen supply to replenish the lattice oxygens used. The catalyst degradation is therefore less in the presence of oxygen since the lattice oxygen(s) (and therefore the structure) can be regenerated. To the author's knowledge, this study is the first evidence that a Mars van Krevelen type (partially or fully involvement of lattice ions) mechanism could contribute to ZnO photocatalytic reactions.

This could indicate that the photocatalysed oxidation reactions do occur through a Mars-van-Krevelen type mechanism (i.e. lattice oxygens used for the oxidation, causing a degradation of the ZnO lattice over time), as previously observed in titanium dioxide and other ZnO-containing catalysts. For example, Lee and Falconer [242] show that lattice oxygens are extracted from titanium dioxide (Degussa P25) during the photocatalytic decomposition of formic acid, and Ovesen *et al.* [243] attributed the change in particle morphology for a ZnO/Cu catalyst to a change in the numbers of oxygen vacancies at the Zn-O interface. However, there is little evidence (until now) of the mechanism occurring in pure ZnO photocatalysis. Understanding the operating 'envelope' of this mechanism could provide a pathway to stabilising these types of ZnO photocatalysts, thus enabling their possible

application by industry, so that the aforementioned economic [42, 244] and performance [14, 244] advantages over TiO_2 can be realised.

4.4 Mass Transfer Limitation Studies

To ensure that the reaction is not mass transfer limited, mass transfer limitation fluid dynamics was studied. The revolution speed was varied, to determine the optimal stirring speed that minimises the mass transfer limitations of this heterogeneous reaction without significantly compromising the mechanical stability of the nanostructures within the films. Since mass transfer is typically maximised when flow is turbulent, minimising or eliminating stagnant boundary layers around catalyst particles, the Reynold's number (N_{Re}) for the stirred tank was calculated to determine whether or not the flow was in the turbulent regime. For a stirred tank, N_{Re} can be defined as [133-137]:

$$N_{Re} = \frac{D^2}{\mu} N \rho$$

Where:

D= Length of the magnetic bar (metres)

N= Number of revolutions per second of stirrer bar (rev/s)

ρ = Density of liquid (kg/m^3)

μ = Viscosity of liquid (N-sec m^{-2})

Four different mixing speeds (100rpm, 200rpm, 300rpm and 400rpm) were used to study their effect on the reaction rates of methylene blue with thin films of the S1-MS morphology. The Reynold's number was used to distinguish between laminar and turbulent flow. Under reaction conditions similar to those in this study, Nagata [133, 135-137] considered the fluid system to have a laminar flow if it had a N_{Re} value less than 1000 and turbulent if it was over 1000. Considering that there is an additional suspended thin film in the system in this study that will be a source of flow instabilities, these limits can be considered to be valid, if not an overestimate.

Table 4.3: Summary of Reynold's Number and reaction rate constant(s) on a liquid volume basis (k_{app} ; s^{-1}) and a UV exposed surface area (*S*) basis (k''_{app} , $m^3\ m^{-2}\ s^{-1}$) for the photocatalysed degradation of methylene blue.

revolution per minute	Reynold's Number	% degradation	k_{app} (s^{-1})	k''_{app} ($m^3\ m^2\ s^{-1}$)	Zn (ppb)
100	2619.71	14.11	2×10^{-6}	1.03×10^{-12}	2151
200	5255.21	23.48	3×10^{-6}	1.55×10^{-11}	7120
300	7890.71	37.76	5×10^{-6}	2.5×10^{-11}	9654
400	10510.44	39.58	5×10^{-6}	2.5×10^{-11}	11231

Table 4.3 shows the summary of the Reynold's number calculated at four different mixing speeds and reaction rate constants (reproducible with a maximum error of ± 3.5%; see Appendix L) on a liquid volume basis (k_{app} ; s^{-1}) and a UV exposed surface area (*S*) basis (k''_{app} , $m^3\ m^{-2}\ s^{-1}$). Based on the Reynold's number, it is clearly seen that both reaction rate, as well as surface degradation, increases (see Fig. 4.7) with the increase in mixing speed up to 300rpm. At 400rpm the reaction rate was exactly the same as at 300rpm; however, the increased mechanical agitation was detrimental to thin film stability, with crystals clearly torn away from the glass substrate (Fig. 4.8D). In contrast, the ZnO structures remained intact on the glass substrate at 300rpm (Fig. 4.8C), indicating that this stirring speed and the concomitant level of mechanical agitation is closer to the optimal in terms of both providing a high overall azo dye degradation rate (i.e. minimising mass transfer limitations) and also ensuring that the thin films remain intact and robust in the hydrodynamic conditions to which they are subjected. To thus ensure the reaction is not mass transfer limited, all the reactions were studied at a mixing speed of 300rpm.

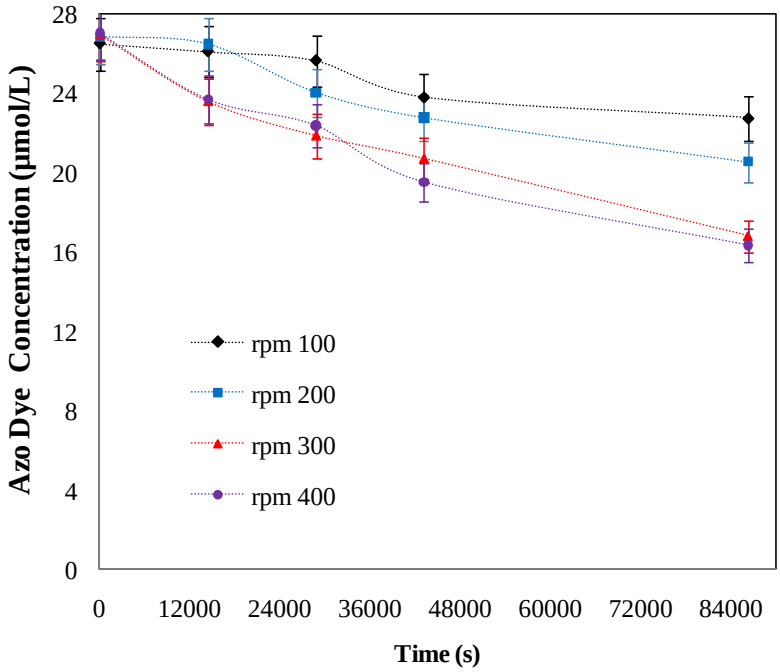

Figure 4.7: Comparison of photocatalytic degradation of Methylene Blue solution at different mechanical stirring speeds.

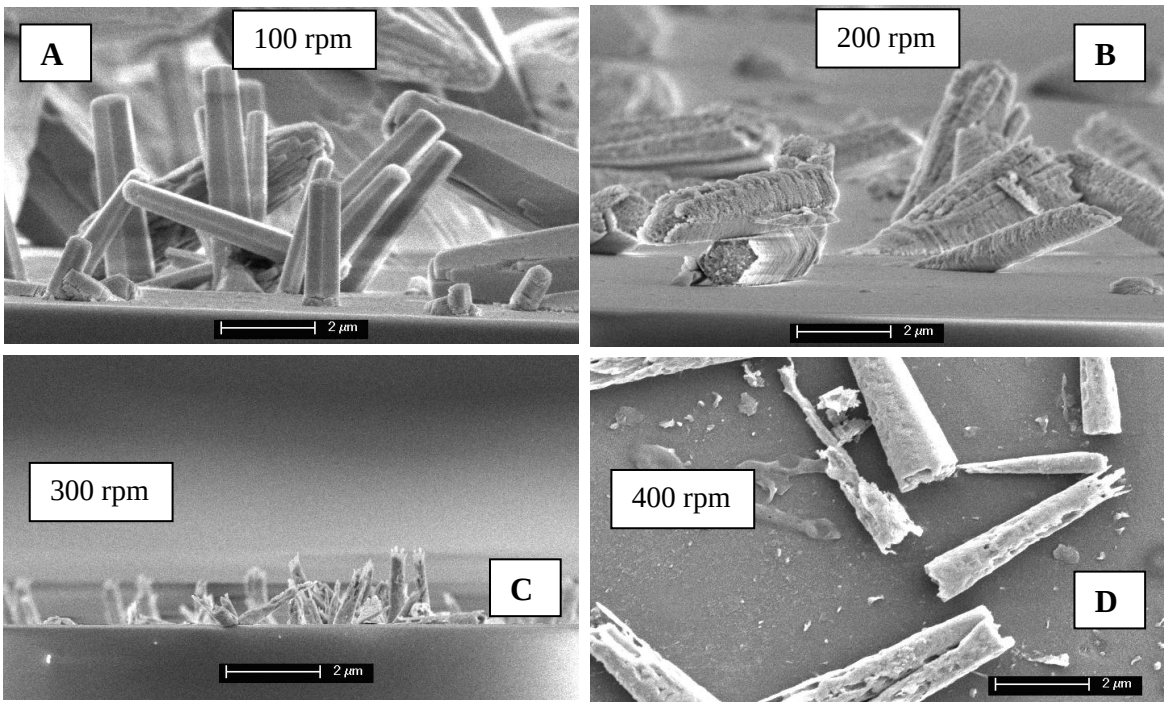

Figure 4.8: Comparison of surface morphology of S1-MS under same reaction conditions at various mixing speeds. (A) 100rpm; (B) 200rpm; (C) 300rpm; (D) 400rpm.

4.5 Relationships with Photocatalytic Activity (Reaction Rate)

4.5.1 Reaction Kinetics

Linear regression of the reaction data shows that the photocatalytic degradation of methylene blue follows the expected first order reaction kinetics for all reactions. Apparent first order reaction rate constants on a reaction liquid volume (V) basis (k_{app}) and UV exposed catalyst surface area (S) basis (k''_{app}) are summarised in Table 4.4.

4.5.2 Oxygen-limited Conditions

Results show that there is a clear relationship between surface morphology (and the related thin film preparation method) and photocatalytic activity for these ZnO thin film supported catalysts. Fig. 4.9 shows that there is no difference in the photocatalytic activity between the S1-MS and S1-CG films despite the surface area of S1-MS being approximately twice the the size of the S1-CG surface area. This is confirmed in Table 4.4, where the rate constants k''_{app} were 4.11 $\times 10^{-9}$ and 8.8 $\times 10^{-9}$ m^3 m^{-2} s^{-1} respectively. Since the film morphologies are different (S1-MS has vertically aligned 1.5 - 2µm tall crystals and S1-CG has random stacks of both horizontal as well as vertical 2 - 2.5µm crystals), this suggests that it is not the surface area which is the most important factor for photocatalytic activity, and that film morphology does indeed have a significant influence, corroborating previous findings by Wahi *et al.* [118] and Li *et al.* [71].

Because of the three-dimensional anfractuous woven structures in S3-MS and S3-CG, it was difficult to calculate the approximate surface area (see Appendix K). However, on the basis of the apparent rate constant k_{app} , S3-MS and S3-CG have more or less the same photocatalytic activity as S1-MS and S1-CG. The only difference is that thin films obtained from S3-MS are slightly more effective than S3-CG ($k_{app} = 8.0 \times 10^{-6}$ s^{-1} and $k_{app} = 1.0 \times 10^{-6}$ s^{-1}).

In contrast, there is a clear difference in the photocatalytic activity between S2-MS and S2-CG films ($k''_{app} = 4.66 \times 10^{-9}$ and 1.33×10^{-8} m^3 m^{-2} s^{-1} respectively, see Table 4.4). For S2 films, S2-MS shows approximately a 2.7 times increase in activity. Its surface microstructure is much smaller and better crystal alignment (Fig. 4.1C), with a surface area approximately seven times larger (an indication that there is no absolute direct proportion between surface area and reaction rate, however, reaction rate increases with the increase in surface area) than that of S2-CG (Fig. 4.1D and Table 4.4). This shows that for S2 films, an increase in surface

area, and perhaps the more aligned structure, will increase the photocatalytic activity, in accordance with previous research [71, 119, 122]. Comparing all the different morphologies, S2-MS is more stable under an oxygen-limited supply.

Table 4.4: Summary of the 1st order reaction rate constants on a liquid volume basis (k_{app} ; s^{-1}) and a UV exposed surface area (S) basis (k''_{app} , $m^3\ m^{-2}\ s^{-1}$) for the photocatalysed degradation of 5 mg L^{-1} methylene blue.

Thin Film photocatalyst	Estimated UV exposed surface area S (m^2)	First order rate constants					
		O_2 limited conditions			O_2 rich conditions		
		k_{app} (s^{-1})	k'_{app} ($m^3 kg^{-1} s^{-1}$)	k''_{app} ($m^3\ m^{-2}\ s^{-1}$)	k_{app} (s^{-1})	k'_{app} ($m^3 kg^{-1} s^{-1}$)	k''_{app} ($m^3\ m^{-2}\ s^{-1}$)
S1-MS	1.296×10^{-1}	1.33×10^{-5}	2.08×10^{-4}	4.11×10^{-9}	1.50×10^{-5}	2.35×10^{-4}	4.60×10^{-9}
S1-CG	5.99×10^{-2}	1.33×10^{-5}	3.80×10^{-3}	8.88×10^{-9}	8.33×10^{-6}	2.41×10^{-3}	5.56×10^{-9}
S2-MS	3.427×10^{-1}	4.0×10^{-5}	2.62×10^{-3}	4.66×10^{-9}	6.0×10^{-5}	3.93×10^{-3}	7.0×10^{-9}
S2-CG	4.45×10^{-2}	1.50×10^{-5}	5.58×10^{-4}	1.33×10^{-8}	1.66×10^{-5}	6.17×10^{-4}	1.49×10^{-8}
S3-MS	-	8.0×10^{-6}	-	-	2.0×10^{-6}	-	-
S3-CG	-	1.0×10^{-6}	-	-	6.0×10^{-6}	-	-
ZnO Powder	7.14×10^{-2}	1.03×10^{-4}	-	2.86×10^{-10}	-	-	-

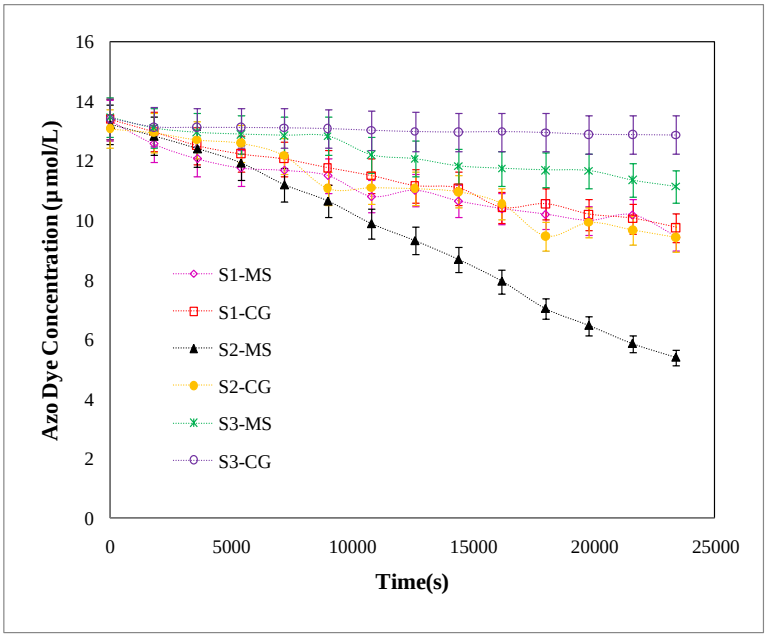

Figure 4.9: Comparison of the degradation of Methylene Blue by the ZnO thin films derived from solutions S1, S2 and S3 under oxygen-limited conditions.

4.5.3 Oxygen-rich Conditions

Photocatalytic activities of all different microstructures were also studied under oxygen-rich conditions (Fig. 4.10 and Table 4.4). Unexpectedly, the additional oxygen affected the different thin films and morphologies quite differently:

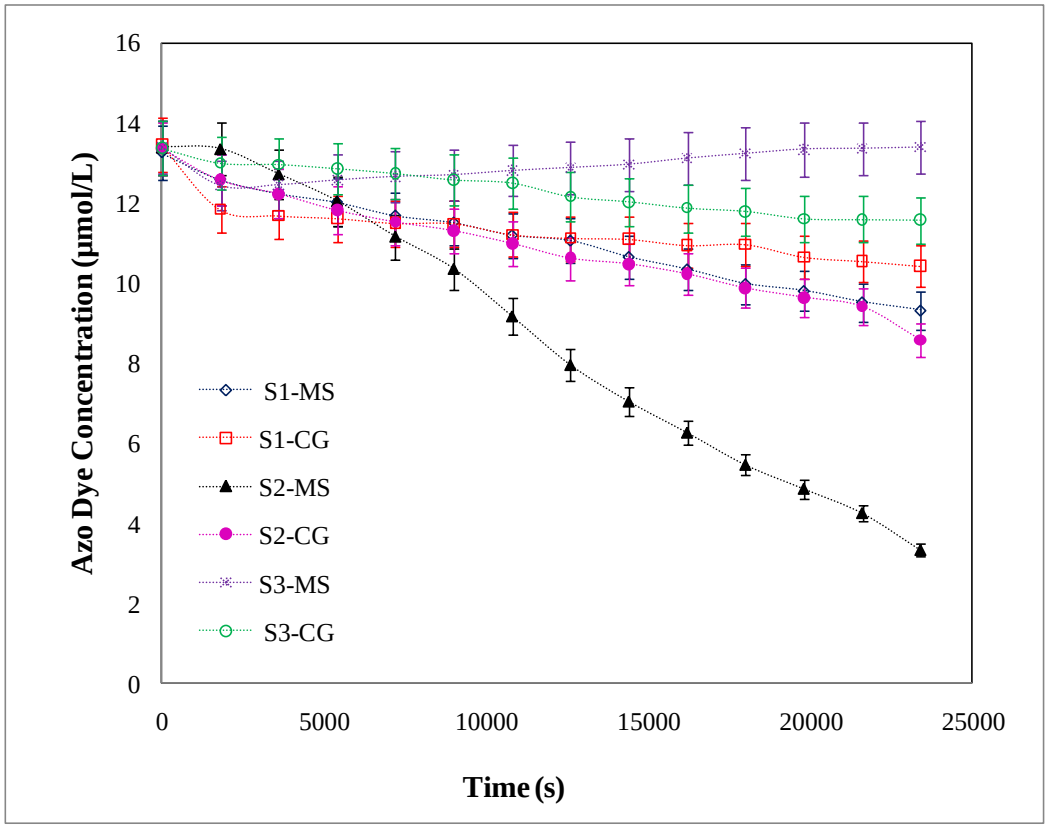

Figure 4.10: Comparison of the degradation of Methylene Blue by the ZnO thin films derived from solutions S1, S2 and S3 under oxygen-rich conditions.

The S2-MS and S2-CG thin films showed a significant increase in photocatalytic activity for the degradation of methylene blue under oxygen-rich conditions, as expected, since studies have shown that the addition of oxygen as an electron acceptor gives a higher reaction rate than either a photocatalyst or oxygen on its own [243]. This may also indicate that the Mars van Krevelen type mechanism is less important when sufficient dissolved oxygen is available (as dissolved oxygen are more readily available than the lattice oxygen which demands its activation energy barrier to be crossed before it become available in the bulk of the aqueous solution) to photocatalysts derived from solution S2, and that this dissolved oxygen can be used in the photocatalytic reaction rather than the lattice oxygen from the ZnO thin film (see Chapter 5 for a further study of this).

In contrast, for the S1-MS thin films, there was no significant difference in photocatalytic activity in comparison to the experiments performed under oxygen-limited conditions. This may indicate that the rate limiting step was not related to the liquid phase dissolved oxygen concentration; perhaps a Mars van Krevelen type mechanism is occurring, where supply and replenishment of the lattice oxygens are key to the reaction rate for photocatalysts derived from solution 1. The extreme of this case is the S1-CG film, which has a lower photocatalytic activity under oxygen-limited conditions. However, this is most likely due to an uneven ZnO coating on the glass substrate surface, as the thin films prepared directly on glass substrate did not show an even structure throughout the film.

Photocatalytic activities of thin films obtained by using solution S3 again differ. S3-CG thin films have a six times higher photocatalytic activity under oxygen-rich conditions. S3-MS showed little photocatalytic activity under similar conditions. Comparing to the photocatalytic activity of S3-MS under oxygen-limited conditions (Fig. 4.5), this could perhaps mean that the rich supply of dissolved oxygen for this film minimised the photocatalytic degradation of the methylene blue by minimising or preventing the lattice oxygens from participating in the reaction.

Comparison between the three template growth films (S1-MS, S2-MS and S3-MS), indicates that again there is a clear relationship between surface morphology (and the related thin film preparation method) and photocatalytic activity for these ZnO thin film-supported catalysts: there is a marked difference in photocatalytic activity (first order rate constant, $k_{app} = 1.33 \times 10^{-5}$,4.0×10^{-5} , 8.0×10^{-6} s^{-1} respectively; see Table. 4.4). S2-MS has the highest photocatalytic activity, S1-MS the second highest and S3-MS the lowest photocatalytic activity. Since S2-MS has a larger surface area than S1-MS, it is expected to have the greater photocatalytic activity. S3-MS, with the smallest ZnO microstructure (in terms of both crystal size and film thickness) and therefore the least amount of ZnO surface area, is therefore consistent with having the lowest volume-basis reaction rate. Furthermore, the alignment of the ZnO microstructure may be playing an important role. S1-MS and S2-MS films have ordered arrays of ZnO columns, grown from the substrate upwards (Fig. 4.1A & C) while the shape and alignment of the S3-MS are quite different (Fig. 4.1E). XRD results, Fig 4.11, indicate that for S2-MS at least, this higher reaction rate could very likely be due to the aligned columnar nanorod structure. S2-MS has a sharply oriented crystalline ZnO structure, with one major peak found at 34.4° which correlates to the (1,0,0) ZnO peak. S2-MS nanostructured films obtained from other batches, however, show (1,0,0), (0,0,2) and (1,0,1)

ZnO peaks, a difference resulting from the large crystal size with almost the same average crystallite size, and sparse distribution (≈ 2-5%). Li *et al.* [245] state that the ZnO surface face exposed to UV light influences the photocatalytic activity, and this aligned structure may therefore provide an orientation for maximising the redox reactions involved in the photocatalytic degradation. Morphologies S1-MS and S2-MS have the highest intensities of (1,0,0) crystallite peak compared to others. The slightly reduced order of reaction rate constant for S1-MS, compared to S2-MS, might also be due to its having more crystallite orientations [(1,0,0), (0,0,2), (1,0,1), (1,0,2) and (1,1,0)], compared to those present in S2-MS [(1,0,0), (0,0,2) and (1,0,1)] (see Figs. 4.2A and 4.2C). It may also be possible that the more regular S2-MS immobilised ZnO structure also prevents the loss of ZnO lattice oxygen (in the Mars van Krevelen type mechanism) as previously noted, indicating an increase in the catalyst's stability, a result of the efficient formation of radicals that initiate and propagate the advanced oxidation degradation via the more conventional photocatalytic redox mechanisms (see Chapter 5 for further study of this).

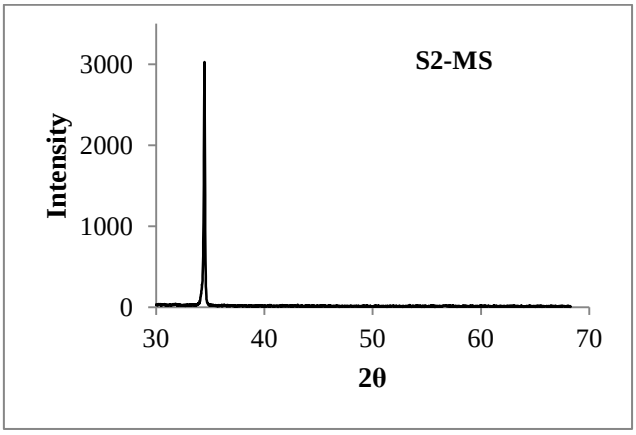

Figure 4.11: XRD analysis of thin flm S2-MS.

4.6 Reuseability of the Thin Films

In addition to ensuring that the thin films have a sufficiently large UV exposed surface area and suitable morphology to maximise photocatalytic activity, a key property of any thin film catalyst is that it must be mechanically and chemically stable, retaining a high catalytic activity over a extended period of use and reuse. This is so that long term use is viable: once it is coated on a support material within a reactor, it can remain there for an economically and practicably viable time for the operation. Consequently, each film was reused in several

reactions in order to determine the effect of these repeated uses on the photocatalytic activity and film morphology.

4.6.1 Oxygen-limited Conditions

Figs. 4.12-4.16 show the effect of the reusability of the films on photocatalytic activity (Fig. 4.12) and surface morphologies (Figs.4.13-4.16) under limited oxygen conditions. One film of each morphology was reused three times for methylene blue degradation (referred to henceforth as repeats 1R, 2R, and 3R respectively). It can be observed that the photocatalytic activity decreases with each experimental run, showing that the catalyst is not suitable for multiple uses under oxygen-limited conditions. This concurs with previous studies which have indicated a low stability of ZnO [246], and Figs. 4.13A-D, Figs. 4.14A-D, Figs. 4.15A-D, and Figs. 4.16A-D, showing that the surface is degraded by the reaction; which would decrease the surface area, crystallinity (See Fig.4.2) and aligned morphology, all of which in turn decrease photocatalytic activity. The amount of Zn metal present at the end of each reaction dwindled (See Figs. 4.17 and 4.18), especially for the morphology S1-MS, on multiple reuse of the same morphology under similar reaction conditions. The reduction in Zn leaching from the ZnO lattice, an indication of the lattice oxygen depletion under oxygen-limited conditions, reaffirms the aforementioned conclusions.

Because of the very low photocatalytic activity of S3-CG (Fig.4.12F) it was not easy to discern any effect on its multiple uses under the same reaction conditions. This low photocatalytic activity is consistent with the low levels of ZnO dissolution, indicating that the Mars van Krevelen type mechanism is likely not prominent for photocatalysis with thin films derived from solution 3 (S3) as discussed in Section 4.3.2.

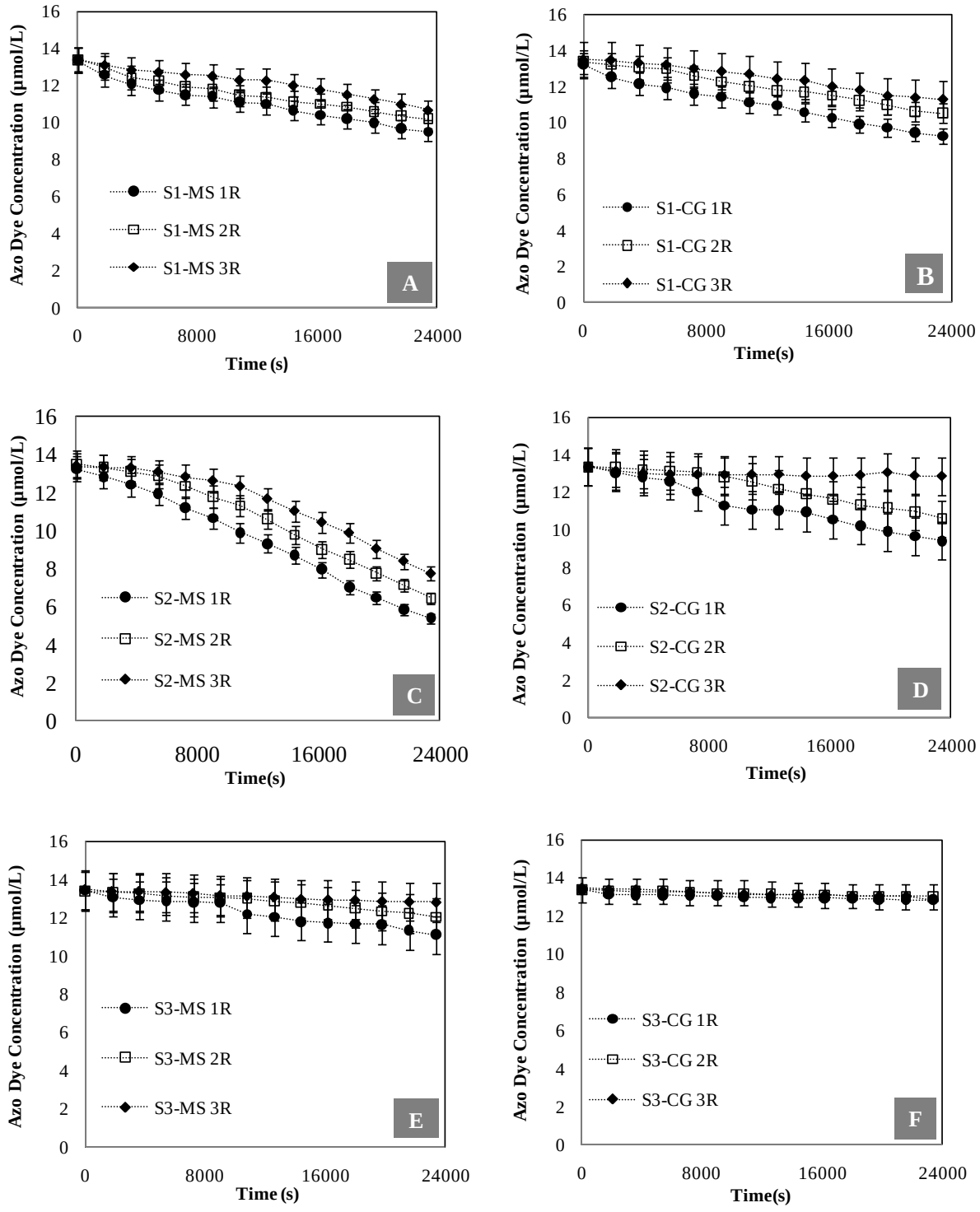

Figure 4.12: Reusability and reproducibility of the ZnO thin films in the photocatalysed degradation of 5mg L^{-1} Methylene Blue under O_2 limited conditions. (A) S1-MS; (B) S1-CG; (C) S2-MS; (D) S2-CG; (E) S3-MS; (F) S3-CG, where 1R denotes initial use of a film, and 2R and 3R denote the first and second reuse of the same film respectively.

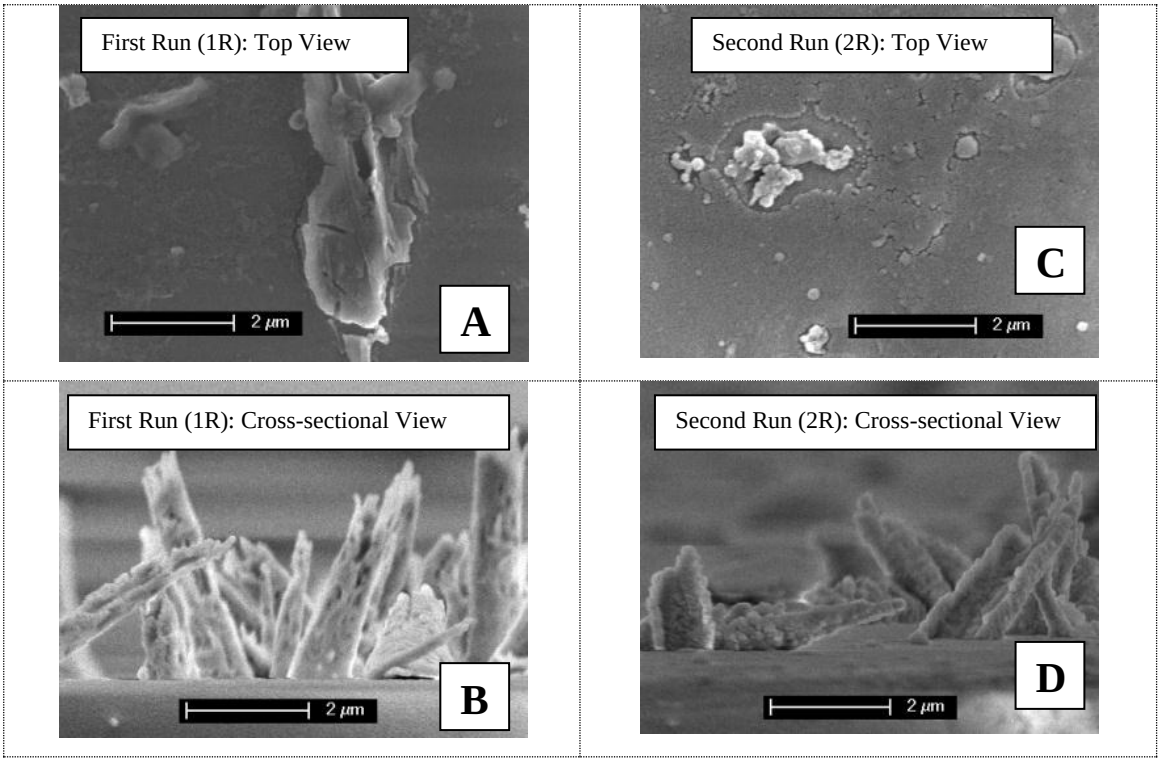

Figure 4.13: SEM images of morphology S1-MS after first (1R) and second run (2R); reproducibility and effect on morphology.(A) S1-MS first run (top view); (B) S1-MS first run (cross-sectional view); (C) S1-MS second run (top view); (D) S1-MS second run (cross-sectional view) under oxygen-limited conditions.

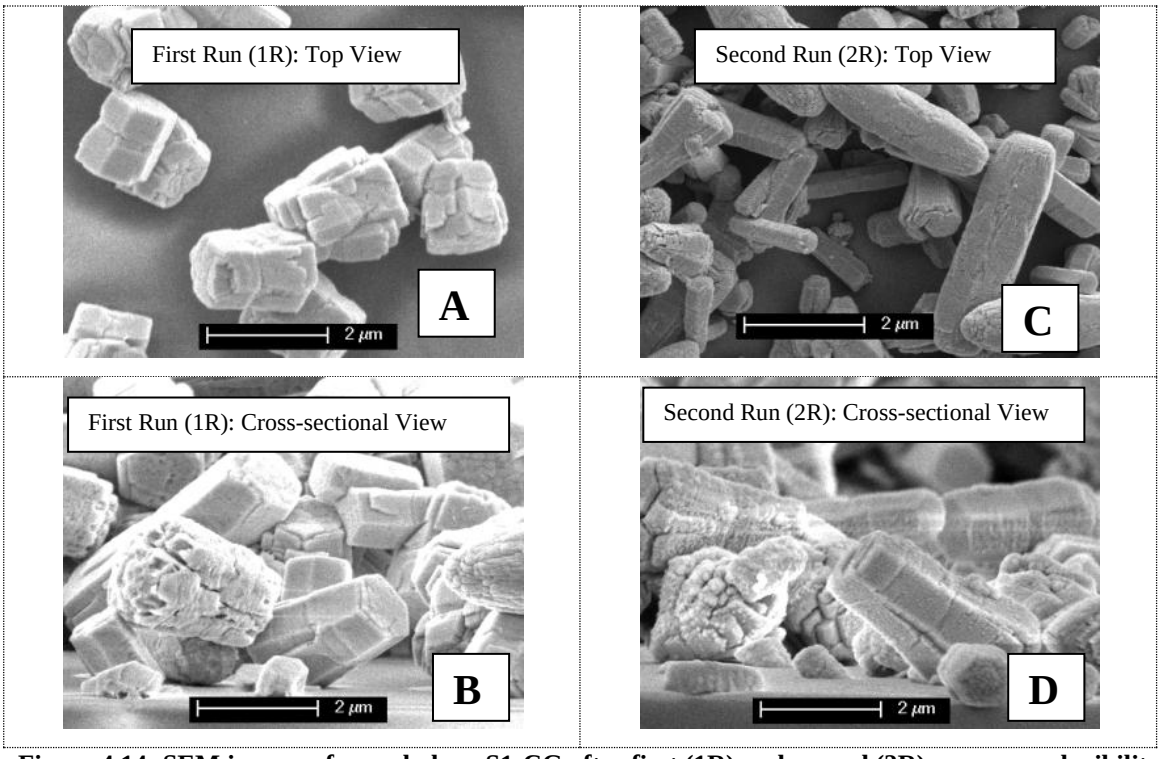

Figure 4.14: SEM images of morphology S1-CG after first (1R) and second (2R) run; reproducibility and effect on morphology.(A) S1-CG first run (top view); (B) S1-CG first run (cross-sectional view); (C) S1-CG second run (top view); (D) S1-CG second run (cross-sectional view) under oxygen-limited conditions.

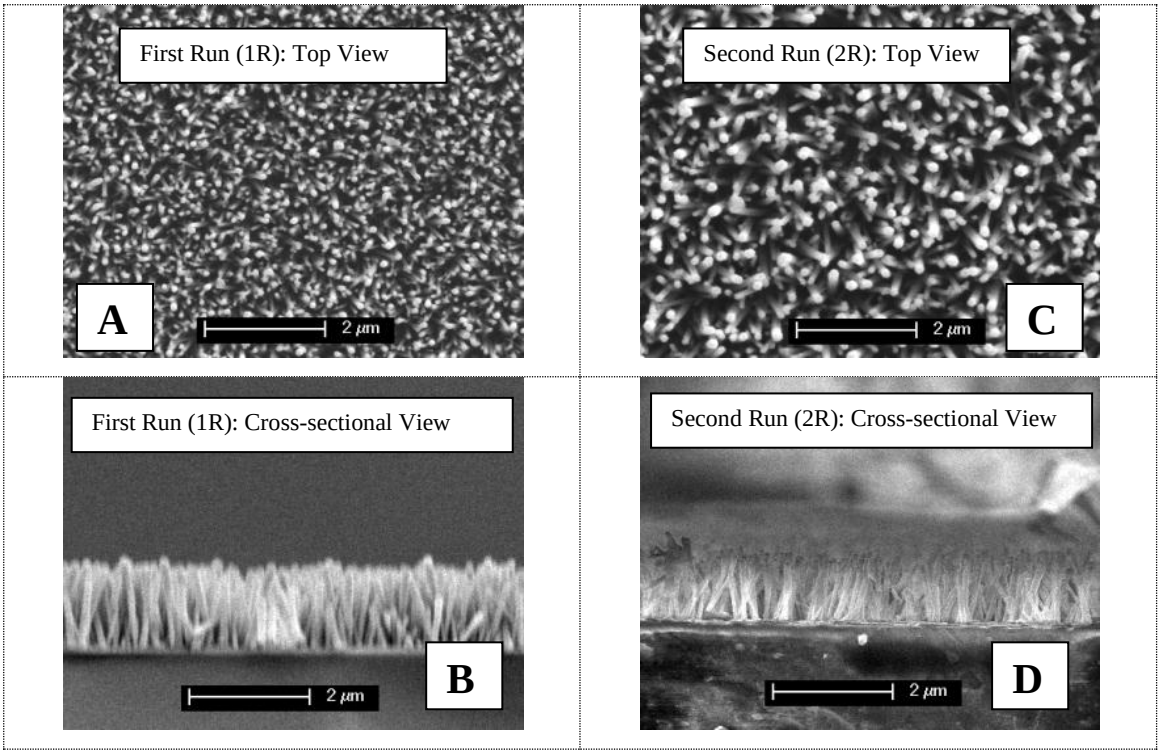

Figure 4.15: SEM images of morphology S2-MS after first (1R) and second run (2R); reproducibility and effect on morphology.(A) S2-MS first run (top view); (B) S2-MS first run (cross-sectional view); (C) S2-MS second run (top view); (D) S2-MS second run (cross-sectional view) under oxygen-limited conditions.

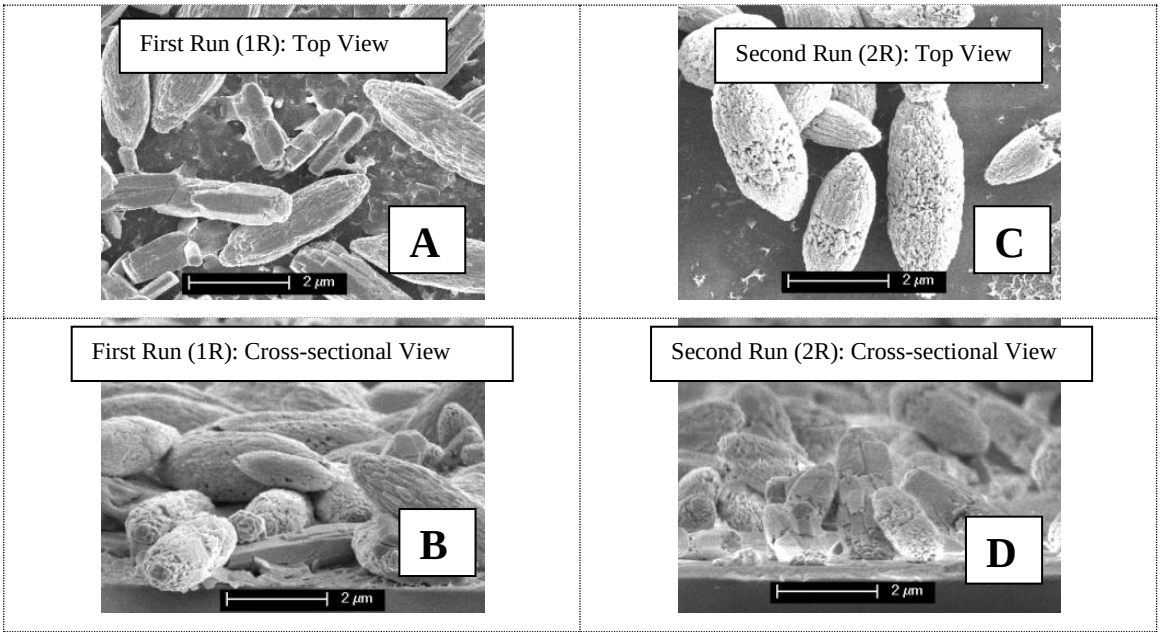

Figure 4.16: SEM images of morphology S2-CG after first (1R) and second run (2R); reproducibility and effect on morphology.(A) S2-CG first run (top view); (B) S2-CG first run (cross-sectional view); (C) S2-CG second run (top view); (D) S2-CG second run (cross-sectional view) under oxygen-limited conditions.

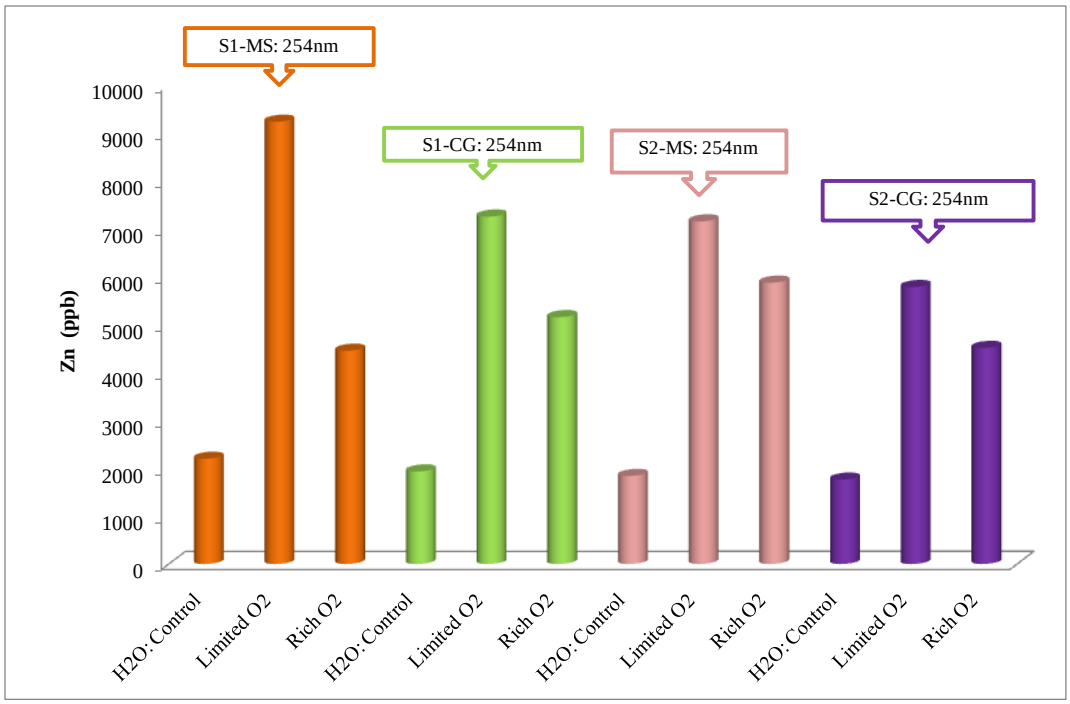

Figure 4.17: Concentration of Zn metal in the final reaction liquid for the first run (1R) as measured by atomic absorption spectroscopy (AAS) for the reactions photocatalysed by the ZnO thin films derived fromsolutions S1 and S2 on both clean glass slides (CG) and magnetron sputtered templates (MS).

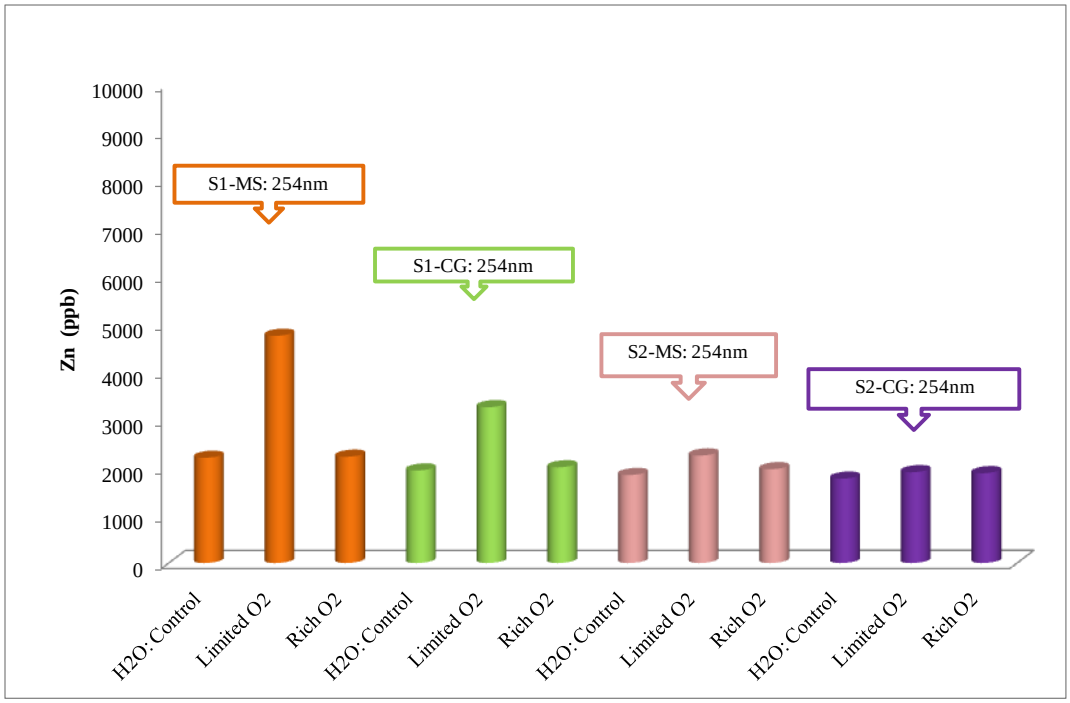

Figure 4.18: Concentration of Zn metal in the final reaction liquid for the second run (2R) as measured by atomic absorption spectroscopy (AAS) for the reactions photocatalysed by the ZnO thin films derived from solutions S1 and S2 on both clean glass slides (CG) and magnetron sputtered templates (MS).

4.6.2 Oxygen-rich Conditions

Figs. 4.19-4.23 show the effect of the reusability of the films on photocatalytic activity (Fig.4.19) and surface morphologies (Figs. 4.20-4.23) under oxygen-rich conditions. For S1-MS, S1-CG, S2-CG, S3-MS and S3-CG, similar azo dye degradation and photocatalytic activity results to those under oxygen-limited conditions were observed. This is surprising, as the surface structure is visibly more intact (Figs. 4.20A-D, Figs. 4.21A-D, Figs. 4.22A-D, and Figs. 4.23A-D) and there is significantly less ZnO dissolved in the liquid (Fig.4.2 and Figs. 4.17-4.18). This confirms the previous observation that there is poorer binding between the glass substrate and solution-deposited ZnO films than for the magnetron sputtered films. The poor reuseability of S1-MS and S3-MS could also be the result of these films having only a thin MS layer remaining after this multiple reuse. With solution S1 dissolving part of the MS layer during deposition of the top layer, as observed in Section 4.3.1, S1-MS has less MS template layer to bind than S2-MS and is therefore less stable for reuse. The lack of stability of S3 films is most likely due to some leached component of solution S3, as discussed in Sections 4.3.2 and 4.3.3.

In contrast, the S2-MS thin film has excellent reproducibility after multiple uses (Figs. 4.22A-D), showing no decrease in photocatalytic activity after multiple runs; this is the morphology that also showed the greatest improvement under oxygen-rich conditions. This again shows that morphology (and the thin film preparation method) influences photocatalytic activity, as previously discussed.

Since thin film S2-MS was the most stable film for reuse and had the highest reaction rate of all the films under both oxygen-limited and oxygen-rich conditions, its photocatalytic activity was therefore compared to that of the benchmark ZnO catalysts and uncatalysed UV photolysis.

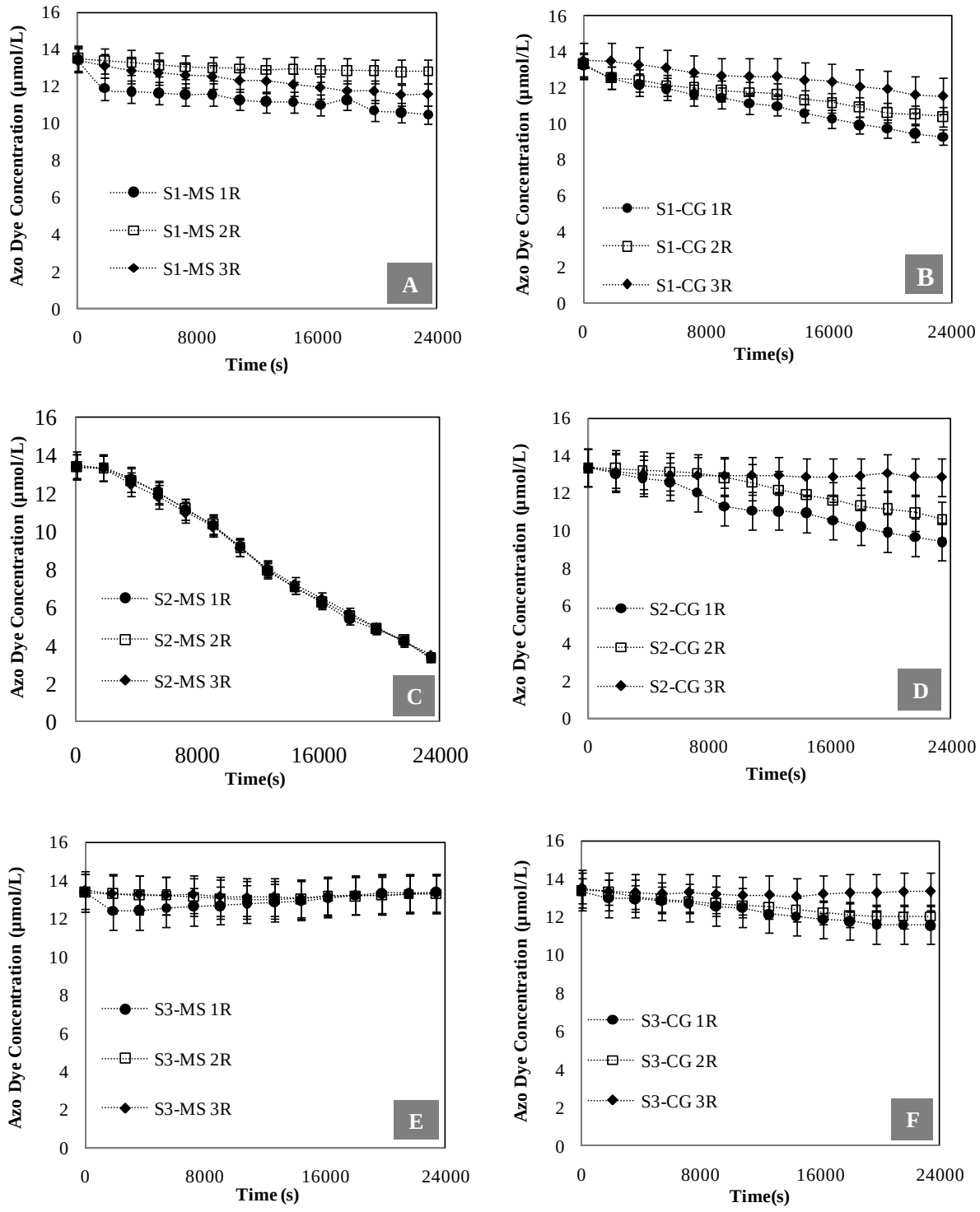

Figure 4.19: Reusability and reproducibility of the ZnO thin films in the photocatalysed degradation of 5mg L^{-1} Methylene Blue under O_2 rich conditions, A) S1-MS; (B) S1-CG; (C) S2-MS; (D) S2-CG; (E) S3-MS; (F) S3-CG, where 1R denotes initial use of a film, and 2R and 3R denote the first and second reuse of the same film respectively.

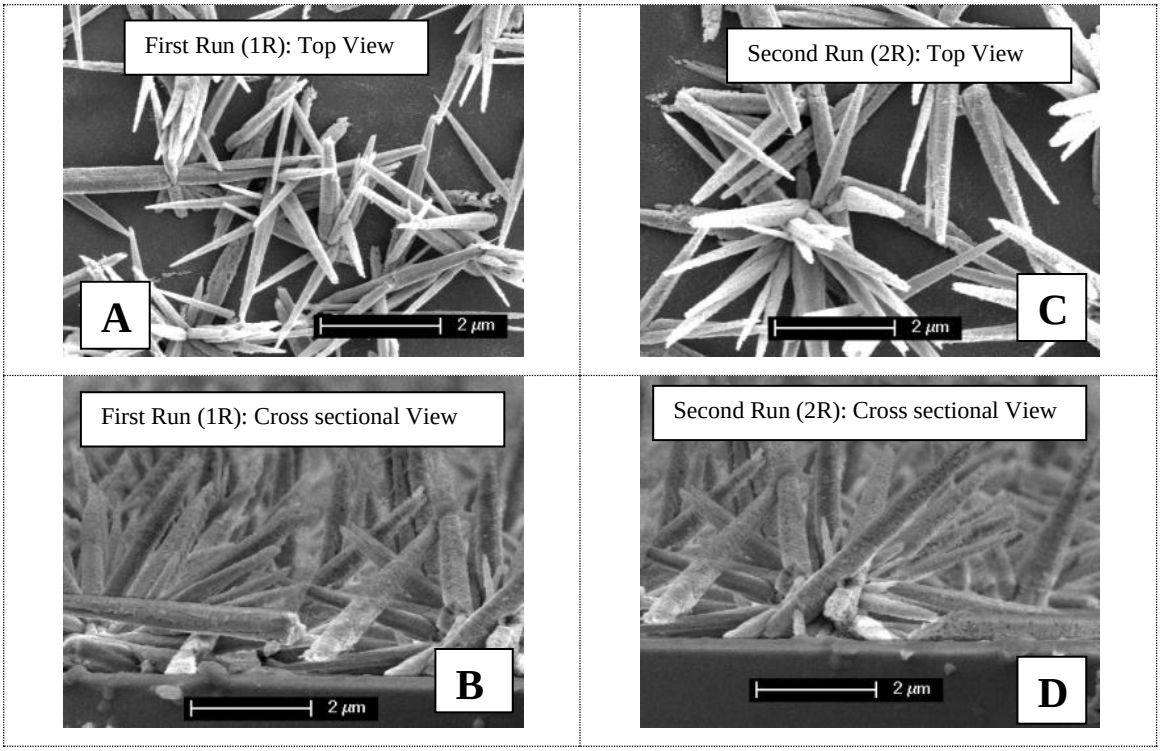

Figure 4.20: SEM images of morphology S1-MS after first (1R) and second run (2R); reproducibility and effect on morphology.(A) S1-MS first run (top view); (B) S1-MS first run (cross-sectional view); (C) S1-MS second run (top view); (D) S1-MS second run (cross-sectional view) under oxygen-rich conditions.

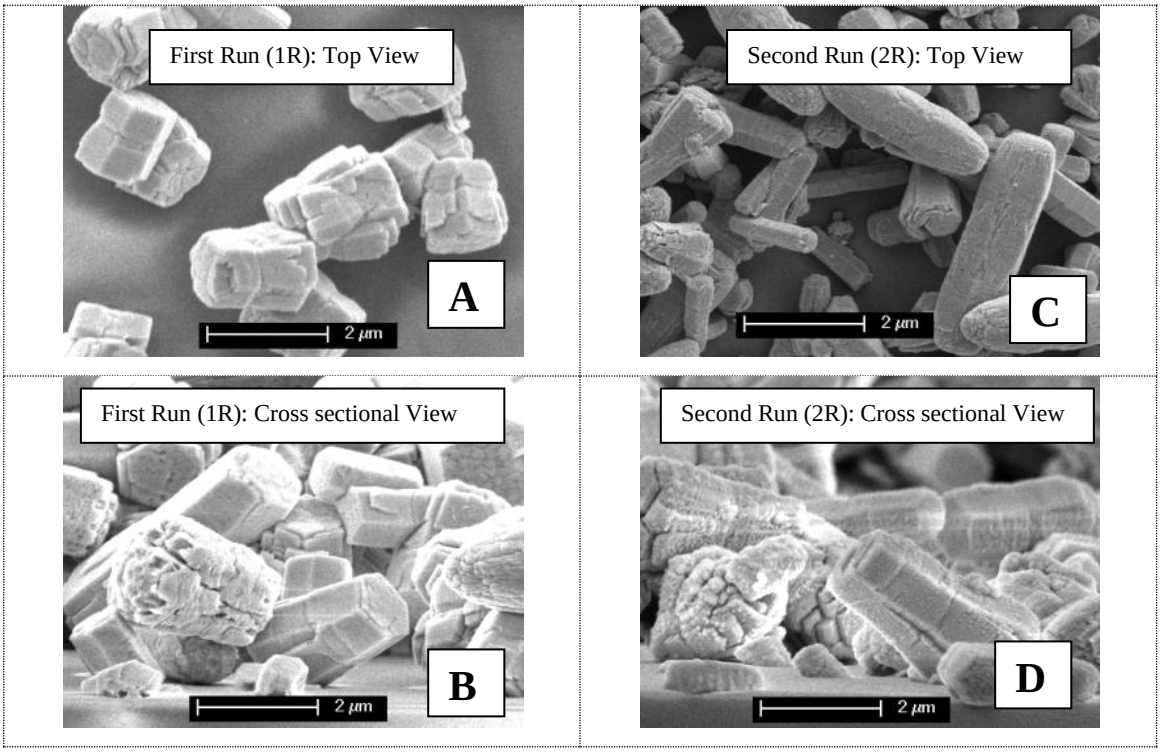

Figure 4.21: SEM images of morphology S1-CG after first (1R) and second run (2R); reproducibility and effect on morphology.(A) S1-CG first run (top view); (B) S1-CG first run (cross-sectional view); (C) S1-CG second run (top view); (D) S1-CG second run (cross-sectional view) under oxygen-rich conditions.

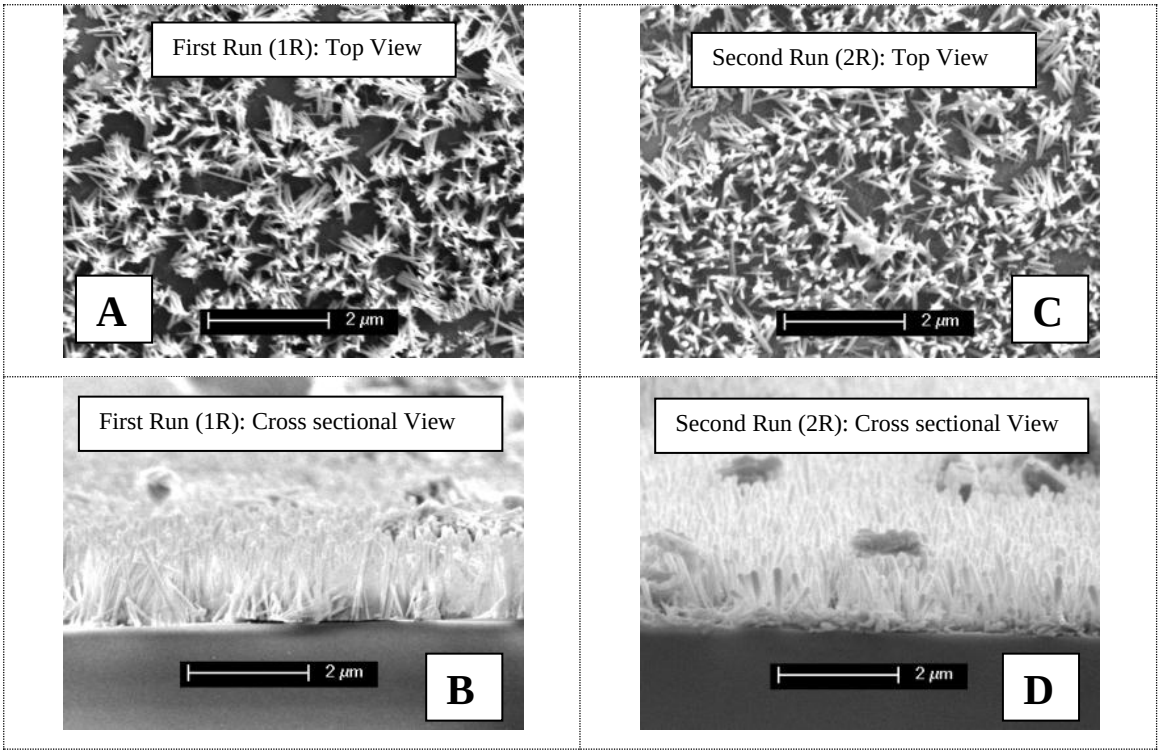

Figure 4.22: SEM images of morphology S2-MS after first (1R) and second run (2R); reproducibility and effect on morphology.(A) S2-MS first run (top view); (B) S2-MS first run (cross-sectional view); (C) S2-MS second run (top view); (D) S2-MS second run (cross-sectional view) under oxygen-rich conditions.

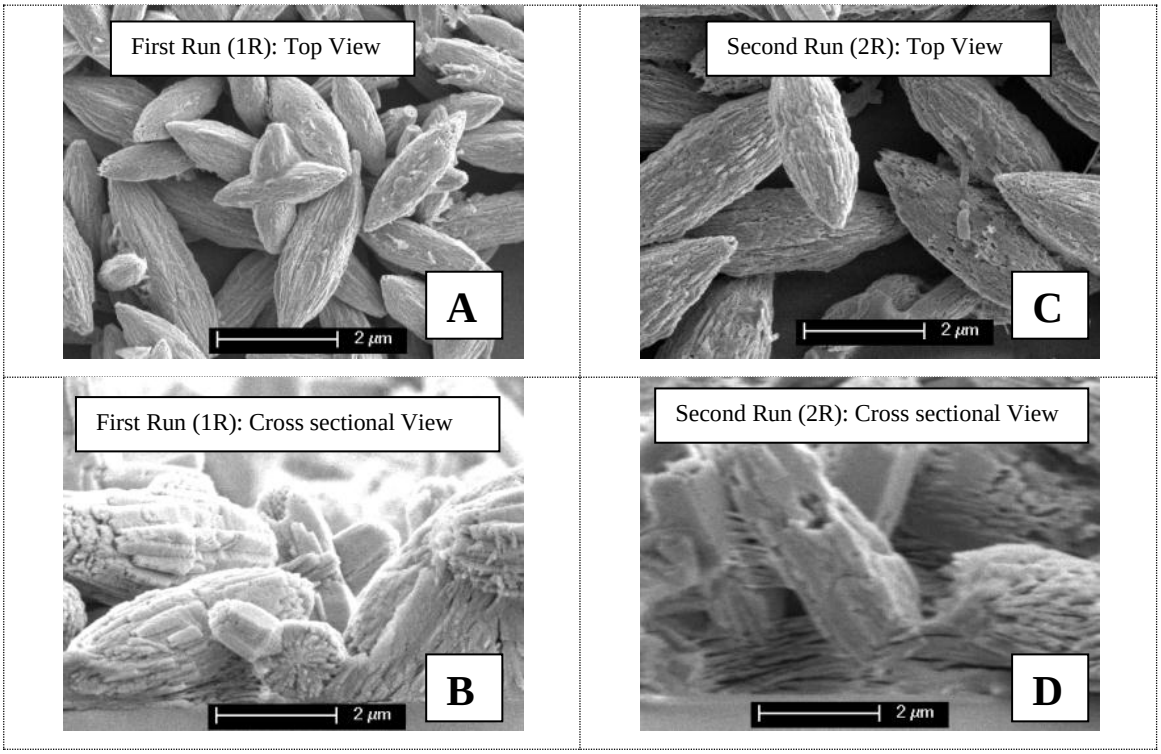

Figure 4.23: SEM images of morphology S2-CG after first (1R) and second run (2R); reproducibility and effect on morphology.(A) S2-CG first run (top view); (B) S2-CG first run (cross sectional view); (C) S2-CG second run (top view); (D) S2-CG second run (cross sectional view) under oxygen-rich conditions.

4.7 Comparison between Photocatalytic Activity of S2-MS, ZnO MS films and ZnO Powder

Fig. 4.24 shows the photocatalytic activity (under both limited and oxygen-rich conditions, unless otherwise stated) of the S2-MS thin film benchmarked (also see Appendix J) against MS only films, commercially available ZnO powder and uncatalysed UV photolysis (under oxygen-rich conditions only). MS-only films showed no photocatalytic activity without oxygen, whilst under oxygen-rich conditions showed some photocatalytic degradation of the methylene blue ($k_{app} = 9.0 \times 10^{-6}$ s^{-1}). Using a considerable mass of ZnO powder compared to that typically in the thin films (50ppm powder, as this was the smallest mass that could be accurately measured and used with the 40mL liquid reaction volume) allowed the methylene blue to be completely degraded during the observed reaction time at a comparatively high reaction rate on a liquid volume basis ($k_{app} = 1.0 \times 10^{-4}$ s^{-1} and $k''_{app} = 2.86 \times 10^{-10}$ m^3 m^2 s^{-1}) under oxygen-limited conditions.

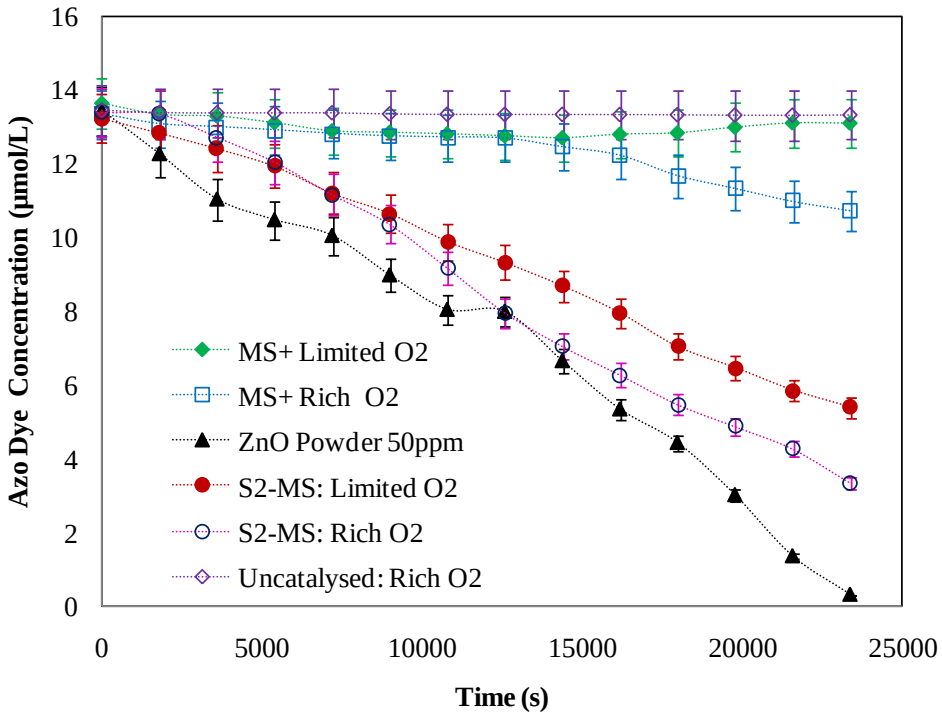

Figure 4.24: Comparison between photocatalytic activity of MS films (S2-MS, ZnO MS) to ZnO powder under both oxygen-limited and oxygen-rich conditions.

The ZnO powder had the largest photocatalytic activity for the mass added; since this mass is greater than that added for the films, this result is not surprising. A fairer basis of comparison

is on a surface area basis. It can be seen from Table 4.4 that the ZnO powder had a lower photocatalytic activity than the films based on the first order reaction rate constant per surface area basis. This indicates that the larger thin film structures (S1-MS, S1-CG, S2MS and S2-CG) might have a higher photocatalytic activity based on surface area. Further studies are required to investigate the mass-to-surface area influence.

Fig. 4.25 shows SEM images of the top surface of the unreacted MS film before and after reaction under oxygen-limited and oxygen-rich conditions. In contrast to the solution growth films, no obvious structural effect is observed on films after reactions under oxygen-limited conditions, which is in accordance with the lack of photocatalytic activity.

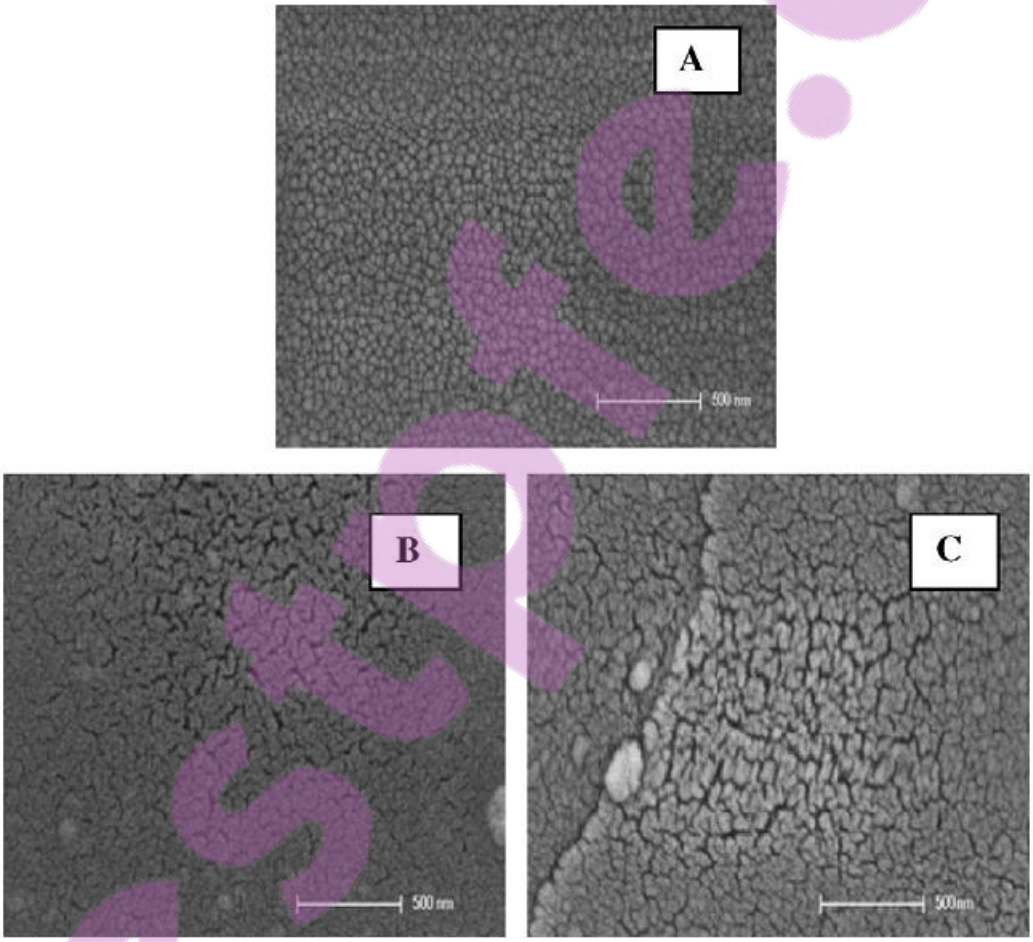

Figure 4.25: The effect of photocatalytic reaction of Methylene Blue on the top surface morphology of the MS films using SEM imaging: (A) MS only; (B) MS film reacted under oxygen-limited conditions O2; (C) MS film reacted under oxygen-rich conditions.

Since the reaction does not significantly change the microstructure nor any material deposition of model compound MB at its surfaces, it can be concluded that these MS–deposited films may not be able to use lattice oxygens and undergo photocatalysed oxidation

using a Mars van Krevelen type mechanism (further work is need to study this in detail). Therefore, it may be either the morphology formed and/or the components used in the hydrothermal solution deposition ZnO thin film growth method that enable the oxygens within the lattice to be available for the solution S1 and solution S2 ZnO thin films. This result is further confirmed by the images after reaction under oxygen-rich conditions, which show that although the structure displays cracks (which are most likely the result of mechanical forces during use and reaction, rather than an artefact caused by the reaction), overall there is little change in the underlying structure of the MS films. Consequently, it can be concluded that it is the hydrothermally solution-deposited ZnO nanostructured thin films (obtained from solution S1 and solution S2) that are photocatalytically oxidising the methylene blue via a Mars van Krevelen type mechanism. Detailed discussion in Chapter 5 determines the structural and chemical reasons for this.

4.8 Effect of Model compound MB Concentration on Photocatalytic Activity

Reactant concentration is one of the key factors that will affect the overall photocatalytic activity of any system. In order to study the effect of model compound concentration, two different concentrations (5 and 10 mgL^{-1}) of the model compound MB were used to study the effect of reactant concentration on photocatalytic activity under both oxygen-limited and oxygen-rich conditions. Reaction rate is normally expected to increase at a higher concentration; however, for MB the UV absorptivity (2461.69 and 2160.26 m^2 mol^{-1} for 5 and 10 mg L^{-1} MB respectively) usually decreases at a higher concentration, making transmittance of light more difficult. The catalyst to reactant ratio also decreases, effectively making the catalyst less available to the MB degradation. This means the reaction rate may decrease at higher concentrations, studied by Tayade *et al.* [247] and Matthews *et al.* [25].

Fig. 4.26 shows an overall affect of MB concentration on its degradation by the thin films derived from solutions S1 and S2 under both oxygen-limited and rich conditions (morphologies obtained from solution S3 (S3-MS and S3-CG) were not used to study photocatalytic activity and reaction kinetics at $10mgL^{-1}$ MB due to their negligible photocatalytic activity at $5mgL^{-1}$ MB). The overall reaction rate constants are summarised in Tables 4.5 and 4.2 and the percentage degradation comparisons in Tables 4.7 and 4.8 for both $5mgL^{-1}$ and $10mgL^{-1}$ respectively. Figs. 4.26a and 4.26c show an overall comparison of the photocatalytic activity of all four morphologies (S1-MS, S1-CG, S2-MS and S2-CG) under

oxygen-limited conditions at two different MB concentrations. In comparison, at different MB concentrations (5 and 10 mgL^{-1}), at higher MB concentration the photocatalytic activity of all nanostructured thin film morphologies (S1-MS, S1-CG S2-MS and S2-CG) was reduced (55%, 62%, 60% and 75% respectively) under oxygen-limited conditions. Morphology S2-CG was most prominent, with the highest total reduction in photocatalytic activity. Little variation in photocatalytic activity and reaction kinetics (see Figs. 4.26b and 4.26d; Table 4.7 and 4.8) was found between 10 mgL^{-1} and 5 mgL^{-1} MB under oxidation rich conditions except for an overall increased photocatalytic activity.

Table 4.5: Summary of 1st order reaction rate constants on liquid volume basis (k_{app} ; s^{-1}), UV exposed surface area (S) basis (k''_{app}, $m^3\ m^{-2}\ s^{-1}$) and mass of the catalyst basis (k''_{app}, $m^3\ kg^{-1}\ s^{-1}$) for the photocatalysed degradation of 5 mg L^{-1} methylene blue.

Thin Film photocatalyst	Estimated UV exposed surface area S (m^2)	First order rate constants (UV irradiation of 254nm): 5 mgL^{-1}					
		O_2 limited conditions			O_2 rich conditions		
		k_{app} (s^{-1})	k'_{app} ($m^3 kg^{-1} s^{-1}$)	k''_{app} ($m^3\ m^{-2}\ s^{-1}$)	k_{app} (s^{-1})	k'_{app} ($m^3 kg^{-1} s^{-1}$)	k''_{app} ($m^3\ m^{-2}\ s^{-1}$)
S1-MS	7.58×10^{-4}	3.32×10^{-1}	31.51	1.75×10^{-2}	3.75×10^{-1}	35.54	1.97×10^{-2}
S1-CG	5.98×10^{-4}	3.32×10^{-1}	14.47	2.22×10^{-2}	2.08×10^{-1}	9.064	1.39×10^{-2}
S2-MS	3.74×10^{-3}	1×10^{0}	65.55	1.06×10^{-2}	1.5×10^{0}	98.32	1.60×10^{-2}
S2-CG	7.7×10^{-4}	3.75×10^{-1}	13.96	1.94×10^{-2}	4.15×10^{-1}	15.45	2.15×10^{-2}

Table 4.6: Summary of I st order reaction rate constants on liquid volume basis (k_{app} ; s^{-1}), UV exposed surface area (S) basis (k''_{app}, $m^3\ m^{-2}\ s^{-1}$) and mass of the catalyst basis (k''_{app}, $m^3\ kg^{-1}\ s^{-1}$) for the photocatalysed degradation of 10 mg L^{-1} methylene blue.

Thin Film photocatalyst	Estimated UV exposed surface area S (m^2)	First order rate constants (UV irradiation of 254nm): 10 mgL^{-1}					
		O_2 limited conditions			O_2 rich conditions		
		k_{app} (s^{-1})	k'_{app} ($m^3 kg^{-1} s^{-1}$)	k''_{app} ($m^3\ m^{-2}\ s^{-1}$)	k_{app} (s^{-1})	k'_{app} ($m^3 kg^{-1} s^{-1}$)	k''_{app} ($m^3\ m^{-2}\ s^{-1}$)
S1-MS	7.58×10^{-4}	2.15×10^{-2}	2.0379	1.13×10^{-3}	2.48×10^{-2}	2.3507	1.30×10^{-3}
S1-CG	5.98×10^{-4}	4.9×10^{-3}	0.2132	3.27×10^{-4}	5.7×10^{-3}	0.2480	3.81×10^{-4}
S2-MS	3.74×10^{-3}	5.87×10^{-2}	3.8479	6.27×10^{-4}	1.03×10^{-1}	6.7649	1.11×10^{-3}
S2-CG	7.7×10^{-4}	6.0×10^{-3}	0.2234	3.12×10^{-4}	6.9×10^{-3}	0.2569	3.59×10^{-4}

Table 4.7: Summary of % photocatalytic degradation for the photocatalysed degradation of 5 and 10 mg L^{-1} methylene blue under oxygen-limited conditions.

	Overall Degradation for 5mgL^{-1} after 6Hrs	*Overall Degradation for 10mgL^{-1} after 6Hrs*	*Overall Degradation for 10mgL^{-1} MB after 24Hrs*
S1-MS	29.43%	13.5%	39.90%
S1-CG	27.26%	10.09%	10.93%
S2-MS	59.33%	23.61%	73.73%
S2-CG	27.97%	6.76%	13.86%

Table 4.8: Summary of % photocatalytic degradation for the photocatalysed degradation of 5 and 10 mg L^{-1} methylene blue under oxygen-rich conditions.

	Overall Degradation for 5mgL^{-1} after 6Hrs	*Overall Degradation for 10mgL^{-1} after 6Hrs*	*Overall Degradation for 10mgL^{-1} MB after 24Hrs*
S1-MS	29.70%	16%	44.47%
S1-CG	22.48%	10.78%	14.13%
S2-MS	75.01%	28%	90.94%
S2-CG	35.82%	9.49%	16.66%

An increase in MB concentration decreased the photocatalytic activity (in terms of reaction rate) of the thin films formed from the S2 solutions. The overall degradation, and degradation rate, of S2-CG decreased the most with 76% and 73% reduction in overall degradation under oxygen-limited and rich conditions respectively for the 5 mgL^{-1} increase in concentration. Photocatalytic activity of S2-MS, at higher concentration of MB, was subject to a slightly smaller level of reduction (~60%) in overall degradation under both oxygen-limited and rich conditions. Morphology obtained from solution S1 (S1-MS and S1-CG) has shown the highest level of reduction (75%, 63%) in photocatalytic activity at the higher MB concentration ($10mgL^{-1}$) under both oxygen-limited and rich conditions (Tables 4.7 and 4.8).

The overall reduction in photocatalytic activity at higher MB concentration is expected, because of light absorption by the darker solution; more UV light is being absorbed by model compound MB and less is reaching the surface of the catalysts. The system is therefore inclined towards more photolysis (with its concomitant lower degradation rate) and reduced photocatalytic effect. Similar results were concluded by Obee *et al.* and Vidal *et al.* [248, 249] who also observed a reciprocal effect of model compound concentration on photocatalytic activity. AAS analysis (Figs. 4.27 and 4.28) showing a decreased amount of Zn metal leaching out of the ZnO lattice at higher MB concentration reaffirmed that fewer UV photons are reaching the ZnO surface because of the decreased penetrative path-length of the photon [25, 247] at higher MB concentration. This is effectively a resistance to UV

photons, in reaching the catalyst surface, to trigger the generation of a higher number of electron-hole pairs.

These results show that there exists an inverse relationship between the MB concentration and photocatalytic activity, independent of thin film type and surface morphologies with slow reaction kinetics, perhaps with some mechanistic difference as well.

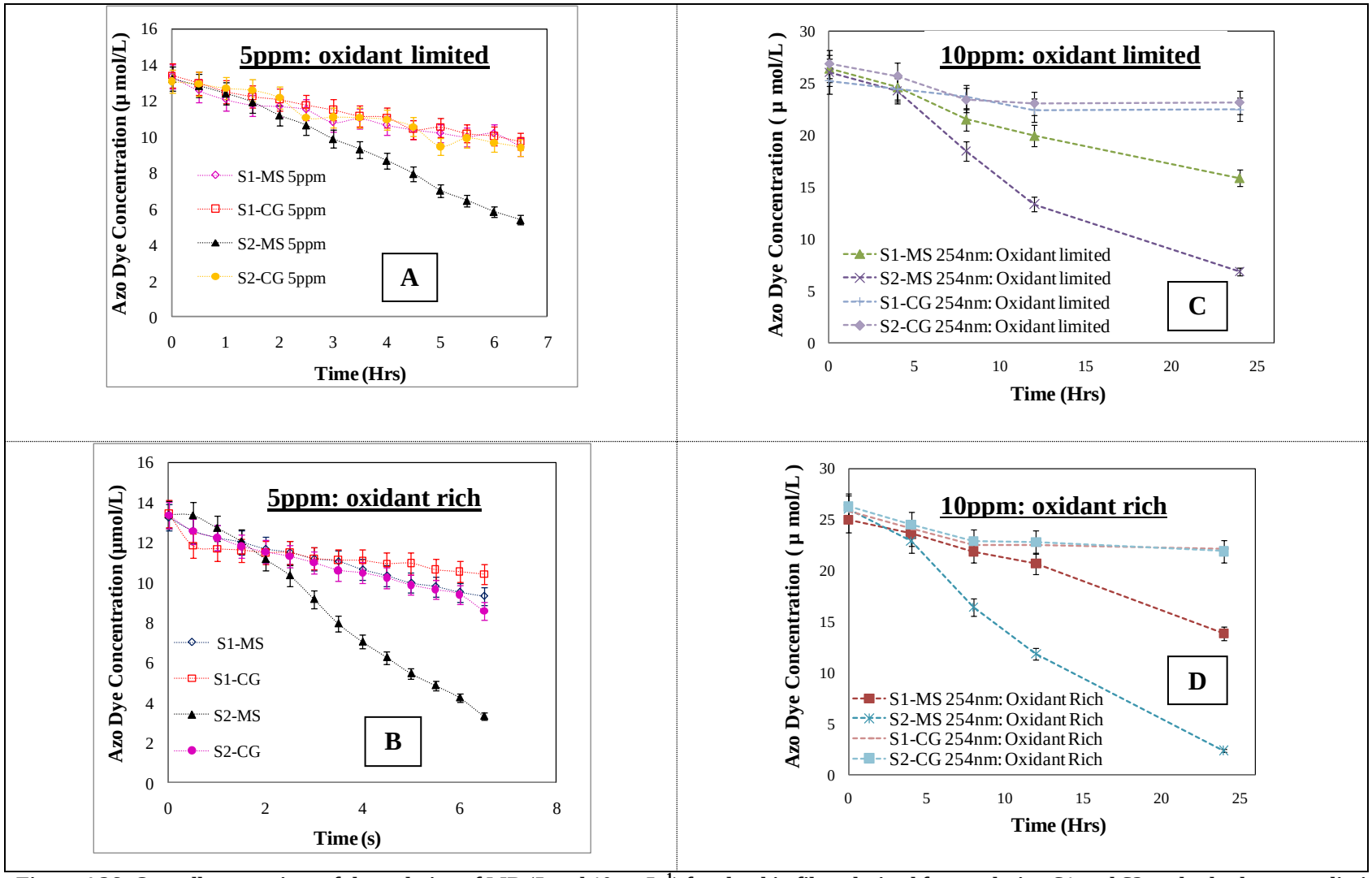

Figure 4.26: Overall comparison of degradation of MB (5 and 10 mgL^{-1}) for the thin films derived from solution S1 and S2 under both oxygen-limited and oxygen-rich conditions.

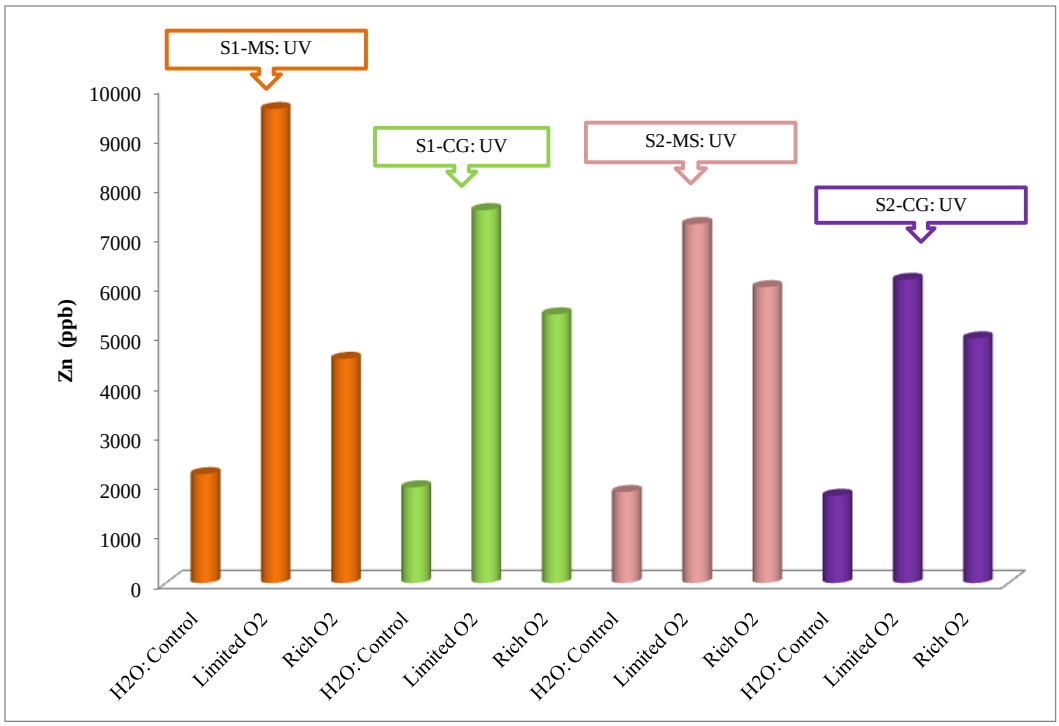

Figure 4.27: Concentration of Zn metal in the final reaction liquid as measured by atomic absorption spectroscopy (AAS) for the reactions(5mgL^{-1} MB) photocatalysed by the ZnO thin film derived from solutions S1 and S2 on both clean glass slides (CG) and magnetron sputtered templates (MS).

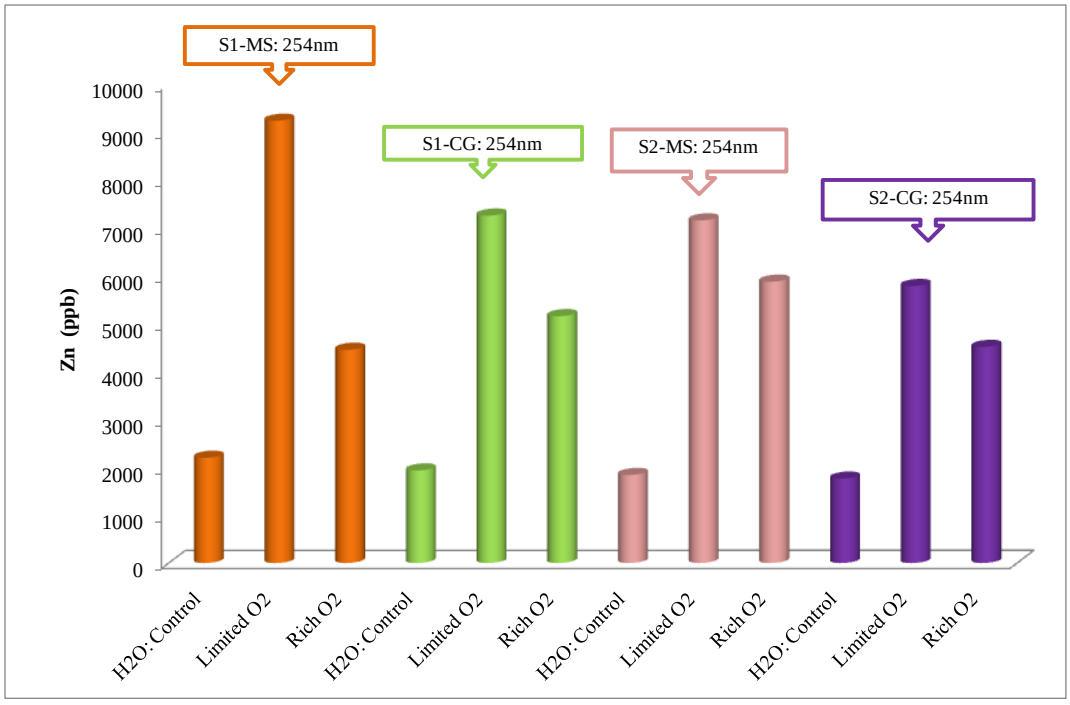

Figure 4.28: Concentration of Zn metal in the final reaction liquid as measured by atomic absorption spectroscopy (AAS) for the reactions(10mgL^{-1} MB) photocatalysed by the ZnO thin film derived from solutions S1 and S2 on both clean glass slides (CG) and magnetron sputtered templates (MS).

4.9 Summary

A clear relationship between surface morphology (and the related thin film preparation method) and photocatalytic activity was observed for ZnO thin film supported catalysts: the most aligned structure (S2-MS) had the highest photocatalytic activity, while the least aligned (S2-CG) had the lowest. Thus, the Methylene Blue degradation rate was the fastest for the ZnO thin film (S2-MS) with a uniform arrayed structure obtained from solution S2 on magnetron sputtered template. The degradation rates of the ZnO thin films were comparable to commercially available ZnO powder on a surface area and/or mass basis. Photocatalytic degradation of MB under oxygen-rich conditions increased. Nanostructured ZnO films obtained on an MS template from solutions S1and S2 are effective as photocatalysts for the liquid-phase photo-oxidation of methylene blue in both oxygen-limited and oxygen-rich conditions. Photocatalytic activity and MB concentration is approximately inversely proportional to each other. At a higher concentration of MB ($10mgL^{-1}$) the photocatalytic activity of the nanostructured thin films obtained from solution S1 (S1-MS and S1-CG) was reduced to almost half compared to reactions with $5mgL^{-1}$ MB; whereas the nanostructured thin films S2-MS and S2-CG have shown more than 50% reduction in photocatalytic activity at higher concentration ($10mgL^{-1}$) compared to reactions with $5mgL^{-1}$ MB. For all the thin films obtained from solution S1 and S2, a rich supply of oxygen decreases the structural erosion during the photoreaction with methylene blue. This suggests that the photocatalysed oxidation by these solution-deposited ZnO thin films occurs (at least partially) through a Mars van Krevelen type mechanism, indicating that oxygen from the catalyst lattice is removed and used in the oxidation reaction. The physical degradation of the catalyst is therefore diminished in the presence of oxygen, since the lattice oxygens (and therefore the catalyst structure) can be regenerated. The photocatalytic activity of all these nanostructures depends strongly on surface morphologies, crystallinity and concentration of MB.

Investigation into a detailed reaction mechanism, and a possible relationship between reaction mechanism and surface morphologies and their association with UV irradiation wavelength, is carried out in a detailed study in Chapter 5.

5 A More Detailed Investigation of Conventional versus Lattice Photocatalysed Reactions at both 254nm and 340nm

5.1 Introduction

This chapter investigates the relationship between surface morphologies of nanostructured ZnO thin films, liquid phase and solid phase reaction mechanisms (including the participation of lattice oxygens in the overall photocatalytic mechanism) and the reaction intermediates and products that could be produced during the various stages of photocatalytic reaction, under both oxygen-rich and limited conditions, at two different wavelengths (254nm and 340nm). The investigation will assist in identifying the possible relationship between surface morphologies, source of oxidant (either present in the bulk of the reaction fluid or lattice oxygen), and the possible impact of oxidant source on reaction mechanism, crystallinity and UV irradiation energy. All reactions were performed under the reaction conditions described in Section 3.2.3 for the four morphologies S1-MS, S1-CG, S2-MS and S2-CG obtained from solutions S1 and S2; however, from a different batch to those described in Chapter 4, the consequences of batch variations are described below.

5.2 Morphologies before Reaction

Since the morphologies of these thin films have been well characterised in Chapter 4 (and ref.[250]), only the results relevant to further discussion will be presented here. For all morphologies, slight variations in film thickness were noticed within the different batches; these are summarised below (there was also significant change in crystal surface smoothness for morphology S2-CG only).

Fig. 5.1 shows the cross-sectional views of SEM images produced from the different preparation methods before carrying out the reaction. For films grown from solution 1 (S1, Fig. 5.1A and 5.1B), surface morphologies for template and clean glass growth display different growth patterns, but similar-sized ZnO deposits. For both S1-MS and S1-CG (Fig. 5.1A and 5.1B), growth is characterised by long ZnO rods (producing a film thickness of approximately 4-6μm for S1-MS and 2-3μm for S1-CG). The only major difference is that for S1-MS, the ZnO structure was well aligned and uniformly arrayed, with single crystals growing up from the magnetron sputtered template (Fig. 5.1A). For S1-CG, the ZnO columns

aggregate randomly, both horizontally and vertically, as would be expected from growth not following a uniform template (Fig. 5.1B).

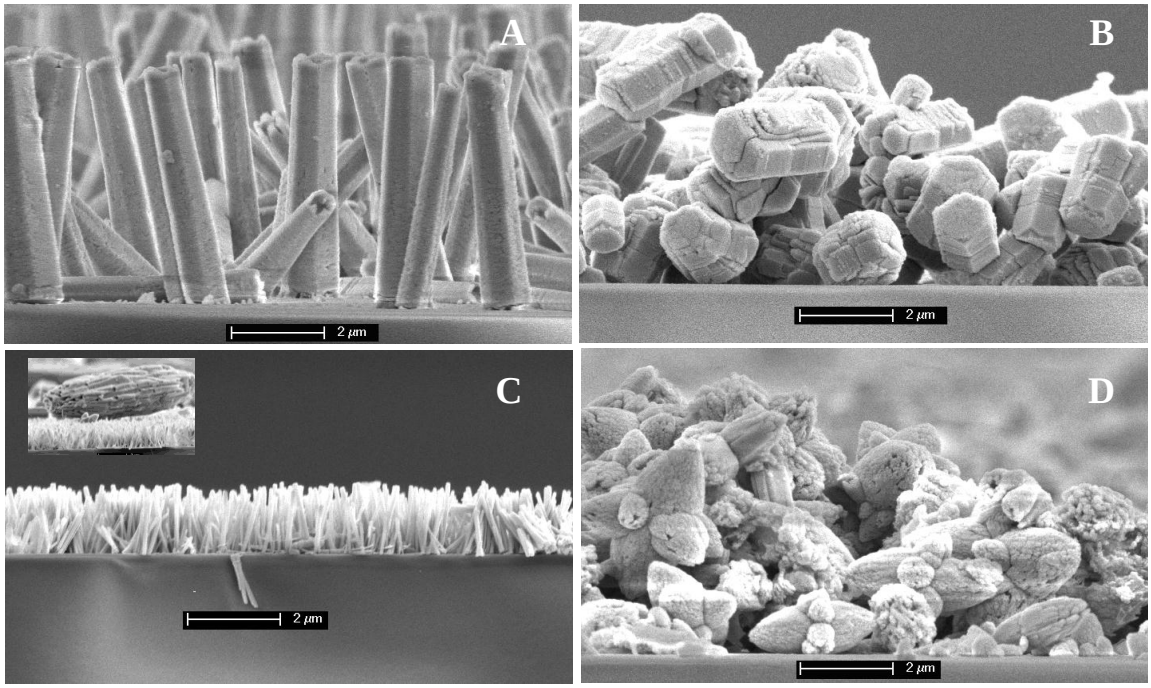

Figure 5.1: SEM cross-sectional views of surface morphologies of the different ZnO thin films on glass substrate before photocatalysis: A, S1-MS; B, S1-CG; C, S2-MS; D, S2-CG.

Fig. 5.1C and 5.1D show the cross-sectional views of the images of thin films obtained from solution S2. A very prominent difference in surface morphologies is noticed between S2-MS and S2-CG. S2-MS (Fig.5.1C) has a few large hexagonal ZnO crystals (8-10μm) scattered uniformly over an array of well aligned rods (~2μm tall). Because of its pH (7.5), the magnetron sputtered layer has remained intact and served as a template for the growth of these thin ZnO crystals. In contrast, the S1-MS aligned crystal rods are much larger and its magnetron sputtered underlayer cannot be readily seen. This is most likely because the acidic growth conditions (pH 5) have caused it to partially dissolve. Therefore it acts only to align the growth rather than as a template for the size of the crystals.

In contrast to both, but similar to S1-CG, S2-CG (Fig.2D) has randomly aggregated stacks of ZnO crystals (1-2μm) lying horizontally upon each other. It is speculated that these edged shaped ZnO crystals may be the result of inefficient growth on the clean glass slide. In comparison to S1-CG, S2-CG is mostly populated with high volumes of crystal stacks.

Total surface area available for different thin film morphologies is outlined in Tables 4.5-4.6 (also see Appendix K). S2-MS appears to have more available surface area per weigh (6.14 ×

10^3 m^2kg^{-1}) of thin film [corrected to significant figures after decimal place; see Appendix K] compared to the rest of the morphologies S1-MS (1.79×10^3 m^2kg^{-1}), S1-CG (6.51×10^2 m^2kg^{-1}) and S2-CG (7.16×10^2 m^2kg^{-1}). It can be seen that the presence of PEI in solution S2, the pH and the magnetron sputtered template play vital roles in the crystal surface formation, confirming results in Chapter 4 and elsewhere [115, 250].

Photocatalytic experiments were conducted under both oxygen-limited and rich conditions upon UV irradiation at wavelengths of 254nm and then 340nm.

5.2.1 Morphologies after Reaction upon UV Irradiation of 254nm

The following two sections describe the effect on surface morphologies both under oxygen-limited and oxygen-rich conditions under low pressure UV irradiation at 254nm.

5.2.1.1 Morphologies after reaction under oxygen-limited conditions

Figs. 5.2E to 5.2H show the cross-sectional views of the surface structure for the four different morphologies (S1-MS, S1-CG, S2-MS and S2-CG) after reaction under oxygen-limited conditions. Experiments without additional oxygen being supplied test the ZnO thin film catalyst under the toughest reaction regime (i.e; reaction under oxygen limited or without the supply of any other source of oxidant other than the surrounding air so that re reaction is limited in oxidant species because of mass transfer limitations), where overall reaction rates, and thus the formation of reaction intermediates and products, could be mass transfer limited due to lack of oxidant. Each morphology was photocatalytically active (see Section 5.3) and reaction rates were comparable to those under oxygen-rich conditions. As in Chapter 4 (and ref [250]) the ZnO surface morphology shows significant degradation from all reactions conducted compared to the initial structures (Figs. 5.1A-D) for this new batch of films. After reaction, the ZnO columnar structures have rougher surfaces and are even hollowed out by the reaction (Fig. 5.2E is an example of this) in spite of the fact that the pH of the reaction fluid remains nearly the same (7.10 ± 0.11) before and after the reaction.

As already shown in Chapter 4 (and ref [250]), since the only significant source of oxidant is the bulk or lattice oxygen of the ZnO thin film, the fact that the photocatalytic reaction rates are comparable to those under oxygen-rich conditions (see Section 5.3) combined with this structural erosion, indicates that it is reasonable to conclude that the oxidant could be the oxygen within the ZnO lattice (see Appendix H) with almost negligible water splitting.

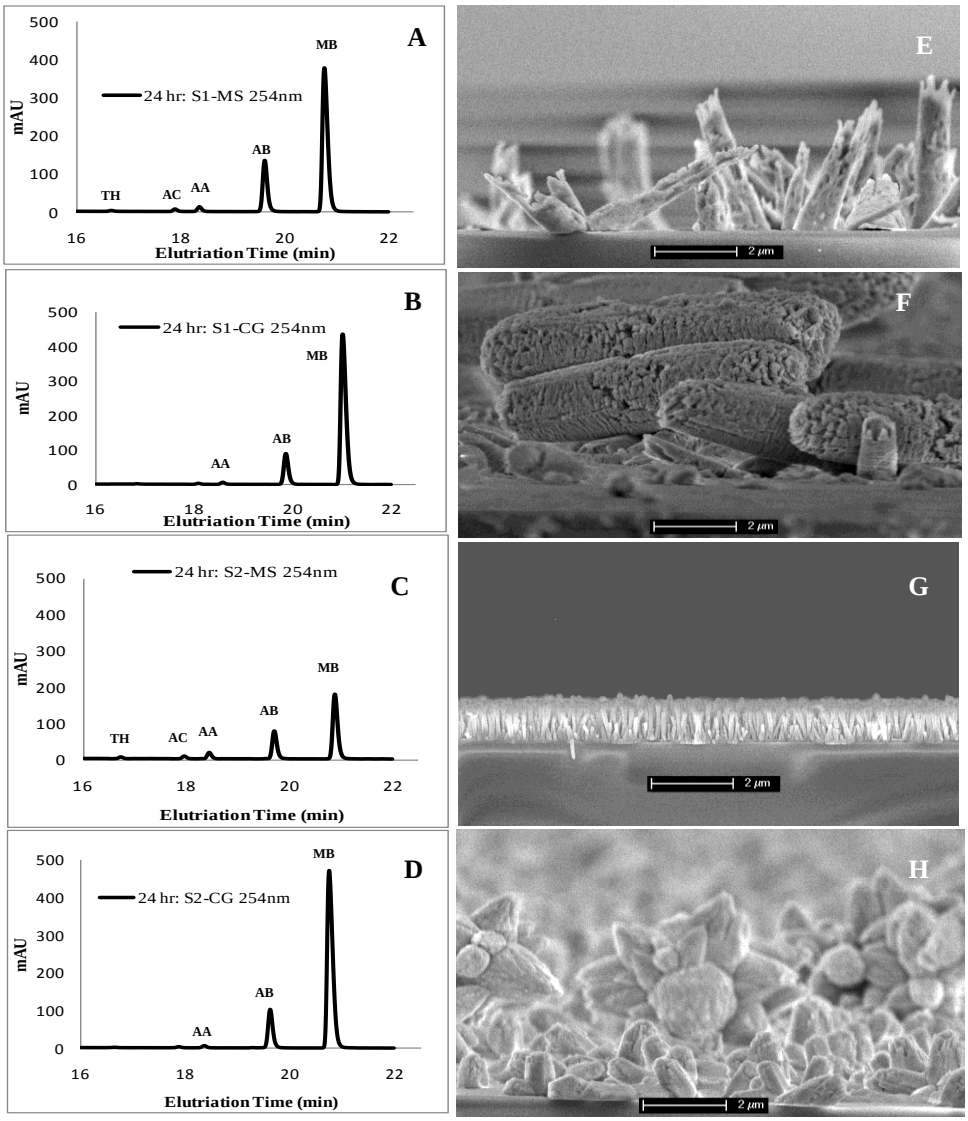

Figure 5.2: HPLC Chromatograms and SEM cross-sectional views of the thin films after the photocatalytic degradation of MB with UV irradiation of 254nm under oxygen-limited conditions: A, reaction intermediates from thin film S1-MS; B, reaction intermediates from thin film S1-CG; C, reaction intermediates from thin film S2-MS; D, reaction intermediates from thin film S2-CG; E, cross-sectional view of thin film S1-MS after reaction; F, cross-sectional view of thin film S1-CG after reaction; G, cross-sectional view of thin film S2-MS after reaction; H, cross-sectional view of thin film S2-CG after reaction.

5.2.1.2 Morphologies after reaction under oxygen-rich conditions

In Chapter 4 (and ref. [250]) it was shown that adding excess oxygen to the ZnO-methylene blue photocatalytic reaction system minimised and/or eliminated the erosion of the ZnO thin films seen in oxygen-limited conditions, whilst still maintaining similar degradation rates. The same results were found for this new batch of films, as shown by Figs.5.3E, 5.3F, 5.3G and 5.3H. For S1-MS (Fig.5.3E), a slight deterioration of the crystal surface is observed, reducing crystal size from 6μm to approximately 5μm and a change in the shape of the top of vertically aligned crystals.

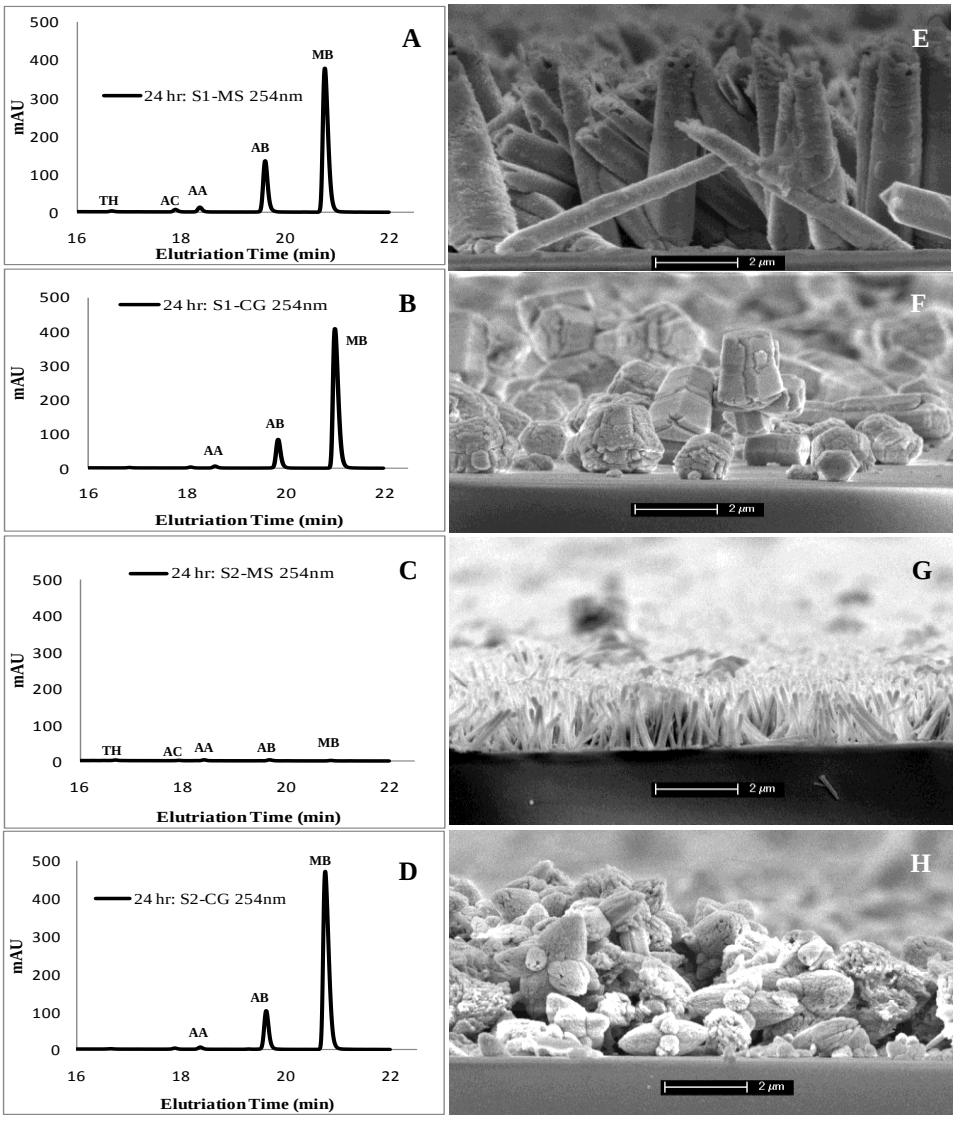

Figure 5.3: HPLC Chromatograms and SEM cross-sectional views of the thin films after the photocatalytic degradation of MB with UV irradiation of 254nm under oxygen-rich conditions: A, reaction intermediates from thin film S1-MS; B, reaction intermediates from thin film S1-CG; C, reaction intermediates from thin film S2-MS; D, reaction intermediates from thin film S2-CG; E, cross-sectional view of thin film S1-MS after reaction; F, cross-sectional view of thin film S1-CG after reaction; G, cross-sectional view of thin film S2-MS after reaction; H, cross-sectional view of thin film S2-CG after reaction.

Thin film S2-CG (Fig. 5.3H) shows a small change in crystal smoothness. In contrast there was no significant change in surface morphology for thin film S1-CG (Fig.5.3F) or S2-MS (Fig. 5.3G). These results again suggest that the lattice oxygen takes part in the reaction under oxygen-limited conditions and may indeed do so under oxygen-rich conditions. Therefore, this mechanism should be incorporated into the overall photocatalytic oxidation reaction mechanism that produces the various reaction intermediates and products that have been identified.

5.2.2 Morphologies after Reaction upon UV Irradiation of 340nm

In the previous two sections, it was further confirmed that the presence of di-atomic oxygen causes increased stability in all thin film morphologies and reaction rates. This, however, does not provide any information on the possible role of UV irradiation energy, because, with the decrease in UV irradiation wavelength, the energy associated with it increases. UV irradiation at a wavelength of 254nm gives a higher energy UV irradiation (4.13-6.20 eV); whilst 340nm is lower (3.10-4.13 eV).

Thus irradiation at a higher energy wavelength may trigger both photolysis and photocatalysis [92], whereas low energy (340nm) may participate only in photocatalysis; it has a greater tendency to be absorbed by ZnO (as it is better matched to the electron band gap of the ZnO) and less for the UV absorption of organics. Therefore it is expected that there would be heterogeneous photocatalysis only, at this wavelength, and little photolysis [95].

Figs. 5.4E, 5.4F, 5.4G and 5.4H show the surface morphologies of nanostructured ZnO thin films after reaction at UV irradiation of 340nm. For S1-MS (Fig. 5.4E), the crystal structure and its morphologies in contrast to reactions at 254nm has changed: the ZnO crystals have swelled and there are small bubbly patches on the crystal surface. However, the size and surface morphologies are less degraded and are therefore more stable as compared to S1-MS upon UV irradiation 254nm under both oxygen-limited and rich conditions. This surface degradation may indicate that only a surface and near surface reaction has occurred, compared to the more global ZnO lattice breakdown observed under irradiation with 254 nm UV light. In the case of S1-CG (Fig.5.4F), a significant change in surface roughness is noticed compared to the reaction at 254nm, whereas the crystal population and their size

more or less remain the same and stable. This indicates that this morphology is less stable with 340nm irradiation, but again indicates increases surface and/or near surface reaction compared to reactions with 25nm irradiation. The reasons for this will be explored in Section 5.3.

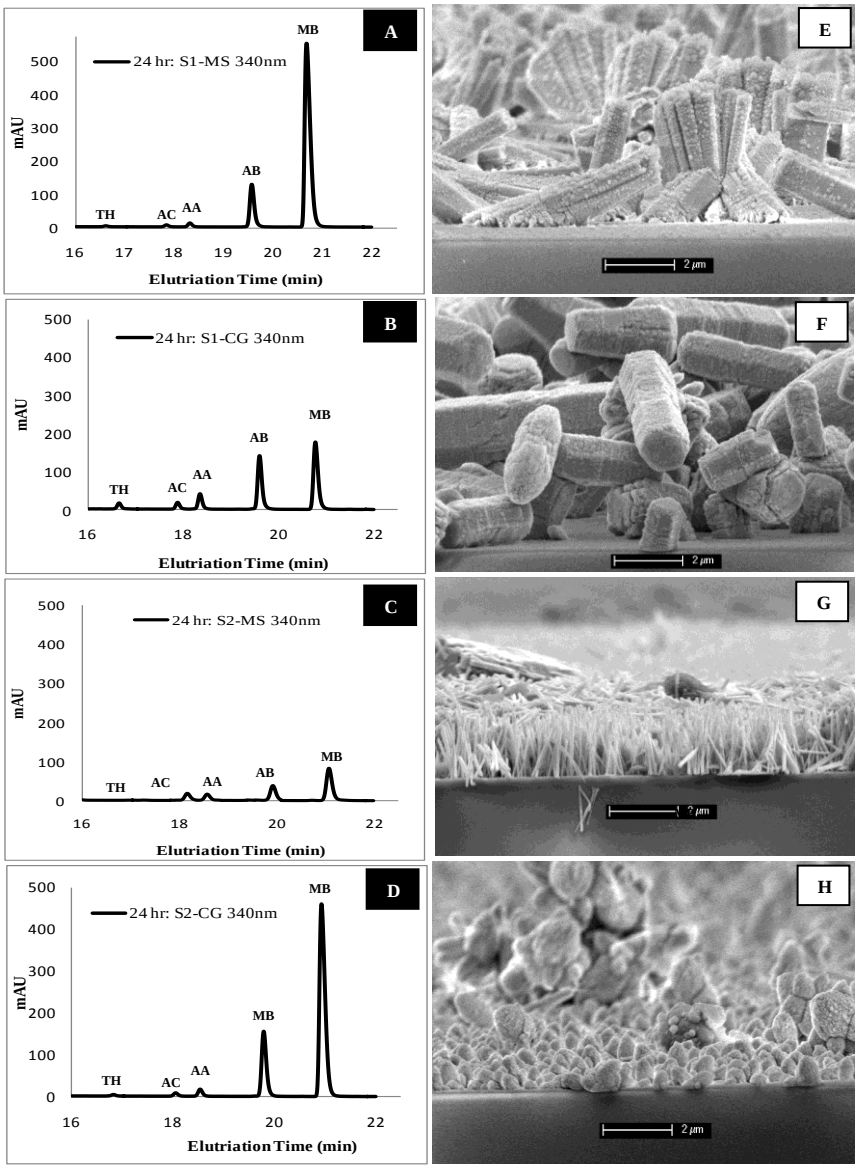

Figure 5.4: HPLC Chromatograms and SEM cross-sectional views of the thin films after the photocatalytic degradation of MB with UV irradiation of 340nm under oxygen-rich conditions: A, reaction intermediates from thin film S1-MS; B, reaction intermediates from thin film S1-CG; C, reaction intermediates from thin film S2-MS; D, reaction intermediates from thin film S2-CG; E, cross-sectional view of thin film S1-MS after reaction; F, cross-sectional view of thin film S1-CG after reaction; G, cross-sectional view of thin film S2-MS after reaction; H, cross-sectional view of thin film S2-CG after reaction.

The morphology of S2-MS (Fig.5.4G) again remained unchanged, further confirming it to be the most stable film, independent of the UV wavelength used. Morphology S2-CG (Fig.5.4H) again showed no appreciable surface morphology changes, confirming that solution 2 film preparations are the most stable to reaction. All thin film morphologies (S1-MS, S1-CG, S2-MS and S2-CG) showed improved stability (see Appendix B) under UV irradiation of 340nm compared to 254nm. AAS analysis showed (see Fig. 5.5) a slightly decreased amount of Zn metal leaching out from the ZnO lattice at the higher UV irradiation of 340nm. Reduction in Zn leaching from ZnO lattice at the higher UV irradiation wavelength is either because of an improved lattice oxygen generation, or increased surface and/or near surface reaction with 254nm UV irradiation. The reasons for this will be explored by looking at the reaction intermediates and products and relating them to these morphologies and the liquid and solid phase reaction mechanisms.

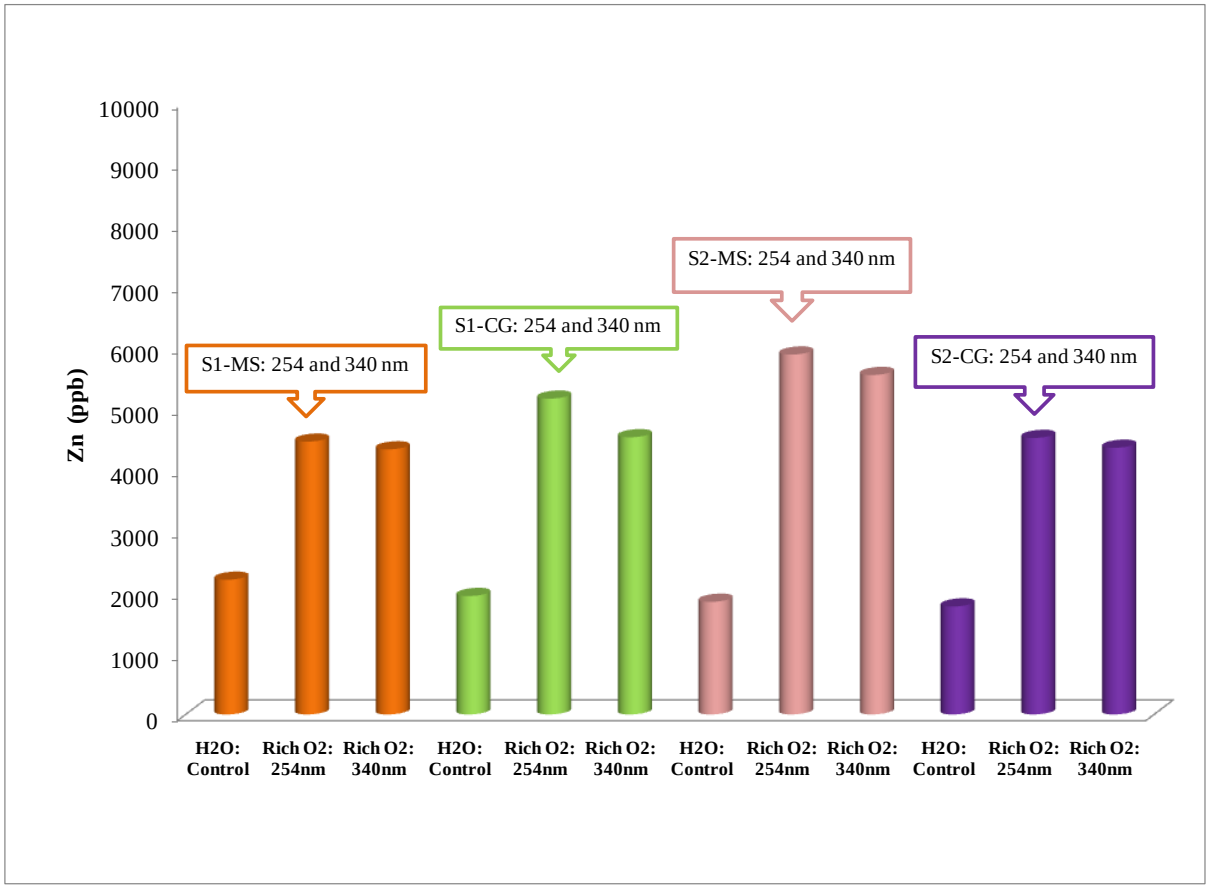

Figure 5.5: Comparison of the concentration of Zn metal in the final reaction liquid as measured by atomic absorption spectroscopy (AAS) for the reaction photocatalysed by the ZnO thin films under oxygen-rich conditions upon UV irradiation 254 and 340nm.

5.3 Reaction Intermediates and Product Analysis.

5.3.1 Species Identification

HPLC and LC-MS were used to identify the different reaction intermediates and products formed during the photocatalytic reaction (yielding the results in Figs. 5.2, 5.3, 5.4, 5.6 and 5.7; Appendix C). The four major identified reaction species were Azure B (AB), Azure A (AA), Azure C (AC) and Thionin (TH). Methylene Blue (MB) was used since it has a well characterised reaction product spectrum making differences in reactions between catalysts more reliably determined. It is therefore expected that these results match with previous MB photocatalysed reaction studies [236, 251-254]: and they do. In this work, intermediates were identified both by the external standard method (i.e. matching HPLC chromatograms under similar analytical conditions) and by the partial mass spectra of positive secondary ions obtained from LC-MS analysis. This analysis shows that for all reactions, parent molecule methylene blue was not fully oxidised in the reaction time studied. This could possibly be overcome by the careful consideration of surface morphology, crystallinity, UV irradiation wavelength and reaction time. To elucidate the mechanistic impact of the participation of lattice oxygen on the degradation of the model compound, a reaction progress analysis quantifying the concentration of each of these species was conducted under both UV irradiations in oxygen-limited and rich conditions.

5.3.2 Reactions with Irradiation at 254nm

Figs. 5.6A-H show the reaction profiles of model compound MB along with the formation and degradation of the four reaction intermediates AB, AA, AC and TH for all thin films S1-MS, S1-CG, S2-MS and S2-CG under both oxygen-limited and rich conditions with UV irradiation at 254nm.

Comparison of the reaction profiles from each film, under different conditions and with each other, reveals differences in kinetics and also possibly in reaction mechanism(s). Comparing the films, the reaction profiles again show that film S2-MS has the most complete degradation of all species at the highest reaction rates (Table 5.1). Thin films S1-MS have shown a significant amount of formation only, whereas morphology S2-MS has shown both: formation and further degradation of all four reaction intermediates. Morphologies S1-CG and S2-CG have been shown to form AB and AA only, under both oxygen-limited and rich conditions. Of the strongly aligned thin film structures, the reaction rate of S2-MS is higher than that of S1-MS (Table 5.1) under both oxygen-limited and rich conditions, because S2-

MS has more UV exposed surface area available (though the intensity of radiation per projected unit of the surface area is the same, but it does not mean at all that surface area in that unit area of the slide remains. Because of very slight change in surface morphologies, surface area per unit projected area also changed, therefore it is best to use exposed surface area to compare the results), compared to S1-MS (Figs 5.1A ,5.1C and Table 5.1) as a result of its more highly aligned micro-rod columnar array (~2µm tall). This further confirms that highly aligned morphologies (having highest overall surface area; may be rate determining step) are more photocatalytically active, not only for the parent molecule (MB), but also the intermediates. This higher reaction rate could most likely be a result of the aligned columnar nano rod structure providing an orientation for maximising the redox reactions involved in the photocatalytic degradation [245].

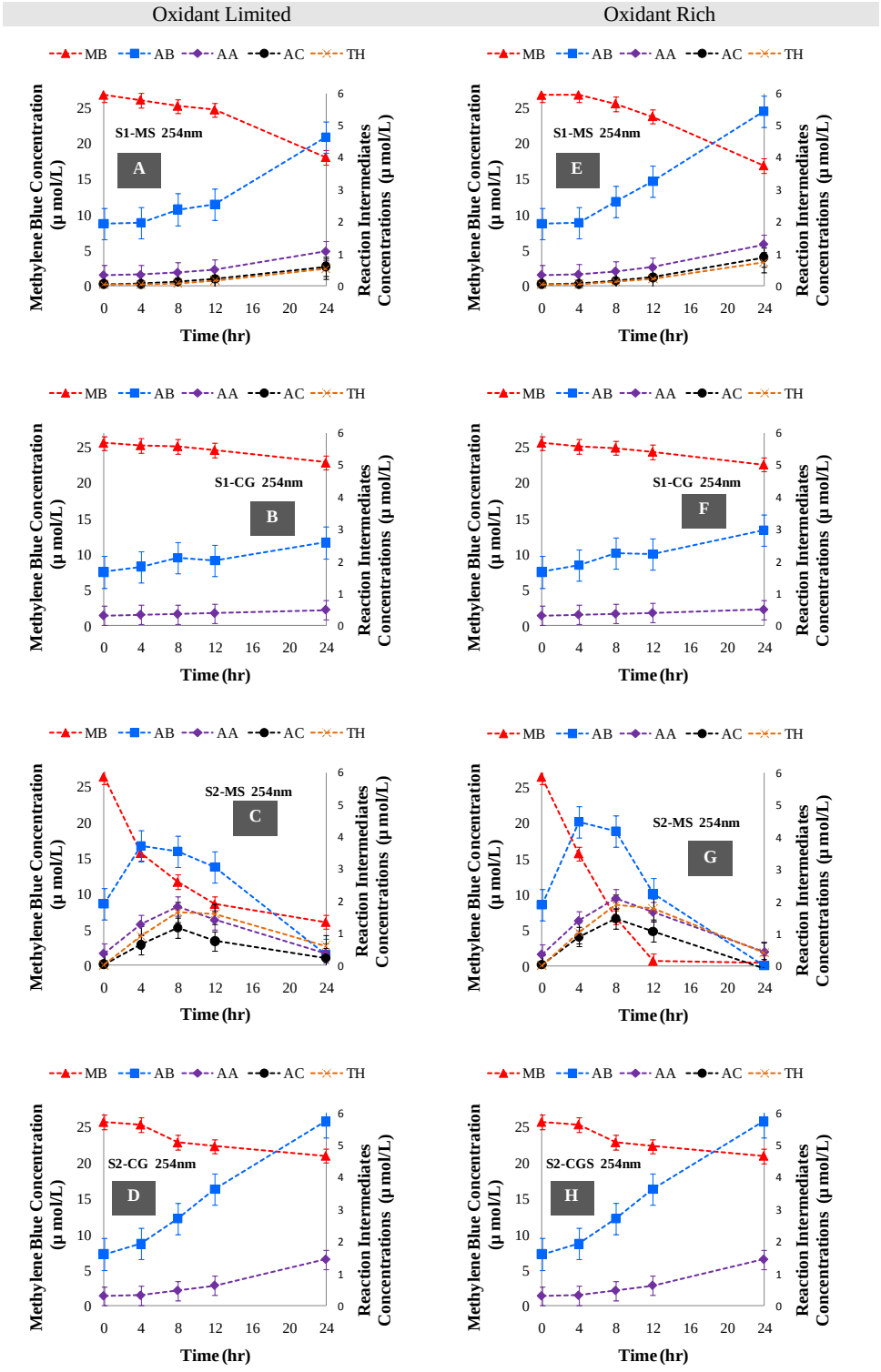

Figure 5.6: Reaction profile comparison of the reaction intermediates from methylene blue photocatalysed by four different ZnO thin films upon UV irradiation at 254nm under oxygen-limited and oxygen-rich conditions, obtained by HPLC: A, S1-MS: oxygen-limited; B, S1-CG: oxygen-limited; C, S2-MS: oxygen-limited; D, S2-CG: oxygen-limited; E, S1-MS: oxygen-rich; F, S1-CG: oxygen-rich; G, S2-MS: oxygen-rich; H, S2-CG: oxygen-rich.

Table 5.1: Summary of 1st order reaction rate constant on liquid volume basis (k_{app}: s^{-1}), catalyst mass basis (k'_{app}: $m^3kg^{-1}s^{-1}$) and a UV exposed surface area (S) basis (k''_{app}: $m^3\ m^{-2}\ s^{-1}$) for the photocatalysed degrdation of 10 mg L^{-1} Methylene Blue under UV irradiation of 254nm.

Thin Film photocatalyst	Estimated UV exposed surface area S (m^2)	First order rate constants (UV irradiation of 254nm)					
		O_2 limited conditions			O_2 rich conditions		
		k_{app} (s^{-1})	k'_{app} ($m^3kg^{-1}s^{-1}$)	k''_{app} ($m^3\ m^{-2}\ s^{-1}$)	k_{app} (s^{-1})	k'_{app} ($m^3kg^{-1}s^{-1}$)	k''_{app} ($m^3\ m^{-2}\ s^{-1}$)
S1-MS	7.58×10^{-4}	2.15×10^{-2}	2.0379	1.13×10^{-3}	2.48×10^{-2}	2.3507	1.30×10^{-3}
S1-CG	5.98×10^{-4}	4.59×10^{-3}	0.4644	2.58×10^{-4}	5.7×10^{-3}	0.5402	3.00×10^{-4}
S2-MS	3.74×10^{-3}	5.87×10^{-2}	5.5639	3.09×10^{-3}	1.03×10^{-1}	9.7819	5.44×10^{-3}
S2-CG	7.7×10^{-4}	6.0×10^{-3}	0.5687	3.17×10^{-4}	6.9×10^{-3}	0.6540	3.64×10^{-4}

Comparing the different reaction conditions for the same films, the reaction profiles with and without oxygen are almost identical for thin films S1-MS, S1-CG and S2-CG. These films all have nearly the same reaction rate constant (see Table 5.1) with and without added oxygen and do not undergo significant degradation of the azo dye reaction intermediates (AA, AB, AC and TH). This most likely indicates that there is little change in the reaction mechanism and kinetics, and the overall reaction is largely independent of the oxygen (although the films are stabilised). This could therefore indicate that the Mars van Krevelen type mechanism, where lattice oxygen is abstracted from the lattice and replaced when dissolved oxygen is present, is the dominant photocatalysed degradation mechanism for these morphologies at 254nm. Based on the lack of intermediate degradation, this mechanism therefore contributes only to the formation of these intermediates and not to their degradation. Furthermore, this would indicate that these films either cannot support significant generation of active species via the other photocatalytic reaction mechanisms, or that the Mars van Krevelen type lattice oxygen abstraction mechanism deactivates the catalyst surface, thereby inhibiting further reaction. Further tests need to be done to definitively verify this, using, for example, radioactive tracers.

In contrast, thin film S2-MS has quite different reaction profiles between oxygen-limited and oxygen-rich conditions. The kinetics differ also (Table 5.1): under oxygen-rich conditions, near complete MB degradation is accomplished twelve hours earlier than under oxygen-

limited conditions (comparing Figs. 5.6C and 5.6G) giving concomitant higher MB degradation rates (Tables 5.1 and 5.2). In terms of the identified reaction intermediates, under oxygen-rich conditions, formation and degradation profiles of all identified reaction intermediates were also increased compared to oxygen-limited conditions (Figs. 5.6C and 5.6G; Table 5.1 and 5.2). This again confirms that the presence of oxygen makes a kinetic difference. Combined with the SEM results and those in Chapter 4 (and ref [250]), these results indicate that the presence of oxygen produces a mechanistic difference also (as not only the reaction rates were higher as well as stability of nanostructured ZnO thin films were also increased). S2-MS is the most stable of the thin film morphologies, indicating that the Mars van Krevelen type mechanism affects reactions with this morphology the least, despite having the highest reaction rate. Furthermore, the fact that significant degradation of these intermediates is catalysed by thin film S2-MS indicates that either the de-activation present in the other films does not occur and/or that the surface is able to photocatalyse active radical species via the other photocatalytic mechanisms at a greater rate than the other thin films. This could indicate that the more conventional photocatalytic mechanism (i.e. electron-hole formation resulting in hydroxyl radical ($OH^{\bullet}$) formation from the oxidant and concomitant liquid phase oxidation) is more dominant for this thin film. This could mean that the solution phase oxygen was more readily available to pick up the UV-induced electron than the more tightly bound solid phase oxygen (lattice oxygen).This may be because of the more regular crystal structure of this film, as observed by other work in the Patterson research group (see: ref [255]). The high crystallinity of the ZnO in this film provides fewer defects around which ZnO lattice structure can be eroded. Increased degradation of lattice structures due to defects and lower crystallinity has been observed in other systems, such as [256, 257].

5.3.3 Reactions with Irradiation at 340nm

To investigate the effect of wavelength on the above phenomena and understand the competition between photolysis and photocatalysis (either by conventional hydroxyl radical mechanism or by the Mars van Krevelen mechanism), all nanostructured thin films were also UV irradiated at 340 nm under the same reaction conditions. Fig. 5.7 shows the resulting reaction profiles under oxygen-rich conditions only.

Fig. 5.7 and the first order reaction rates calculated from this data (see Table 5.2) show that all reaction rates (MB and the identified intermediates) are increased by irradiation at 340nm. The extent of the rate increases varies with the morphology, as shown in Table 5.2.

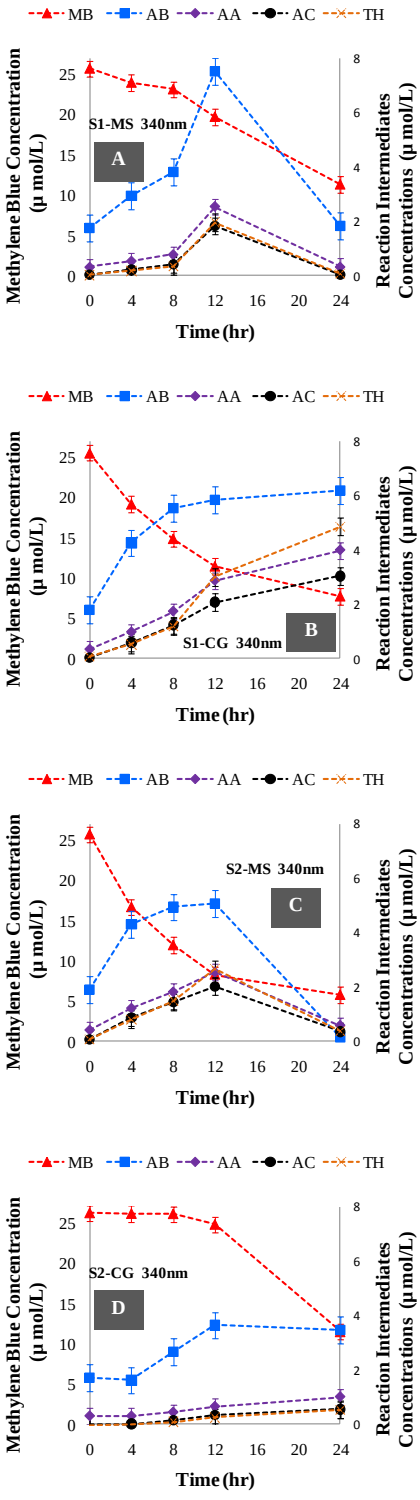

Figure 5.7: Reaction profile comparison of the reaction intermediates from methylene blue photocatalysed by four different ZnO thin films upon UV irradiation at 340nm under oxygen-rich conditions only, obtained by HPLC: A, S1-MS; B, S1-CG; C, S2-MS; D, S2-CG.

Table 5.2: Summary of 1st order reaction rate constant on liquid volume basis (k_{app}: s^{-1}), catalyst mass basis (k'_{app}: $m^3kg^{-1}s^{-1}$) and a UV exposed surface area (S) basis (k''_{app}: $m^3\ m^{-2}\ s^{-1}$) for the photocatalysed degradation of 10 mg L^{-1} Methylene Blue under UV irradiation of 340nm.

Thin Film photocatalyst	Estimated UV exposed surface area S (m^2)	First order rate constants (UV irradiation of 340nm)		
		O_2 rich conditions		
		k_{app} (s^{-1})	k'_{app} ($m^3kg^{-1}s^{-1}$)	k''_{app} ($m^3\ m^{-2}\ s^{-1}$)
S1-MS	7.58×10^{-4}	3.89×10^{-2}	3.6872	2.05×10^{-3}
S1-CG	5.98×10^{-4}	3.47×10^{-2}	3.2890	1.83×10^{-3}
S2-MS	3.74×10^{-3}	7.12×10^{-2}	6.7488	3.75×10^{-3}
S2-CG	7.7×10^{-4}	3.64×10^{-2}	3.4502	1.92×10^{-3}

Under UV irradiation of the 340nm morphology, S1-MS has shown (Fig.5.7A) the largest increase in reaction rate compared to reaction with irradiation at 254nm, with the reaction rates and reaction profile of S1-MS being comparable to those of S2-MS. This increase in reaction rate, however, does not come at the expense of the S1-MS ZnO lattice: Fig. 5.4 shows that surface degradation at 340nm is lower than for reactions at 254nm. There could be two reasons: firstly it may indicate that the replacement of oxygen(s) in the proposed Mars van Krevelen type mechanism at 340nm is more effective than at 254nm, or secondly (and the more likely case) that the more conventional photocatalytic production of OH radicals from electron-holes is more efficient at 340nm with this ZnO thin film (as evidenced in other literature [24, 43, 45]) and the ZnO Mars van Krevelen type photocatalytic mechanism (Chapter 4 and [250]) thus has less prominence at this wavelength. As noted in Section 5.3.2, reaction rate with irradiation at 254nm is expected to be higher than at 340nm. If this is the case, it would indicate that the ZnO Mars van Krevelen type photocatalytic mechanism has a slower reaction rate than the more conventional photocatalytic electron-holes mechanism. This is perhaps not unexpected, since the Mars van Krevelen mechanism theoretically has a number of rate limitations not affecting the other photocatalytic mechanisms, including: 1. The fact that only surface adsorbed species can be oxidised, so the mechanism is surface-area limited (or else they are unable to obtain the lattice oxygen). 2. The activation energy barrier for lattice oxygen removal must be overcome for reaction to occur. Since there is less energy available from UV at a wavelength of 340nm, compared to 254nm, the energy to activate the

Mars van Krevelen type mechanism may not be available if the activation energy barrier is too high; for instance, when there are few defects available in the crystal lattice (such as in the more aligned films S1-MS and S2-MS). 3. The rate of lattice oxygen replacement (affected by mass transfer and competing with photocatalytic radical formation for the oxygen) is likely to differ according to the rate of oxygen lattice reaction. This all competes with the radical formation from the dissolved oxidant species, which can release $OH^{\bullet}$ radicals**,** a powerful oxidising species, into the solution (or other species depending on the pH). In terms of the above results, this may mean that S1-MS is perhaps aligned and sufficiently defect free not to be able to undergo lattice degradation with the lower energy provided by UV irradiation at 340nm; similar to thin film morphology S2-MS, it is unable to photocatalyse MB using the slower Mars van Krevelen mechanism, meaning that the ZnO surface is also not deactivated for the more conventional mechanism. Consequently, the more conventional $OH^{\cdot}$ formation photocatalysis mechanism is dominant for the more aligned morphologies with 340nm UV irradiation.

Similar conclusions can be drawn from the results for the poorer-performing morphologies. Firstly, despite large MB degradations by S1-CG and S2-CG, comparable to those seen in S1-MS and S2-MS, the intermediate compounds did not degrade, their concentration plateau being an indication that they were recalcitrant to further oxidation with these catalysts under all the conditions studied. Less ordered structures such as S1-CG and S2-CG were unable to produce sufficient radical concentrations or provide sufficient oxidation via the Mars van Krevelen mechanism for ring cleavage and further degradation of AA, AB, AC and TH.

Secondly, both S1-CG and S2-CG showed greater photo-efficiency with increased reaction rates at UV irradiation of 340nm. Morphology S1-CG has a 6.5 times higher MB degradation rate along with an increased formation of all of the identified reaction intermediates under UV irradiation of 340nm (Fig. 5.7B) compared to 254nm (Fig. 5.6F). An increase in ZnO surface degradation (Figs. 5.4F and 5.4H) indicates that both the rate of the Mars van Krevelen reaction, as well as reaction rate due to radical mechanism, had increased. For morphology S2-CG, the overall degradation was 5.2 times higher than at 254nm after 24 hours. However, there is a clear lag period at the start of the reaction (Fig. 5.7D), an indication of a radical reaction mechanism. Since surface morphology did not change significantly (Figs. 5.1D and 5.4H) it can be concluded that like thin film morphology S2-MS, photocatalytic reactions with thin film S2-CG occur mainly by conventional radical formation from the available dissolved oxidant.

Based on the above results, a further possible reason for the different mechanisms for the different thin films lies in the species that are preferentially adsorbed by the surface of the nanostructured thin film – the oxygen and/or the methylene blue. If methylene blue dominates the adsorption, the lattice oxygen would be the most readily available oxidant source. If they can both adsorb, or the oxygen preferentially adsorbs, photocatalytic radical formation occurs. Preferential or shared surface adsorption of dissolved oxygen (O_2 in this case) instead of the methylene blue domination may also be an additional reason for an overall slower Mars van Krevelen mechanism than the conventional mechanism. A possible relationship between the crystallinity of the thin films and the activation energy for O_2 radical formation might be playing an extra role in the overall increase in reaction rate. In any case, if radical formation could prevent the adsorption of methylene blue onto the surface of the ZnO, the Mars van Krevelen mechanism would not occur. This may be what is happening for thin film morphologies S2-MS and S2-CG at both wavelengths and for S1-MS at 340nm.

5.4 Proposed Reaction Mechanism

It is likely that different thin films, due to their morphology, crystallinity, alignment, defects and chemistry, photocatalyse with different photocatalytic reaction mechanisms. Therefore, based on the above results and analysis, the photocatalytic reactions occur via an established reaction mechanism that can be summarised as follows:

In the conventional photocatalysed oxidation reaction, charge separation or electron-hole pair generation is induced upon the UV irradiation of energy greater than the band gap of the semiconductor metal oxide. These charges, usually called ‘valence band hole’ and ‘conduction band electrons’, may participate in the formation of active oxidising species such as hydroperoxyl radicals, hydroxyl radicals, and hydrogen peroxide and superoxide [1, 42, 67, 258]. Most of the literature attributed the oxidation of stringent organic compounds to positive hole and/or hydroxyl radical [1, 42, 143, 233, 259-264]. These mechanisms are well known and will contribute to the study of the oxidation of methylene blue reported here. However, based on changes in the surface morphologies of nanostructured ZnO thin films before and after reaction, both under oxygen-limited and oxygen-rich conditions, as well as the various identified reaction intermediates, a new photocatalytic reaction mechanism – a Mars van Krevelen type mechanism where the oxidation proceeds via lattice oxygen depletion - is proposed, to contribute to the overall oxidation.

The results indicate that there is competition between two different photocatalytic mechanisms: that of the conventional surface-photocatalysed radical formation from dissolved oxidant species, and either degradation of methylene blue adsorbed near to the radical species on the ZnO surface or in the solution by these radicals; and that of the photocatalytic degradation of adsorbed methylene blue by lattice oxygens (via the Mars van Krevelen type mechanism): in short a competition between radical oxidation that can oxidise species in solution, and surface species-adsorbed lattice oxygen-driven oxidation. The dominant reaction mechanism depends on the thin film morphology, crystallinity, availability of oxidant and the wavelength of the incident UV. The surface photocatalysed radical formation is predominant for more aligned highly crystalline morphologies (i.e. with fewer defects), where there is plentiful oxygen and UV irradiation at 340nm. Lattice oxygen photodegradation is predominant for less aligned, more amorphous, morphologies (with more defects) and UV irradiation at 254nm. This is because the higher energy available allows the activation energy barrier to be overcome for lattice oxygen abstraction, and a higher number of lattice defects lowers the overall activation energy required for this.

The reaction species identified in this work and in literature [236, 251-253] indicate that the reaction mechanism for the degradation of methylene blue by ZnO thin film photocatalysis can be summarised as shown in Fig. 5.8:

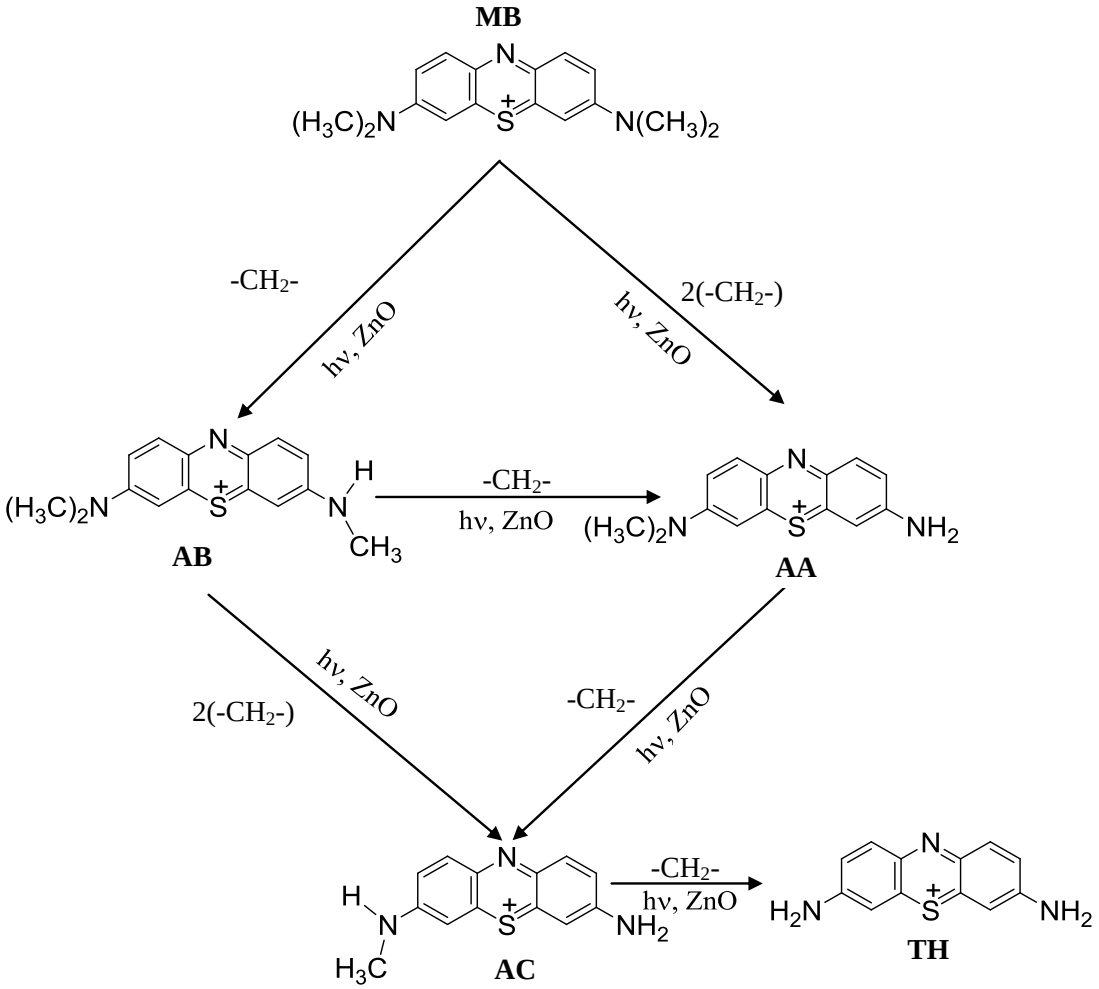

In summary

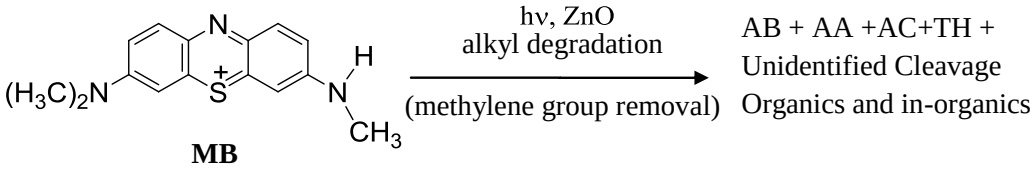

Figure 5.8: Proposed methylene blue ZnO photocatalysed reaction mechanism for the thin films studied based on the identified intermediates and reaction profiles in this work.

If the above is combined with previous studies of the methylene blue photocatalytic reaction mechanism, the overall known reaction mechanism can be summarised as in Fig. 5.9**.**

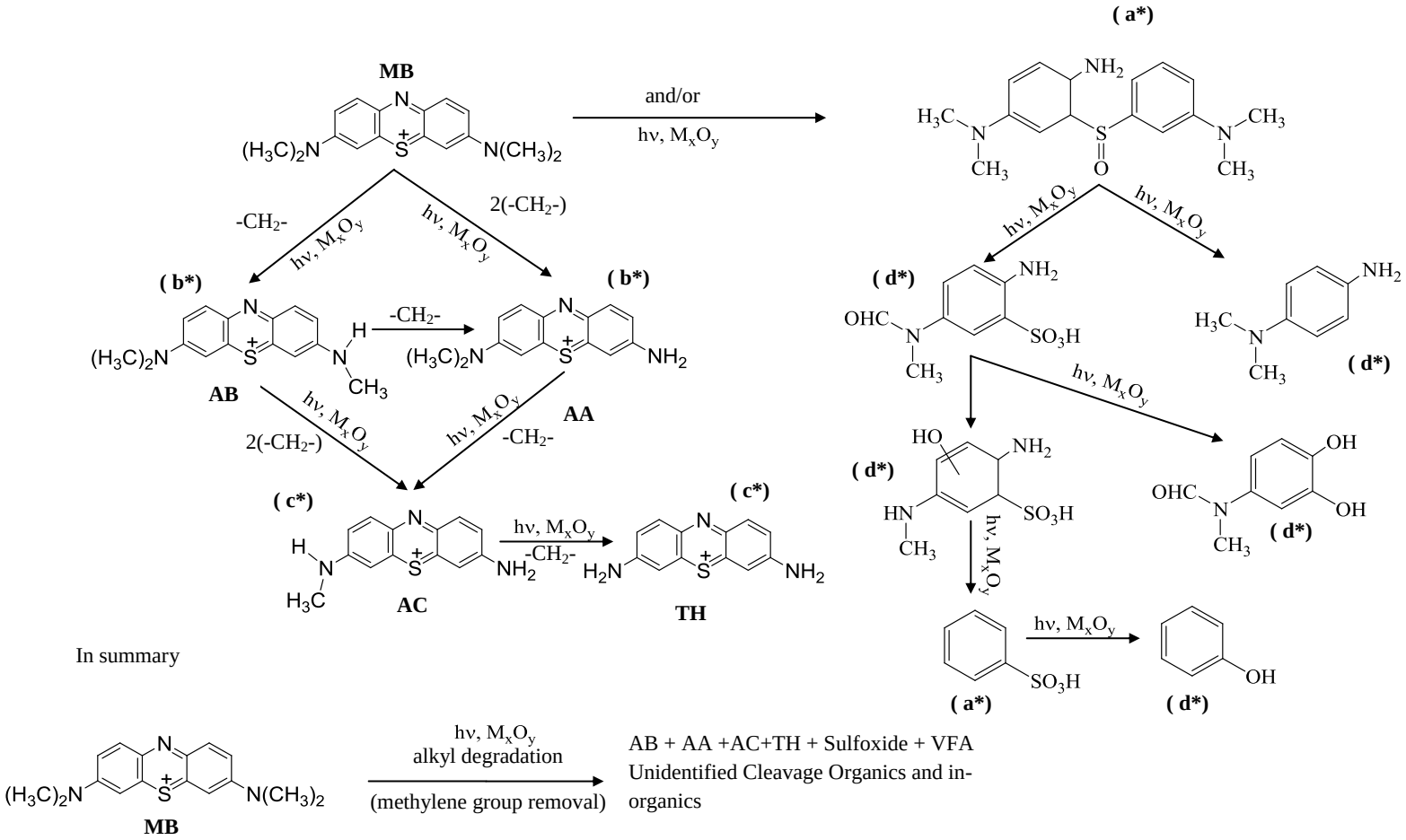

Note: a*: Identified by [239, 263] b*: Identified as well by [238, 253] c*: Identified as well [253]
d*: Identified by [239] only *M_xO_y = ZnO and/or TiO_2

Figure 5.9: Overall reaction mechanism for the photocatalytic degradation of methylene blue based on this work and literature.

Using the previous findings as a basis, under oxygen-limited conditions the Mars van Krevelen type mechanism for MB proceed as follows: initial bond cleavage is of the CH_3-group on the methylene blue. If this is by the lattice oxygen of the ZnO, a possible surface-based mechanism is: oxidation via the α-carbon [265], which generates a highly unstable methylene blue radical ($MB^{\bullet}$), which on further re-arrangement releases a methylene(carbene) [236] to form AB only. This bond cleavage may take place on either side of the conjugation of MB, which may also generate two reaction intermediates, AB and AA, at the same time. Upon secondary photocatalytic oxidation (i.e. oxidation of reaction intermediates) AB further oxidises to AA and AC simultaneously, which on further oxidation generates TH by further loss of another methylene group [236]. This is presented schematically in Fig. 5.10(a)**.**

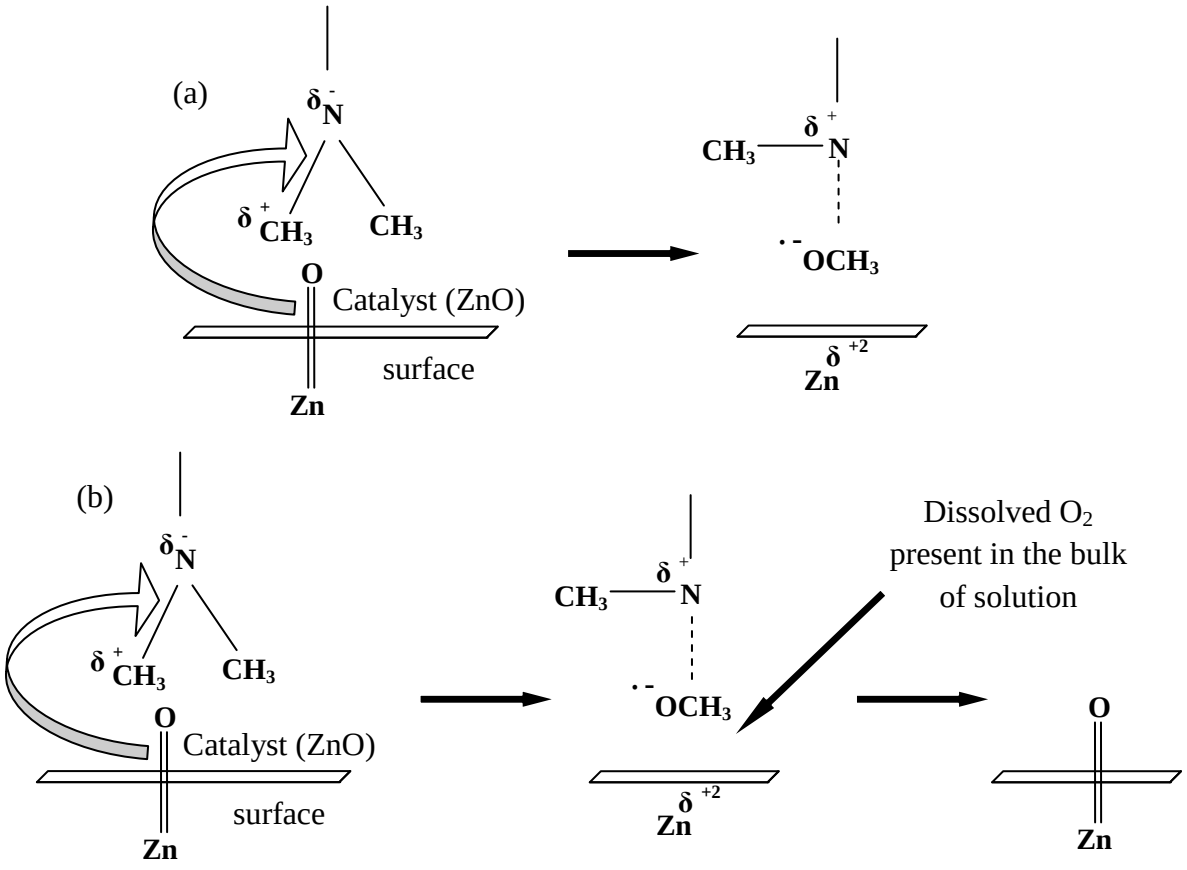

Figure 5.10: Schematic representation of the initial stages of the proposed Mars Van Krevelen type ZnO photocatalysed methylene blue reaction mechanism: (a) under oxygen-limited conditions, (b) under oxygen-rich conditions.

With oxygen in plentiful supply (oxygen-rich conditions), the ZnO surface reaction mechanism incorporating lattice oxygen loss and regeneration could similarly be speculated to be as presented in Fig. 5.10(b). This shows that after the same initial steps of lattice oxygen

abstraction from the surface as in the oxygen-limited mechanism, since there is sufficient diatomic oxygen, the surface oxygen lost is replaced by the oxygen to form ZnO and thus to regenerate ZnO surfaces. This has also been observed by Lee and Falconer [242]. The precise mechanism for this is not yet known. In addition, the presence of oxygen for some films (in particular S2-MS) allows the more conventional photocatalytic oxidation mechanism to dominate.

5.5 Summary

Four different nanostructured thin film morphologies (S1-MS, S1-CG, S2-MS and S2-CG) were photocatalytically tested under both oxygen-limited and rich conditions under two different UV irradiation wavelengths (254nm and 340nm). The results indicate that there is a competition between two different photocatalytic mechanisms: conventional redox-formed radical and lattice oxygen-driven oxidation. The dominant reaction mechanism depends on the thin film morphology, crystallinity, availability of oxidant and the wavelength of the incident UV. Surface photocatalysed radical formation degradation is predominant for more highly aligned morphologies (such as S1-MS and S2-MS) with plentiful oxygen and UV irradiation at 340nm. Mars van Krevelen type lattice oxygen photodegradation is predominant for less aligned and more amorphous surface morphologies (such as S1-CG and S2-CG) with UV irradiation at 254nm, because the high energy associated with 254nm UV irradiation allows the activation energy barrier to be overcome for lattice oxygen abstraction, and a higher number of lattice defects lowers the activation energy required for this.

An extension to the methylene blue photocatalytic reaction mechanism has also been proposed. Four azo dye reaction intermediates were identified: AA, AB, AC and TH, corroborating previous studies. However, a new reaction mechanism for when the Mars van Krevelen type reaction occurs is proposed as follows: initial bond cleavage of CH_3-group on methylene blue by lattice oxygen, followed by a possible surface-based reaction mechanism i.e., oxidation via α-carbon, which generates highly unstable methylene blue radical ($MB^{\bullet}$); this on further re-arrangement, releases a methylene ($-CH_2-$) group to form the first reaction intermediate AB, which upon secondary oxidation gives rise to AA and further intermediates until eventual mineralisation.

Moreover, to the author's knowledge, these results provide the first account of the individual and combined effect of UV wavelength, thin film nanostructure and oxidant availability on both the solution and solid phase photocatalytic reaction mechanisms and reaction rates. This

work therefore provides an important first step towards understanding this area and shows that in order to properly design and understand thin film catalytic processes, the combined effect of these parameters must be accounted for.

6 Doped Nanostructured ZnO Thin Films: Impact Of Dopant On Photocatalytic Activity, Reaction Mechanism and Stability

6.1 Introduction

To investigate the photocatalytically induced surface defects in the undoped nanostructured ZnO thin films and to identify the behaviour and/or participation of lattice, kinetics of other source of oxidant(s) (if any) on reaction mechanism(s), doped nanostructured ZnO thin films were prepared using both anionic (nitrogen) and cationic (cobalt) dopant. The effect of dopant on structure, morphology, band gap, crystallinity and other important parameter(s) that may assist in increased photocatalytic activity, were studied and compared with undoped nanostructured ZnO under oxygen-limited and rich conditions upon two different UV irradiations (as this project is focused on 254nm and 340nm UV lights irradiations and visible light was outside the scope of the project). The first part of this chapter is devoted to discussing the nature and effect of dopant on surface morphology, and the second to the possible impacts of dopant on photocatalytic activity, stability and the reaction mechanism(s) suggested in Chapter 5.

6.2 Impact of Dopant on Surface Morphologies

The nature and type of morphology, summarised in previous chapters (see Sections 4.3.1 and 5.2), plays an important role in photocatalytic activity and reaction mechanism. Therefore and in order to preserve this parameter, both anionic and cationic dopant [160-164] (also see Appendix I) were used to obtain a morphology as close as possible to undoped ZnO thin films. Dopant usually reduces the band gap (hence metal oxide is expected to be more active at low UV energy or at higher UV irradiation wavelength) [179] and the delocalisation of the d-states in the band gap of metal oxide, which helps in reducing the recombination chances of UV-induced electron-hole pairs [266]. The extent of dopant, both type and concentration, on both surface morphology and band gap, is summarised in the following sections.

6.2.1 Nitrogen-doped Zinc Oxide (N:ZnO) Nanostructured Thin Films

Two different sources of nitrogen, nitrogen gas (N_2) and Triethylamine (TEA), were used to obtain N:ZnO nanostructured thin films. The effect of each source of nitrogen on surface

morphology, and the evidence for nitrogen incorporation, are summarised in the following sections.

6.2.1.1 N:ZnO thin film morphologies obtained by using N_2 gas as nitrogen source

A top surface view of the SEM image of the nitrogen-doped morphology, obtained from the mixture of solutions (N:S1) on a magnetron sputtered coated ZnO glass template, (N:S1-MS) is shown in Fig. 6.1A. The morphology (N:S1-MS) was nearly same as undoped S1-MS. No significant differences in crystal structure, size and smoothness were noticed except in the population and the orientation of crystals. However, no clear indication of N_2 incorporation was depicted by EDX analysis (Fig.6.1B). Most of the crystals are positioned at a greater inclination than that for undoped nanostructured ZnO thin films (Fig. 4.1A). The band gap was approximately the same as for the undoped: another indication of inefficient dopant incorporation in the ZnO crystal.

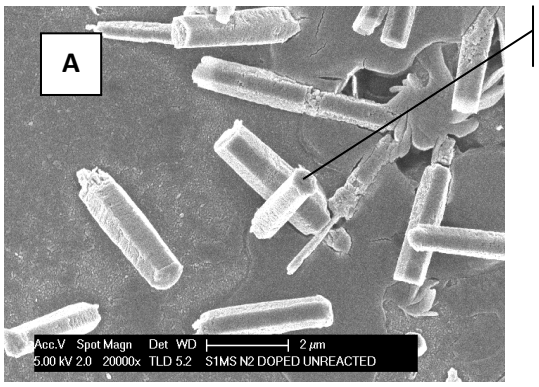

Element	Wt %	At %	K-Ratio	Z	A	F
N K	7.65	16.11	0.016	1.1109	0.1885	1.0009
O K	27.46	50.61	0.0635	1.1018	0.2097	1.0007
SiK	13.97	14.67	0.0547	1.0544	0.3712	1
PtM	14.54	2.2	0.083	0.7614	0.7496	1
ZnK	36.37	16.41	0.3333	0.9181	0.9979	1
Total	100	100				

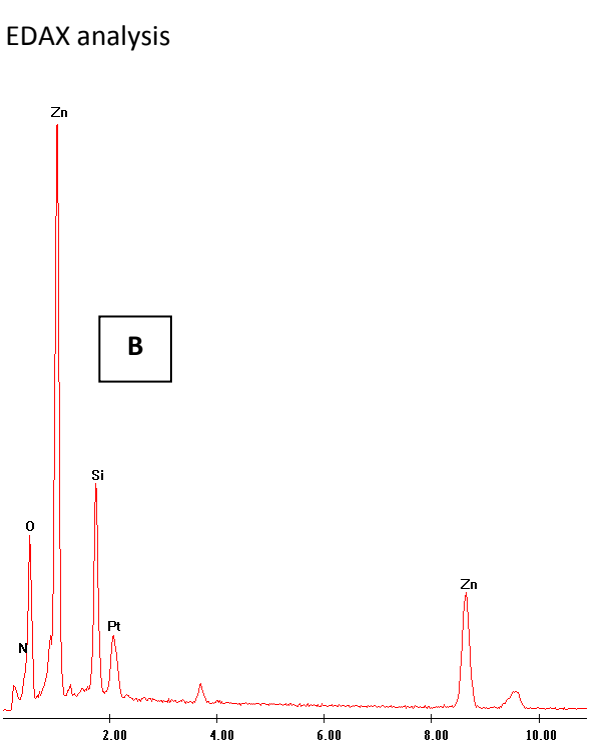

Figure 6.1: A: SEM image (top view) of nitrogen-doped nanostructured ZnO thin films N:S1-MS; B:EDX analysis at position P1(ZnO single crystal)

Morphology (N:S1-CG; Fig 6.2A), obtained on a clean glass slide from a mixture of solutions (N:S1), shows a clear difference in the surface morphology, compared to undoped nanostructured ZnO thin films (Fig.4.1B). Both crystal structure and smoothness were severely affected. EDX analysis (Fig.6.2B) did not show any solid evidence of the presence,

(and hence the incorporation) of nitrogen that might be due to the lack of interaction of nitrogen source species with ZnO, in the ZnO crystal.

Morphologies obtained from a mixture of solutions N:S2, on MS and CG substrate, are shown in Figs.6.3-4; morphology N:S2-MS showed a significant variation in the surface structure (Fig. 6.3) compared to undoped S2-MS (Chapter 4; Fig. 4.1C). A huge proportion of large crystal similar to undoped S2-CG was seen on the top of the MS layer with little growth and reduced porosity. Morphology N:S2-CG (Fig.6.4) was almost similar to undoped nanostructured ZnO thin films S2-CG. No evidence of N_2 incorporation into morphologies N:S2-MS and N:S2-CG, similar to N:S1-MS and N:S1-CG, was noticed (Fig.6.3B and Fig.6.4B).

The doped morphologies (N:ZnO), obtained by using N_2 gas as a nitrogen dopant source, were affected not only in terms of surface morphologies; as well as EDX analysis did not show any solid evidence of the presence of nitrogen in the ZnO lattice or lattice interstices and these cannot therefore be considered to be as nitrogen doped morphologies, although the presence nitrogen gas (nitrogen saturated mixture of solutions N:S1 and N:S2) had imparted a significant effect on surface morphologies. In general, the bubbling/mixing of nitrogen gas technique, to achieve a nitrogen saturated reaction mixture, is not an efficient way to enable nitrogen to produce N:ZnO thin films. Therefore another soluble source of nitrogen, such as TEA, was attempted to obtain N:ZnO nanostructured thin films.

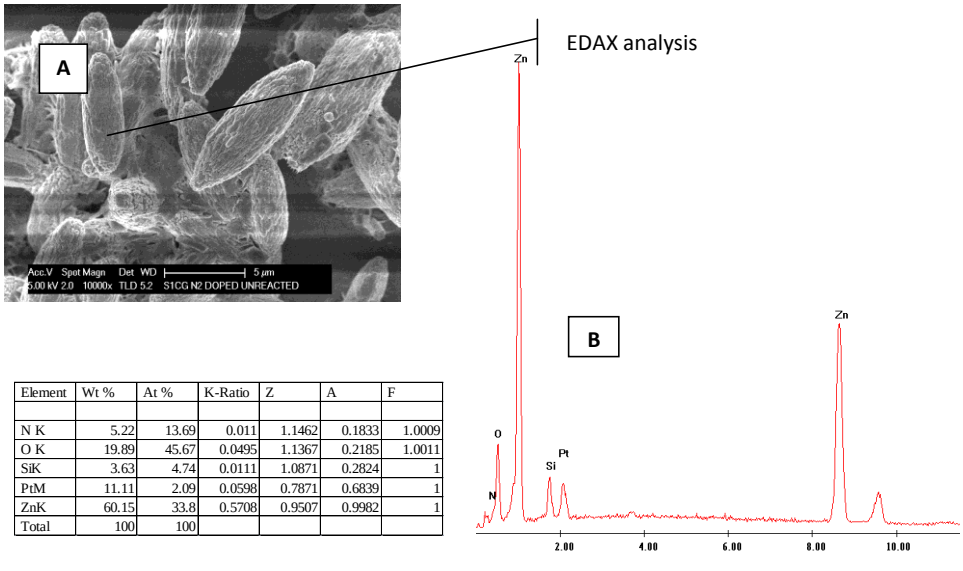

Element	Wt %	At %	K-Ratio	Z	A	F
N K	5.22	13.69	0.011	1.1462	0.1833	1.0009
O K	19.89	45.67	0.0495	1.1367	0.2185	1.0011
SiK	3.63	4.74	0.0111	1.0871	0.2824	1
PtM	11.11	2.09	0.0598	0.7871	0.6839	1
ZnK	60.15	33.8	0.5708	0.9507	0.9982	1
Total	100	100				

Figure 6.2: A: SEM image (top view) of N:S1-CG; B:EDX analysis at position P1(ZnO single crystal).

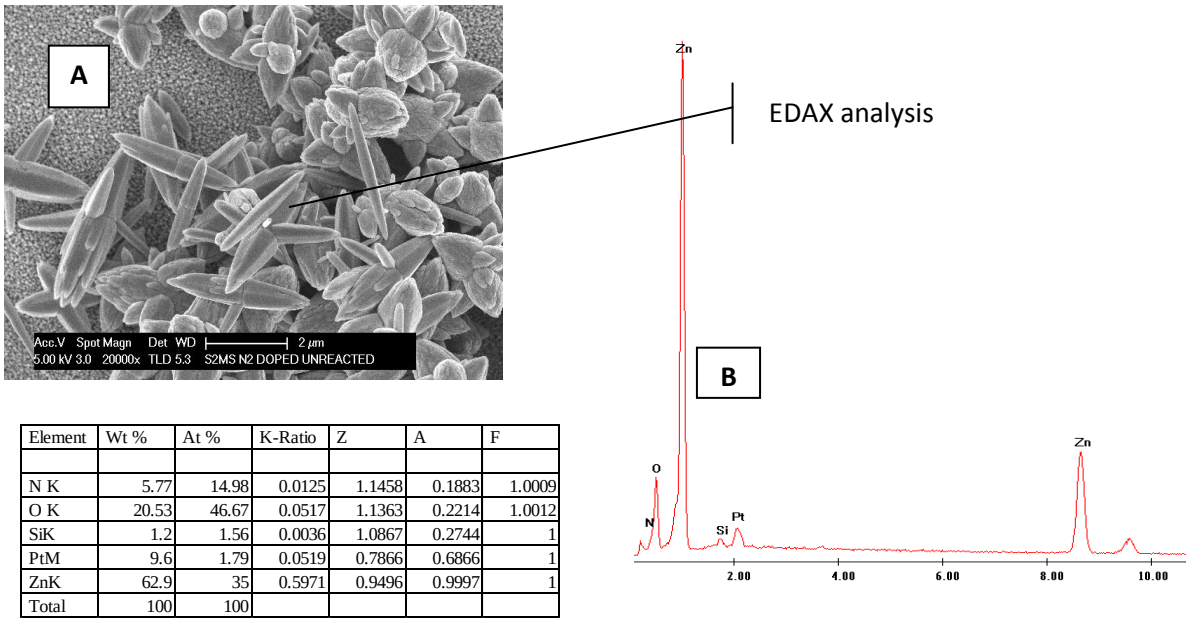

Element	Wt %	At %	K-Ratio	Z	A	F
N K	5.77	14.98	0.0125	1.1458	0.1883	1.0009
O K	20.53	46.67	0.0517	1.1363	0.2214	1.0012
SiK	1.2	1.56	0.0036	1.0867	0.2744	1
PtM	9.6	1.79	0.0519	0.7866	0.6866	1
ZnK	62.9	35	0.5971	0.9496	0.9997	1
Total	100	100				

Figure 6.3: A: SEM image (top view) of N:S2-MS; B: EDX analysis at position P1(complex ZnO single crystal).

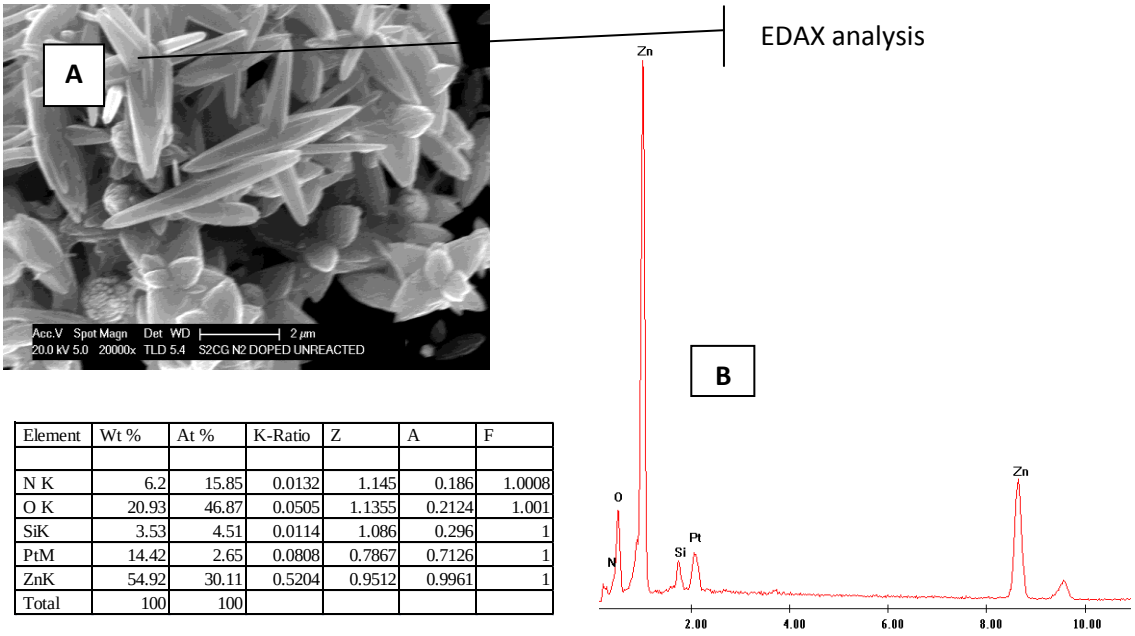

Element	Wt %	At %	K-Ratio	Z	A	F
N K	6.2	15.85	0.0132	1.145	0.186	1.0008
O K	20.93	46.87	0.0505	1.1355	0.2124	1.001
SiK	3.53	4.51	0.0114	1.086	0.296	1
PtM	14.42	2.65	0.0808	0.7867	0.7126	1
ZnK	54.92	30.11	0.5204	0.9512	0.9961	1
Total	100	100				

Figure 6.4: A: SEM image (top view) of N:S2-CG; B: EDX analysis at position P1(complex ZnO single crystal).

6.2.1.2 N:ZnO thin films morphologies obtained by using TEA as an N_2 source

Six attempts were made to prepare N:ZnO thin films by using TEA as a nitrogen dopant source at two different concentrations (high and low concentrations of TEA; 37% or 16.7%

respectively) with and without pH control. The effect of TEA as a nitrogen source on surface morphology is summarised in the following sections.

6.2.1.2.1 Morphologies obtained at high concentration of TEA with pH control

Figs.6.5-6.8 shows three different morphologies, N1:S1-MS, N1:S1-CG and N2:S2-MS, obtained from a high concentration of TEA (37.5%), on MS or CG glass substrate by using two different mixtures of solutions N′:S1 and N′:S2, with pH control 5 or 7.5. N:ZnO morphologies obtained by using TEA as an N_2 dopant source also showed huge variations in morphologies compared to undoped ZnO thin films (see Fig. 4.1). Morphology N1:S1-MS (Fig. 6.5A) obtained, at pH 5, had both solid and X-shaped, horizontally aligned, hollow crystal structures. Again, no solid evidence of nitrogen incorporation as dopant was found (see Fig. 6.5B: EDX analysis at position P1 (X-shaped hollow crystal) and Fig. 6.5C: EDX analysis at position P2 (crystal growth near to MS layer).

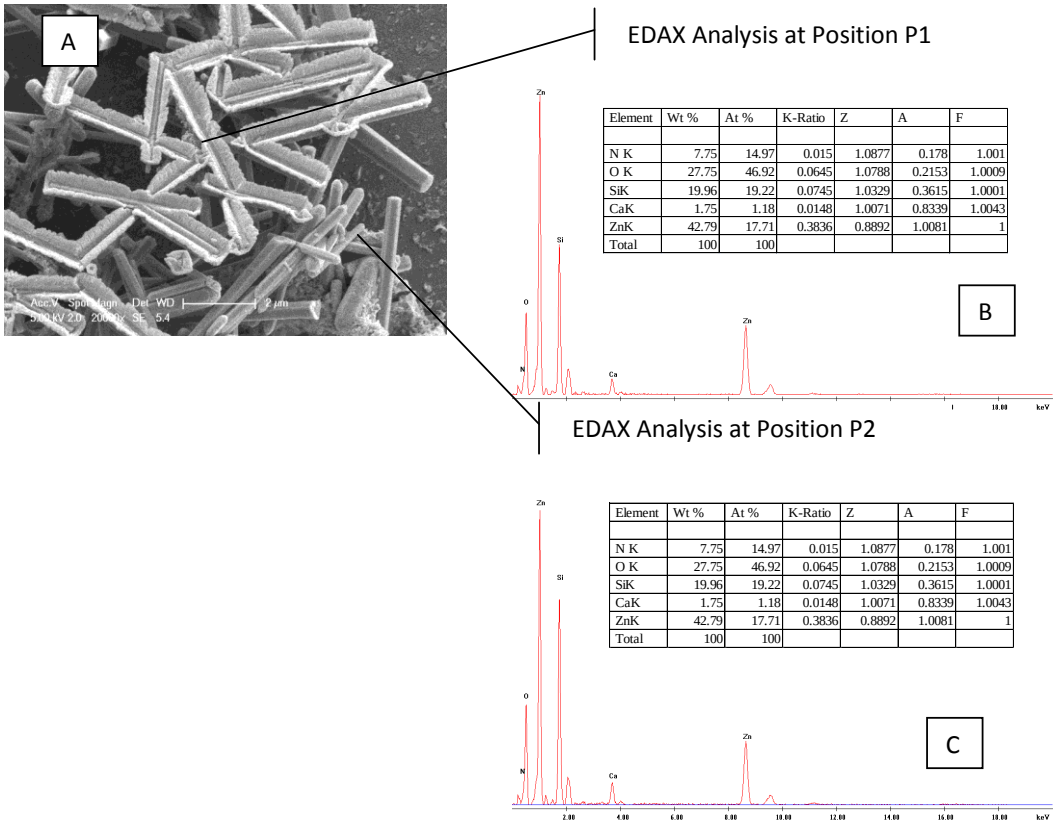

Element	Wt %	At %	K-Ratio	Z	A	F
N K	7.75	14.97	0.015	1.0877	0.178	1.001
O K	27.75	46.92	0.0645	1.0788	0.2153	1.0009
SiK	19.96	19.22	0.0745	1.0329	0.3615	1.0001
CaK	1.75	1.18	0.0148	1.0071	0.8339	1.0043
ZnK	42.79	17.71	0.3836	0.8892	1.0081	1
Total	100	100				

Element	Wt %	At %	K-Ratio	Z	A	F
N K	7.75	14.97	0.015	1.0877	0.178	1.001
O K	27.75	46.92	0.0645	1.0788	0.2153	1.0009
SiK	19.96	19.22	0.0745	1.0329	0.3615	1.0001
CaK	1.75	1.18	0.0148	1.0071	0.8339	1.0043
ZnK	42.79	17.71	0.3836	0.8892	1.0081	1
Total	100	100				

Figure 6.5: A: SEM image (top view) of N1:S1-MS; B: EDX analysis at position P1 (X-shaped ZnO crystal); C: EDX analysis at position P2 (layer upon magnetron sputtered coating and small ZnO crystal) at high concentration of TEA with pH control.

Morphology N1:S1-CG (Fig. 6.6A) obtained on the CG substrate from the reaction mixture of solution N′:S1, at pH 5, had also shown a significant variation in crystal orientation, size and population, compared to undoped S1-CG thin films (see Fig. 4.1B). Although the

presence of TEA left a huge impact on surface morphologies, no evidence of the presence of nitrogen was revealed by EDX analysis (Fig.6.6B-C) at the two different positions on surface P1 and P2. Inductive Coupled Plasma (ICP) would be better technique, but it was not available to detect and analyze trace and ultra trace elements.

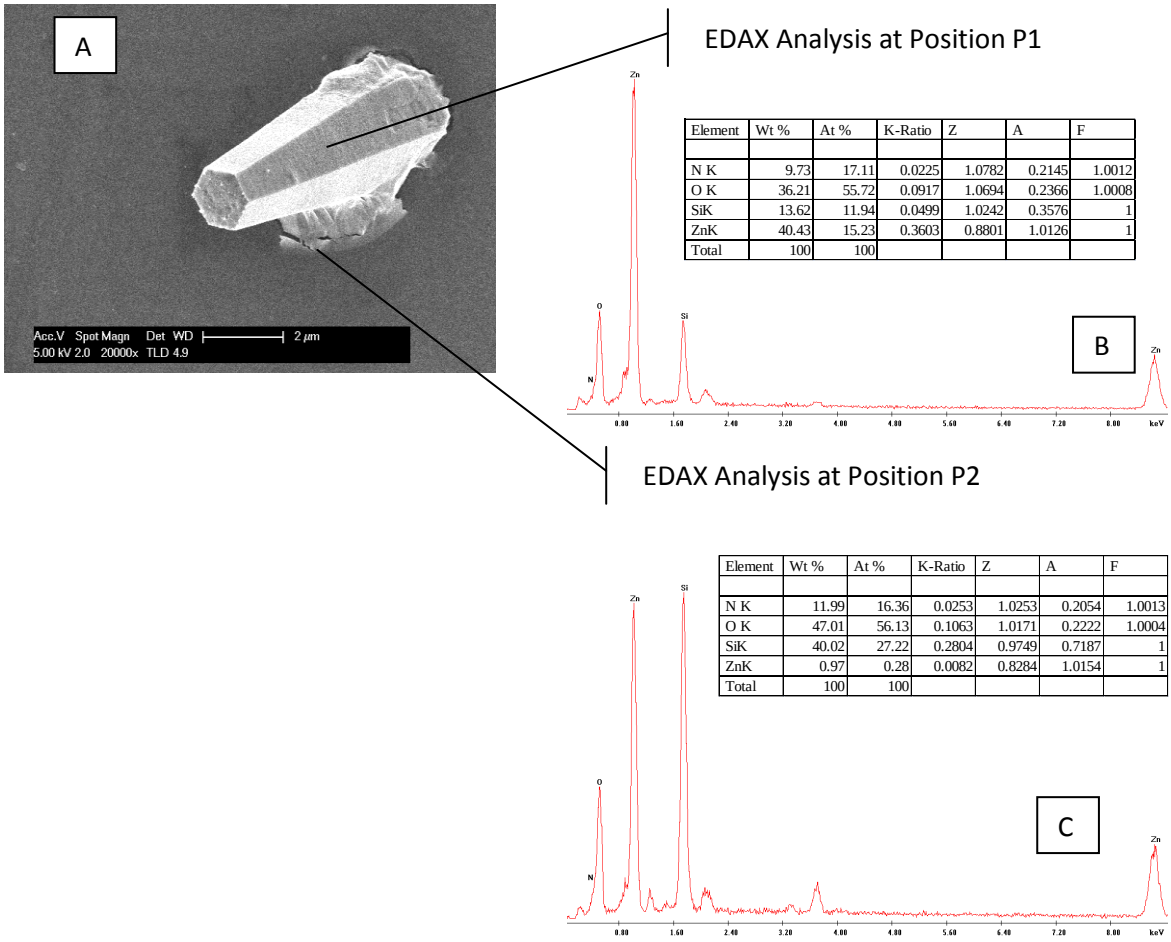

Figure 6.6: A:SEM image (top view) of N1:S1-CG; B:EDX analysis at position P1(regular ZnO crystal); C:EDX analysis at position P2(layer upon magnetron sputtered coating) at high concentration of TEA with pH control.

The top surface and cross-sectional views of the morphology N2:S2-MS (Figs. 6.7A and 6.8A), obtained on MS substrate by using solution N′:S2 at pH 7.5, differ greatly in crystal structure, crystal smoothness, crystal size and orientation compared to undoped S2-MS (see Fig. 4.1C) obtained under similar conditions, except for the presence of TEA. Horizontally oriented cusps of ZnO were seen that could be caused by the interaction of TEA with other reacting species like $Zn(NO)_3.6H_2O$, HMT and PEI. No evidence of the incorporation of nitrogen as a doped element was noticed, similar to N1:S1-MS and N1:S1-CG, as shown by EDX analysis (Figs 6.7B-C and 6.8B-C).

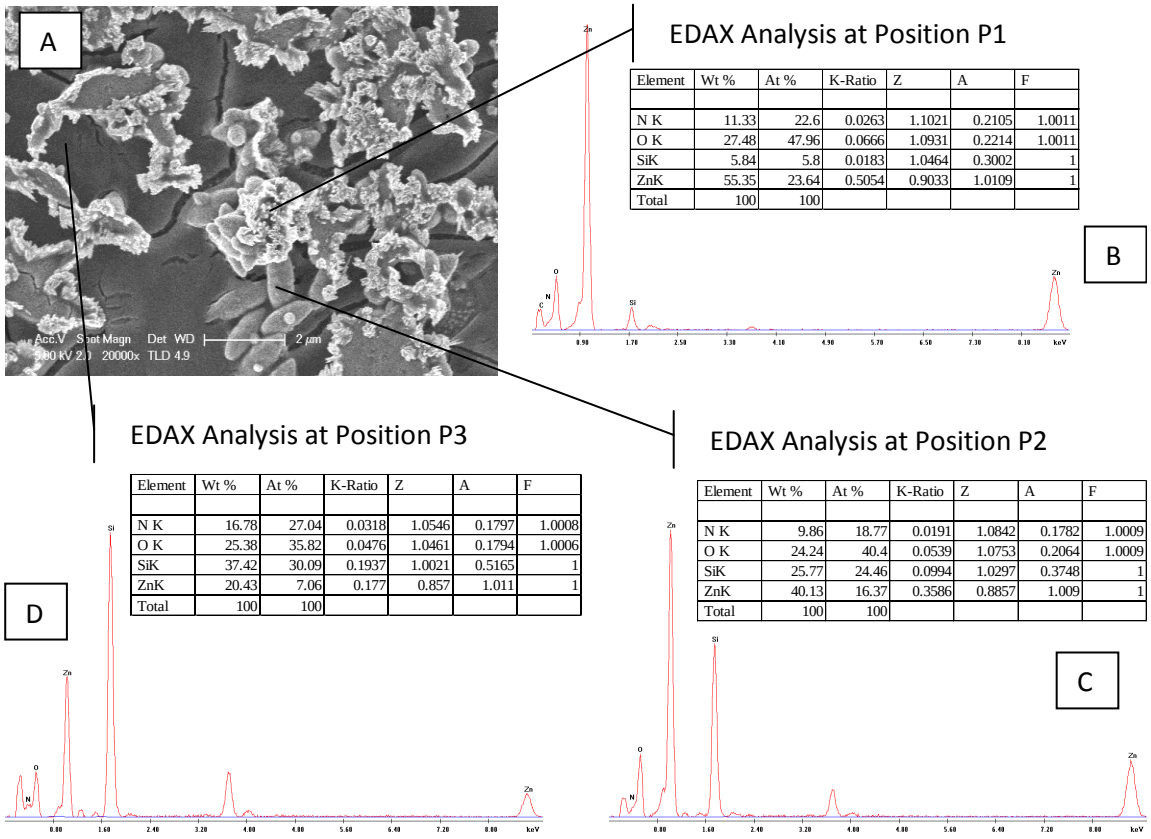

Element	Wt %	At %	K-Ratio	Z	A	F
N K	11.33	22.6	0.0263	1.1021	0.2105	1.0011
O K	27.48	47.96	0.0666	1.0931	0.2214	1.0011
SiK	5.84	5.8	0.0183	1.0464	0.3002	1
ZnK	55.35	23.64	0.5054	0.9033	1.0109	1
Total	100	100				

Element	Wt %	At %	K-Ratio	Z	A	F
N K	16.78	27.04	0.0318	1.0546	0.1797	1.0008
O K	25.38	35.82	0.0476	1.0461	0.1794	1.0006
SiK	37.42	30.09	0.1937	1.0021	0.5165	1
ZnK	20.43	7.06	0.177	0.857	1.011	1
Total	100	100				

Element	Wt %	At %	K-Ratio	Z	A	F
N K	9.86	18.77	0.0191	1.0842	0.1782	1.0009
O K	24.24	40.4	0.0539	1.0753	0.2064	1.0009
SiK	25.77	24.46	0.0994	1.0297	0.3748	1
ZnK	40.13	16.37	0.3586	0.8857	1.009	1
Total	100	100				

Figure 6.7: A: SEM image (top view) of N2:S2-MS; B: EDX analysis at position P1(cluster of ZnO crystal); C: EDX analysis at position P2(ZnO single crystal); D: EDX analysis of at position P3 (layer upon magnetron sputtered coating).

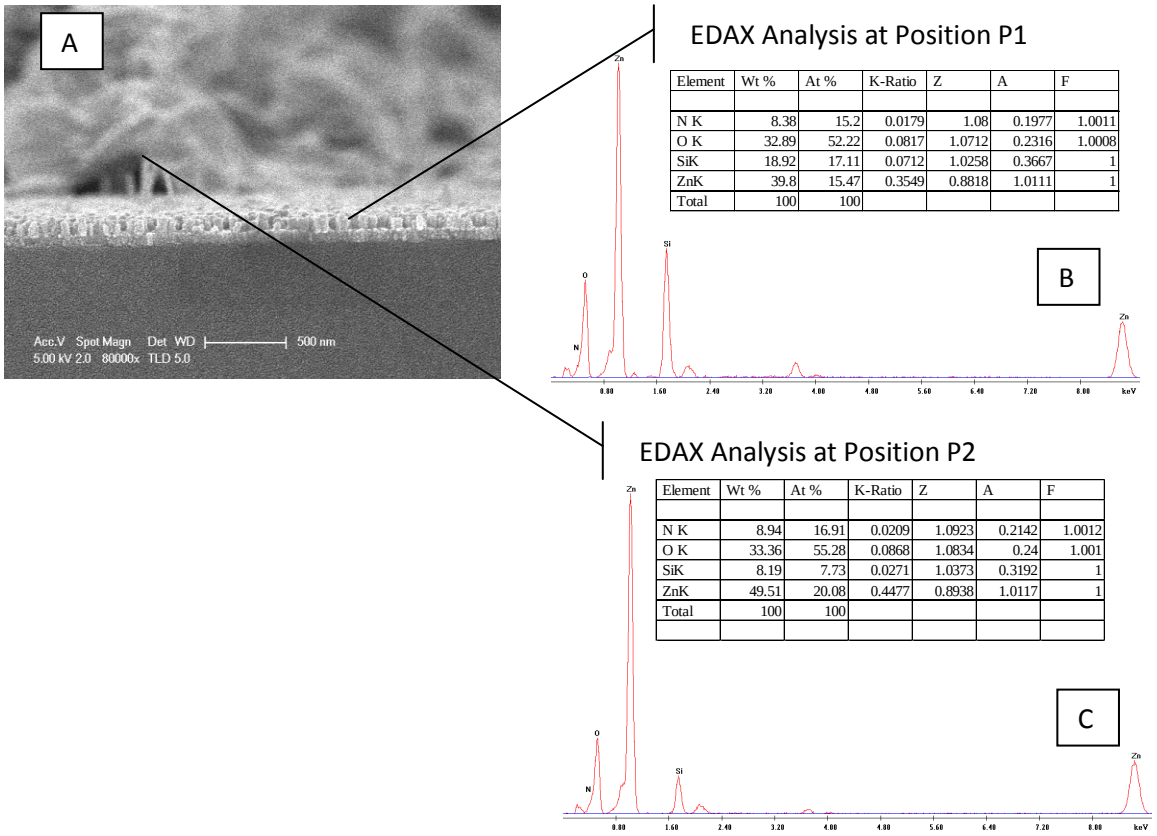

Element	Wt %	At %	K-Ratio	Z	A	F
N K	8.38	15.2	0.0179	1.08	0.1977	1.0011
O K	32.89	52.22	0.0817	1.0712	0.2316	1.0008
SiK	18.92	17.11	0.0712	1.0258	0.3667	1
ZnK	39.8	15.47	0.3549	0.8818	1.0111	1
Total	100	100				

Element	Wt %	At %	K-Ratio	Z	A	F
N K	8.94	16.91	0.0209	1.0923	0.2142	1.0012
O K	33.36	55.28	0.0868	1.0834	0.24	1.001
SiK	8.19	7.73	0.0271	1.0373	0.3192	1
ZnK	49.51	20.08	0.4477	0.8938	1.0117	1
Total	100	100				

Figure 6.8: A: SEM image (cross-sectional) of N2:S2-MS; B: EDX analysis at position P1 (cluster of ZnO crystal); C: EDX analysis at position P2(complex ZnO single crystal).

6.2.1.2.2 Morphologies obtained at low concentration of TEA with pH control

A marked variation in surface morphologies of N:ZnO thin films could be a result of higher concentration of the TEA. In order to investigate and to optimise nitrogen incorporation as a dopant as well as the concentration of TEA, and to have lower impact of dopant on surface morphologies, a lower concentration of TEA (16.7%) was used. Figs. 6.9-11 show the morphologies obtained at low TEA concentration with pH 5 or 7.5. Little effect of the TEA concentration was noticed. Nearly similar patterns of morphologies N4:S2-MS (Figs 6.10A) and N4:S2-CG (Fig. 6.11A) i.e. complex, hollow and fragile crystals, were obtained at a lower concentration of TEA, except for morphology N3:S1-MS (Fig. 6.9A), which had shown a lower level of crystal population and incomplete growth of crystals. Little presence of nitrogen incorporation in the crystal lattice could be measured (see Figs. 6.9B-C, 6.10B-C and Figs. 6.11B-C; EDX analysis at two different positions P1: crystal surface and P2: layer on MS or CG substrate).

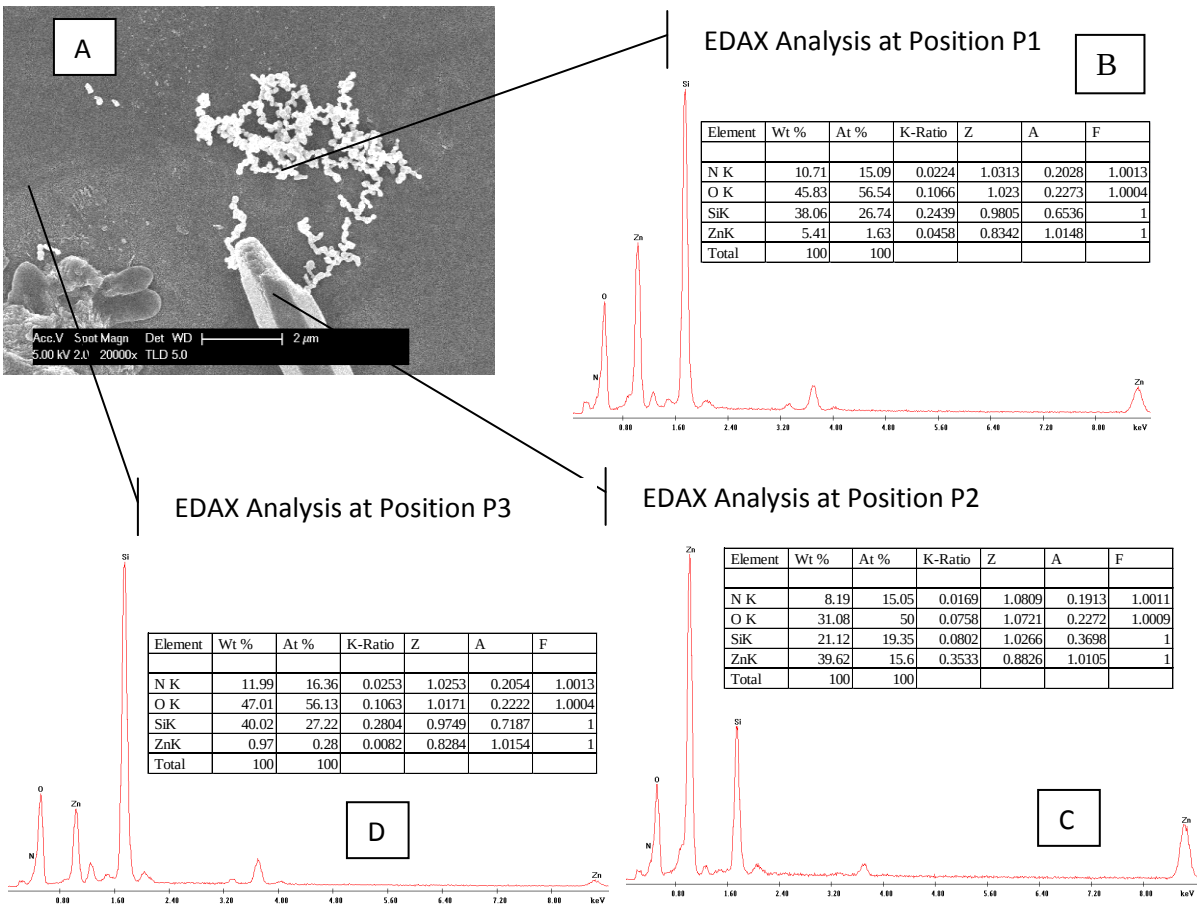

Element	Wt %	At %	K-Ratio	Z	A	F
N K	10.71	15.09	0.0224	1.0313	0.2028	1.0013
O K	45.83	56.54	0.1066	1.023	0.2273	1.0004
SiK	38.06	26.74	0.2439	0.9805	0.6536	1
ZnK	5.41	1.63	0.0458	0.8342	1.0148	1
Total	100	100				

Element	Wt %	At %	K-Ratio	Z	A	F
N K	11.99	16.36	0.0253	1.0253	0.2054	1.0013
O K	47.01	56.13	0.1063	1.0171	0.2222	1.0004
SiK	40.02	27.22	0.2804	0.9749	0.7187	1
ZnK	0.97	0.28	0.0082	0.8284	1.0154	1
Total	100	100				

Element	Wt %	At %	K-Ratio	Z	A	F
N K	8.19	15.05	0.0169	1.0809	0.1913	1.0011
O K	31.08	50	0.0758	1.0721	0.2272	1.0009
SiK	21.12	19.35	0.0802	1.0266	0.3698	1
ZnK	39.62	15.6	0.3533	0.8826	1.0105	1
Total	100	100				

Figure 6.9: A: SEM image (top view) of N3:S1-MS; B: EDX analysis at position P1 (cluster of small ZnO crystals); C: EDX analysis at position P2 (large ZnO crystal); D: EDX analysis at position (layer upon magnetron sputtered coating) at low concentration of TEA with pH control.

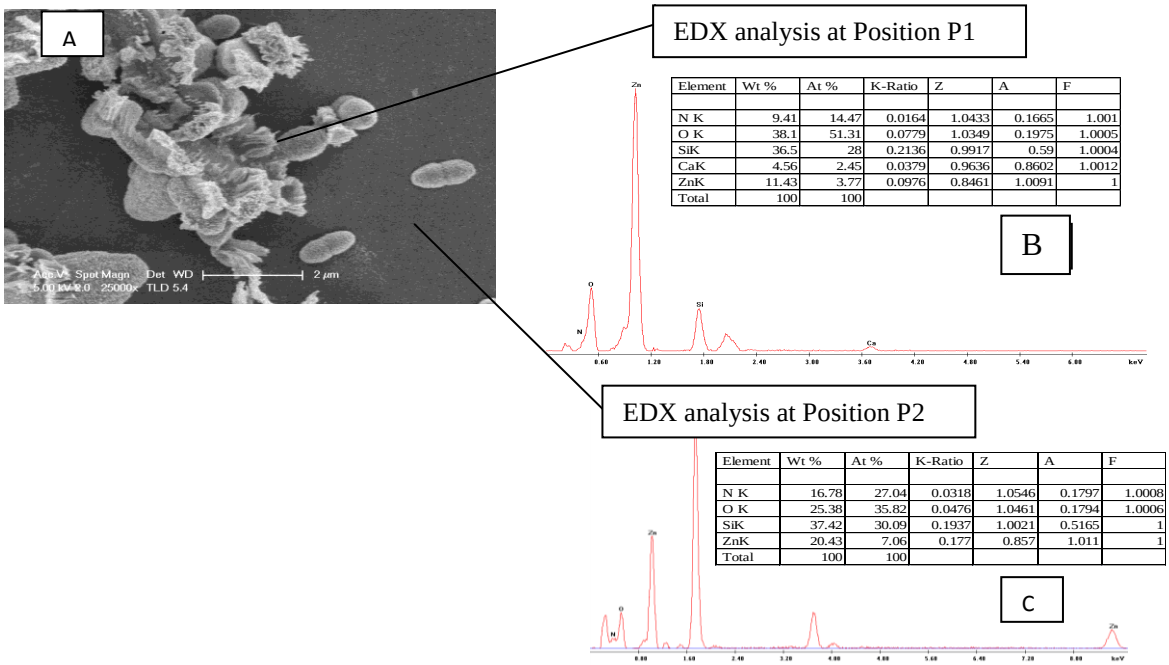

Element	Wt %	At %	K-Ratio	Z	A	F
N K	9.41	14.47	0.0164	1.0433	0.1665	1.001
O K	38.1	51.31	0.0779	1.0349	0.1975	1.0005
SiK	36.5	28	0.2136	0.9917	0.59	1.0004
CaK	4.56	2.45	0.0379	0.9636	0.8602	1.0012
ZnK	11.43	3.77	0.0976	0.8461	1.0091	1
Total	100	100				

Element	Wt %	At %	K-Ratio	Z	A	F
N K	16.78	27.04	0.0318	1.0546	0.1797	1.0008
O K	25.38	35.82	0.0476	1.0461	0.1794	1.0006
SiK	37.42	30.09	0.1937	1.0021	0.5165	1
ZnK	20.43	7.06	0.177	0.857	1.011	1
Total	100	100				

Figure 6.10: A: SEM image (top view) of N4:S2-MS; B: EDX analysis at position P1(cluster of ZnO crystal); C: EDX analysis at position P2(layer upon magnetron sputtered coating).

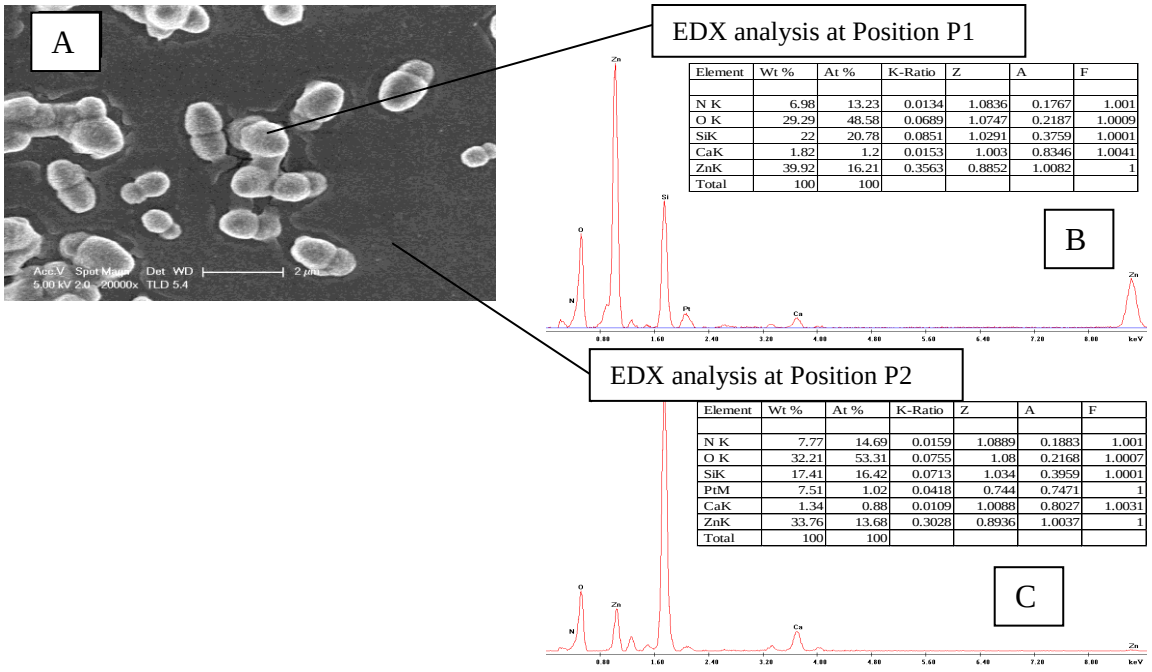

Element	Wt %	At %	K-Ratio	Z	A	F
N K	6.98	13.23	0.0134	1.0836	0.1767	1.001
O K	29.29	48.58	0.0689	1.0747	0.2187	1.0009
SiK	22	20.78	0.0851	1.0291	0.3759	1.0001
CaK	1.82	1.2	0.0153	1.003	0.8346	1.0041
ZnK	39.92	16.21	0.3563	0.8852	1.0082	1
Total	100	100				

Element	Wt %	At %	K-Ratio	Z	A	F
N K	7.77	14.69	0.0159	1.0889	0.1883	1.001
O K	32.21	53.31	0.0755	1.08	0.2168	1.0007
SiK	17.41	16.42	0.0713	1.034	0.3959	1.0001
PtM	7.51	1.02	0.0418	0.744	0.7471	1
CaK	1.34	0.88	0.0109	1.0088	0.8027	1.0031
ZnK	33.76	13.68	0.3028	0.8936	1.0037	1
Total	100	100				

Figure 6.11: A: SEM image (top view) of N4:S2-CG; B: EDX analysis at position P1(ZnO jointed crystal); C: EDX analysis at position P2 (layer upon magnetron sputtered coating) at low concentration of TEA with pH control.

6.2.1.2.3 Morphologies obtained at high and low concentrations of TEA without pH control

A change in TEA concentration did not reveal any significant improvement in the nitrogen incorporation as dopant into the ZnO crystal lattice. The only other parameter that might control the surface morphology is the pH of the reaction mixture. To study and investigate the role of pH, a set of nitrogen-doped structures/morphologies (N5:S2-MS, N5:S2-CG and N6:S2-MS) were also prepared under both high and low concentration of TEA without maintaining pH (results obtained are shown in Figs. 6.12-14). A significant effect of pH was noticed on the crystals formed (fairly large compact structures), although none of the nitrogen-doped morphologies were suitable, from the point of view of either nitrogen incorporation (see Figs. 6.12B-C, 6.13B-C and 6.14B-C), or surface morphology, as shown in Figs. 6.12A, 6.13A and 6.14A.

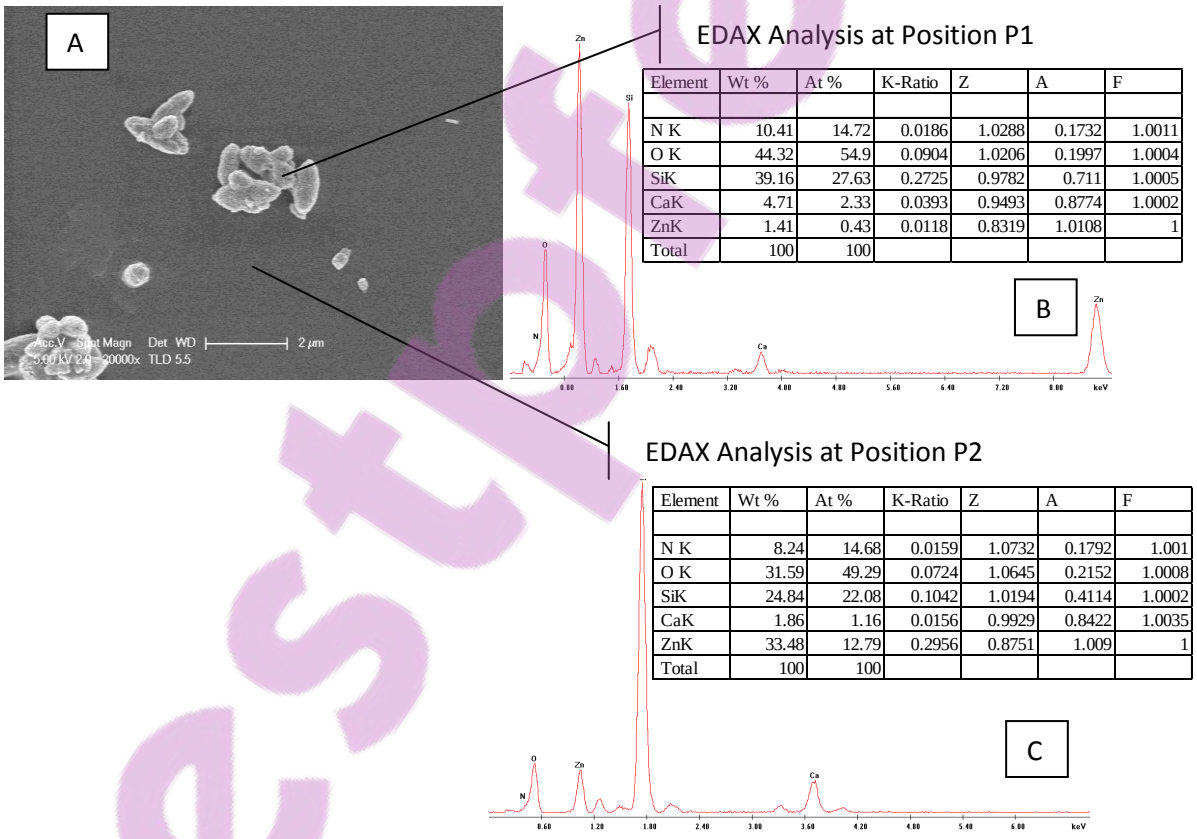

Figure 6.12: A:SEM image (top view) of N5:S2-MS; B:EDX analysis at position P1(cluster of ZnO crystal); C:EDX analysis at position P2(layer upon magnetron sputtered coating) at high concentration of TEA without pH control.

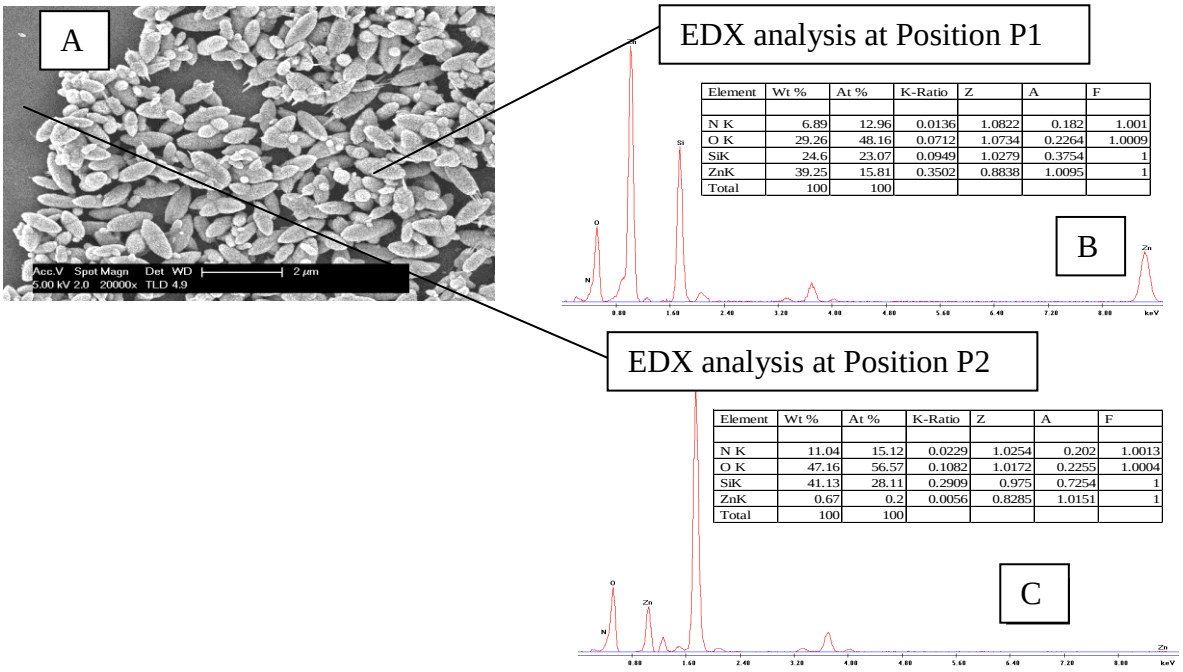

Figure 6.13: A:SEM image (top view) of N5:S2-CG; B:EDX analysis at position P1(edged ZnO crystal); C:EDX analysis at position P2(layer upon magnetron sputtered coating) at high concentration of TEA without pH control.

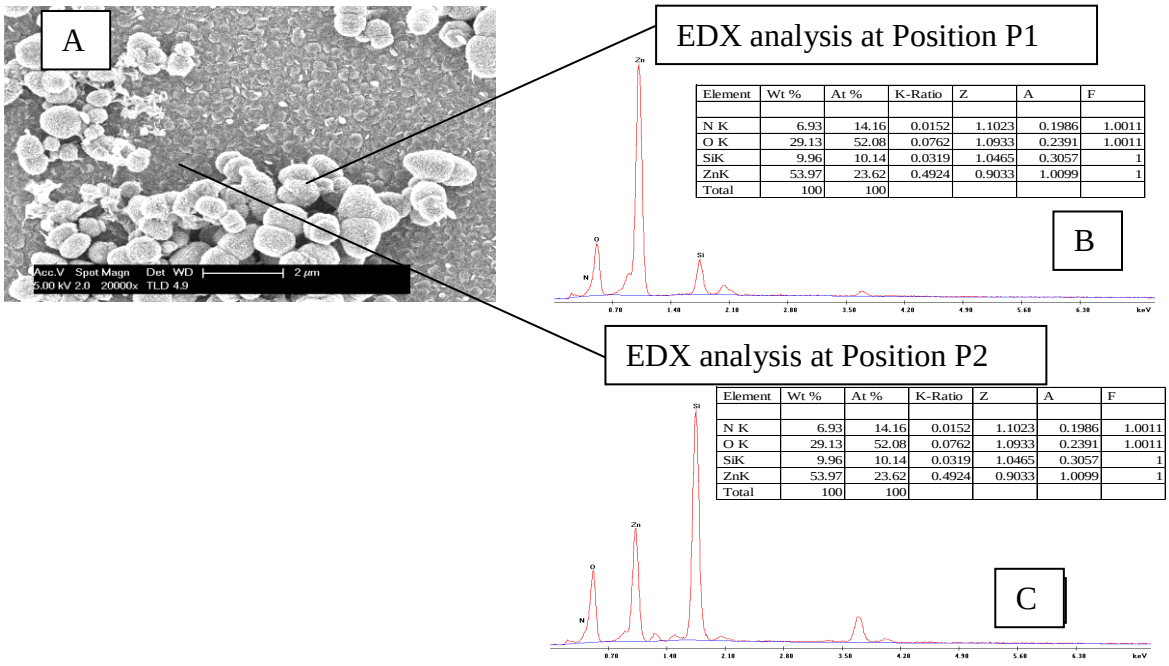

Figure 6.14: A:SEM image (top view) of N6:S2-MS; B:EDX analysis at position P1(cluster of ZnO crystal); C:EDX analysis at position P2(flowery layer upon magnetron sputtered coating) at low concentration of TEA without pH control.

In summary, huge variation in surface morphologies (crystal size, porosity and orientation) was obtained for almost all of the attempted nitrogen-doping of the nanostructured thin films

by using TEA as a nitrogen source, under both high and low concentrations of TEA, with and without pH control. None of the doped structures showed any substantial amounts of nitrogen incorporation as nitrogen dopant. Both concentration and pH of the reaction mixture played significant roles in changing the surface morphologies, indicating that the presence of TEA in the reaction mixture has a marked effect on the affinity of various reaction species ($Zn(NO_3).6H_2O$, HMT and/or PEI). A lack of evidence of incorporated nitrogen (as dopant), huge variation and very fragile surface morphologies make nanostructured zinc oxide thin films developed in this section not suitable for evaluation as photocatalysts. As a consequence, the successful incorporation of an anionic dopant in the ZnO lattice by using either nitrogen gas or TEA was not achieved.

6.2.2 Cobalt-doped Nanostructured ZnO (Co:ZnO) Thin Films

In the previous section it was concluded that production of a viable thin film structure incorporating a nitrogen anionic dopant is difficult unless a significantly different film growth method is used (i.e. higher temperature and pressure may have allowed doping). However, it is important to not only have a comparable method that produces films as similar as possible to the undoped films (so that only a minimal number of changed characteristics must be accounted for in comparisons between the doped and undoped films) but to also have a low temperature and low cost method, thereby precluding the use of much higher temperatures and pressures in the hydrothermal deposition. Therefore in order to achieve doped ZnO films with as similar as possible structural characteristics, the use of a cationic dopant – cobalt – was instead attempted. Keeping in view that dopant concentration and pH of the reaction mixture may severely affect the surface morphologies, a different dopant concentration and pH of the reacting mixture solutions Co:S1 and Co:S2 was used to prepare cobalt-doped nanostructured ZnO thin films by using $Co(NO_3).6H_2O$ as a cobalt source. The surface morphologies obtained at different cobalt nitrate concentrations are summarised in Section 3.3.3.

6.2.2.1 Comparison of cobalt-doped and undoped ZnO nanostructure

Figs. 6.15-6.18 respectively show a cross-sectional view of cobalt-doped surface morphologies Co:S1-MS, Co:S1-CG, Co:S2-MS and Co:S2-CG obtained from a mixture of solutions Co:S1 and Co:S2 by hydrothermal deposition growth (preparation method is outlined in Section 3.2.2.2) with four different cobalt nitrate concentrations as dopant (25, 15, 10 and 5 wt% $Co(NO_3).6H_2O$).

Morphologies obtained from a mixture of solutions Co:S1 and Co:S2, on MS and CG substrate, vary in crystal size, morphology, structure, and crystallinity.

6.2.2.1.1 Variation of Co:S1-MS morphology with Co concentration

Fig. 6.15 shows a comparison of undoped S1-MS (Fig. 6.15A) and cobalt-doped Co:S1-MS (Figs. 6.15B-E) at different cobalt dopant concentrations. Overall surface morphologies of Co:S1-MS change with changing cobalt concentration. For Co:S1-MS (Figs. 6.15B-E), as the cobalt concentration increases, the MS template has a decreasing impact on crystal orientation. Thus, the MS template remained active up to 15wt% cobalt concentration, and showed no template growth at the higher concentration of 25wt% of cobalt as the dopant source, where there are no longer highly aligned and well oriented crystals like those of the undoped S1-MS. The crystal sizes Co:S1-MS (2.4 µm, 2.2 µm, 2 µm, and 1-1.5µm at 5,10,15 and 25 wt% respectively) are smaller than undoped S1-MS (4-6 µm). The porosity of all of the Co:S1-MS was very low compared to undoped S1-MS; however, both porosity and crystal size of the doped ZnO structure increased with the decreased concentration of cobalt. The decreased porosity (reduction in space surrounding the ZnO as evident in SEM images) might be due to increased crystal diameter as cobalt ions in ZnO lattice have radius 0.65-0.75 Å greater than the ionic radii of zinc ions (0.60 Å). Thus, increased volumetric size is observed with the increased concentration of cobalt. This was also suggested by Bhatti *et.al.* [267]. This could also be due to the incorporation of cobalt ions into the ZnO lattice involving either the replacement of zinc ions or the positioning of cobalt in the interstices, as suggested by Djerdj *et al.* [268]. These results indicate that to achieve a Co:S1-MS thin film with the characteristics shown in Chapters 4 and 5 to produce a high photocatalytic activity, a lower Co concentration is preferable.

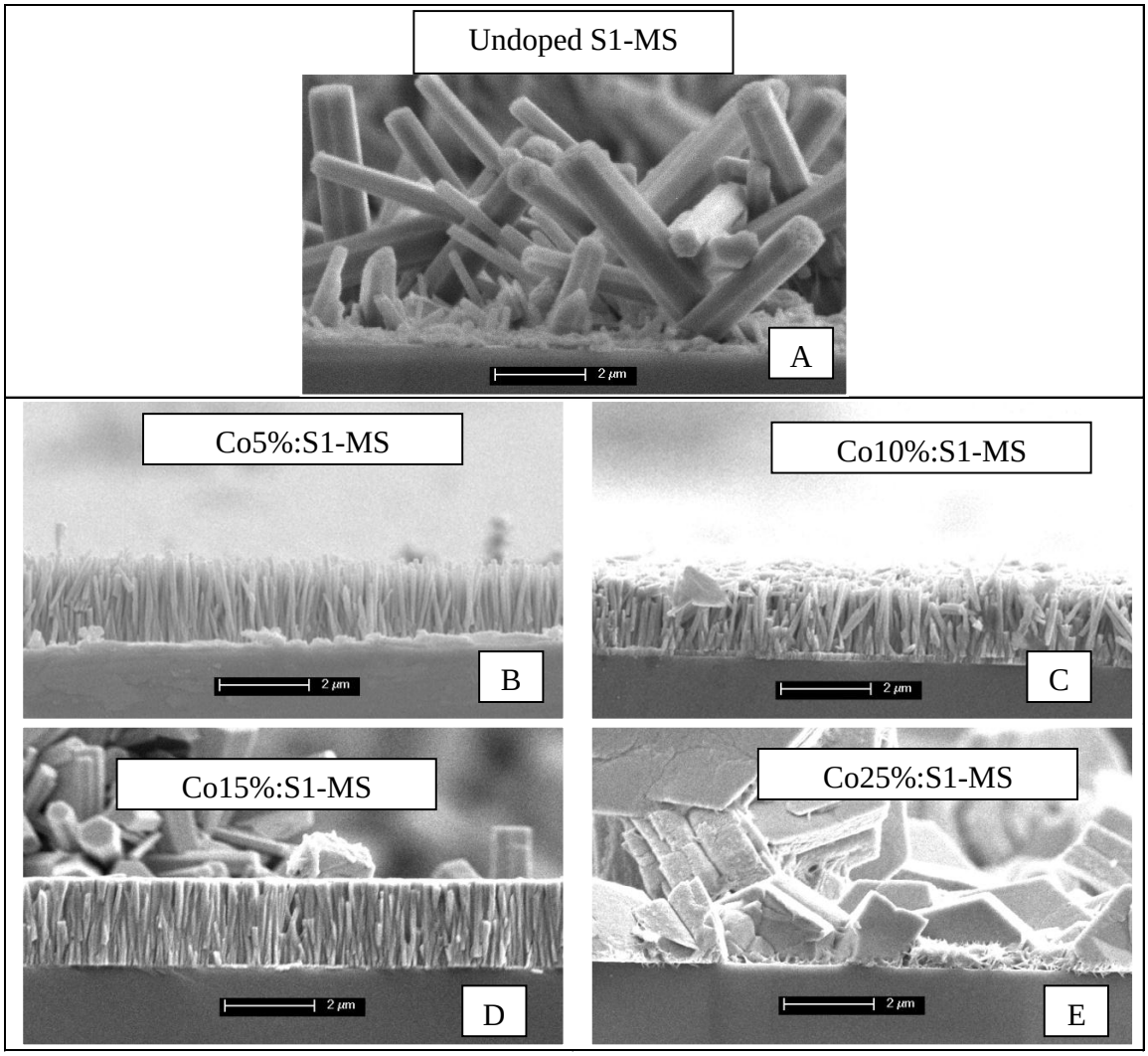

Figure 6.15: Cross-sectional SEM images of cobalt doped and un-doped ZnO nanostructured thin films. A: Un-doped S1-MS; B: Co5%:S1-MS, C: Co10%:S1-MS, D: Co15%:S1-MS and E: Co25%:S1-MS.

6.2.2.1.2 Variation of Co:S1-CG morphology with Co concentration

Fig. 6.16 shows a comparison of Co:S1-CG morphologies: cross-sectional views are shown in Fig. 6.16 (B-E) obtained at the same four concentrations of cobalt nitrate (5, 10, 15 and 25 wt% $Co(NO_3).6H_2O$) as undoped S1-CG. The crystal sizes of Co:S1-CG (1µm, 5 µm, 4.5 µm and ~4µm at 25,15,10 and 5 wt% respectively) were approximately the same, but more aligned and better oriented compared to the undoped S1-CG (4-6µm). Contrary to Co:S1-MS, the crystal size of Co:S1-CG changed very little up to 15wt% cobalt concentration, afterwards reducing to 1µm.

Another important feature of Co:S1-CG was the increase in crystal diameter with increasing cobalt concentration which leads to decreased overall film density (less dense cluster of

crystals per surface area of the glass). Morphologies Co:S1-MS and Co:S1-CG differ in surface, structure, crystal size and their orientation. Overall there was no dopant impact on the band gap of nanostructured ZnO thin films (see Appendix D). Reduction of crystal size with the increase in dopant concentration was in accordance with the study carried out by Ling *et al.* [168]. Similar to the Co:S1-MS results, these results indicate that to achieve Co:S1-CG thin film with the characteristics shown in Chapters 4 and 5 to produce a high photocatalytic activity, a lower Co concentration is preferable. Doped nanostructures, Co:S1-MS and Co:S1-CG, have comparatively smoother crystals with the least defects compared to undoped S1-MS and S1-CG. Thus, the impact of crystal smoothness (as both physical and chemical aspects may change on doping because of the impact of dopant on both valence and conduction band as previously discussed in section 2.9.2) on the previously identified Mars van Krevelen reaction mechanism can be studied here, knowing that it is aided by defects in the crystal structure.

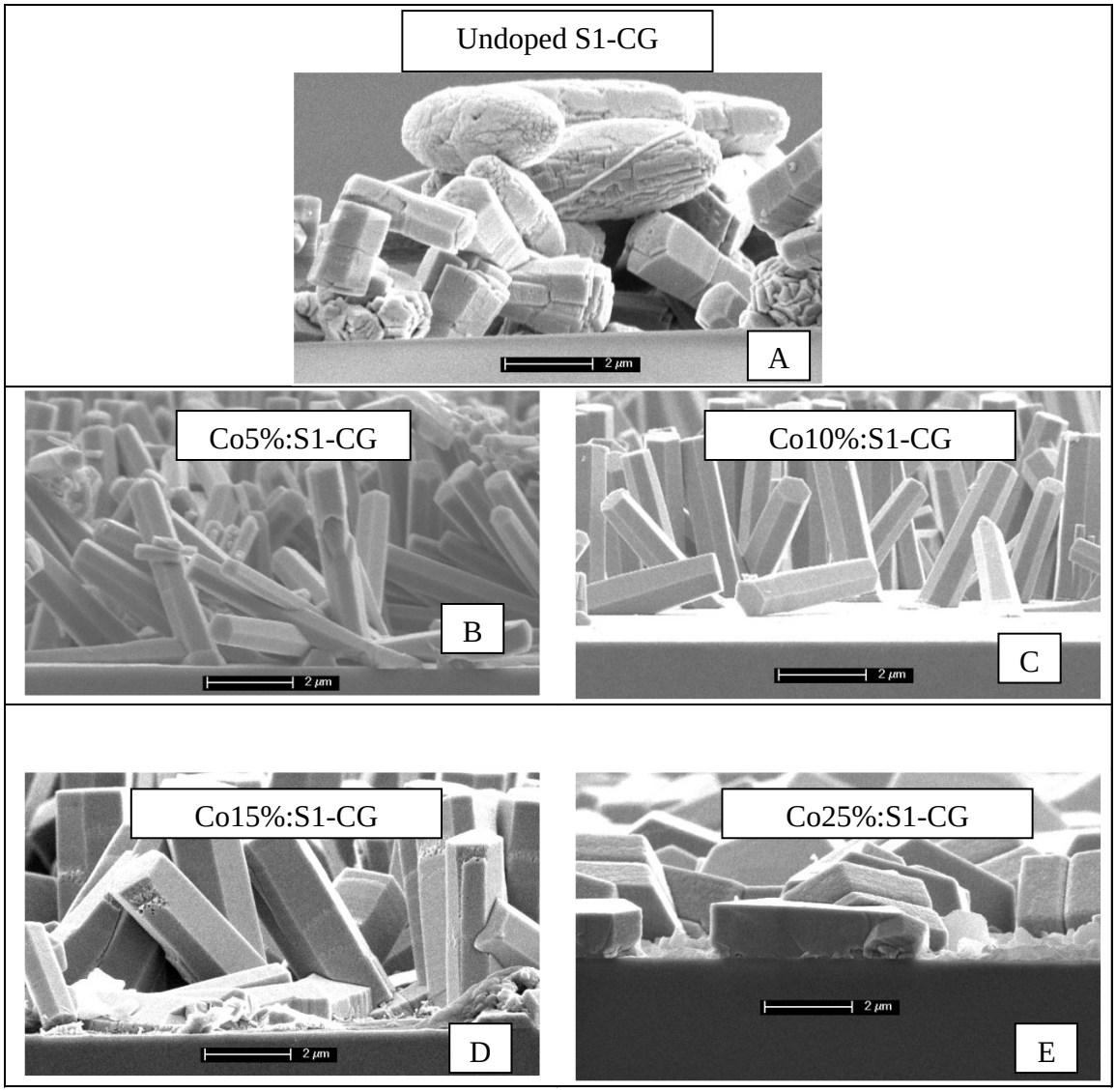

Figure 6.16: Cross-sectional SEM images of cobalt doped and un-doped ZnO nanostructured thin films. A: Un-doped S1-CG; B: Co5%:S1-CG, C: Co10%:S1-CG, D: Co15%:S1-CG and E: Co25%:S1-CG.

6.2.2.1.3 Variation of Co:S2-MS and Co:S2-CG morphology with Co concentration

Figs. 6.17-18 show the doped morphologies (Co:S2-MS and Co:S2-CG) on the MS and CG substrates grown from solution Co:S2. Both Co:S2-MS and Co:S2-CG varied in terms of crystal surface structure, size and porosity similarly to the doped morphologies (Co:S1-MS and Co:S1-CG) obtained from solution Co:S1. Fig.6.17 shows a comparison of undoped S2-MS (Fig. 6.17A) with cobalt-doped Co:S2-MS (Figs. 6.17B-E). The presence of cobalt, as dopant, produced a huge variation in surface morphologies, structure, porosity and crystal orientation, essentially removing all of the characteristics that allow S2-MS to be both stable and to produce a high photocatalytic activity, as detailed in Chapters 4 and 5. Crystal sizes of

Co:S2-MS (0.20µm and 0.20µm, 1µm and 0.15µm at 5,10,15 and 25 wt% respectively) were very small compared with undoped S2-MS (2 ~2.5µm).

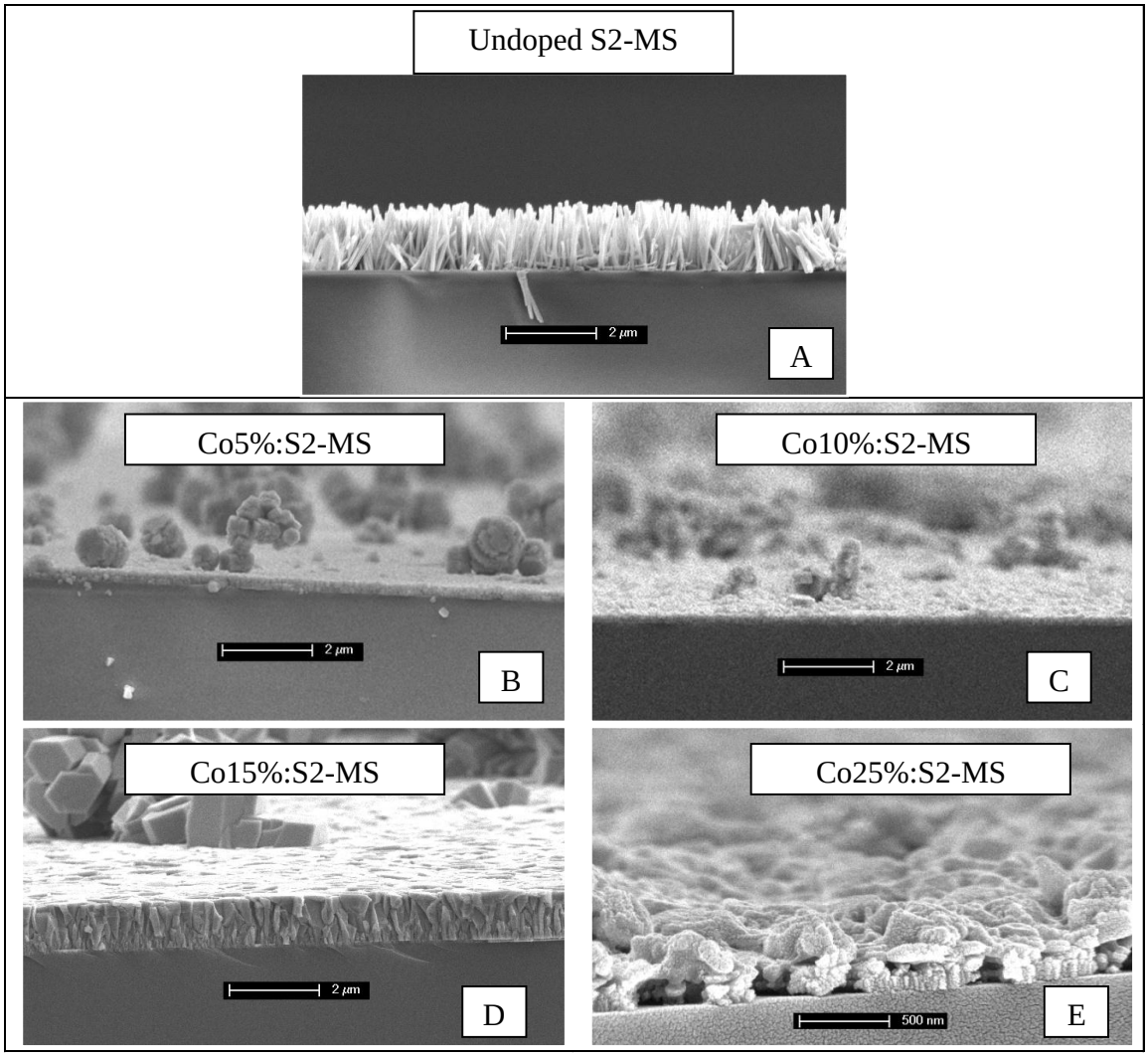

Figure 6.17: Cross-sectional SEM images of cobalt doped and undoped ZnO nanostructured thin films. A: Undoped S2-MS; B: Co5%:S2-MS, C: Co10%:S2-MS, D: Co15%:S2-MS and E: Co25%:S2-MS.

No clear relationship was observed between the crystal size and dopant concentration for Co:S2-MS. Crystal sizes at 5 and 10 wt% cobalt concentration were nearly the same, (0.20µm), increasing at 15wt% and then drastically dropping to 0.15 µm. Unlike the doped structures, the MS underlayer had little effect as a template from which aligned ZnO crystal growth could be obtained at all cobalt concentrations. Furthermore, there was less binding to glass substrate at higher dopant concentration, producing films that would not be robust under the mechanical stresses of use in a photocatalytic reactor.

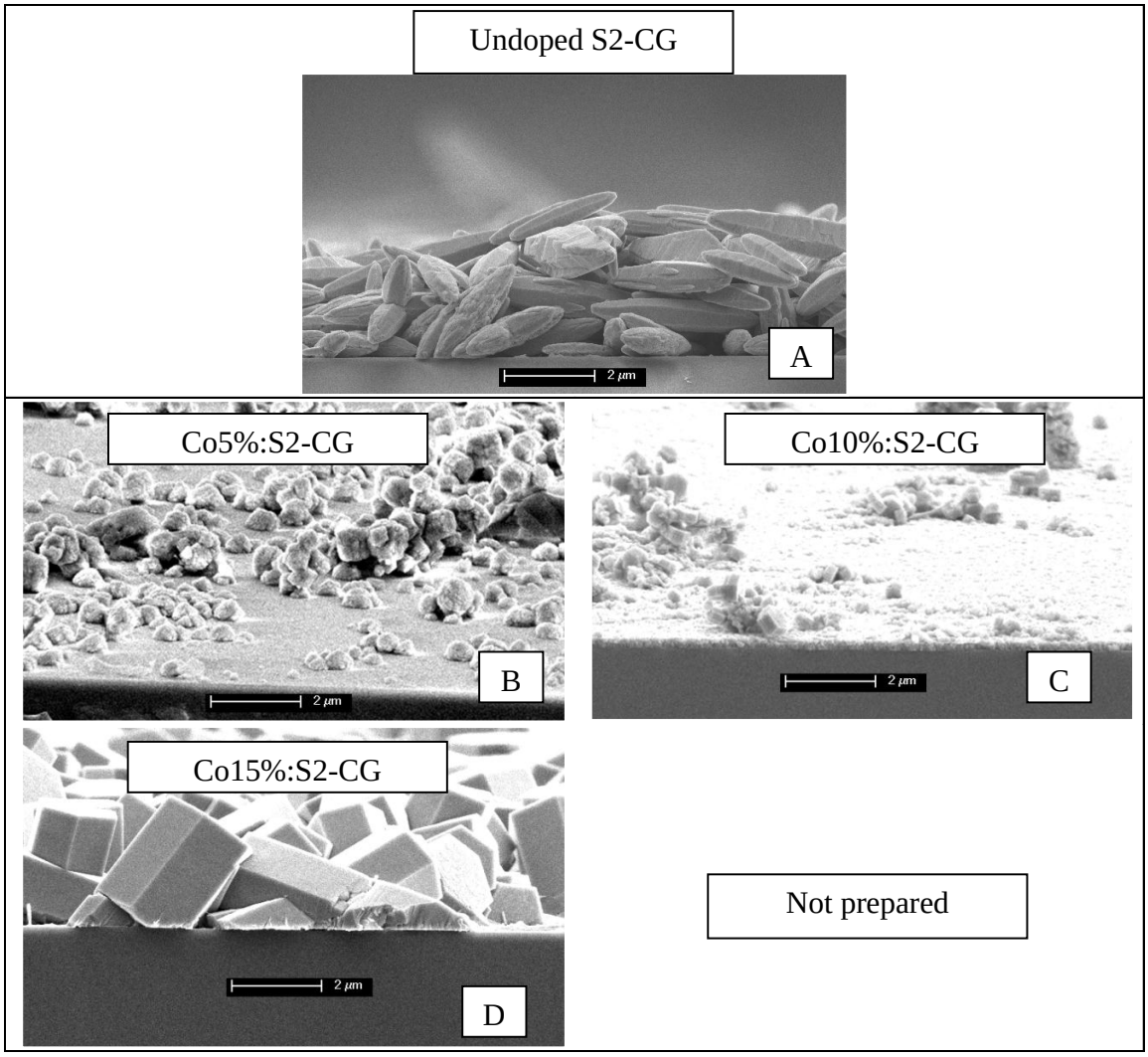

Figure 6.18: Cross-sectional SEM images of cobalt doped and undoped ZnO nanostructured thin films. A: Undoped S2-CG; B: Co5%:S2-CG, C: Co10%:S2-CG, D: Co15%:S2-CG.

It is assumed that porosity decreased because of the incorporation of the octahedral structure of cobalt within the interstices of ZnO lattice as pointed out by Djerdj *et al.* [268]. The 15wt% cobalt dopant was found to be mildly efficient in generating a slightly improved surface morphology with almost zero porosity. Similar patterns and changes may also be seen for Co:S2-CG morphologies which again differ in crystal alignment and their orientation to undoped S2-CG nanostructured ZnO thin films.

6.2.2.1.4 Overall morphology comparison between all doped and undoped films

Overall, at 15wt%, cobalt morphologies Co:S1-MS and Co:S1-CG resemble Co:S2-MS and Co:S2-CG respectively, in surface structure, crystal orientation and porosity (if any). The content of cobalt incorporation increased with increased cobalt concentration (see Tables. 6.1

and 6.2; Figs. 6.15-6.18), whereas the band gap of the cobalt-doped thin films was nearly the same as for the undoped ZnO thin films (see Appendix D).

An inverse relationship between dopant concentration and crystal size was depicted by morphologies obtained from the mixture of solution Co:S1; no specific relationship exists for those obtained from the mixture of solution Co:S2. The ability of the dopant element to become incorporated depends on the dopant nature (cationic or anionic) and dopant concentration plays a pivotal role in the structural and morphological nature of the doped nanostructure. The doped morphologies are generally smaller in crystal length and more densely packed than the undoped nanostructured ZnO thin films. In general, the film thickness of the films obtained from solution Co:S1 decreases with the increase in dopant concentration, and no particular relationship of dopant concentration to film thickness was found for the doped thin films obtained from solution Co:S2. However, the exposed surface areas were nearly the same at 5 and 10wt% dopant concentration (3.519×10^{-3}, 9.11×10^{-4} , 5.73×10^{-5} , 4.09×10^{-4} $m^2kg^{-1}$for Co:S1-MS, Co:S1-CG, Co:S2-MS respectively) which increases further with the increases in dopant concentration up to 15wt% and remains nearly same, even at 25wt % dopant concentration (9.49×10^{-3}, 8.82×10^{-4} , 2.22×10^{-3}, 1.28×10^{-3} m^2kg^{-1} for Co:S1-MS, Co:S1-CG, Co:S2-MS respectively).

6.2.2.2 Comparison of crystal planes and dopant concentration

6.2.2.2.1 Comparison of XRD analysis between doped and undoped films

XRD analysis of the films showed distinct differences also. Co:S1-CG and Co:S2-CG (Figs. 6.19 F and H) have almost similar crystal planes and phases (wurtzite; also called B4 type strcuture) compared with undoped S1-CG and S2-CG ([1,0,0], [0,0,2], [1,0,1], [1,0,2], [1,1,0]; see Figs 6.19 B and D) except for crystal plane [1,0,3]: an indication of cobalt incorporation within the ZnO lattice. The only major difference was the intensity of the crystal planes. [0,0,2] crystal planes were more dominant in Co-doped than [1,0,0] planes in undoped zinc oxide thin films.

However, Co:S1-MS and Co:S2-MS (Figs. 6.19 E and G) have only one prominent crystal plane [0,0,2] compared to crystal planes [1,0,0], [0,0,2], [1,0,1], [1,0,2], [1,1,0] of undoped S1-MS and S2-MS. Based on the results in Chapters 4 and 5 and the literature [166, 170], it would be expected that cobalt-doped nanostructured ZnO thin films could have a higher photocatalytic activity than the undoped films (see Section 6.4 for further details).

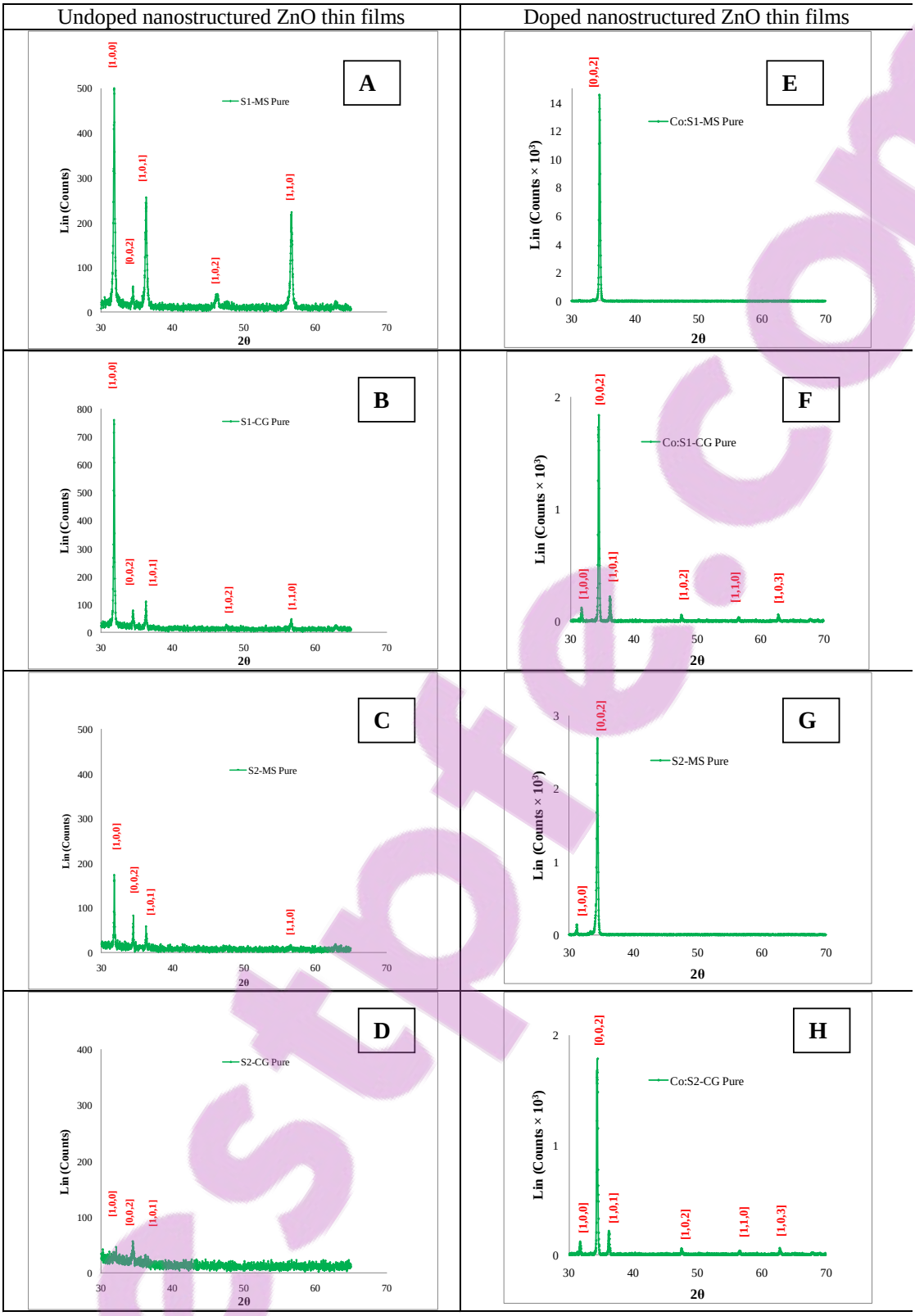

Figure 6.19: XRD comparison of undoped and cobalt-doped ZnO nanostructured thin films.

6.2.2.2.1 Comparison of dopant concentration

The dopant incorporation into the formed thin films increased with the increase in dopant concentration in the mother solutions from which they were grown (results are summarised in Tables 6.1 and 6.2). EDX analysis (see Tables 6.1-6.2) showed that morphologies Co:S2-MS and Co:S1-MS had the highest incorporation of cobalt (Co^{+2}) as dopant. In comparison to Co:S1-MS, Co:S2-MS had the highest amount of cobalt incorporation at the higher cobalt concentrations (25wt% $Co(NO)_3.6H_2O$). Less cobalt incorporation was found for morphologies Co:S1-CG and Co:S2-CG (see Tables 6.1 and 6.2). The higher incorporation of cobalt in the Co:S2-MS films is therefore likely to be a result of favourable interaction between the $Co(NO)_3.6H_2O$, the other species in solution Co:S2, and the MS template. Overall, doped morphologies obtained on the MS template had the most incorporation of cobalt as dopant, at the higher dopant concentration (25wt% of $Co(NO)_3.6H_2O$). Modification of the hydrothermal reaction such as increased in reaction temperature may incorporate cobalt better. However, based on results, it can be concluded that cobalt is not a good dopant and further modification is not warranted.

Four different concentrations of $Co(NO)_3.6H_2O$ (5wt%, 10wt%, 15wt% and 25wt%) were used to produce varying concentrations of cobalt-doped nanostructured ZnO thin films. It was seen that the dopant concentration had a significant impact on the surface morphology, crystal size (both in length and diameter), film thickness and crystal population on films grown on both MS and CG substrates. For all the morphologies (Co:S1-MS, Co:S1-CG, Co:S2-MS and Co:S2-CG), film thickness, crystal size (in terms of length), and crystal density were lowered with an increase in $Co(NO)_3.6H_2O$ concentration. However, crystal diameter was enlarged with increased $Co(NO)_3.6H_2O$ concentration (Figs. 6.15-6.18).

In summary, the incorporation of cobalt as dopant in the grown films increased with an increase in $Co(NO)_3.6H_2O$ concentration in the solutions from which they were hydrothermally grown, with increasing dopant concentration impacting significantly on surface morphology, film thickness, crystal size (both diameter and length) and crystal density.

Table 6.1: Comparison of Cobalt content in the Co:ZnO thin films at two different concentration of $Co(NO)_3.6H_2O$, derived from EDX analysis.

	15wt% $Co(NO)_3.6H_2O$							25wt% $Co(NO)_3.6H_2O$					
	Element	**Wt %**	**At %**	**K-Ratio**	**Z**	**A**	**F**	**Wt %**	**At %**	**K-Ratio**	**Z**	**A**	**F**
Co:S1-MS	***N K***	4.57	11.57	0.0091	1.1542	0.1542	1.0009	4.77	12.73	0.0096	1.1422	0.1761	1.0009
	O K	16.95	38.25	0.0401	1.1120	0.2023	1.0015	17.02	39.73	0.0431	1.1328	0.2232	1.0015
	Si K	5.41	6.86	0.0105	1.0742	0.2413	1.0001	4.41	5.86	0.0125	1.0835	0.2613	1.0001
	Pt M	2.11	0.40	0.0101	0.7457	0.6124	1	2.17	0.42	0.0108	0.7829	0.6321	1
	Ca K	0.89	0.72	0.0069	1.0204	0.7752	1.0064	0.85	0.79	0.0072	1.0605	0.7948	1.0064
	Co K	**0.56**	**0.40**	**0.0070**	**0.9124**	**0.9665**	**1.1698**	**0.67**	**0.42**	**0.0074**	**0.9514**	**0.9897**	**1.1698**
	Zn K	69.51	41.80	0.6227	0.9027	1.000	1.001	70.1	40.05	0.6627	0.9427	1.0027	1
Co:S1-CG	***O K***	24.21	56.99	0.0565	1.198	0.2124	1.0012	26.21	58.99	0.0787	1.123	0.2573	1.0012
	Si K	6.8	6.65	0.0145	1.0635	0.2745	1	6.3	7.87	0.0198	1.0743	0.2888	1
	Ca K	0.51	0.42	0.0040	1.102	0.7195	1.0051	0.55	0.48	0.0046	1.0512	0.7814	1.0051
	Co K	**0.19**	**0.11**	**0.0019**	**0.9124**	**0.945**	**1.1418**	**0.24**	**0.13**	**0.0023**	**0.9435**	**0.986**	**1.1418**
	Zn K	58.88	32.31	0.5436	0.9104	1.0024	0.98	59.83	31.38	0.5538	0.9352	1.0015	1
	Pt L	9.41	3.52	0.0599	0.7114	1.0625	1.02	6.87	1.16	0.0499	0.7214	1.0615	1

Table 6.2: Comparison of Cobalt content in the Co:ZnO thin films at two different concentration of $Co(NO)_3.6H_2O$, derived from EDX analysis.

	15wt% $Co(NO)_3.6H_2O$							25wt% $Co(NO)_3.6H_2O$					
	Element	**Wt %**	**At %**	**K-Ratio**	**Z**	**A**	**F**	**Wt %**	**At %**	**K-Ratio**	**Z**	**A**	**F**
Co:S2-MS	***O K***	27.01	60.65	0.0623	1.1105	0.2598	1.0001	27.54	61.66	0.0854	1.1308	0.2738	1.0012
	Si K	0.44	0.49	0.0008	1.0639	0.2465	0.954	0.41	0.52	0.0012	1.0816	0.2698	1
	Ca K	0.15	0.10	0.0010	1.0458	0.7845	1.005	0.13	0.12	0.0011	1.0588	0.7938	1.0062
	Co K	**2.14**	**2.12**	**0.0399**	**0.9304**	**0.9654**	**1.1254**	**3.81**	**2.32**	**0.0411**	**0.9504**	**0.9896**	**1.1455**
	Zn K	63.78	35.82	0.5652	0.9254	0.9478	0.874	62.82	34.42	0.5903	0.9421	0.9975	1
	Pt L	6.48	0.82	0.0506	0.7125	1.0104	0.99	5.28	0.97	0.0406	0.7268	1.0586	1
Co:S2-CG	***O K***	25.85	56.99	0.0587	1.101	0.2541	1.0001	27.21	58.99	0.0787	1.123	0.2573	1.0012
	Si K	7.65	7.14	0.0087	1.0701	0.2786	0.954	6.37	7.87	0.0198	1.0743	0.2888	1
	Ca K	0.41	0.42	0.0042	1.0514	0.7112	1.0051	0.55	0.48	0.0046	1.0512	0.7814	1.0051
	Co K	**0.18**	**0.10**	**0.0021**	**0.9432**	**0.946**	**1.2145**	**0.22**	**0.13**	**0.0023**	**0.9435**	**0.986**	**1.1418**
	Zn K	62.13	32.98	0.5505	0.9347	1.000	0.874	59.13	31.38	0.5538	0.9352	1.0015	1
	Pt L	3.78	1.47	0.0452	0.7286	1.0452	0.978	6.52	1.16	0.0499	0.7214	1.0615	1

6.2.2.3 Cobalt-doped ZnO nanostructure and pH

With the cobalt-doped nanostructured ZnO thin films being more compact (in terms of film thickness) and more densely packed (i.e. overall a less porous thin film) compared to the undoped films, an attempt was made to achieve more porous overall film by changing the pH of reacting solutions Co:S1 and Co:S2 (this work was performed by undergraduate student Nadiah K. Zaman under the author's co-supervision). The reasoning behind this was to provide a suitable environment for the interaction of the reacting species of solutions Co:S1 and Co:S2 (in particular with the MS templates); as noted in Chapters 4 and 5, pH plays an important role in the surface morphologies of undoped nanostructured ZnO thin films (in particular in dissolving the MS template or not).

6.2.2.3.1 Effect of pH on the morphologies of Co:S1-MS and Co:S1-CG

Fig. 6.20 shows a comparison of cobalt-doped surface morphologies Co:S1-MS and Co:S1-CG obtained on MS and CG substrate from a mixture of solutions Co:S1 at two different pH values (4 and 5) at 5wt% dopant concentration. The 5wt% cobalt dopant was chosen since this had previously generated a comparatively more porous structure than that achieved using a higher cobalt dopant concentration. This shows that a change in pH, even by one magnitude, impacted significantly on surface morphologies.

For Co:S1-MS, as shown in Figs. 6.20A-B, at the lower pH of 4, the MS template was ineffective in aligning growth since it had been dissolved by the more acidic conditions; it therefore generated random, vertically aligned crystals with a larger diameter and size compared to those of the Co:S1-MS film formed at the higher pH of 5, which was less acidic. Note that the larger diameter of ZnO crystals might be an indication that cobalt becomes incorporated in the ZnO lattice rather than in the interstices within the ZnO lattice. Morphology Co:S1-CG (Figs. 6.20C-D) obtained on CG substrate at lower pH also showed an enlarged crystal diameter (with a concomitant decrease in packing density) compared to Co:S1-CG obtained at pH 5.

A change in the pH generally increased the crystal diameter (and therefore decreased crystal packing density). However, this further altered the thin film characteristics from the optimal established in Chapters 4 and 5.

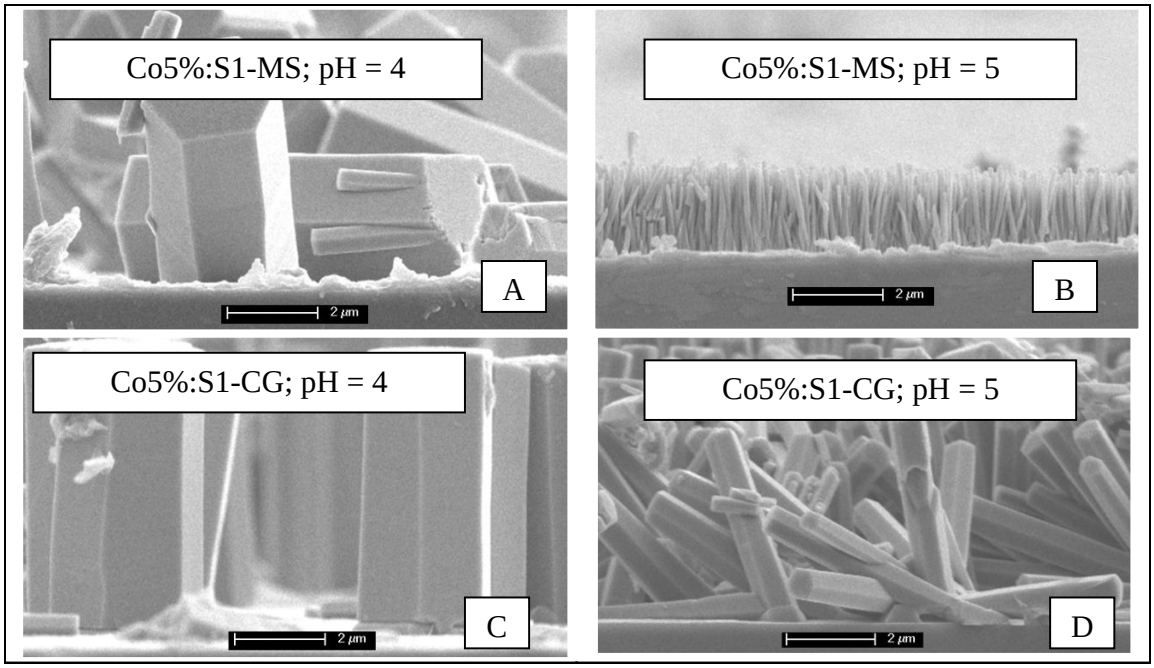

Figure 6.20: Cross-sectional SEM images of the cobalt doped ZnO nanostructured thin films. A: Co5%:S1-MS at pH=4, B: Co5%:S1-MS at pH=5, C: Co5%:S1-CG at pH=4 and D: Co5%:S1-CG at pH=5.

6.2.2.3.2 Effect of pH on the morphologies of Co:S2-MS and Co:S2-CG

Cobalt-doped nanostructured morphologies (Co:S2-MS and Co:S2-CG) obtained from a mixture of solutions Co:S2 on MS and CG at different pH (7.5 and 6.5) and 5wt% dopant concentration, are shown in Fig. 6.21. As discussed in Section 6.2.2.3, it was seen that lowering the pH – even by one magnitude – makes the MS template less effective at aligning the growth of ZnO crystals, giving a decreased crystal packing density. It can be seen that for Co:S2-MS, a reduction in pH value by one magnitude allowed the MS template to better align the growth, with film thickness increasing from 0.20µm to 0.75µm (see Figs. 6.21A-B), and well separated aligned columns, but with large stacks of ZnO over the MS template growth. Thus there was more growth but no visible decrease in thin film porosity (i.e. less dense film growth; see Figs. 6.21A-B) at the lower pH. The film also resembles the Co:S1-MS at pH 5: an indication that the proprietary additives used in mixture Co:S2 do not function to create the required type of structure at pH 6.5 and, as indicated in the original paper [115], have a major role in shaping the surface morphology of films from Co:S2.

For Co:S2-CG, lowering of the pH from 7.5 to 6.5 did result in significant changes on the surface morphology, as shown in Figs. 6.21C-D. More crystal growth, and improved alignment, having better surface coverage with smoother crystal surfaces, took place at the lower pH. Again this resembles morphology Co:S1-CG, showing that proprietary additives (such as PEI) have a lesser role in determining the character of Co:S2-CG morphology at a lower pH (i.e. are unable to function at the lower pH). The lower dopant percentage cobalt-doped thin films (obtained at 5wt% of $Co(NO)_3.6H_2O$ and pH 4 and 6.5) were closer in morphology to the undoped ZnO thin films than those with higher cobalt-doped concentrations.

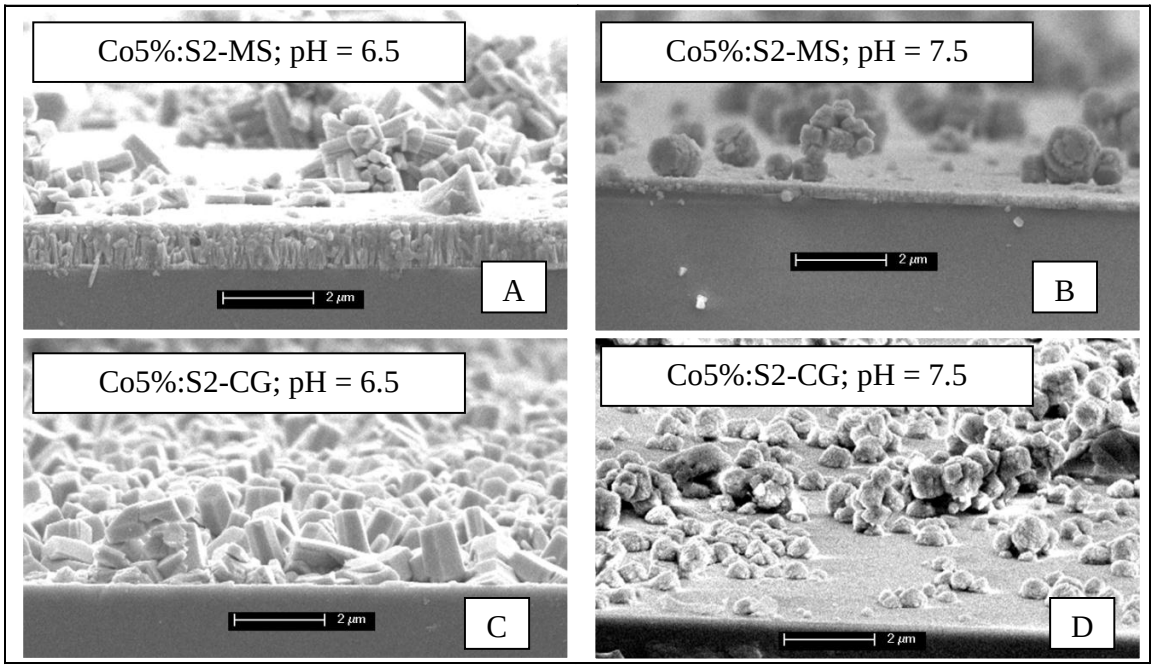

Figure 6.21: Cross-sectional SEM images of cobalt doped ZnO nanostructured thin films. A: Co5%:S2-MS at pH=6.5, B: Co5%:S2-MS at pH=7.5, C: Co5%:S2-CG at pH=6.5 and D: Co5%:S2-CG at pH=7.5.

6.3 Impact of Photocatalytic Reactions on Cobalt-Doped Nanostructured Zinc Oxide (Co:ZnO) Thin Films

Photocatalytic experiments with Co:ZnO thin films were performed under the same reaction conditions as for undoped ZnO thin films, to study the photocatalytic reaction effects on

doped surface morphologies under both oxygen-limited and rich conditions upon two different UV irradiations (254 and 340nm).

6.3.1 Morphologies after Reaction upon UV Irradiation at 254nm

6.3.1.1 Under oxygen-limited conditions

Previous results described in Chapters 4 and 5 showed that undoped ZnO thin film structures were found to be degraded in parallel to the photocatalytic degradation of MB under oxygen-limited conditions, where the overall reaction rate could be mass transfer limited by the supply of oxidant available for the reaction. The reaction was believed to have been caused by a Mars Van Krevelen type mechanism. To study the effect of cobalt as dopant to reduce the surface degradation of ZnO thin films, all cobalt-doped Co:ZnO thin films were photocatalytically studied under the same reaction conditions as those for the undoped ZnO thin films. Figs.6.22(B, E, H), 6.23(B, E, H), 6.24(B, E, H, K) and 6.25(B, E, H) show the cross-sectional images of Co:S1-MS, Co:S1-CG, Co:S2-MS and Co:S2-CG respectively at various dopant concentrations (25wt%, 15wt%,10wt% and 5wt%) under oxygen-limited conditions upon UV irradiation of 254nm.

Under oxygen-limited conditions, the doped morphologies obtained from Co:S1 (i.e. Co:S1-MS and Co:S1-CG), showed only a minute degradation on the doped ZnO crystal surface compared to undoped (S1-MS, S1-CG), as shown in Figs 4.2B and E, Chapter 4. Surface degradation was found to be less at higher dopant concentrations (15wt% and 10wt%; Figs. 6.22A-B, 6.22D-E and 6.23A-B, 6.23D-E respectively) as compared to a more significant change in surface morphologies at low dopant concentration (5wt%; Figs 6.22G-H and 6.23G-H). These characteristics may be an indication that the reaction does not involve the Mars van Krevelen type mechanism at higher cobalt concentrations, the cobalt increasing the activation energy required to initiate lattice breakdown to release the oxygens, and/or there is participation of dopant (the cobalt) as a charge transfer/carrier during the reaction (as already shown in other work [198, 199]).

Variations in doped surface morphologies (Co:S2-MS and Co:S2-CG) obtained from a mixture of solution Co:S2 after photocatalytic reaction under oxygen-limited conditions are shown in Fig. 6.24(B, E, H,K) and Fig. 6.25(B, E, H). These are for 25wt%, 15wt%, 10wt% and 5 wt% cobalt dopant for Co:S2-MS and 15wt%, 10wt% and 5 wt% cobalt dopant for Co:S2-CG respectively. Neither Co:S2-MS nor Co:S2-CG show any of the characteristic surface or lattice degradation associated with the Mars van Krevelen type mechanism (as

described in Chapters 4 and 5) at any dopant concentration, in contrast to Co:S1-MS and Co:S1-CG. The attachment between the Co10%:S2-MS and their MS and glass substrates and the Co5%:S2-CG and Co10%:S2-CG thin films and the clean glass substrates, are, however, less stable than the other films, with detachment and loss of the films occurring during reaction. As a consequence, these films are unsuitable for further use.

6.3.1.2 Under oxygen-rich conditions

As discussed above, under oxygen-limited conditions the cobalt-doped nanostructure showed an overall increased photocatalytic stability related to the dopant concentration. To study the behaviour of doped nanostructured surface morphology, all doped nanostructures were also photocatalytically tested under oxygen-rich conditions.

Fig 6.22(C, F, I), Fig 6.23(C, F, I), Fig 6.24(C, F, I, L) and Fig 6.25(C, F, I) show the cross-sectional views of surface morphologies of Co:S1-MS, Co:S1-CG, Co:S2-MS and Co:S2-CG after reaction under oxygen-rich conditions at four different dopant concentrations (25wt%, 15wt%, 10wt% and 5 wt% cobalt nitrate) for Co:S2-MS and at three different dopant concentrations (15wt%, 10wt% and 5 wt%) for Co:S1-MS, Co:S1-CG and Co:S2-CG respectively, upon UV irradiation of 254nm. Under oxygen-rich conditions, the surface morphologies after reaction were nearly the same as after reaction under oxygen-limited conditions (Figs 6.22-6.25). This reveals that the presence of oxygen did not suggest any major or significant difference to the photocatalytic stability of Co:ZnO thin films as it had for undoped nanostructured ZnO thin films (Figs 4.3 and 4.5; see Chapter 4). Less significant changes in surface morphologies, after reaction under oxygen-rich compared to oxygen-limited conditions, indicate that either the Mars van Krevelen reaction mechanism is occurring, and that free oxygen cannot be used (perhaps the cobalt prevents its participation in the surface reaction); and/or another reaction that requires neither lattice oxygens nor free oxidant is occurring in parallel with it. Since it has been established that increasing concentrations of the cobalt dopant stabilises the lattice, it is likely that this reaction is more predominant for the films with higher cobalt dopant concentrations (where the stability also implies that the Mars van Krevelen type mechanism is inhibited because of an increased activation energy barrier, for the removal of oxygen from the Co:ZnO lattice). A possible reaction is a charge transfer reaction of methylene blue with the Co:ZnO surface, which would break down the former in a non-photocatalytic manner. This has been shown to occur in methylene blue systems . Further work to determine if this reaction is occurring is detailed in Section 6.4.

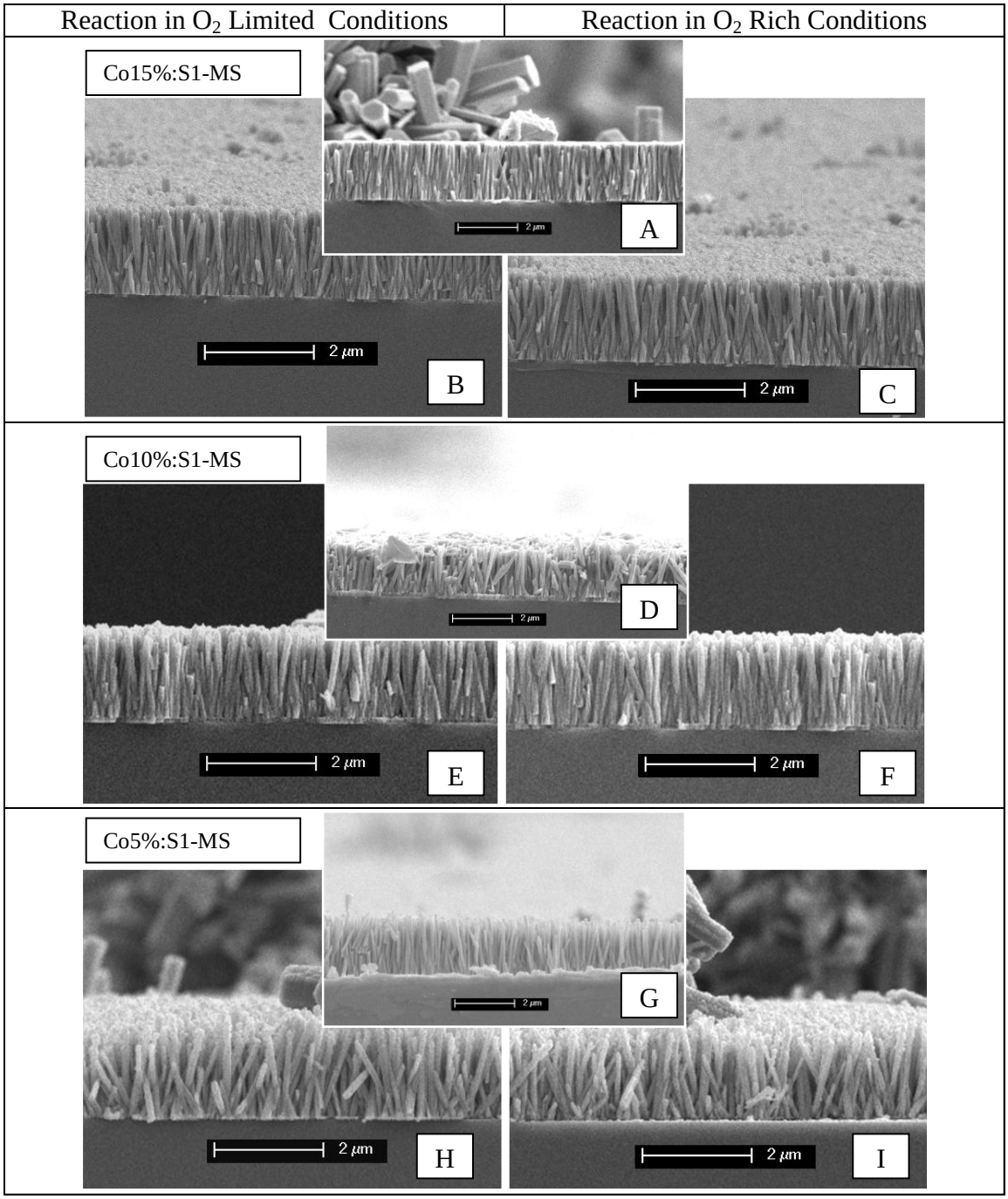

Figure 6.22: Cross-sectional SEM images of cobalt-doped nanostructured ZnO thin films surface morphologies before and after reaction under oxygen-limited and rich conditions upon UV irradiation of 254nm. A: Co15%:S1-MS unreacted, B: Co15%:S1-MS reacted under O_2 limited conditions, C: Co15%:S1-MS reacted under O_2 rich conditions, D: Co10%:S1-MS unreacted, E: Co10%:S1-MS reacted under O_2 limited conditions, F: Co10%:S1-MS reacted under O_2 rich conditions, G: Co5%:S1-MS unreacted, H: Co5%:S1-MS reacted under O_2 limited conditions, I: Co5%:S1-MS reacted under O_2 rich conditions.

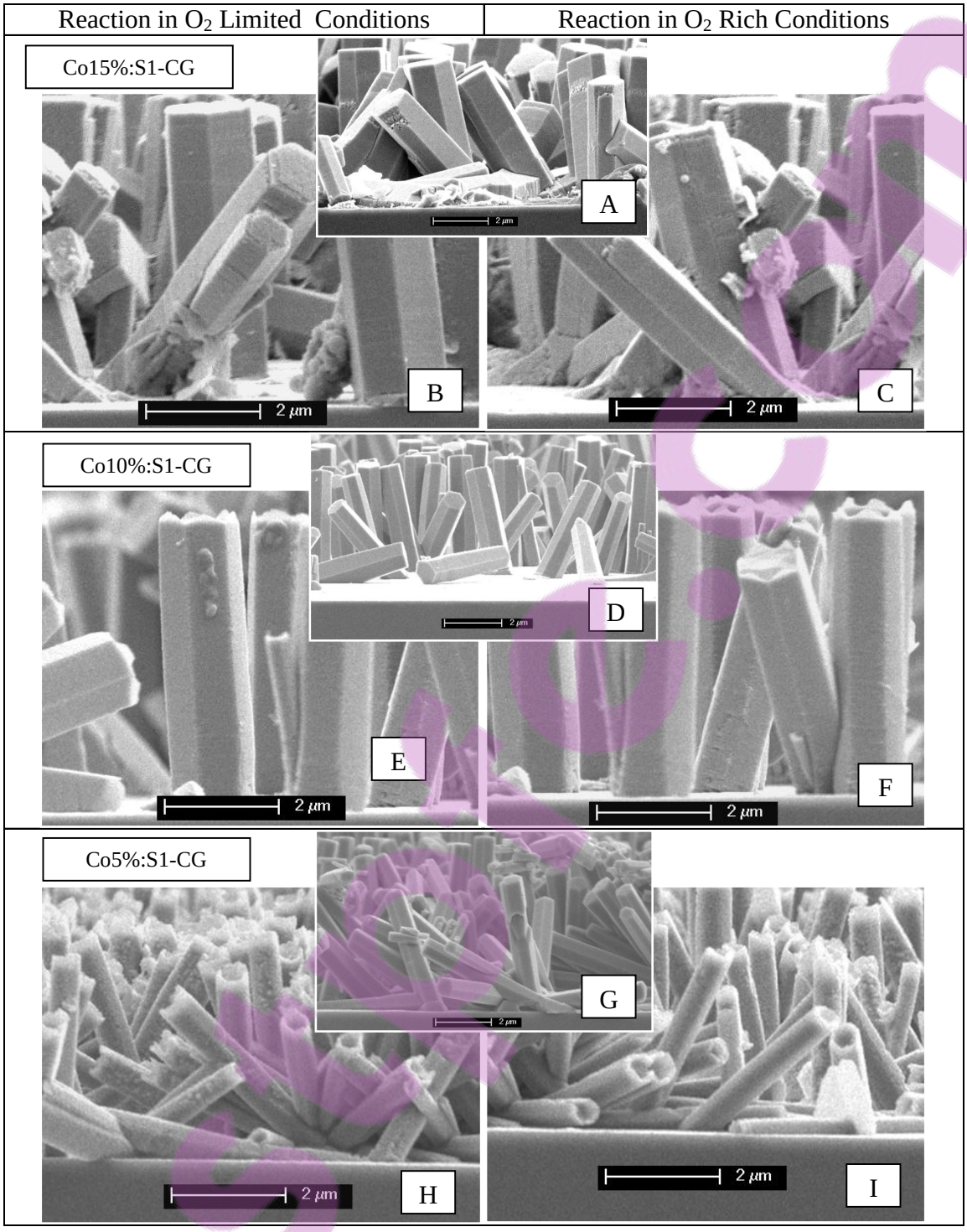

Figure 6.23: Cross-sectional SEM images of cobalt-doped nanostructured ZnO thin films surface morphologies before and after reaction under oxygen-limited and rich conditions upon UV irradiation of 254nm. A: Co15%:S1-CG unreacted, B: Co15%:S1-CG reacted under O_2 limited conditions, C: Co15%:S1-CG reacted under O_2 rich conditions, D: Co10%:S1-CG unreacted, E: Co10%:S1-CG reacted under O_2 limited conditions, F: Co10%:S1-CG reacted under O_2 rich conditions, G: Co5%:S1-CG unreacted, H: Co5%:S1-CG reacted under O_2 limited conditions, I: Co5%:S1-CG reacted under O_2 rich conditions.

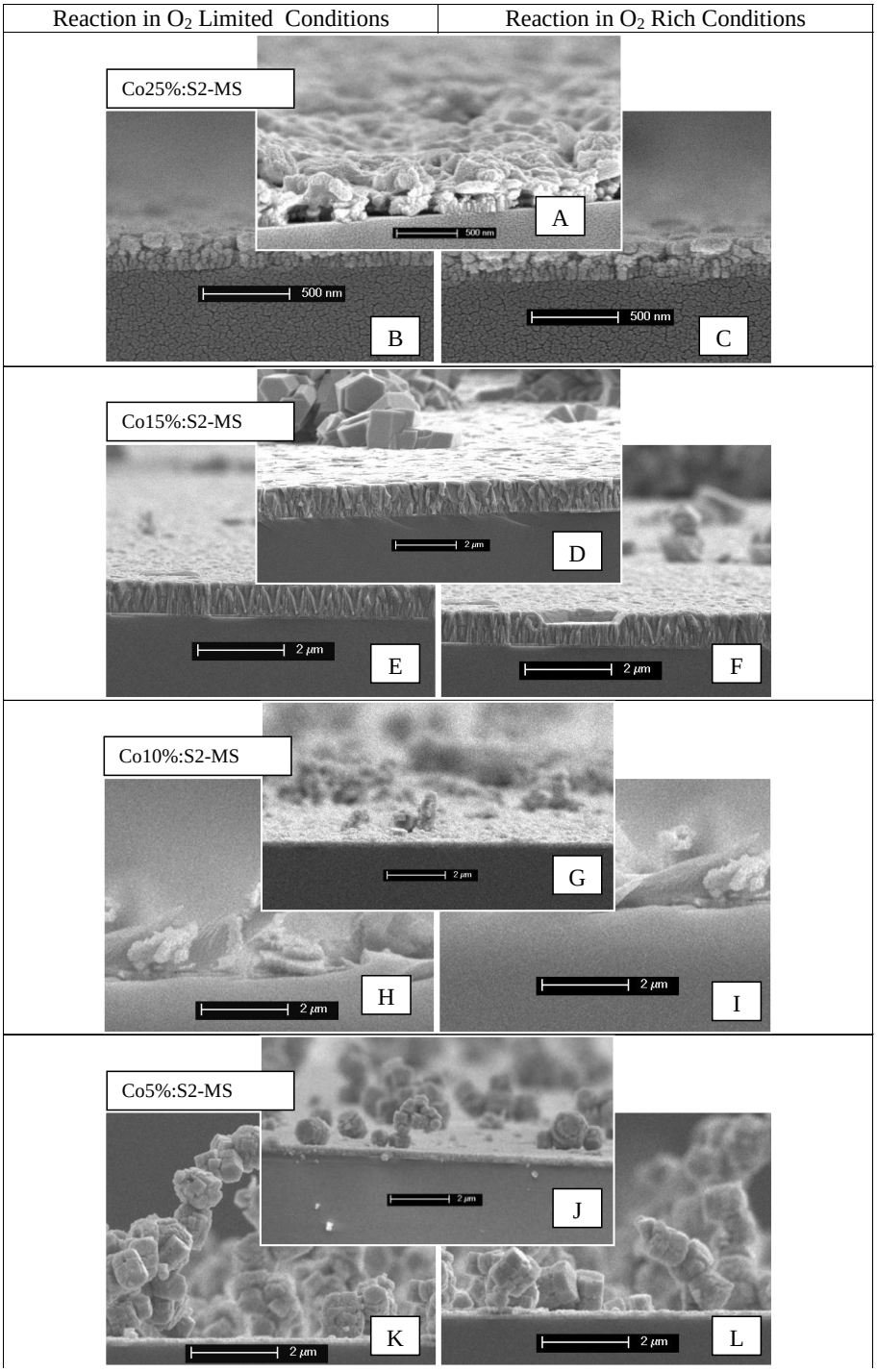

Figure 6.24: Cross-sectional SEM images of cobalt-doped nanostructured ZnO thin films surface morphologies before and after reaction under oxygen-limited and rich conditions upon UV irradiation of 254nm. A: Co25%:S2-MS unreacted, B: Co25%:S2-MS reacted under O_2 limited conditions, C: Co25%:S2-MS reacted under O_2 rich conditions, D: Co15%:S2-MS unreacted, E: Co15%:S2-MS reacted under O_2 limited conditions, F: Co15%:S2-MS reacted under O_2 rich conditions, G: Co10%:S2-MS unreacted, H: Co Co10%:S2-MS reacted under O_2 limited conditions, I: Co Co10%:S2-MS reacted under O_2 rich conditions, J: Co5%:S2-MS unreacted, K: Co5%:S2-MS reacted under O_2 limited conditions, L: Co5%:S2-MS reacted under O_2 rich conditions.

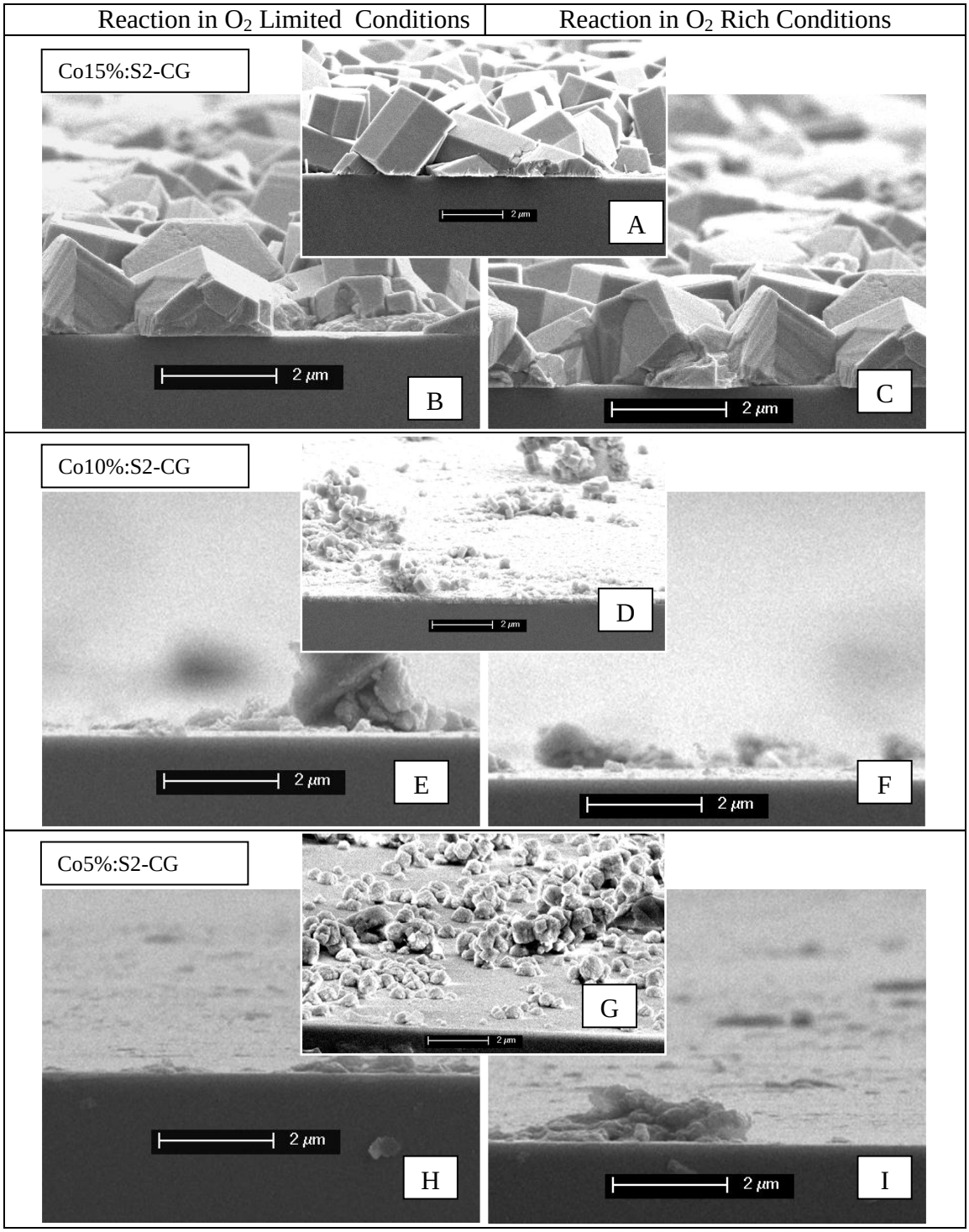

Figure 6.25: Cross-sectional SEM images of cobalt-doped nanostructured ZnO thin films surface morphologies before and after reaction under oxygen-limited and rich conditions upon UV irradiation of 254nm. A: Co15%:S2-CG unreacted, B: Co15%:S2-CG reacted under O_2 limited conditions, C: Co15%:S2-CG reacted under O_2 rich conditions, D: Co10%:S2-CG unreacted, E: Co10%:S2-CG reacted under O_2 limited conditions, F: Co10%:S2-CG reacted under O_2 rich conditions, G: Co5%:S2-CG unreacted, H: Co5%:S2-CG reacted under O_2 limited conditions, I: Co5%:S2-CG reacted under O_2 rich conditions.

6.3.2 Morphologies after Reaction upon UV Irradiation at 340nm

In Chapter 5, it was argued that both conventional and Mars van Krevelen reaction mechanisms were taking place in the reaction at UV irradiation of 340nm. To elucidate this, a few cobalt-doped morphologies (Co15%:S1-MS, Co15%:S2-MS and Co25%:S2-MS) were also photocatalytically tested upon UV irradiation of 340nm under both oxygen-limited and rich conditions.

Fig. 6.26 shows the cross-sectional view of the doped surface morphologies under both oxygen-limited and rich conditions. At first, the morphologies of both thin films (Co:S1-MS and Co:S2-MS) remain practically unchanged (Figs. 6.26B-C, 6.26E-F and 6.26H-I) at both low and high cobalt concentration after reaction under both oxygen-limited and rich conditions upon UV irradiation of 340nm. Secondly, the concentration of dopant did not appear to have any significant impact on the extent of photocatalysis (see Section 6.4.3). Overall the low photocatalytic activity at UV irradiation of 340nm indicated that UV energy was either not sufficient to initiate the reaction, or if it had been sufficient, the charge separation [199], because of the presence of cobalt ion, might have overtaken the photo-ionisation, leading to a lower reaction rate. Lack of photo-induced electrons, because of the energy barrier, meant that both formation of key hydroxyl radicals, or take-up of electrons either by lattice oxygen or oxygen present in the bulk of reaction fluid, was therefore, (if this were the case), not significant. The lack of change in surface morphology upon UV irradiation of 340nm therefore indicates that the Mars van Krevelen type mechanism does not occur (since there is no possible participation of lattice oxygen).

6.3.3 XRD Analysis of All Cobalt-Doped Thin Films

XRD analysis (Fig. 6.27) showed that there was no change in crystal planes of all the doped morphologies after photocatalytic reaction either under oxygen-limited or rich conditions, confirming further that the doped morphologies are either highly stable under photocatalytic reaction because of the lack of Mars van Krevelen type reaction mechanism or might, if any, have high efficiency in regenerating the lattice oxygen under oxygen-rich conditions only, after taking part in chemical reaction.

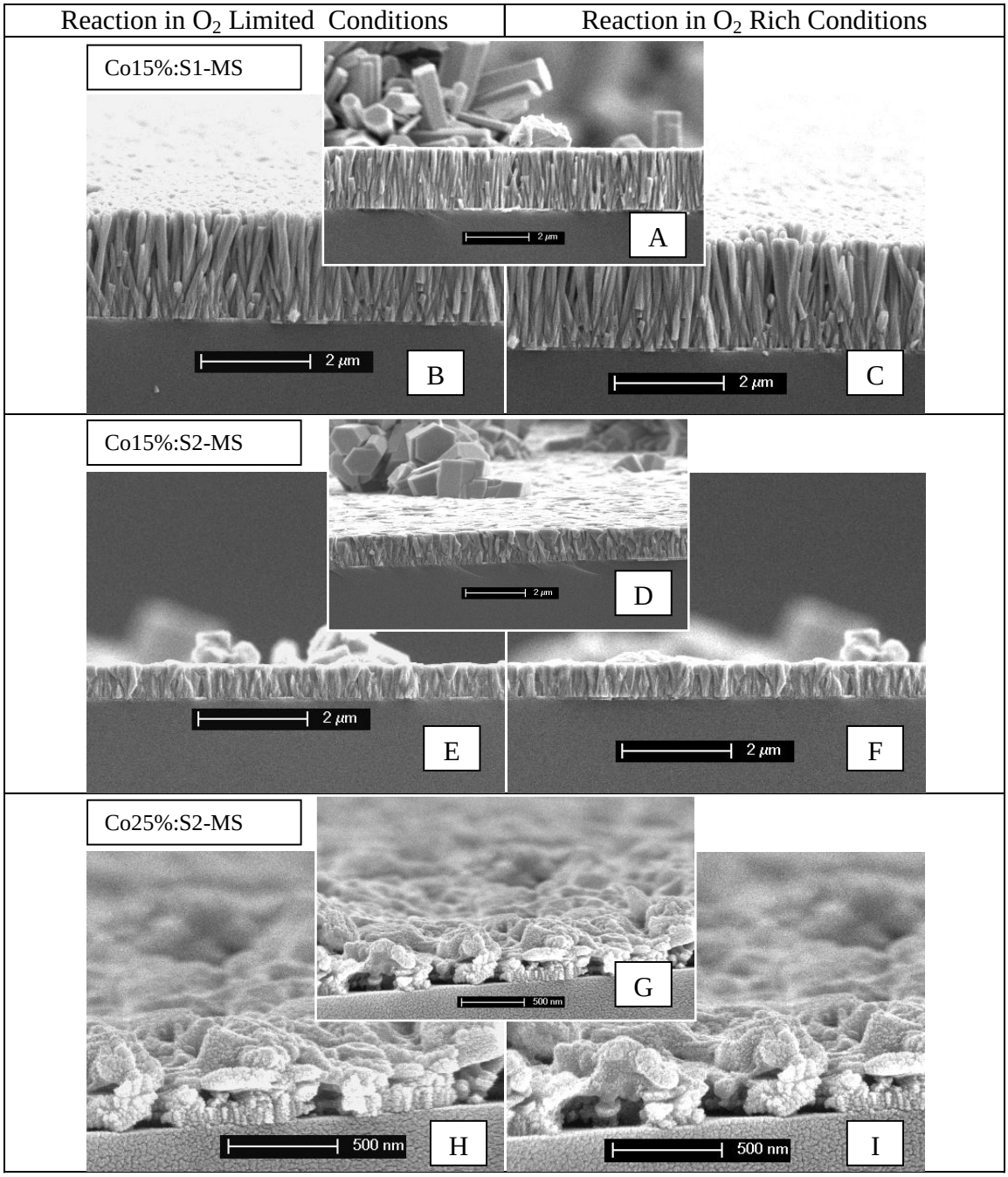

Figure 6.26: Cross-sectional SEM images of cobalt-doped and undoped nanostructured ZnO thin films surface morphologies before and after reaction under oxygen-limited and rich conditions upon UV irradiation of 340nm. A: Co:S1-MS(15wt%) unreacted, B: Co:S1-MS(15wt%) reacted under O_2 limited conditions, C: Co:S1-MS(15wt%) reacted under O_2 rich conditions, D: Co:S2-MS(25wt%) unreacted, E: Co:S2-MS(25wt%) reacted under O_2 limited conditions, F: Co:S2-MS(25wt%) reacted under O_2 rich conditions, G: Co:S2-MS(15wt%) unreacted, H: Co:S2-MS(15wt%) reacted under O_2 limited conditions, I: Co:S2-MS(15wt%) reacted under O_2 rich conditions.

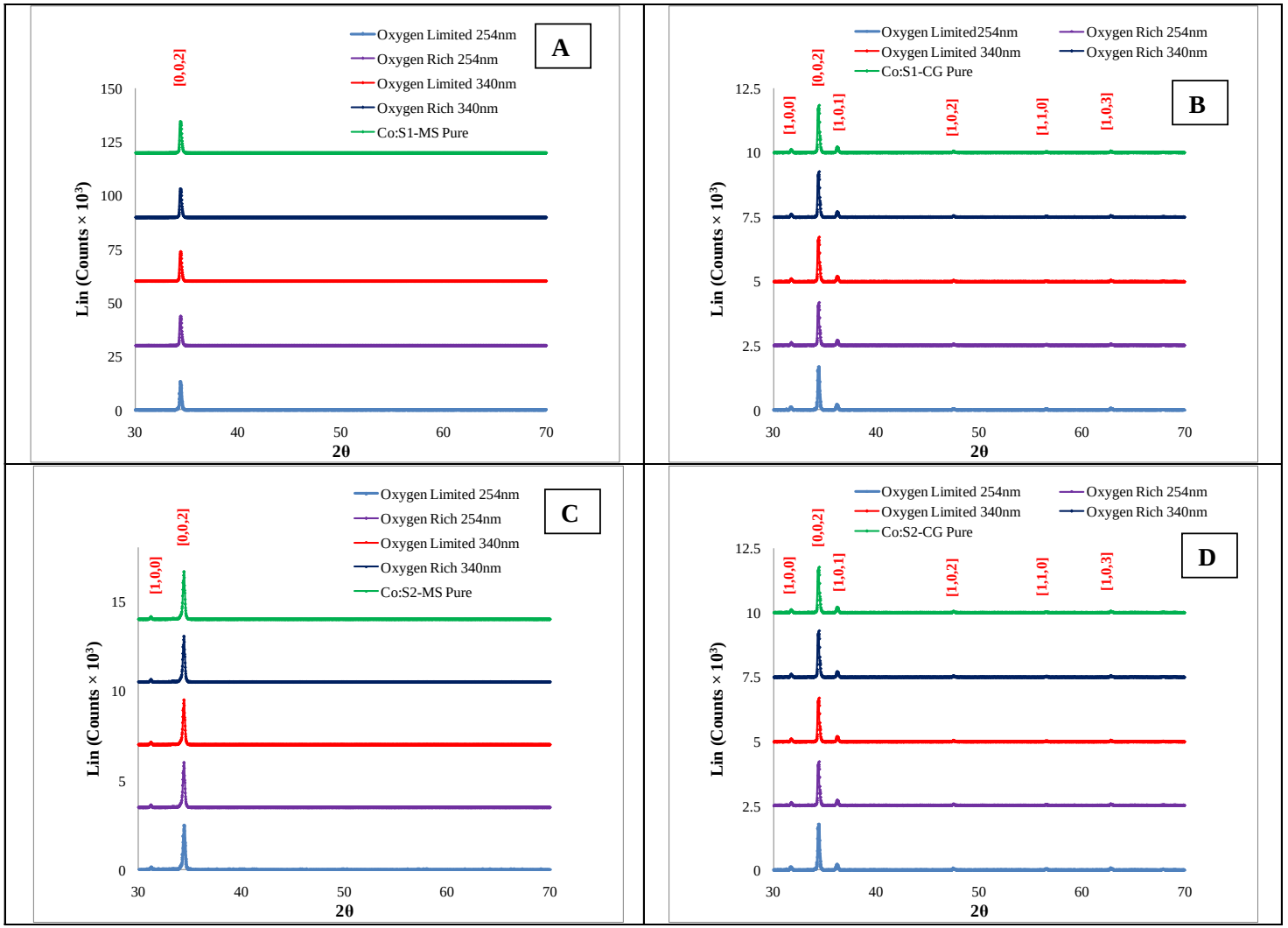

Figure 6.27: Comparison of XRD analysis of photocatalytically reacted cobalt doped nanostrcutred ZnO thin films upon UV irradition of 254nm and 340nm under both oxygen-limited and oxygen-rich conditions.

6.4 Doped Surface Morphologies and Photocatalytic Activity Relationship

6.4.1 Photocatalytic Activity, Reaction Rate and Reaction Kinetics

Photocatalytic degradation of methylene blue by using cobalt-doped nanostructured ZnO thin films followed first order reaction kinetics similar to undoped nanostructured ZnO thin films. This could indicate the presence of the monolayer of the reaction species at the solid-liquid interface. Apparent first order reaction rate constants on the basis of the mass of the catalyst (k'_{app}), UV exposed catalyst surface area (k''_{app}) and volume of the catalyst (k'''_{app}), are summarised in Tables 6.3-6.5 under both oxygen-limited and rich conditions upon UV irradiation 254nm and 340nm. Some of the data discussed (see Appendix E) in this section was collected by Nadiah K. Zaman under the author's co-supervision.

6.4.2 Photocatalytic Activity and Reaction Intermediate Kinetics under UV Irradiation of 254nm

6.4.2.1 Oxygen-limited conditions

As described in the previous sections, describing the morphological changes, cobalt-doped nanostructured zinc oxide thin films (Co:ZnO) obtained at different dopant concentrations were photocatalytically studied under the same reaction conditions as the undoped ZnO thin films. The following discusses the reaction results.

Effect of Co dopant concentration*:* Fig. 6.28A-D shows an overall comparison of photocatalytic degradation profiles of MB by Co:ZnO thin films (Co:S1-MS, Co:S1-CG, Co:S2-MS and Co:S2-CG obtained at 5, 10, 15 and 25wt% cobalt nitrate respectively) under oxygen-limited conditions upon UV irradiation of 254nm. The photocatalytic activity of Co:ZnO thin films at 5wt% cobalt nitrate was higher than that of Co:ZnO thin films obtained at 10, 15 and 25wt% cobalt nitrate. In general, an inverse relationship exists between photocatalytic activity and dopant concentration; i.e. photocatalytic activity decreases with an increas**e** in dopant concentration which has a direct relation to the cobalt nitrate concentration. This coincides with an increased stability of the films, confirming that the Mars van Krevelen mechanism is most likely being inhibited by the increased cobalt dopant concentrations. This is also an indication that the Mars van Krevelen mechanism is again the main photocatalytic mechanism and that the other speculated mechanism (such as charge transfer) occurs at a much lower reaction rate.

Confirmed by Figs. 6.30-6.33, these results show the kinetic profiles of various reaction intermediates (AB, AA, AC and TH), identified by HPLC and LC-MS, formed during the photocatalytic reaction carried out by using Co:ZnO nanostructured thin films upon UV irradiation 254nm under both oxygen-limited and rich conditions. In almost all cases, the parent molecule was not fully degraded and was therefore present during the entire course of the reaction with comparatively high concentration at the end of the reaction compared to that with undoped nanostructured ZnO thin films.

Under oxygen-limited conditions, morphology Co:S1-MS [5wt% of $Co(NO_3)_2$; see Fig. 6.30A] has the highest level of overall photocatalytic degradation of MB and the formation of reaction intermediates AB, AA, AC and TH compared to the same morphology Co:S1-MS [10, 15wt% of $Co(NO_3)_2$ respectively; see Figs. 6.30 C and E] obtained under different dopant concentrations. All identified reaction intermediates AB, AA, AC and TH were prominently formed with no further degradation, unlike for the undoped films, where intermediates were also degraded (see Appendix M). This indicates that these films have a lower overall photocatalytic activity for the complete set of reactions compared to the undoped films – further confirming the negative impact of cobalt on the photocatalytic activity.

The photocatalytic activity of Co:S1-MS and Co:S1-CG decreased significantly with the increase in dopant concentration, compared to Co:S2-MS and Co:S2-CG. However, degradation profiles follow similar trends (Fig. 6.28), generally low photocatalytic activity accompanying the increased dopant concentration. Therefore, only photocatalytic activity results of the Co:ZnO thin films obtained at 5wt% cobalt nitrate are discussed in detail, and are compared to the undoped ZnO thin films.

Comparison between doped films at 5% Co: When comparing films from solution Co:S1, the trends were not consistent (but still explainable from the results). Thus, Co5%:S1-MS had a higher photocatalytic activity than Co5%:S1-CG, based on overall degradation trends and as quantified by the apparent reaction rate constants k'_{app} and k'''_{app} (see Table 6.3). Thus, a generally increased photocatalytic activity for Co5%:S1-MS was noticed compared to that for Co5%:S1-CG (see Figs. 6.30A-B), due to the lower density of Co:ZnO mass and surface area in the Co5%:S1-CG films (Fig. 6.16B) compared to the Co5%:S1-M9999S films (Fig. 6.15B). Co:S1-MS films are clearly superior, however, with a higher overall degradation rate of azo dyes for an equivalent substrate surface area.

In contrast, the degradation and rate results for thin films from solution Co:S2 were more consistent, with thin film Co5%:S2-MS more photocatalytically active on the basis of all three apparent reaction rate constants (k'_{app}; k''_{app} and k'''_{app}; see Table 6.3) compared to those from thin film Co5%:S2-CG (k'_{app}; k''_{app} and k'''_{app}; see Table 6.3). This shows that the reaction mechanisms, either conventional radical formation and/or Mars van Krevelen type lattice oxygen abstraction and regeneration, if any, and/or charge transfer, are more active in morphologies Co5%:S2-MS as compared with Co5%:S2-CG, again showing that aligned crystalline morphologies have a high photocatalytic activity. These trends were further confirmed by the reaction intermediates kinetic profiles from the reaction of Co:S2-MS (5, 10, 15 and 25wt%) under oxygen-limited conditions (Figs 6.32A,C,E,G). These show that Co5%:S2-MS was again more efficient in generating significant amounts of reaction intermediates with no further degradation.

Consequently, thin films grown from the MS template again had the highest photocatalytic activity, where Co5%:S2-MS (k'_{app}; k''_{app} and k'''_{app} ; see Table 6.3) had a higher photocatalytic activity than thin film Co5%:S1-MS (based on k'_{app}; k''_{app} and k'''_{app}; see Table 6.3). On an overall degradation basis, however, (i.e. comparing the films on a surface area of MS and glass substrate basis), Co5%:S1-MS produced the highest degradation rate and extent for MB and all the reaction intermediates. These results, in general, indicate that Co5%:S2-MS is the more photocatalytically active structure and chemistry; however, the greater surface area on the Co5%:S1-MS film allows the thin film to have the best overall degradation. Therefore, the Co5%:S2-MS film has the best potential to have the greatest photocatalytic activity, so long as the surface area per substrate surface can be increased.

The morphologies obtained from growth on the CG substrate had a lower photocatalytic activity, similar to the trends detailed in Chapters 4 and 5. Of these, Co5%:S1-CG had a higher photocatalytic activity (based on k'_{app}; k''_{app} ; see Table 6.3) compared to Co5%:S2-CG (based on k'_{app}; k''_{app} ; see Table 6.3). Again, reaction intermediate kinetic profiles of Co5%:S1-CG and Co5%:S2-CG were almost similar, with the least formation of reaction intermediates under oxygen-limited conditions for different dopant concentrations (See Figs. 6.31A,C,E and 6.33A,C,E) except for morphology Co5%:S1-CG, which depicted a sizeable amount of formation of the reaction intermediate AB. No further degradation in reaction intermediates occurred. In comparison with undoped S1-CG and S2-CG, a reduced extent of formation of reaction intermediates was noticed, with S2-CG being more effective at forming AB and AA. The lower effectiveness at forming and degrading reaction intermediates again

shows that the films have a lower photocatalytic activity, and that the cobalt inhibits both the Mars van Krevelen and conventional photocatalytic mechanisms.

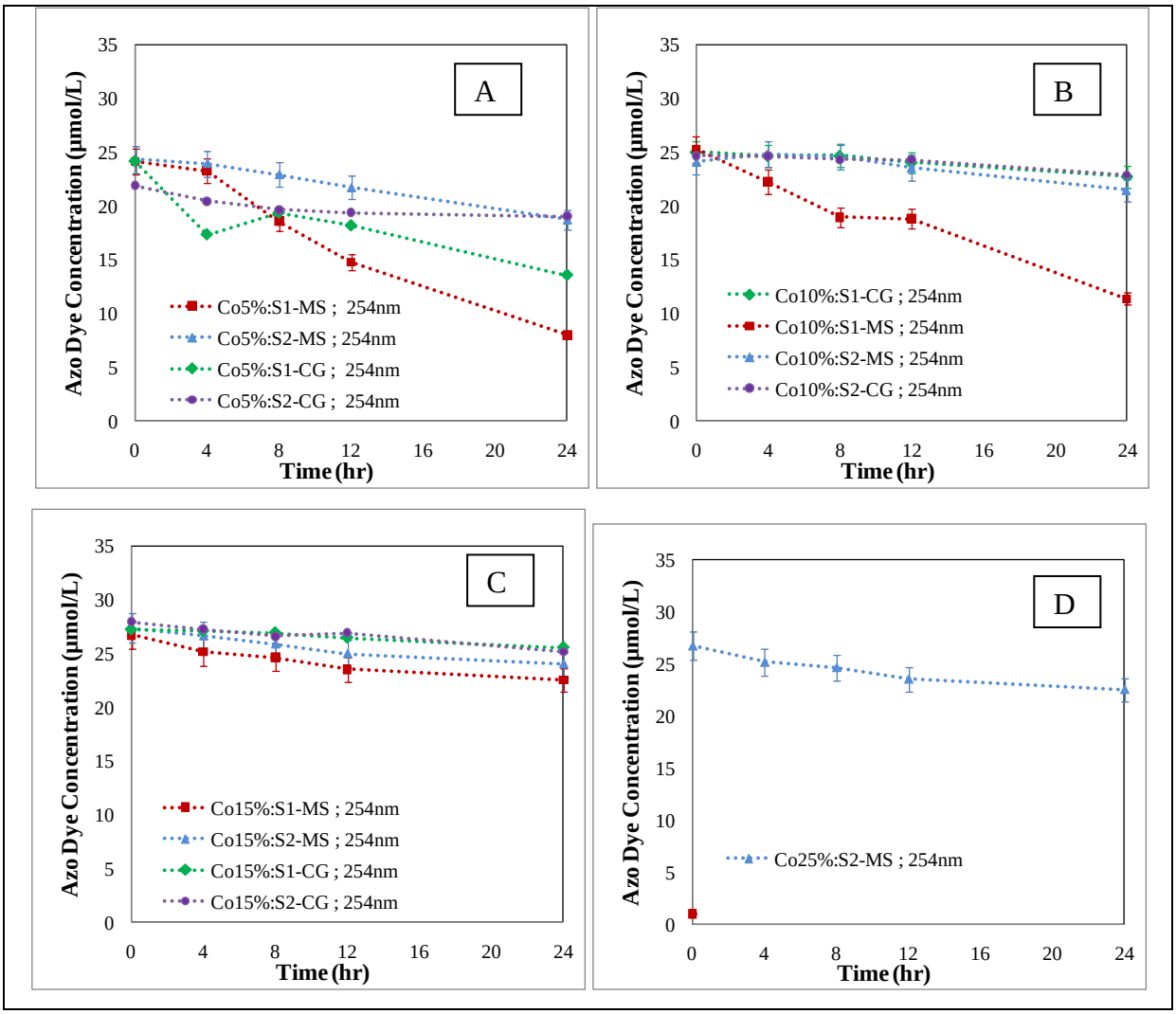

Figure 6.28: Overall comparison of photocatalytic degradation profiles of MB by using nanostructured Co:ZnO thin films under oxygen-limited conditions upon UV irradiation of 254nm. A: Co5%:ZnO thin films; B: Co10%:ZnO thin films; C: Co15%:ZnO thin films; D: Co25%:ZnO thin films.

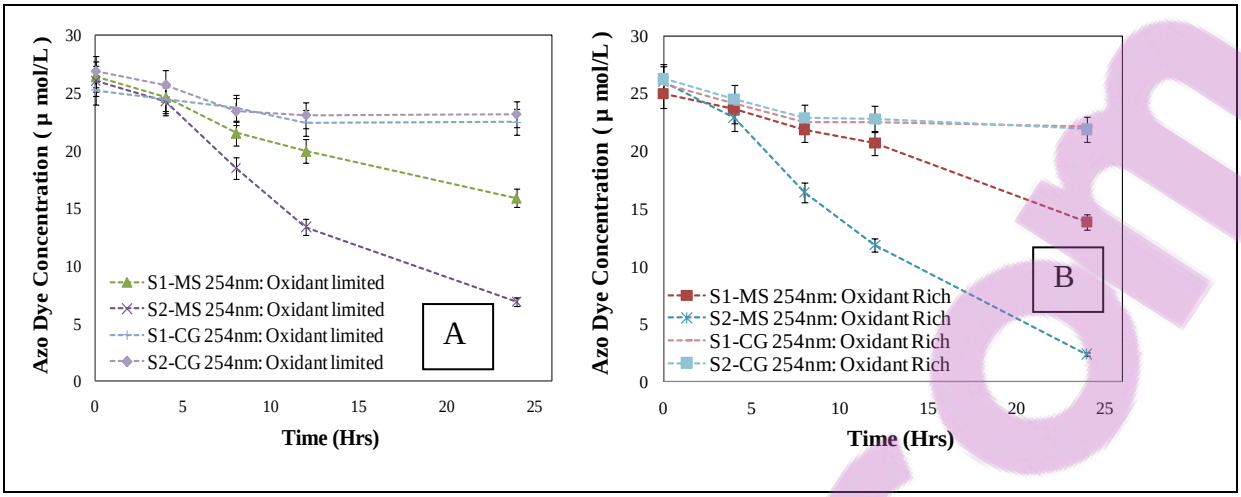

Figure 6.29: Overall comparison of photocatalytic degradation profiles of MB by using undoped nanostructured Co:ZnO thin films under oxygen-limited and rich conditions upon UV irradiation of 254nm. A: undoped ZnO thin films under oxygen-limited conditions; B: undoped ZnO thin films under oxygen-rich conditions.

Further comparison to undoped thin films: The undoped morphologies obtained from solution S1 (S1-MS and S1-CG) were more photocatalytically active than doped morphologies (Co:S1-MS and Co:S1-CG) based on k''_{app}; see Tables 4.5 and 6.3 respectively. This is most likely because of the greater extent of reaction by the Mars van Krevelen mechanism for the undoped films as well as the cobalt having an inhibitory/deactivating effect in the cobalt doped films. However, morphologies Co5%:S1-MS and Co10%:S1-MS had shown a slightly higher azo dye removal rate (based on extent and degradation rate) compared to undoped S1-MS. The rate of degradation of both MB and AB were higher for cobalt-doped morphology (Co:S1-MS) compared to undoped morphology S1-MS. This could likely because of the following:

- The Co5%:S1-MS thin film resembles the structure of the best undoped film - S2-MS, further confirming that this is the model type of structure for the attainment of high photocatalytic activity. This is further confirmed by the presence, in the XRD spectra, of [0,0,2] crystal peak in Co:S1-MS (see Fig. 6.19E). The same crystal peak [0,0,2] was also present in undoped S2-MS at a higher intensity than with undoped S1-MS.
- Co:S1-MS has a higher surface area compared to undoped S1-MS.

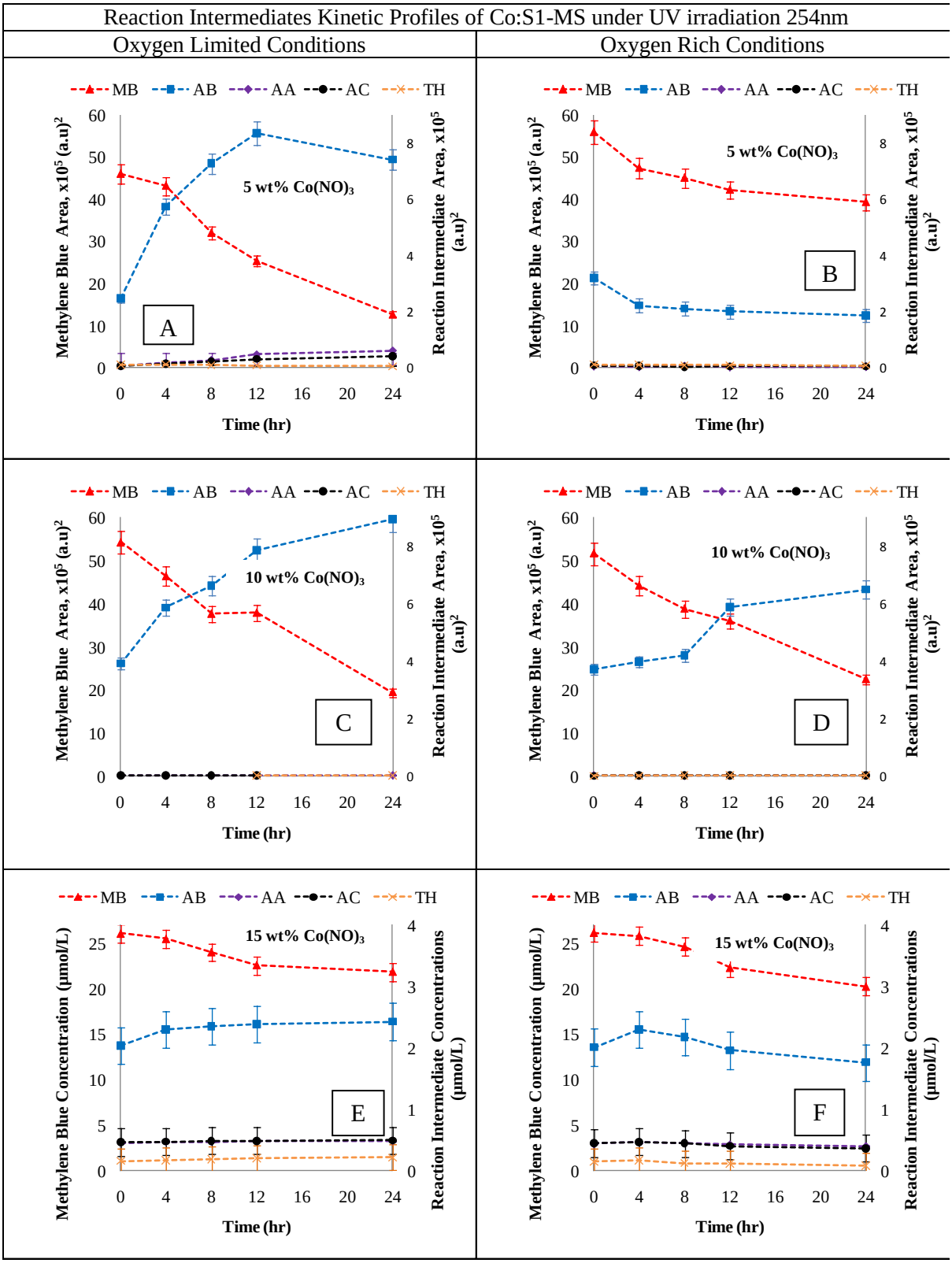

Figure 6.30: Reaction profile comparison of the reaction intermediates from methylene blue photocatalysed by three different Co:S1-MS thin films upon UV irradiation at 254nm under both oxygen-limited and oxygen-rich conditions. A: Co5%:S1-MS under O_2 limited conditions, B: Co5%:S1-MS under O_2 rich conditions, C: Co10%:S1-MS under O_2 limited conditions, D: Co10%:S1-MS under O_2 rich conditions, E: Co15%:S1-MS under O_2 limited conditions, F: Co15%:S1-MS under O_2 rich conditions.

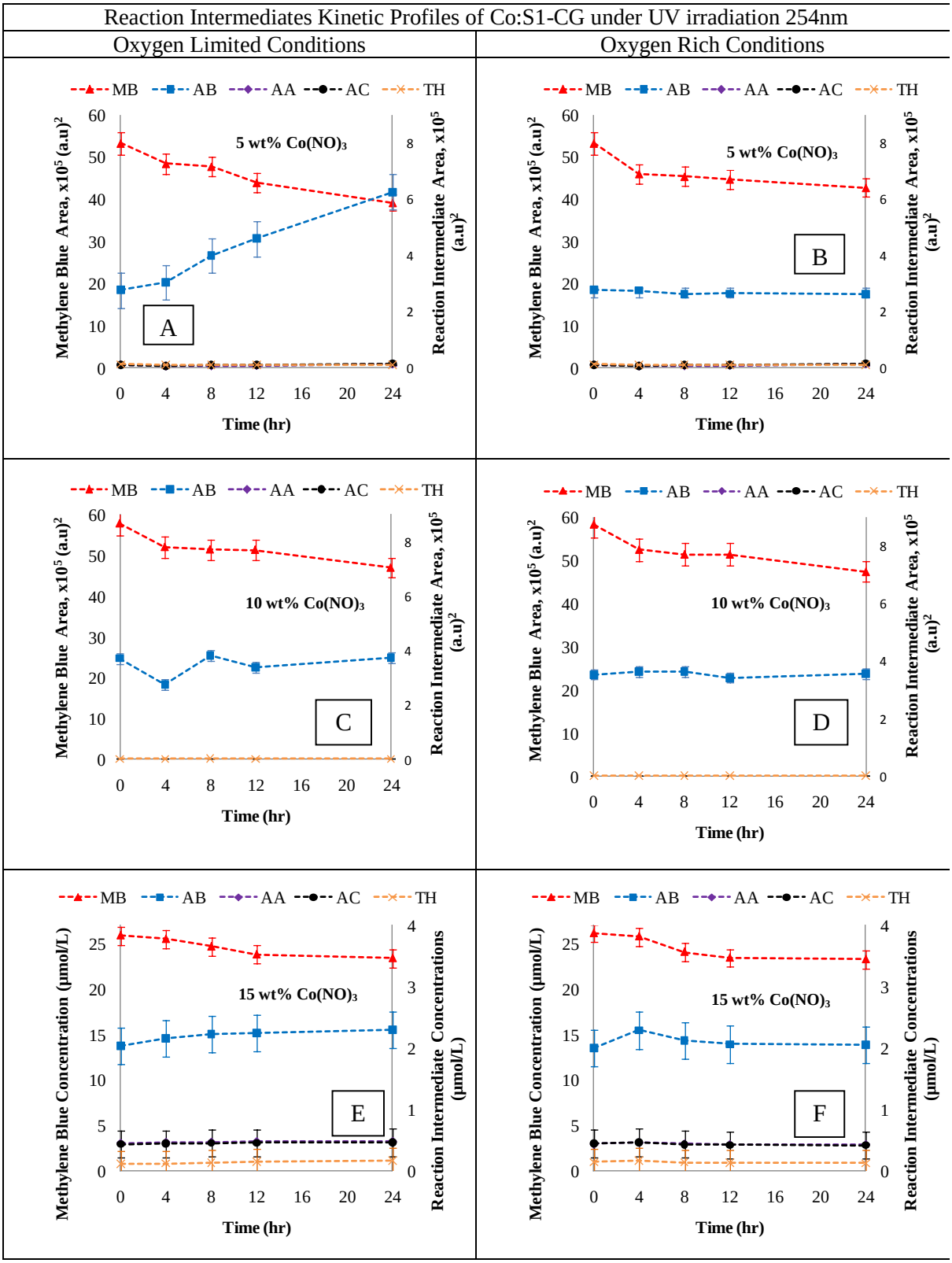

Figure 6.31: Reaction profile comparison of the reaction intermediates from methylene blue photocatalysed by three different Co:S1-CG thin films upon UV irradiation at 254nm under both oxygen-limited and oxygen-rich conditions. A: Co5%:S1-CG under O_2 limited conditions, B: Co5%:S1-CG under O_2 rich conditions, C: Co10%:S1-CG under O_2 limited conditions, D: Co10%:S1-CG under O_2 rich conditions, E: Co15%:S1-CG under O_2 limited conditions, F: Co15%:S1-CG under O_2 rich conditions.

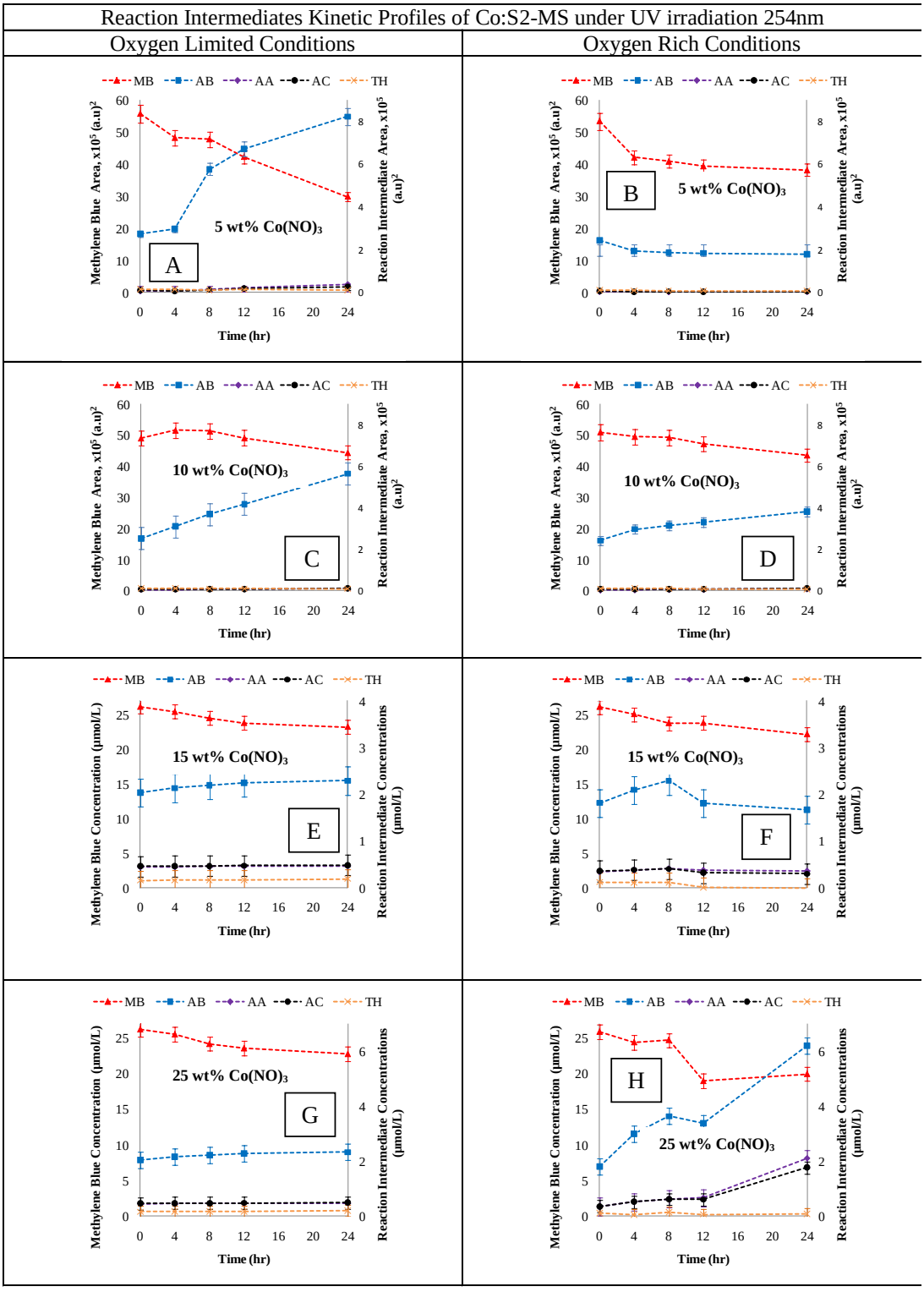

Figure 6.32: Reaction profile comparison of the reaction intermediates from methylene blue photocatalysed by four different Co:S2-MS thin films upon UV irradiation at 254nm under both oxygen-limited and oxygen-rich conditions. A: Co5%:S2-MS under O_2 limited conditions, B: Co5%:S2-MS under O_2 rich conditions, C: Co10%:S2-MS under O_2 limited conditions, D: Co10%:S2-MS under O_2 rich conditions, E: Co15%:S2-MS under O_2 limited conditions, F: Co15%:S2-MS under O_2 rich conditions, G: Co25%:S2-MS under O_2 limited conditions, H: Co25%:S2-MS under O_2 rich conditions.

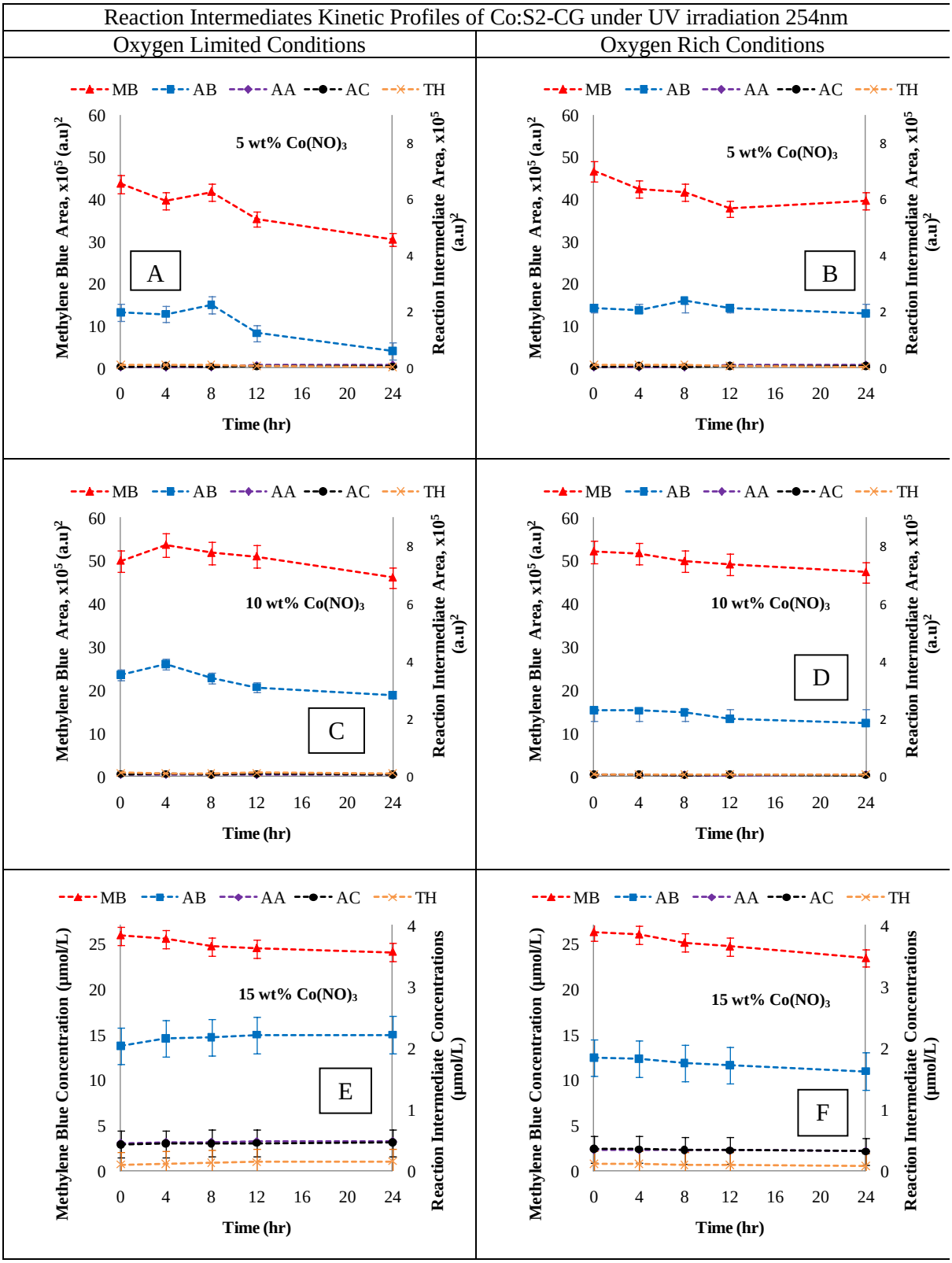

Figure 6.33: Reaction profile comparison of the reaction intermediates from methylene blue photocatalysed by three different Co:S2-CG thin films upon UV irradiation at 254nm under both oxygen-limited and oxygen-rich conditions. A: Co5%:S2-CG under O_2 limited conditions, B: Co5%:S2-CG under O_2 rich conditions, C: Co10%:S2-CG under O_2 limited conditions, D: Co10%:S2-CG under O_2 rich conditions, E: Co15%:S2-CG under O_2 limited conditions, F: Co15%:S2-CG under O_2 rich conditions.

The undoped morphologies obtained from solution S2 (S2-MS, S2-CG) have shown higher photocatalytic activity, reaction rates, formation and further degradation – if any – than Co5%:S2-MS and Co5%:S2-CG, based on both the apparent rate constant k''_{app} (see Tables 4.5 and 6.3) and an overall extent and degradation rate.

Interim summary: These results indicate that the higher the Co concentration, the lower the photocatalytic activity. This is related to the increase in thin film density and crystal size seen in the SEMs and the decreasing alignment of the films. The photocatalytic activity of two of the four doped films is lower than that of the undoped films. Cobalt therefore is a photocatalytic inhibitor under oxygen-limited conditions: it deactivates both conventional and Mars van Krevelen type photocatalytic oxidations of methylene blue.

6.4.2.2 Oxygen-rich conditions

Fig.6.34A-D shows a comparison of photocatalytic degradation profiles of the azo dyes (as measured by UV-Vis) by Co:ZnO thin films (Co:S1-MS, Co:S1-CG, Co:S2-MS and Co:S2-CG obtained at 5, 10, 15 and 25wt% of $Co(NO)_3.6H_2O$ respectively) under oxygen-rich conditions upon UV irradiation of 254nm.

Again a higher cobalt dopant concentration decreased the photocatalytic activity, as with the oxygen-limited reactions. Surprisingly, the added oxygen does not increase the extent of MB degradation, nor the rate of reaction for either MB or the intermediates, compared to oxygen-limited conditions. This is very different from the undoped films results (Chapters 4 and 5). The reaction profiles (Figs 6.30 – 6.33), however, show that there are some exceptions to this, with the Co:S2-MS having a more complicated relationship between the effect of cobalt concentration, methylene blue degradation, and reaction intermediate profiles (this will be described in more detail below). Most notably, thin films Co5%:S1-MS, Co5%:S1-CG and Co5%:S2-MS all have the same higher overall degradation in oxygen-limited conditions as all the other films, but in terms of the reaction intermediates they also have a flatter concentration profile for AB also, which may indicate that either it is not being formed to the extent it did in the oxygen-limited conditions or it is being degraded under oxygen-rich conditions. Looking at Figure 6.30 B for Co5%:S1-MS and Figure 6.32B for Co5%:S2-MS, it is seen that the AB concentration drops from its initial value, indicating that the latter is more likely, and perhaps indicates that some of the difference between the oxygen-limited and oxygen-rich AB concentration profiles is that the AB rate of degradation is equal to, or

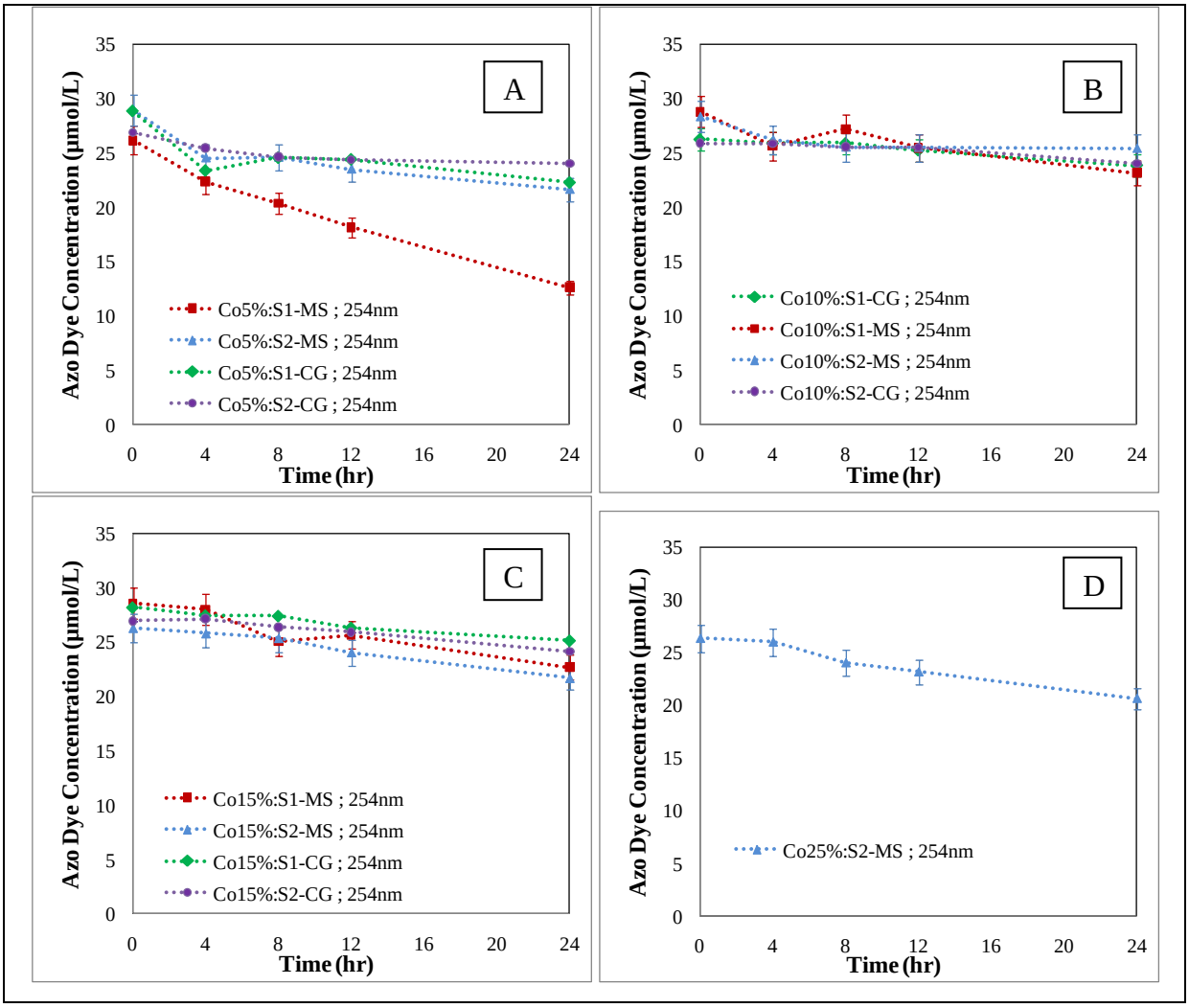

Figure 6.34: Over all comparison of photocatalytic degradation profiles of MB by using nanostructured Co:ZnO thin films under oxygen-rich conditions upon UV irradiation of 254nm. A: Co:ZnO thin films at 5wt%; B: Co:ZnO thin films at 10wt%; C: Co:ZnO thin films at 15wt%; D: Co:ZnO thin films at 25wt%.

greater than, its formation rate. The lower MB degradation in AB in the first place would also contribute to this difference. The same is probably true of the other intermediates; rate of formation is equal to or less than the rate of degradation, giving a zero concentration for these throughout the reaction in oxygen-rich conditions, whilst in oxygen-limited conditions they form and accumulate. This shows that for these films although the MB degradation rate and extent is lower, the intermediate degradation rate is higher, and these films therefore have a higher photocatalytic activity for the intermediates in the presence of oxygen. This would indicate that the conventional photocatalytic mechanism is favoured under oxygen-rich conditions with a small percentage of cobalt dopant in the films, and the lower MB degradation rate and the absence of the increased intermediate oxidation at the higher cobalt

dopant concentrations perhaps indicates that this conventional oxidation is inhibited by the added cobalt.

However, the photocatalytic activity (in terms of overall azo dye removal) of the films is lower under oxygen-rich conditions. Take, for example, the 5% cobalt doped thin films. The photocatalytic activity of thin films Co5%:S2-MS and Co5%:S2-CG was decreased by approximately 12% and 22% respectively, on a surface area basis, under oxygen-limited conditions (k''_{app}; see Table 6.4 and k''_{app}; see Table 6.3) and the photocatalytic activity of Co5%:S1-MS and Co5%:S1-CG under oxygen-rich conditions (k''_{app}; see Table 6.4 and Table 6.3) was decreased by 40% and 60% respectively. This could be because of the following two reasons:

- Reduction in the formation of the most commonly known hydroxyl radical because of an increased overall charge transfer rate (taking place in the valence band: reduction of Co^{+2} ion by the acceptance of free electrons helpful in increasing the oxidising species) rather than the photo-ionisation of cobalt (in the conduction band or below the conduction: oxidation of Co^{+2} ion into Co^{+3} ion with the release of electrons) as concluded by Kobayashi *et al.* [199] in their study.
- Prevention of, or reduced charge transfer between MB and the doped ZnO surface because of the preferential adsorption of oxygen on the doped zinc oxide nanostructure surface.

The same trends are seen in the reaction profile results (Fig. 6.30 – 6.33):

Co:S1-MS films: No significant formation of any of the identified reaction intermediates (Figs. 6.30 B and F) were noticed for photocatalytic reactions under oxygen-rich conditions for Co5%:S1-MS and Co15%:S1-MS, although thin film Co10%:S1-MS did catalyse/enable the formation of AB. This could be because of the presence of a slightly more open structure of Co10%: S1-MS (see Fig. 6.15C). This would indicate that at an optimum dopant concentration and the more open structure, either preferential adsorption of oxygen on cobalt-doped ZnO surface was low, or greater photo-ionisation of cobalt (compared to the charge transfer rate) was taking place for this morphology only. These results further confirm that photocatalytic activity and the extent of formation of reaction intermediates (albeit with no further degradation) were highest under oxygen-limited conditions.

Co:S2-MS films: Reaction profiles (see Figs. 6.32 B, D, F and H) show a more complicated relationship between the cobalt dopant concentration and the presence of oxygen than the other films. As already mentioned above, under oxygen-limited conditions the Co5%:S2-MS was more effective at degrading MB and generating significant amounts of reaction intermediates than under oxygen-rich conditions. However, these reactions and the rates (and thus the photocatalytic activity) decreased with increasing dopant concentration up to 15wt% of $Co(NO_3)_2$. However, at a higher dopant concentration, Co25%:S2-MS films catalysed/enabled increased the formation of reaction intermediates under oxygen-rich conditions (Fig. 6.32H) compared to under oxygen-limited conditions (Fig. 6.32G).

This could indicate that for thin film Co:S2-MS, up to a certain dopant concentration (which for this thin film is 15wt%), the formation of an active oxidising species is suppressed or atleast unavailable to either parent molecule MB and/or their attack on the lattice oxygen under oxygen-rich conditions. This may be the result of a decreased oxidation state of cobalt ion (from Co^{+2} to Co^{+1}) because of the excessive acceptance of UV-induced electrons present in the valence band of Co:ZnO thin film. This change may be the result of a change in surface morphology at higher dopant concentration (see Fig. 6.24) as well as the presence of oxygen, providing a greater chance of UV-induced electron acceptance by the lattice oxygen and/or bulk oxygen to participate in a reaction, and a greater tendency to replace the depleted lattice oxygen after taking part in a chemical reaction.

Furthermore, in comparison to Co:S1-MS, thin film Co:S2-MS is less effective in degrading MB to its reaction intermediates. This is most likely a result of its having less crystallite density and UV-exposed surface area, which can be readily seen in the SEMs (because of the increased crystal radius of Co:ZnO) of Co:S2-MS up to 15wt%, pH and the presence of PEI.

When comparing doped (Co:S2-MS) and undoped (S2-MS) thin films, the doped was worse in terms of both extent of MB degradation and the formation and further degradation of reaction intermediates into AB, AA, AC and TH under both oxygen-limited and rich conditions compared to the undoped films.

Co:S1-CG and Co:S2-CG films: As shown in the UV-Vis kinetic data, these films have the lowest reaction rates of all the doped films. The reaction profiles of Co:S1-CG and Co:S2-CG (see Figs. 6.31A-F and 6.33A-F) were similarly poor in comparison to the MS films, with the least formation of reaction intermediates under both oxygen-limited and rich conditions for different dopant concentrations. The exception to this rule was morphology Co5%:S1-CG

which produced a sizeable amount of the reaction intermediate AB formation under oxygen only. This may be a further indication of better formation of hydroxyl radical due to the excessive electrons either from UV-induced or from photo-ionisation of cobalt. No further degradation in reaction intermediates was noticed, in spite of the clear variation in surface morphologies (see Figs.6.16B-E and 6.18B-E). When compared to undoped S1-CG and S2-CG, there is a reduced extent of formation of reaction intermediates, with S2-CG being more effective at forming AB and AA from MB. Since the undoped S1-CG and S2-CG films are already not photocatalytically active, the lowered photocatalytic activity and decreased MB degradation, and formation of reaction intermediates, results in the cobalt dopant making them even less so.

6.4.2.3 Overall implications of Co doping on the photocatalytic reaction mechanism at 254nm

From the rate constants (Tables 6.3 and 6.4) and reaction profiles discussed, it can be concluded that at 254nm UV irradiation, the cobalt dopant is generally seen to decrease the photocatalytic activity of the thin films studied in Chapters 4 and 5. The exceptions are Co5%:S1-MS films under both oxygen-limited and oxygen-rich conditions and Co10%:S1-MS films under oxygen-limited conditions. For all films, however, the reaction profiles show that little degradation of azo dye into reaction intermediates (AB, AA, AC and TH) is photocatalysed, with less (if any) further degradation and mineralisation of these intermediates once formed. This indicates that these doped films are less active in the generation of the active species required for the propogation of an oxidative degradation of MB and its reaction intermediates, via the conventional photocatalytic reaction mechanism and/or the Mars van Krevelen type of lattice oxygen abstraction mechanism. Further discussion of the reasons surrounding this can be found in Section 6.5.

Table 6.3: Summary of the 1st order reaction rate constants on mass of the catalyst (k'_{app}), UV exposed catalyst surface area (k''_{app}) and volume of the catalysts (k'''_{app}) basis for the photodegradation of 10 mg L^{-1} methylene blue by using cobalt-doped ZnO thin films under oxygen-limited conditions upon UV irradiation of 254nm.

	k'_{app} ($m^3kg^{-1}s^{-1}$)				k''_{app} ($m^3m^{-2}s^{-1}$)				k'''_{app} ($m^3m^{-3}s^{-1}$)			
	25 wt%	*15wt%*	*10wt%*	*5wt%*	*25 wt%*	*15wt%*	*10wt%*	*5wt%*	*25 wt%*	*15wt %*	*10wt%*	*5wt%*
Co:S1-MS		0.05306	3.4829	5.2030		2.82×10^{-5}	3.70×10^{-4}	5.53×10^{-4}		301.15	19504.47	29137.04
Co:S1-CG		0.0844	0.4205	2.1028		1.17×10^{-4}	1.75×10^{-4}	8.77×10^{-4}		478.60	736.30	3681.54
Co:S2-MS	0.107	0.0854	7.1982	14.396	1.22×10^{-4}	9.71×10^{-5}	3.97×10^{-3}	7.95×10^{-3}	564.31	448.13	40309.99	80619.98
Co:S2-CG		0.0660	0.8173	1.3281		1.28×10^{-4}	3.13×10^{-4}	5.08×10^{-4}		374.77	4577.96	7439.199

Table 6.4: Summary of the Ist order reaction rate constants on mass of the catalyst (k'_{app}), UV exposed catalyst surface area (k''_{app}) and volume of the catalysts (k'''_{app}) basis for the photodegradation of 10 mg L^{-1} methylene blue by using cobalt-doped ZnO thin films under oxygen-rich conditions upon UV irradiation of 254nm.

	k'_{app} ($m^3kg^{-1}s^{-1}$)				k''_{app} ($m^3m^{-2}s^{-1}$)				k'''_{app} ($m^3m^{-3}s^{-1}$)			
	25 wt%	*15wt%*	*10wt%*	*5wt%*	*25 wt%*	*15wt%*	*10wt%*	*5wt%*	*25 wt%*	*15wt%*	*10wt%*	*5wt%*
Co:S1-MS		0.07524	0.8440	3.1624		4.00×10^{-5}	8.97×10^{-5}	3.3×10^{-4}		427.01	4726.54	17709.58
Co:S1-CG		0.1529	0.42056	0.8201		2.13×10^{-4}	1.75×10^{-4}	3.42×10^{-4}		865.16	736.30	1435.80
Co:S2-MS	0.1693	0.1313	4.5462	12.62	1.92×10^{-4}	1.49×10^{-4}	2.51×10^{-3}	6.97×10^{-3}	887.96	688.79	25458.94	70719.28
Co:S2-CG		0.0805	0.8173	1.0471		1.56×10^{-4}	3.13×10^{-4}	4.01×10^{-4}		457.03	4577.96	5865.52

Table 6.5: Summary of the 1st order reaction rate constants on mass of the catalyst (k'_{app}), UV exposed catalyst surface area (k''_{app}) and volume of the catalysts (k'''_{app}) basis for the photodegradation of 10 mg L^{-1} methylene blue by using cobalt doped ZnO thin films under both oxygen-limited and rich conditions upon UV irradiation of 340nm.

	k'_{app} ($m^3kg^{-1}s^{-1}$)				k''_{app} ($m^3m^{-2}s^{-1}$)				k'''_{app} ($m^3m^{-3}s^{-1}$)			
	Oxygen-limited		*Oxygen-rich*		*Oxygen-limited*		*Oxygen-rich*		*Oxygen-limited*		*Oxygen-rich*	
	25 wt%	*15 wt%*	*25 wt%*	*15 wt%*	*25 wt%*	*15 wt%*	*25 wt%*	*15 wt%*	*25 wt%*	*15 wt%*	*25 wt%*	*15 wt%*
Co:S1-MS		0.0364		0.0435		1.93×10^{-5}		2.32×10^{-5}		206.76		247.21
Co:S2-MS	0.110	0.0838	0.1677	0.1139	1.25×10^{-4}	9.53×10^{-5}	1.91×10^{-4}	1.30×10^{-4}	580.91	439.83	879.66	597.51

6.4.3 Photocatalytic Activity and Reaction Intermediate Kinetics under UV irradiation 340nm

In Chapter 5, it was shown that undoped ZnO thin films displayed different photocatalytic activities at different incident UV wavelengths (having almost the same light intensities, see Section 3.2.3.3) because of the different reaction mechanisms in oxygen-limited and rich conditions. Therefore, to investigate the impact of cobalt as dopant on the reaction mechanisms and photocatalytic activity, doped films were also photocatalytically tested at the higher UV irradiation of 340nm under both oxygen-limited and rich conditions.

The UV-Vis-derived azo dye degradation profile under oxygen-limited conditions is shown in Fig. 6.35A. The photocatalytic activity of Co15%:S1-MS was decreased by 32% upon UV irradiation of 340nm under oxygen-limited conditions compared to 254nm (compare to Fig. 6.28C, and see Table 6.4 and Table 6.5), whereas the photocatalytic activity of Co15%:S2-MS and Co:25%S2-MS were only slightly reduced (see Table 6.3 and Table 6.5) with almost no visible change in surface morphologies after reaction, as shown in Figs. 6.26 (D-E and G-H).

Under oxygen-limited conditions, there was no difference in overall degradation of azo dyes. Co15%:S1-MS underwent some structural degradation: an indication of Mars van Krevelen type reaction mechanism. There was no obvious surface degradation for other morphologies (such as Co15%:S2-MS and Co25%:S2-MS), perhaps an indication of conventional radical mechanism and the charge transfer mechanism. Degradation rates and derived apparent rate constants were generally lower than at 254nm. Under oxygen-rich conditions, Co25%:S2-MS surface morphology had shown an overall increased degradation rate, but for other films (Co15%:S2-MS and Co15%:S1-MS) it remained roughly the same.

Similar trends were also seen in the reaction intermediates profiles of photocatalytic degradation of MB, and the formation of different reaction intermediates, by using Co15%:S1-MS, Co15%:S2-MS and Co25%:S2-MS nanostructured thin films under both oxygen-limited and rich conditions upon UV irradiations of 254 and 340nm (see Figs. 6.30, 6.33, 6.36 and 6.37 respectively).

Co:S1-MS films: Morphology Co15%:S1-MS has shown similar trends in the formation of reaction intermediates along with photocatalytic degradation of MB upon UV irradiation of 340nm, see Figs. 6.36A and 6.37B: under oxygen-limited and rich conditions respectively, with slightly increased photocatalytic activity and degradation of MB under oxygen-rich

conditions. The formation and degradation of AB were also seen to be slightly increased (Figs. 6.36A and 6.37B) under oxygen-rich conditions, a further indication that under similar conditions, the reaction could have occurred via both the Mars van Krevelen and conventional radical mechanisms.

Co:S2-MS films: Morphology Co15%:S2-MS showed (Figs 6.37B and D) a greater extent of MB degradation, formation and degradation (AB, AA, AC and TH), under oxygen-rich compared to oxygen-limited conditions (Figs. 6.37A and C). Morphology Co25%:S2-MS showed the highest extent of MB degradation, and the highest extent of formation of reaction intermediates (AB, AA, AC and TH) only, as shown in Fig. 6.37D, under oxygen-rich conditions (Fig. 6.37C). A higher dopant concentration increased the level of formation and degradation of some of the reaction intermediates under oxygen-rich conditions (see Figs. 6.37 B and D). This again confirms the complicated relationship between Co dopant concentration and photocatalytic activity for this film, as previously discussed. The fact that this increase in photocatalytic activity occurs with an increase in intermediate formation (but not degradation) further indicates that the reaction mechanism may be more than just conventional photocatalytic oxidation, and that charge transfer may again be playing a role in forming AB with cobalt inhibiting the photocatalytic mechanisms.

Overall: Co15%:S1-MS, Co15%:S2-MS and Co25%:S2-MS were slightly more photocatalytically active (k''_{app} = 2.32 × 10^{-5}, 1.30 × 10^{-4}, 1.91 × 10^{-4} $m^3m^{-2}s^{-1}$ respectively; see Table 6.5) with better formation and degradation of some of the reaction intermediates upon UV irradiation of 340 nm under oxygen-rich compared to oxygen-limited conditions (k''_{app} = 1.93 × 10^{-5}, 9.53 × 10^{-5}, 1.25 × 10^{-4} $m^3m^{-2}s^{-1}$ respectively; see Table 6.5).

In comparison with UV irradiation at 254nm, there was a greater overall formation and degradation of different reaction intermediates, for Co15%:S1-MS Co15%:S2-MS and Co25%:S2-MS, compared with UV irradiation of 340nm under both oxygen-limited and oxygen-rich conditions.

The cobalt-doped nanostructured ZnO thin films (Co:ZnO), in general, have a lower photocatalytic activity than the undoped, although there is considerable increase in photocatalytic stability of Co:ZnO thin films under oxygen-limited conditions. The reasons for this are discussed in Section 6.5.

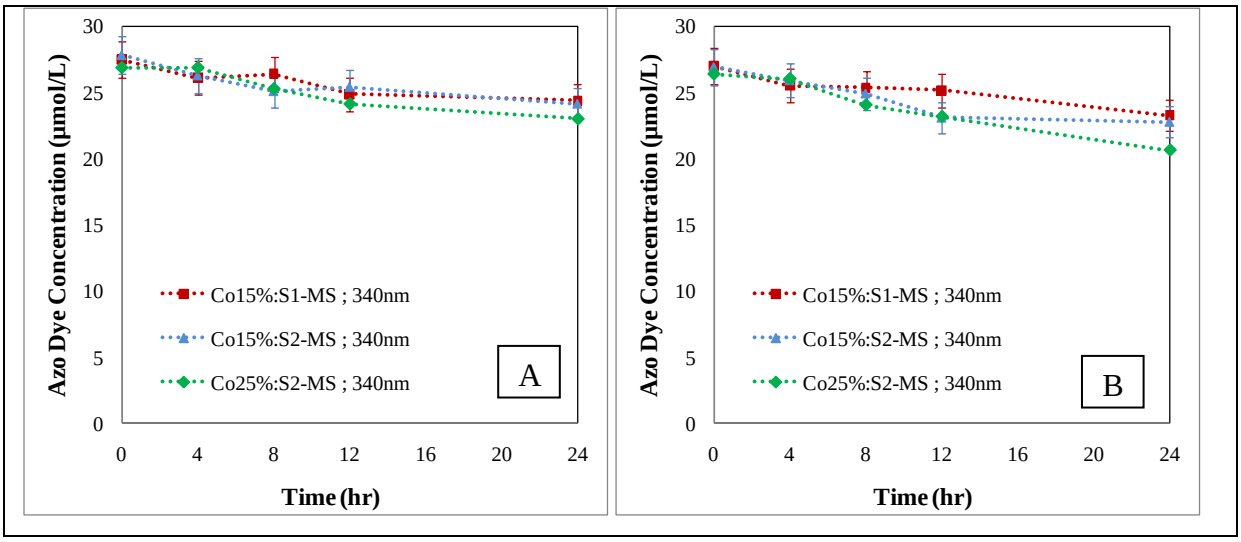

Figure 6.35: Overall comparison of photocatalytic degradation profiles of MB by using nanostructured Co:ZnO thin films under oxygen-limited and rich conditions upon UV irradiation of 340nm. A: Co:ZnO thin films (Co15%:S1-MS, Co15%:S2-MS and Co25%:S2-MS) under oxygen-limited conditions; B: Co:ZnO thin films (Co15%:S1-MS, Co15%:S2-MS and Co25%:S2-MS) under oxygen-rich conditions.

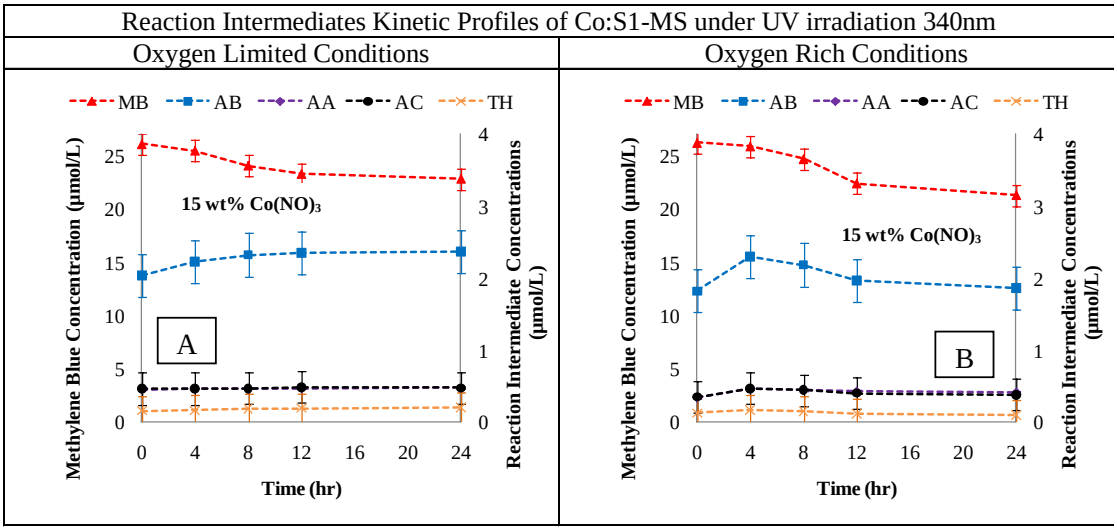

Figure 6.36: Reaction profile comparison of the reaction intermediates from methylene blue photocatalysed by Co:S1-MS thin films upon UV irradiation at 340nm under both oxygen-limited and oxygen-rich conditions. A: Co15%:S1-MS under O_2 limited conditions, B: Co15%:S1-MS under O_2 rich conditions.

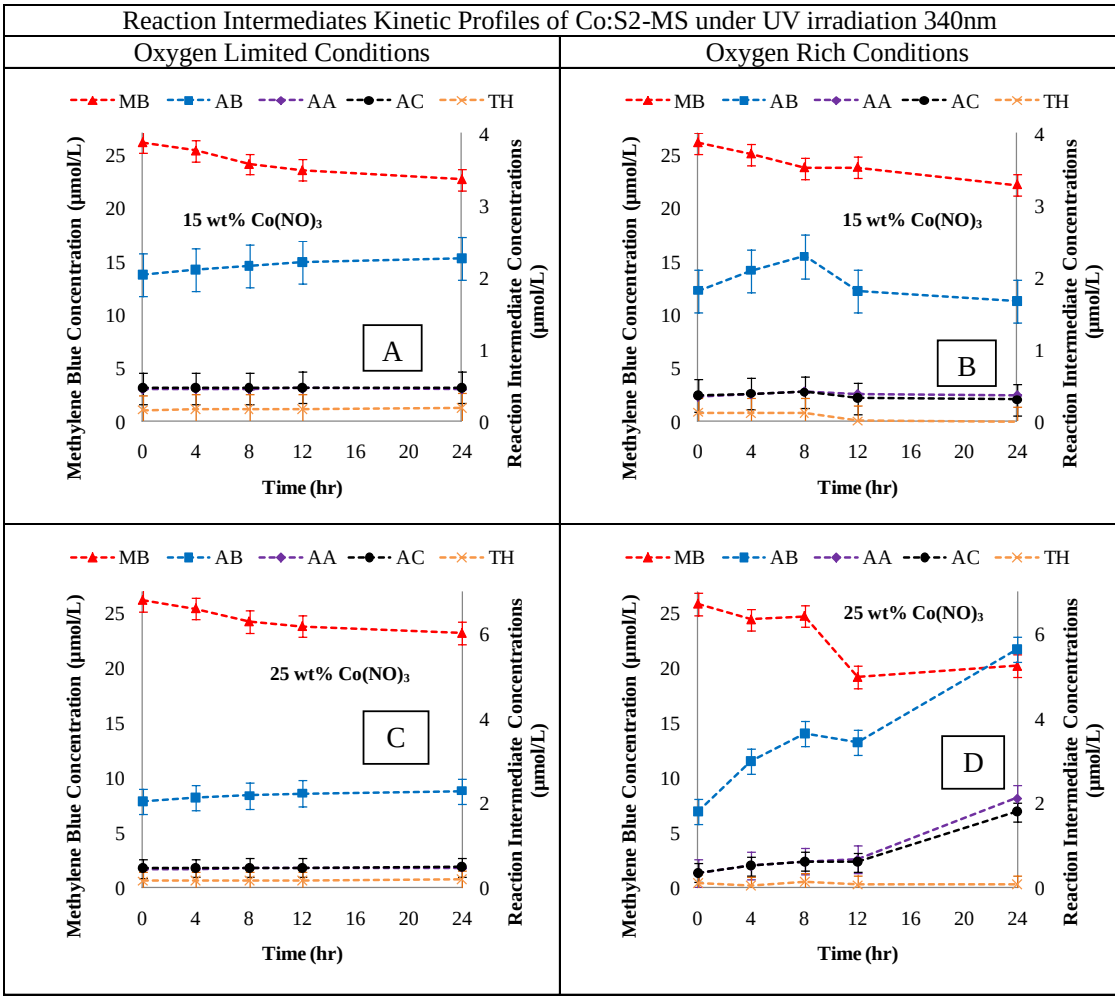

Figure 6.37: Reaction profile comparison of the reaction intermediates from methylene blue photocatalysed by two different Co:S2-MS thin films upon UV irradiation at 340nm under both oxygen-limited and oxygen-rich conditions. A: Co15%:S2-MS under O_2 limited conditions, B: Co15%:S2-MS under O_2 rich conditions, C: Co25%:S2-MS under O_2 limited conditions, D: Co25%:S2-MS under O_2 rich conditions.

6.5 Impact of Dopant on Reaction Mechanism(S)

The presence of dopant and its concentration have a significant impact on the surface morphology, crystallinity, and porosity of Co:ZnO nanostructured thin films. Doped surface morphology had a severe impact on the photocatalytic reaction mechanism, both in terms of dopant concentration and with or without the presence of oxygen. Either conventional or Mars van Krevelen types of photocatalytic reactions mechanism are believed to occur depending upon the dopant concentration and the limited or rich conditions of oxygen.

At lower dopant concentrations (i.e. 5 and 10wt% in solutions Co:S1 and Co:S2 from which the films were grown) the photocatalytic activity of the Co:ZnO nanostructured thin films is

higher under oxygen-limited than under oxygen-rich conditions with UV irradiation at both 254 and 340nm. Therefore the Mars van Krevelen type reaction mechanism is almost certainly the prime mechanism propagating the oxidation of MB under these conditions. This is substantiated by the fact that significant changes in the surface morphologies of these films were observed for these low dopant concentration films (see Figs. 6.22E-F,H-I; 6.23E-F,H-I; 6.24H-I,K-L and 6.25E-F, H-I). As with the undoped films (Chapters 4 and 5), the change in morphology after reaction is more striking for the films reacted under oxygen-limited than under oxygen-rich conditions: an indication of the reactivity of lattice oxygen in accepting the UV induced electron. In general, since photocatalytic activity decreases with higher cobalt concentration, so cobalt is an inhibitor of both Mars van Krevelen and conventional mechanisms also. The absence of the Mars van Krevelen mechanism in these doped nanostructured zinc oxide thin films is indicated by the minimal changes in surface morphology under both oxygen-limited or rich conditions. The Co dopant thus stabilises the lattice of these Co:ZnO thin films. For Co:S2-MS, an exception to this was observed, where under UV irradiation at both 254 and 340nm wavelengths, there is a higher photocatalytic effectiveness under oxygen-rich conditions, giving a greater MB degradation, with a higher extent of formation, and further degradation of the azo dye reaction intermediates. This may indicate that in these films the conventional radical photocatalytic reaction mechanism, with a charge transfer mechanism, is able to occur. This may be caused by a higher rate of photo-ionisation (oxidation of Co^{2+} ions into Co^{3+} with a release of an electron taking place below or within the conduction band) at these high dopant concentrations (15 and 25 wt%) compared to charge separation (taking place in the valence band of Co:ZnO) [199] and because of the oxidation states of cobalt (CoO, Co_3O_4 and Co_2O_3) as suggested by Ling Wei *et al.* [168].

When compared to undoped films under the same reaction conditions (Chapters 4 and 5), it can be seen that the Co dopant increased the stability of the films during photocatalytic reactions (i.e. the lattice dissolved less). This would indicate that the Mars van Krevelen mechanism is less prominent during the aqueous oxidative degradation of MB, with the Co stabilising the lattice, providing an activation barrier for this mechanism. From the reaction results, it can be seen that this increased stability comes with a price: the photocatalytic activity and concomitant degradation of MB and its azo dye reaction intermediates is lower for the cobalt-doped films compared to the undoped films. This may in part be because the Mars van Krevelen mechanism is inhibited/deactivated, but also indicates that the Co dopant

inhibits photocatalytic activity. Many of the reaction profiles show that during reaction, it is only the MB degrades that result in AB formation only (the other azo dye reaction intermediates do not form). This could be because of the rapid formation and degradation of the other intermediates so that their concentrations are not measured; however, it may also indicate that only AB formation is occurring: i.e., normal complete oxidation through the azo dye intermediates, as proposed in Chapter 5, is not occurring. Instead, these Co:ZnO films may be energetically favouring a charge transfer reaction to occur, one that only initiates the MB to AB reaction. This could be attributed to the induction of deep energy levels between the valence and the conduction band due to cobalt incorporation within the ZnO lattice. Such energy levels are able to act as efficient recombination centres ultimately leading to the charge transfer of MB into AB only. Furthermore, the most probable reasons for the decrease in photocatalytic activity of the Co:ZnO thin films is their lack of efficiency in absorbing the photo-induced electrons [269], the behaviour of dopant ion [193, 199, 269], an optimum amount of dopant ion (it is crucial to have at least the same level of photocatalytic activity as the undoped nanostructure [166, 199, 269, 270]) and the absorptive properties of the model compound in the UV range [95]. Furthermore, the reduced photocatalytic activity under oxygen-rich conditions could also be associated with the various oxidation states of cobalt that might be present within the cobalt Co:ZnO thin films [168], as well as the less UV-exposed surface area and crystalline variation as compared with undoped nanostructure ZnO thin films.

It is concluded that dopant concentration, surface morphology, porosity, crystallinity and the lack or presence of oxygen in the reaction vessel are the key parameters dictating the photocatalytic reaction mechanism for Co:ZnO thin films. An optimum value of dopant was found to have a direct relationship with either conventional or Mars van Krevelen type reaction mechanisms but is independent of the UV irradiation wavelengths tested. The reaction mechanism for undoped surface morphology was found to be dependent on undoped surface morphology, crystallinity, porosity and type of UV irradiation wavelength.

6.6 Summary

Hydrothermal solution deposition can be used to prepare cobalt-doped surface morphologies. Dopant concentration and pH of the solutions play a crucial role in shaping the morphology of the thin films in terms of crystal/crystallite size, film thickness, size (both in length and diameter) and concomitant packing density. Dopant nature (cationic or anionic) and its source

have severe effects on crystallite and compactness (in terms of film thickness) of the doped surface morphologies. N and Co dopant concentration is inversely proportional to the packing density of the crystallites within the doped nanostructured zinc oxide thin films. The Co dopant, however, increases the photo-stability of the corresponding undoped films under oxygen-limited conditions, the photo-stability increasing with increasing Co dopant concentration. This increased stability of Co:ZnO nanostructure thin film comes with a price: the photocatalytic activity and concomitant degradation of MB and its azo dye reaction intermediates is lower than for undoped ZnO nanostructure thin film. The Co dopant has a combined effect on the photocatalytic activity. Undoped morphologies S2-MS and S2-CG were more photocatalytically active than their corresponding doped morphologies (Co5%:S2-MS, and Co5%:S2-CG). The exceptions were undoped S1-MS and S1-CG, which had a lower overall degradation rate and extent than doped Co5%:S1-MS and Co5%:S1-CG under similar reaction conditions**.**

At lower dopant concentrations (i.e. 10wt% and below), under oxygen-limited conditions upon UV irradiation 254nm and 340nm, indications are that the Mars van Krevelen type reaction mechanism is the mechanism propagating the oxidation of MB, this based on observable changes in the film's surface morphologies at lower dopant concentration. At higher dopant concentrations (i.e. 15wt% and above), under oxygen-rich conditions upon UV irradiation at 254nm and 340nm, the oxidation occurs in the absence of the Mars van Krevelen type mechanism. For Co:S2-MS, the conventional photocatalytic reaction mechanism could be reactivated in films made with S2 with 15% Co and above. This could result from the higher rate of photo-ionisation as compared to charge separation.

In contrast to the undoped films (Chapter 5), while UV irradiation wavelength (or energy) decreased photocatalytic activity, no effect on the reaction mechanism was discernable from the results. The photocatalytic activity of the doped nanostructured ZnO thin films under oxygen-rich conditions was lower than under oxygen-limited. This could be because of reduction in the formation of oxidising species such as hydroxyl radicals due to: 1- Prevented or reduced charge transfer between MB and doped ZnO surface because of the preferential adsorption of oxygen on the doped zinc oxide nanostructure surface. 2- Most likely, the increased overall charge transfer rate (taking place in valence band: reduction of Co^{+2} ion by the acceptance of free electrons helpful in increasing the oxidising species) rather than the photo-ionisation of cobalt (in the conduction band or below the conduction: oxidation of Co^{+2} ion into Co^{+3} ion with the release of electron) concluded by Kobayashi *et al.* [199]. The

incorporation of a cobalt ion into the ZnO lattice or interstices lowers the photocatalytic activity of the Co:ZnO thin films. Dopant concentration, surface morphology, porosity, crystallinity and the lack or presence of oxygen in the reaction vessel are the key influencing parameters in the overall photocatalytic reaction mechanism for Co:ZnO thin films, where an inverse relationship exists between photocatalytic activity and the Co dopant concentration.

7 Conclusions and Future Work

7.1 Conclusions

7.1.1 Undoped Nanostructured ZnO Thin Films, Photocatalytic Activity and Reaction Mechanism

Several different types of undoped nanostructured ZnO morphologies were obtained by using a hydrothermal solution deposition technique. A clear relationship between surface morphology (and the related thin film preparation method) and photocatalytic activity, was observed for undoped ZnO thin film-supported catalysts: the most aligned structure, undoped S2-MS, had the highest photocatalytic activity, whilst the least aligned structure, undoped S2-CG, had the lowest, both in terms of model compound degradation, formation, and further degradation of identified reaction intermediates. The degradation rates of undoped ZnO thin films were comparable to those of commercially available ZnO powder on a surface area and/or mass basis. Undoped nanostructured thin films showed significant physical degradation under oxygen-limited reaction conditions. A rich supply of oxygen decreases structural erosion during the photoreaction with methylene blue. This suggests that the photocatalysed oxidation by these solution-deposited ZnO thin films occurs, at least partially, through a Mars van Krevelen type mechanism. This would mean that oxygen from the catalyst lattice is removed and used in the oxidation reaction. The physical degradation of the catalyst is therefore diminished in the presence of oxygen, since the lattice oxygens (and therefore the catalyst structure) can be regenerated. An inverse relationship was found between MB concentration and photocatalytic activity. Undoped nanostructured ZnO films obtained on an MS template from solutions S1 and S2 (undoped S1-MS and S2-MS) are effective as photocatalysts for the liquid-phase photo-oxidation of methylene blue in both oxygen-limited and oxygen-rich conditions.

Results also indicated that there is a competition between two different photocatalytic mechanisms: conventional redox-formed radical and lattice oxygen-driven oxidation. The dominant reaction mechanism depends on the thin film morphology, crystallinity, availability of oxidant and the wavelength of the incident UV. Surface-photocatalysed radical formation degradation is predominant for more highly aligned morphologies (such as undoped S1-MS and undoped S2-MS) with plentiful oxygen and UV irradiation at 340nm. Mars van Krevelen type lattice oxygen photo-degradation is predominant for less aligned and more amorphous

surface morphologies (such as S1-CG and S2-CG) with UV irradiation at 254nm; because the high energy associated with 254nm UV irradiation allows the activation energy barrier to be overcome for lattice oxygen abstraction, and the higher number of lattice defects lowers the activation energy required for this.

An extension to the methylene blue photocatalytic reaction mechanism has also been proposed. Four azo dye reaction intermediates were identified: AA, AB, AC and TH, corroborating previous studies. However, a new reaction mechanism, when the Mars van Krevelen type reaction occurs, is proposed: initial bond cleavage of CH_3-group on methylene blue by lattice oxygen, followed by a possible surface-based reaction mechanism i.e., oxidation via α-carbon, generates a highly unstable methylene blue radical ($MB^{\bullet}$), which on further re-arrangement releases a methylene ($-CH_2-$) group to form the first reaction intermediate AB, which upon secondary oxidation gives rise to AA and further intermediates, until eventual mineralisation. The results provide an account of the individual and combined effects of UV wavelength, thin film nanostructure and oxidant availability on both the solution and solid phase photocatalytic reaction mechanisms and reaction rates: an important step towards understanding thin film catalytic processes and proper photocatalytic reactor design.

Overall, the photocatalytic activity, and the liquid and solid phase photocatalytic reaction mechanisms in the photocatalytic oxidation of MB by undoped nanostructured ZnO thin films, are dependent on surface morphologies, crystallinity, UV exposed surface area, concentration of MB, supply of oxygen, and UV type irradiation wavelength.

7.1.2 Impact of Dopant on Nanostructured ZnO Thin Films, Photocatalytic Activity and Reaction Mechanism

Dopant nature (cationic or anionic) and its source have severe effects on crystallites and the compactness (in terms of film thickness) of the doped surface morphologies (N:ZnO, Co:ZnO). N and Co dopant concentration were found to be inversely proportional to the packing density of the crystallites within the doped nanostructured zinc oxide thin films. Cationic doped nanostructured ZnO thin films (Co:ZnO), obtained by using hydrothermal solution deposition, had a better match to the thin film characteristics that were understood to give a high photocatalytic activity in the undoped films, compared to the N:ZnO thin films in terms of crystal/crystallite size, film thickness, size (both in length and diameter) and concomitant packing density, depending upon pH and cobalt dopant concentration. Thus only

Co:ZnO thin films were photocatalytically tested under the same reaction conditions as for undoped ZnO thin films.

Reaction results showed that the Co dopant increased the photo-stability of the corresponding undoped films under oxygen-limited conditions; the photo-stability increased with increasing Co dopant concentration. The increased stability of Co:ZnO nanostructured thin film comes with a price, however: the photocatalytic activity and simultaneous degradation of MB and its azo dye reaction intermediates, was in general lower compared to that of the undoped ZnO nanostructured thin films. There were exceptions to this and the Co dopant has a mixed effect on the photocatalytic activity for the different types of films. For example, Co%:S2-MS was in general more photocatalytically active (on a UV-exposed surface area basis) than the Co5%:S1-MS, Co5%:S1-CG and Co5%:S2-CG thin films under oxygen-limited conditions upon UV irradiation at 254nm and 340nm. However, in general the Co5%:S1-MS film had the highest degradation extent and rate of MB and its reaction intermediates (on a volumetric rate and degradation basis). Thus undoped morphologies S2-MS and S2-CG were generally more photocatalytically active than their corresponding doped morphologies (Co5%:S2-MS, Co5%:S1-CG and Co5%:S2-CG). Undoped S1-MS and S1-CG had a lower photocatalytic activity than doped Co5%:S1-MS and Co5%:S1-CG, respectively, under similar reaction conditions. The photocatalytic activities of Co:ZnO thin films under oxygen-rich conditions were lower than under oxygen-limited.

Dopant concentration appeared to have an effect on the photocatalytic reaction mechanism also. At higher dopant concentrations (15 and 25wt% Co), under oxygen-rich conditions upon UV irradiation of 254nm and 340nm, the oxidation occurs most likely via the conventional photocatalytic reaction mechanism and/or via charge transfer of the MB into AB with the absence of the Mars van Krevelen type mechanism. This could be due to the higher rate of photo-ionisation as compared to charge separation. At lower dopant concentrations (5 and 10wt% Co), under oxygen-limited conditions upon UV irradiation of 254nm and 340nm, the Mars van Krevelen type reaction mechanism is most probably the main mechanism propagating the oxidation of MB. This was indicated by the significant changes in surface morphologies at the lower dopant concentrations. UV irradiation wavelength (or energy) appeared to have a less significant effect on the photocatalytic activity or reaction mechanism compared to that of the undoped films.

Incorporation of a cobalt ion into the ZnO lattice or interstices lowers the photocatalytic activity of the Co:ZnO thin films. Dopant concentration, surface morphology, porosity, crystallinity and the lack or presence of oxygen in the reaction vessel, are the key influencing parameters in the overall photocatalytic reaction mechanism for Co:ZnO thin films, where an inverse relationship exists between photocatalytic activity and the Co dopant concentration.

7.2 Implications for Industrial Applications

The preceding results and discussion point to a solution to a major problem in the industrial application of these nanostructured thin films in photocatalytic reactions and reactors: the photo-stability of the nanostructured ZnO thin films is crucial in photocatalytic reactor economics. As established in Chapter 2, ZnO is well known to be unstable and to dissolve during photocatalytic reactions. This work has shown that this is in part likely caused by the presence of a Mars van Krevelen type mechanism, where photo-dissolution of the undoped, and partly doped nanostructured ZnO thin films, caused by an ineffective regeneration of lattice oxygens from the ZnO crystal under oxygen-limited conditions. These dissolved Zn ions in the reaction fluid could also hinder the mass transfer of the reacting species at the solid-liquid reaction interface, as well as reduce the overall photocatalytic activity of the photocatalyst. This could potentially require a post-catalyst separation step which ultimately can increase the process economics. Furthermore, the possible accumulation of the leached Zn^{+2} ion may reduce the availability of the superoxide radicals that have more inclination towards the Zn^{+2} rather than participating in the important oxidation step necessary to degrade the toxic and harmful compounds and concomitant reaction intermediates to mineralise.

This work has shown that this physical degradation of the catalyst is diminished in the presence of oxygen, since the lattice oxygens (and therefore the catalyst structure) can be regenerated, minimising or preventing the problem.

7.3 Future Work

To increase the effectiveness of nanostructured ZnO thin films, involving reaction mechanism(s) in the solid-liquid photocatalytic reaction(s), and to further expand the practical usability of these supported photocatalysts, future work could possibly focus on:

1. Increasing both the durability and activity of the S2-MS nano-rod thin films and exploring the stable operating 'envelope' around loss of ZnO through the Mars van Krevelen type mechanism. This may finally provide a pathway enabling the application of ZnO photocatalysts by industry and allowing the previously reported practical and economic advantages of the former over titanium oxide to be realised.
2. Deposition of metal oxides such ZnO, WO_3, etc, on the outer surface of UV lamps for the possible enhancement of the formation of UV-induced electron-hole pairs to trigger the photocatalytic reaction at the solid-liquid interface. This could also reduce the diffusional mass transfer of the model compound from the bulk of the reaction fluid to the surface of the catalyst.
3. In situ photocatalytic kinetics studies that could shed light on the possible un-identified reaction species that are difficult to discern otherwise due either to their low concentration, or their short life. This might be helpful in determining if any other potential toxic reaction intermediates or species are formed that might lead to photo-corrosion of the photocatalyst.
4. Study of the impact of different dopant(s) such as Al, Mg, and K on surface morphologies, photocatalytic activity and reaction mechanisms that could reveal/expand the involved photo-chemistry; new reaction mechanisms that could possibly dominate overall photocatalytic reaction characteristics.
5. Low cost preparation techniques to have doped nanostructured ZnO thin films with high surface to mass ratio, crystal/crystallite size, film thickness, size (both in length and diameter) and concomitant packing density: all are helpful in increasing the UV-exposed surface area.

Appendix A: Control Experiments

(A) Methylene Blue solution in dark

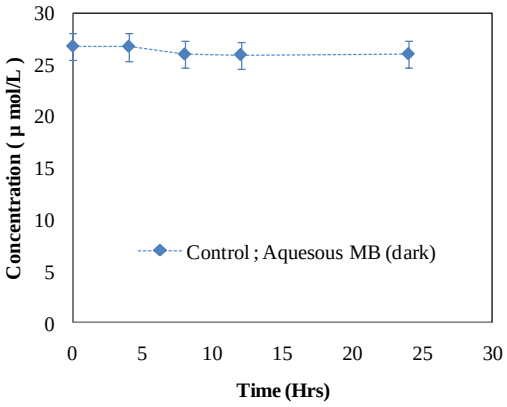

(B) Methylene Blue solution irradiated with UV (photolysis)

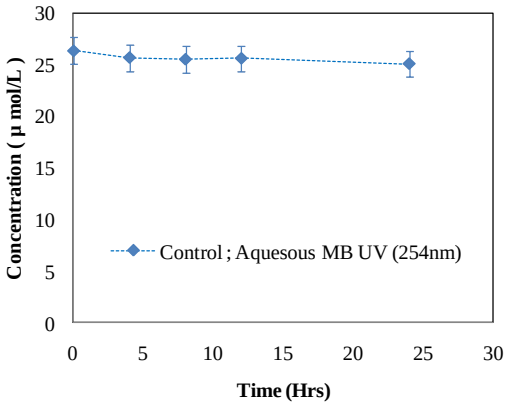

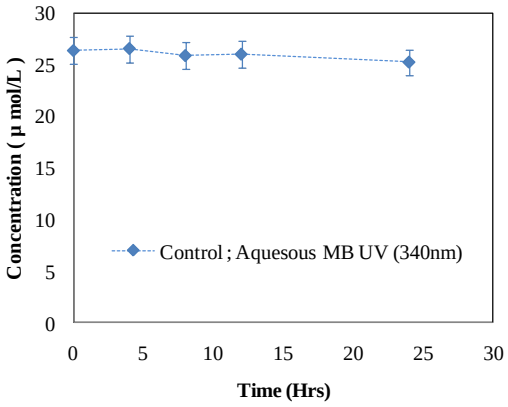

(C)ZnO thin film in deionised water in the dark

Nanostructured ZnO thin films obtained from solution S1	**Nanostructured ZnO thin films obtained from solution S2**	**Nanostructured ZnO thin films obtained from solution S3**
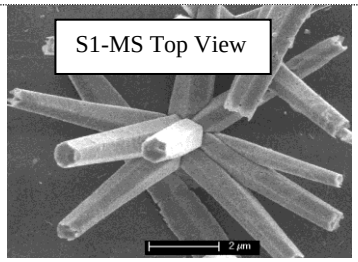	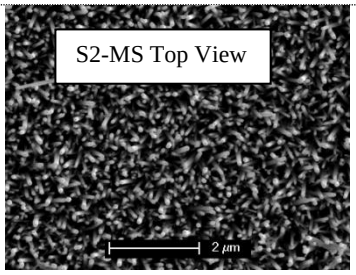	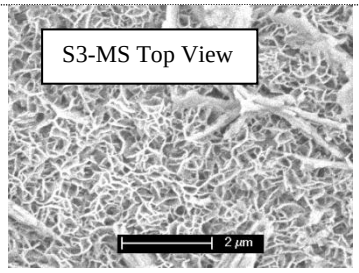
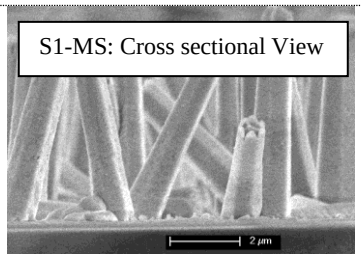	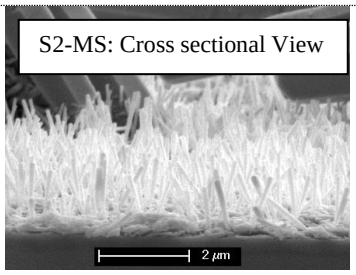	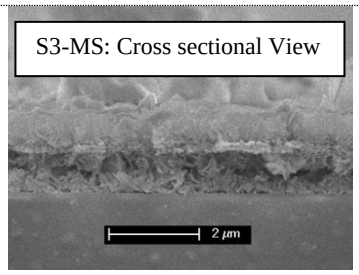
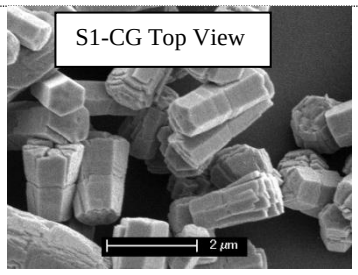	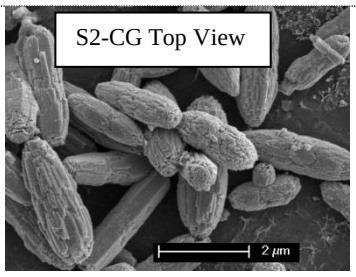	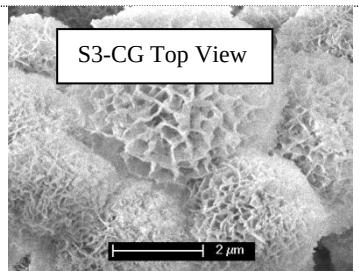
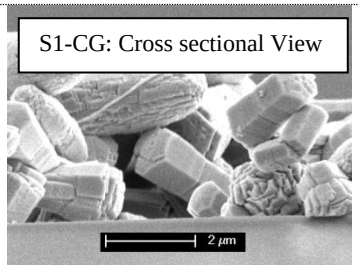	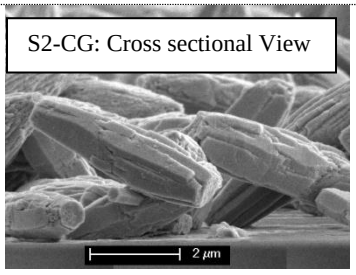	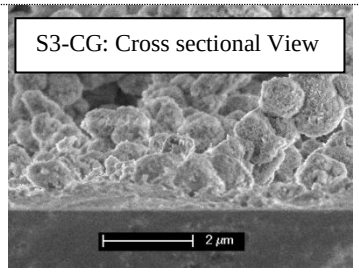

(D1) ZnO thin film without water irradiated by UV (254nm)

Nanostructured ZnO thin films obtained from solution S1	**Nanostructured ZnO thin films obtained from solution S2**	**Nanostructured ZnO thin films obtained from solution S3**
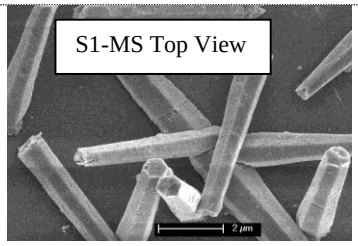	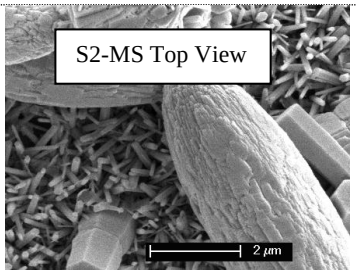	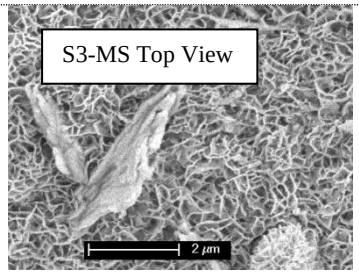
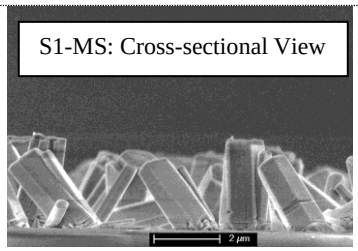	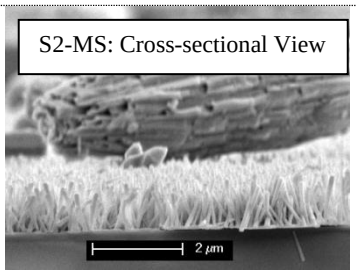	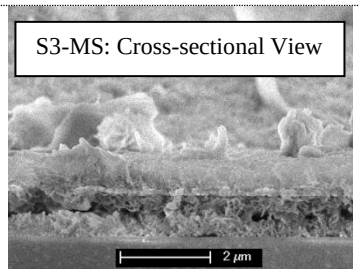
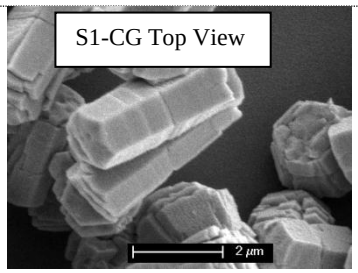	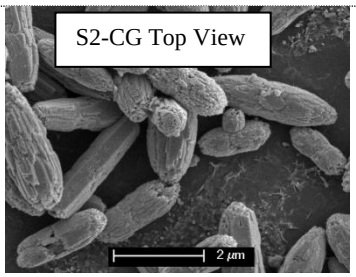	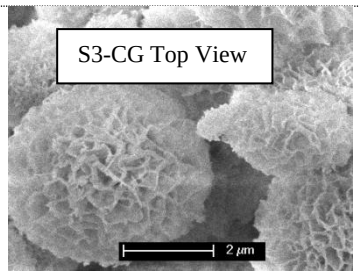
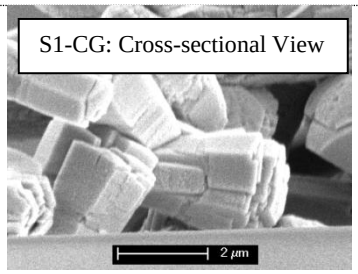	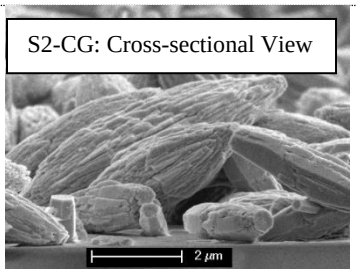	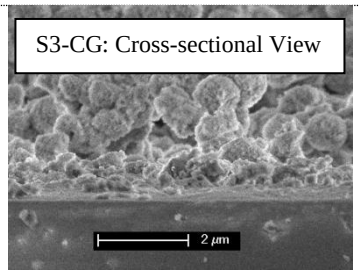

(D2) ZnO thin film without water irradiated by UV (340 nm)

Nanostructured ZnO thin films obtained from solution S1	**Nanostructured ZnO thin films obtained from solution S2**	**Nanostructured ZnO thin films obtained from solution S3**
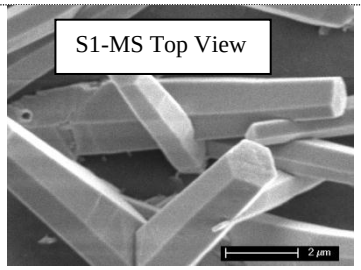	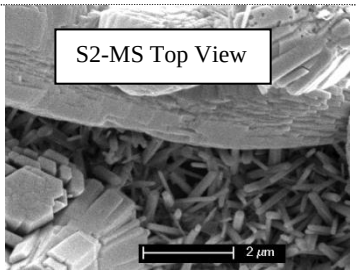	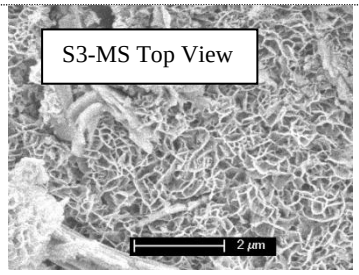
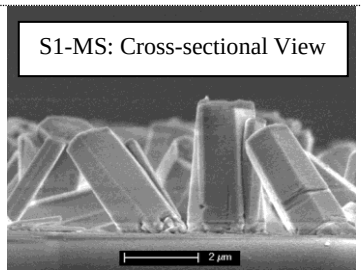	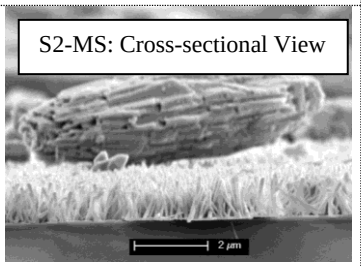	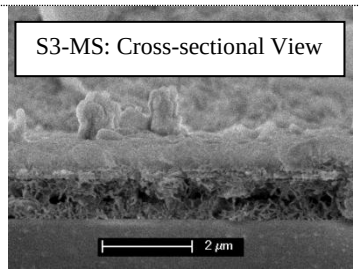
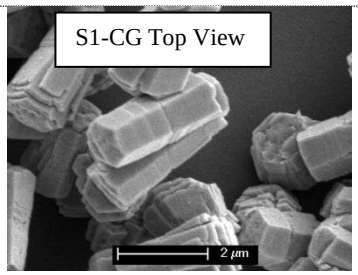	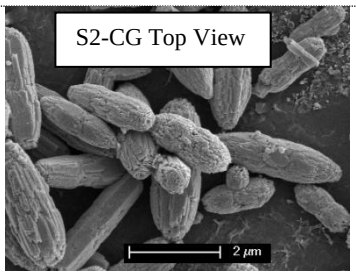	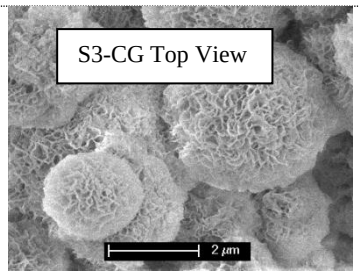
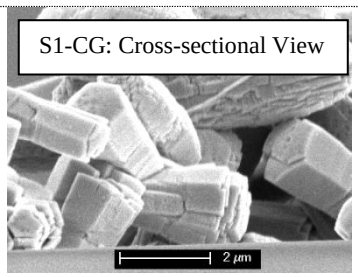	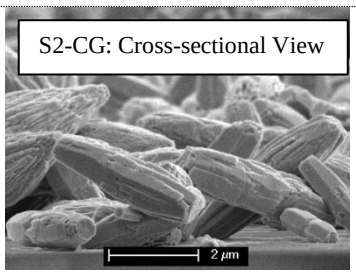	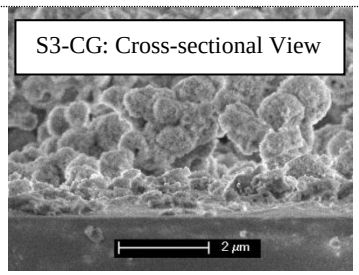

(E1) ZnO thin films in water irradiated with UV (254nm)

Nanostructured ZnO thin films obtained from solution S1	**Nanostructured ZnO thin films obtained from solution S2**	**Nanostructured ZnO thin films obtained from solution S3**
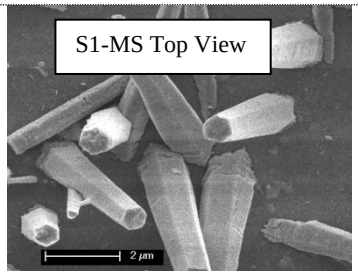	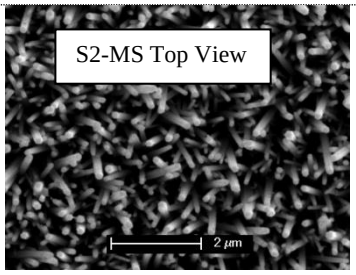	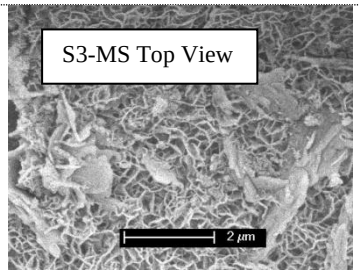
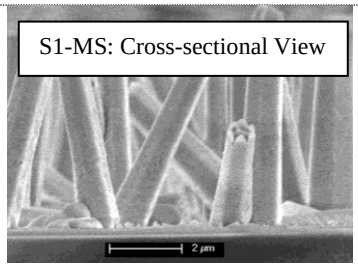	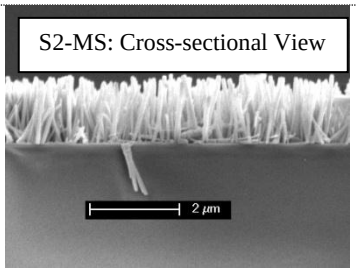	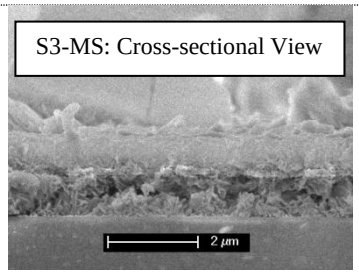
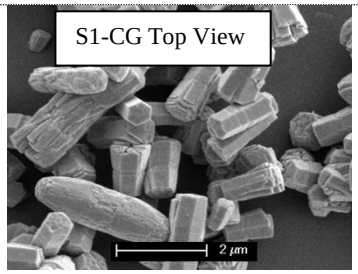	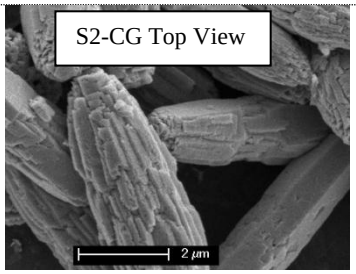	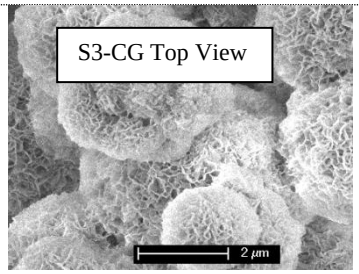
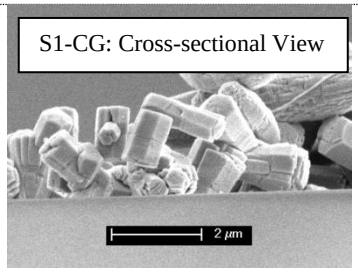	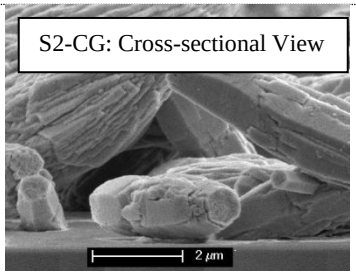	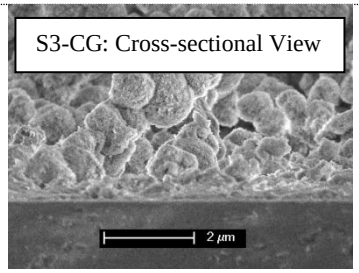

(E2) ZnO thin films in water irradiated with UV (340nm)

Nanostructured ZnO thin films obtained from solution S1	**Nanostructured ZnO thin films obtained from solution S2**	**Nanostructured ZnO thin films obtained from solution S3**
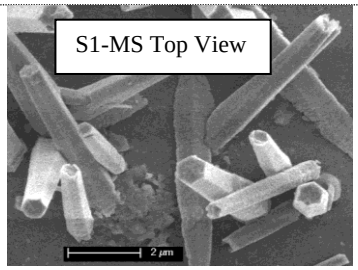	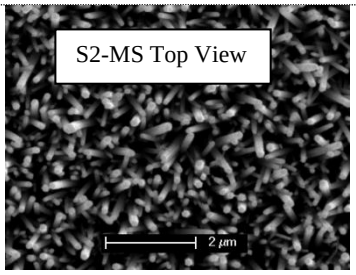	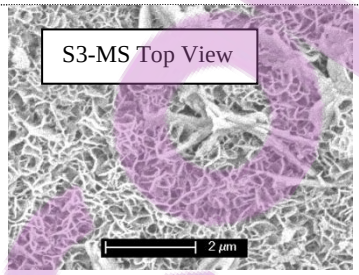
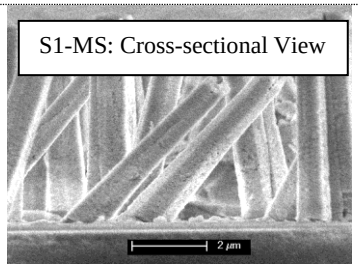	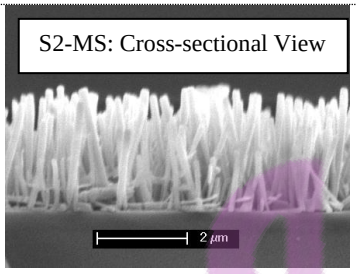	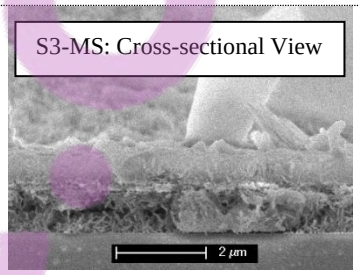
	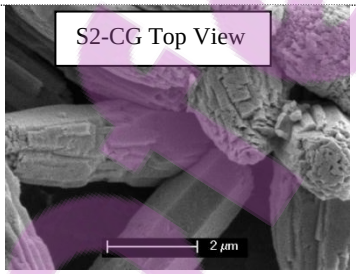	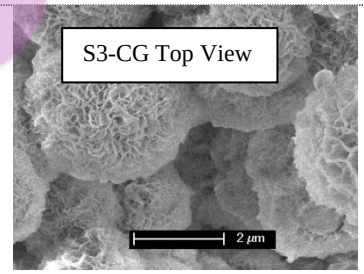
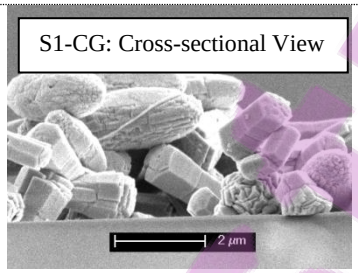	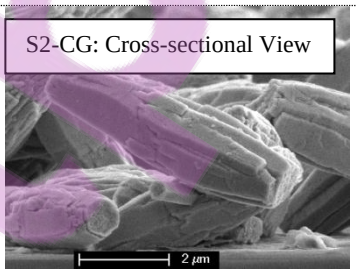	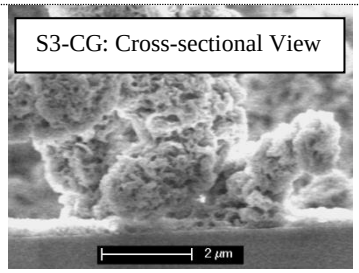

Appendix B: Reproducibility and effect on of nanostructured ZnO thin films morphologies under UV irradiation of 340nm.

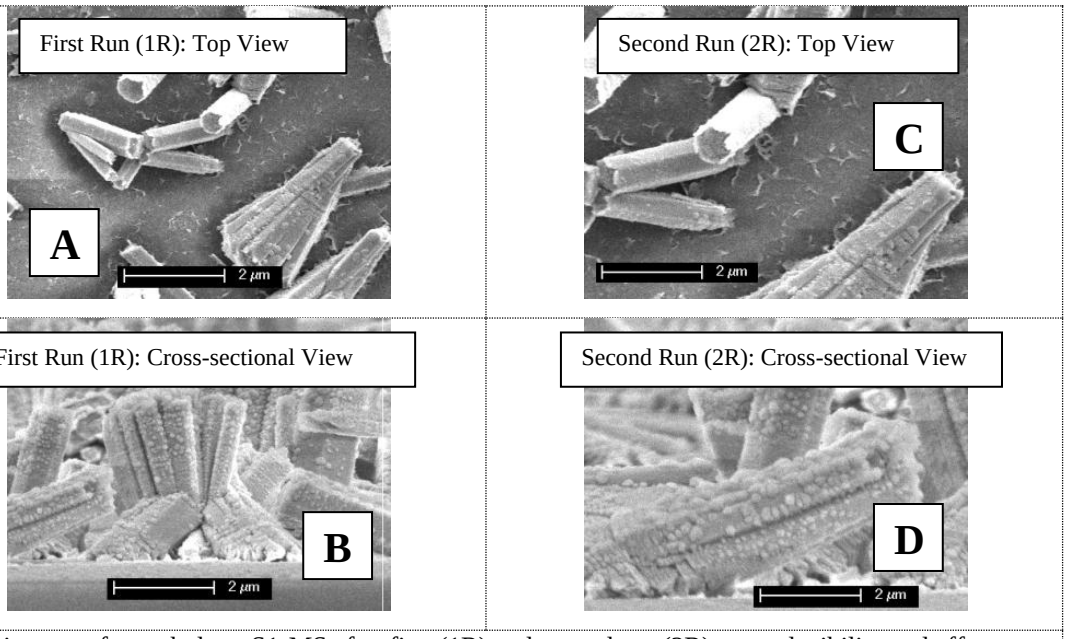

SEM images of morphology S1-MS after first (1R) and second run (2R); reproducibility and effect on morphology.(A) S1-MS first run (top view); (B) S1-MS first run (cross-sectional view); (C) S1-MS second run (top view); (D) S1-MS second run (cross-sectional view) under oxygen rich conditions.

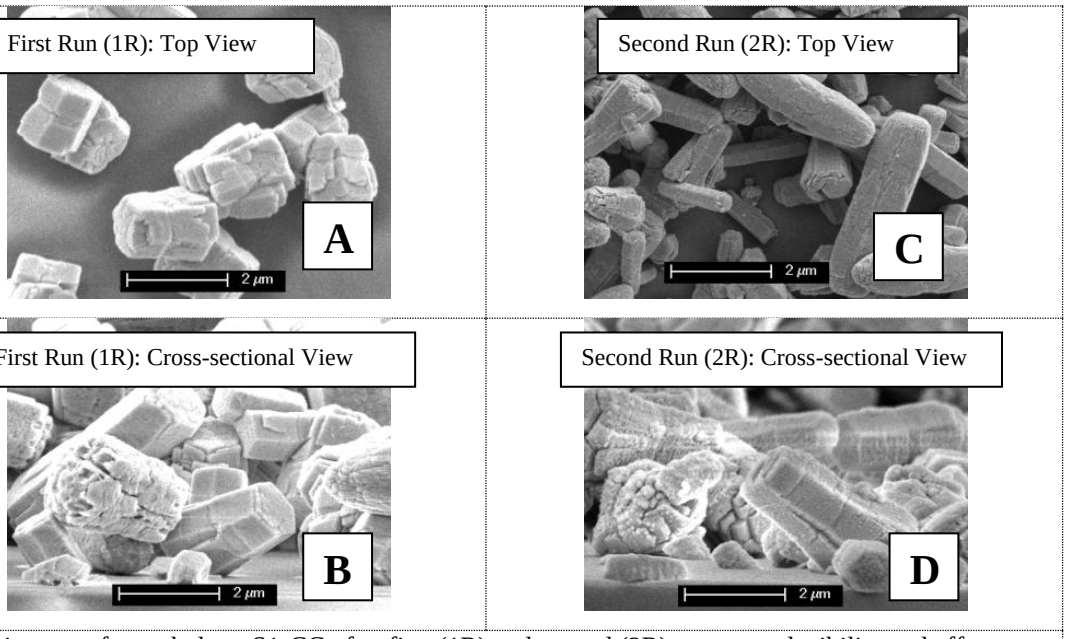

SEM images of morphology S1-CG after first (1R) and second (2R) run; reproducibility and effect on morphology.(A) S1-CG first run (top view); (B) S1-CG first run (cross-sectional view); (C) S1-CG second run (top view); (D) S1-CG second run (cross-sectional view) under oxygen rich conditions.

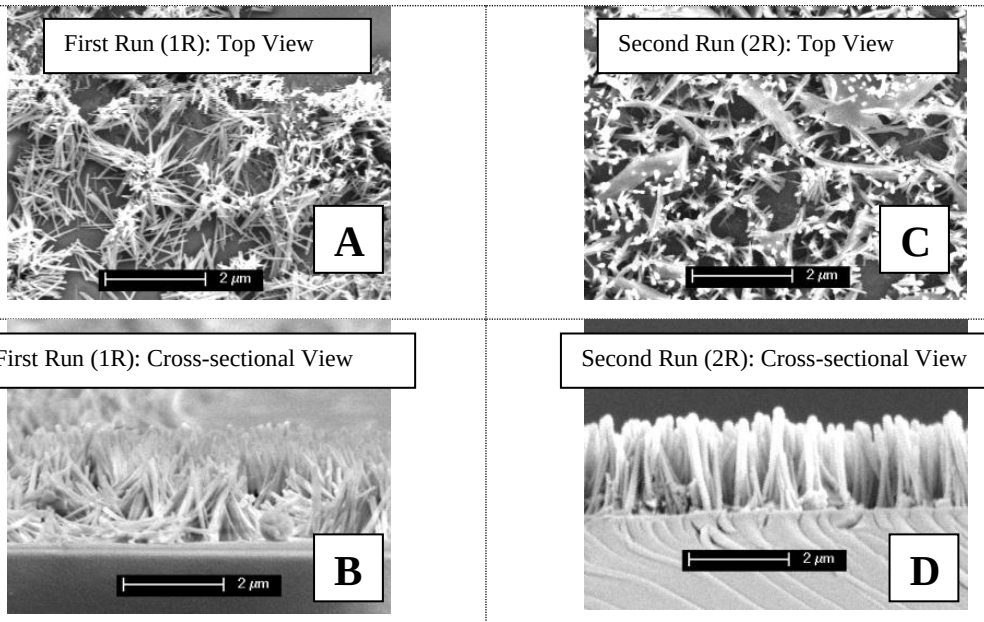

SEM images of morphology S2-MS after first (1R) and second run (2R); reproducibility and effect on morphology.(A) S2-MS first run (top view); (B) S2-MS first run (cross-sectional view); (C) S2-MS second run (top view); (D) S2-MS second run (cross-sectional view) under oxygen rich conditions.

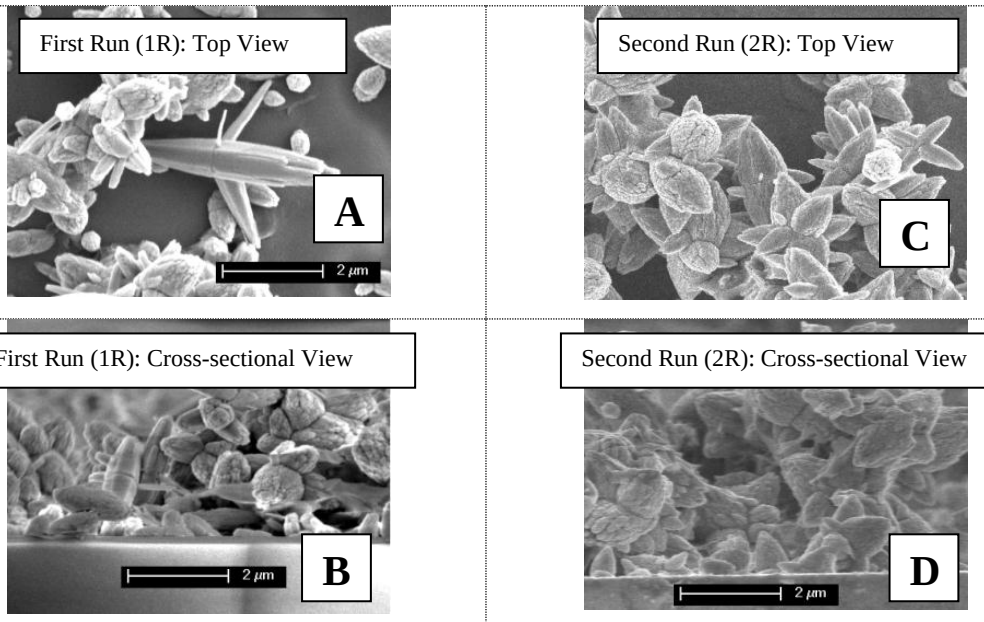

SEM images of morphology S2-CG after first (1R) and second run (2R); reproducibility and effect on morphology.(A) S2-CG first run (top view); (B) S2-CG first run (cross-sectional view); (C) S2-CG second run (top view); (D) S2-CG second run (cross-sectional view) under oxygen rich conditions.

Appendix C: Reaction Intermediate analysis by using LC-MS.

m/z	rt	formula	name
284.121595	0.7	C16H17N3S1	Methylene Blue
270.105945	0.7	C15H15N3S1	Azure B
256.090295	0.7	C14H13N3S1	Azure A
242.074645	0.7	C13H11N3S1	Azure C
228.058994	0.7	C12H9N3S1	Thionin

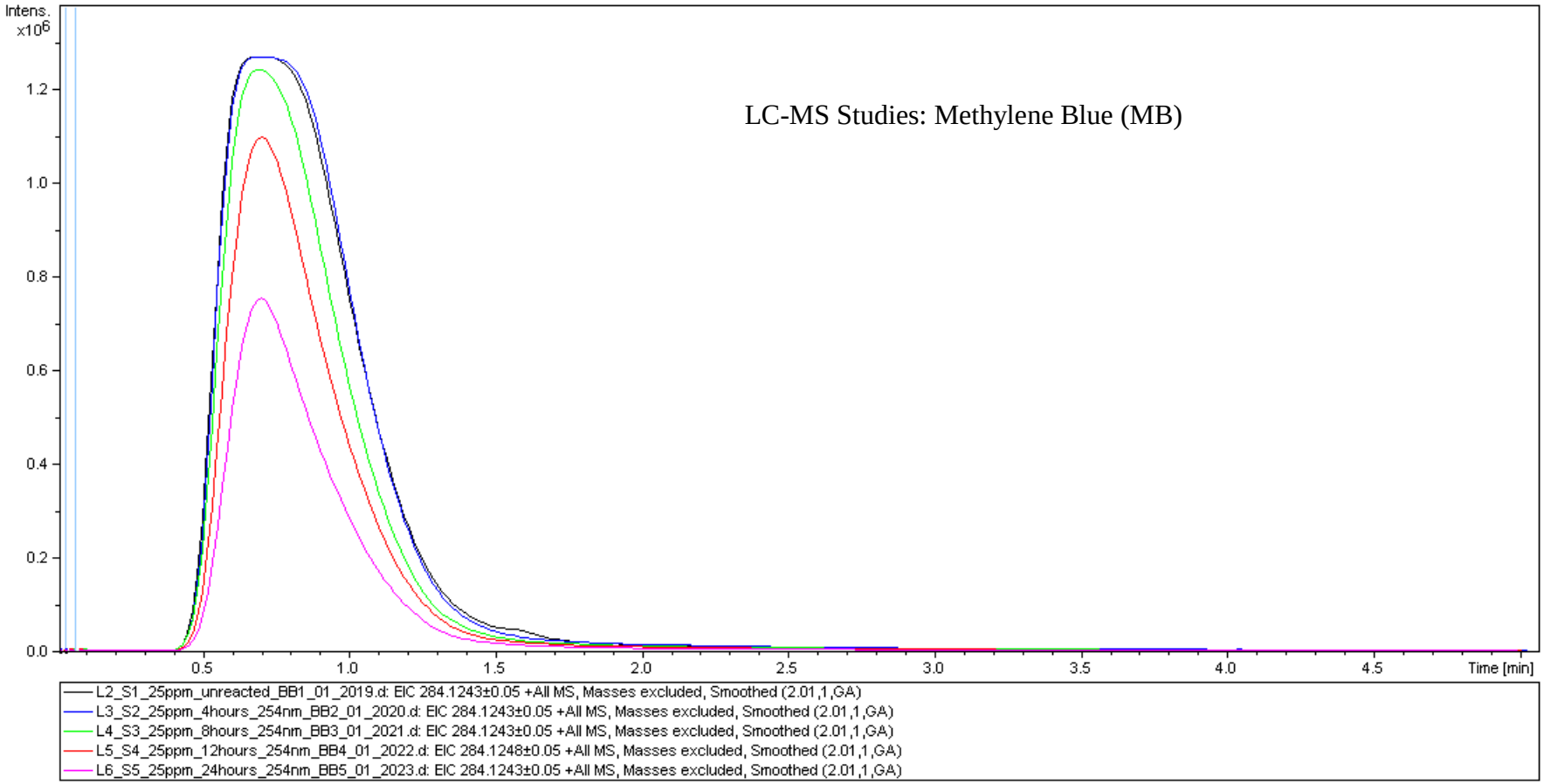

LC-MS Studies: Methylene Blue (MB)

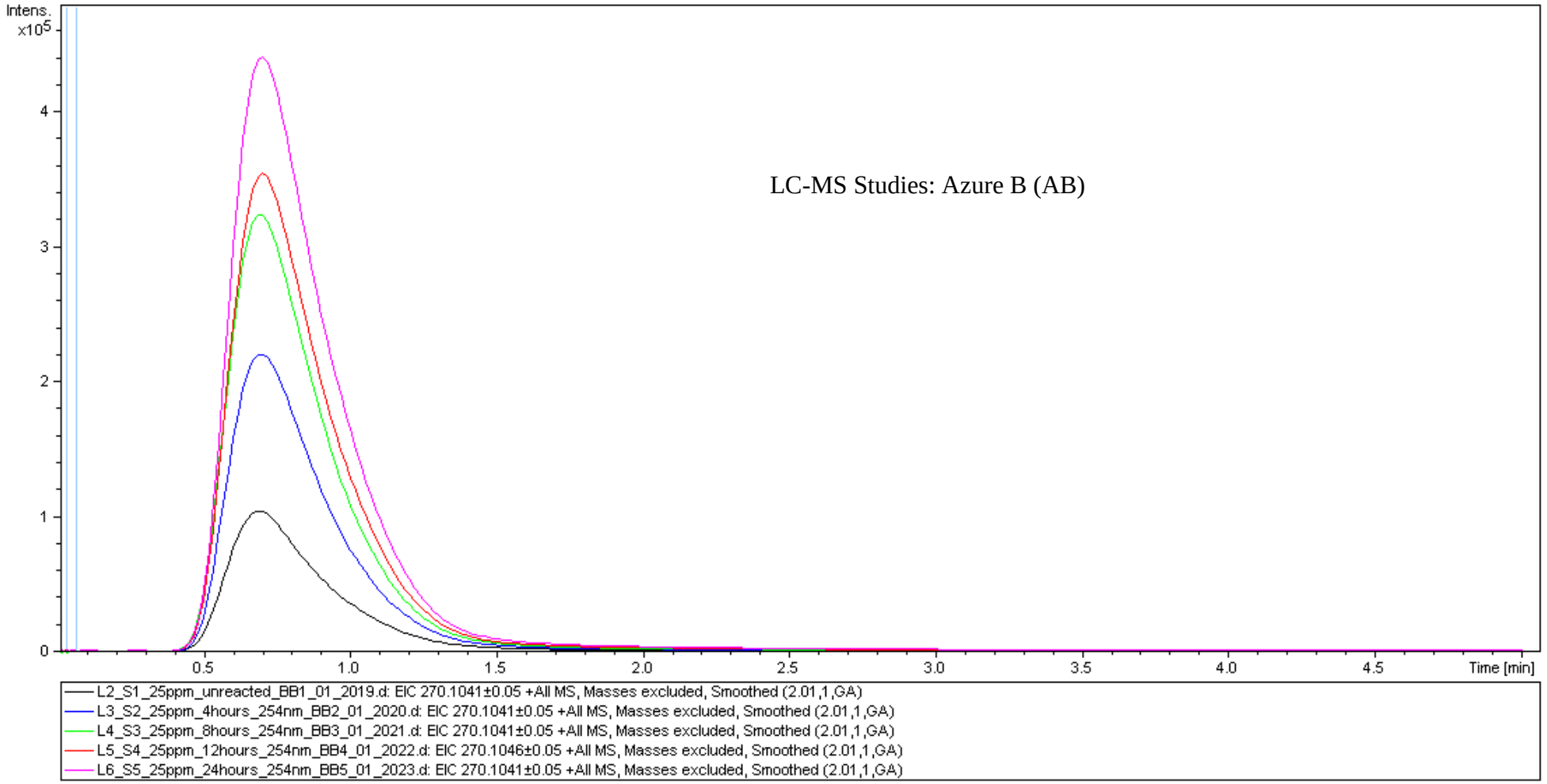

LC-MS Studies: Azure B (AB)

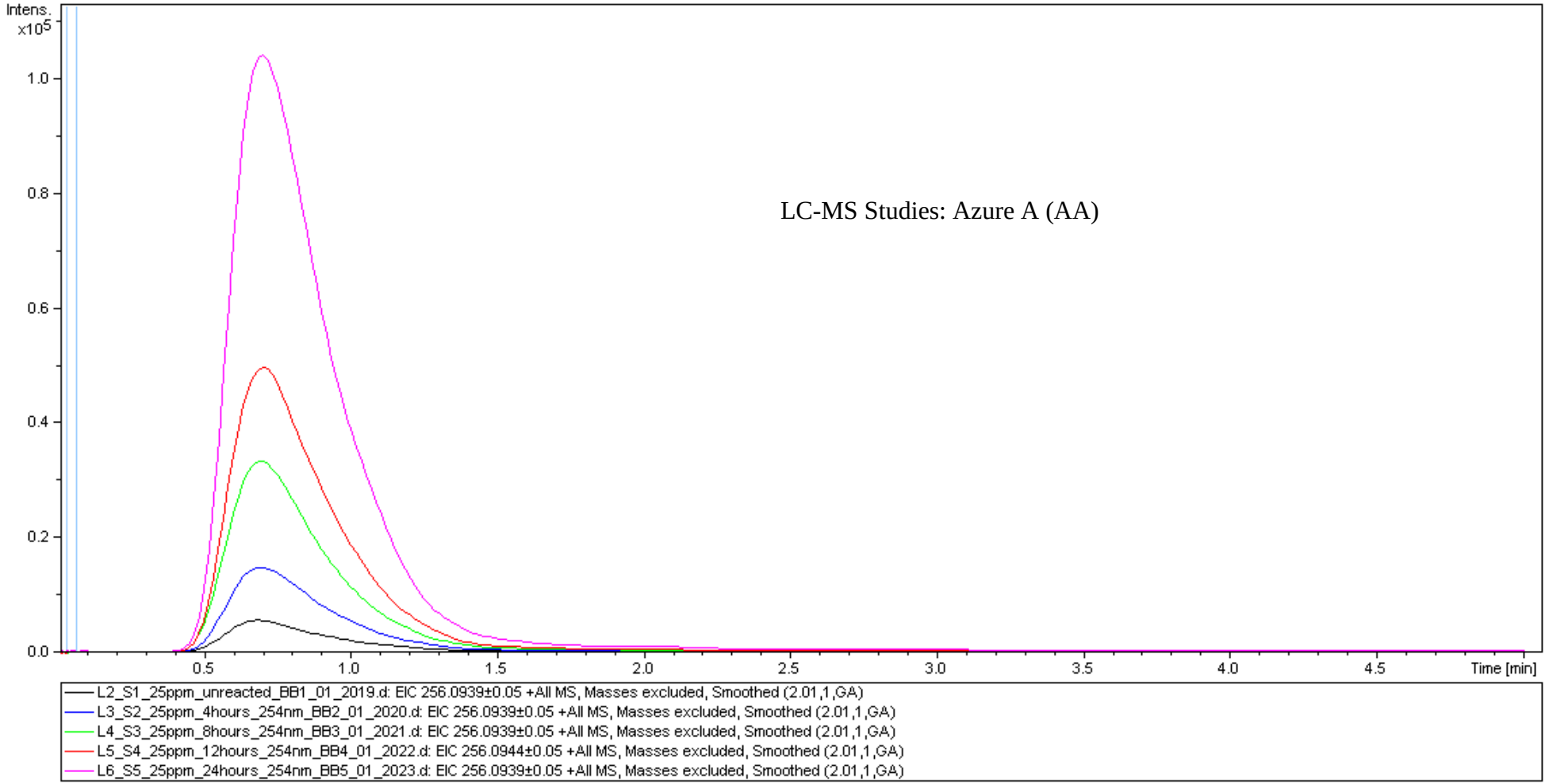

LC-MS Studies: Azure A (AA)

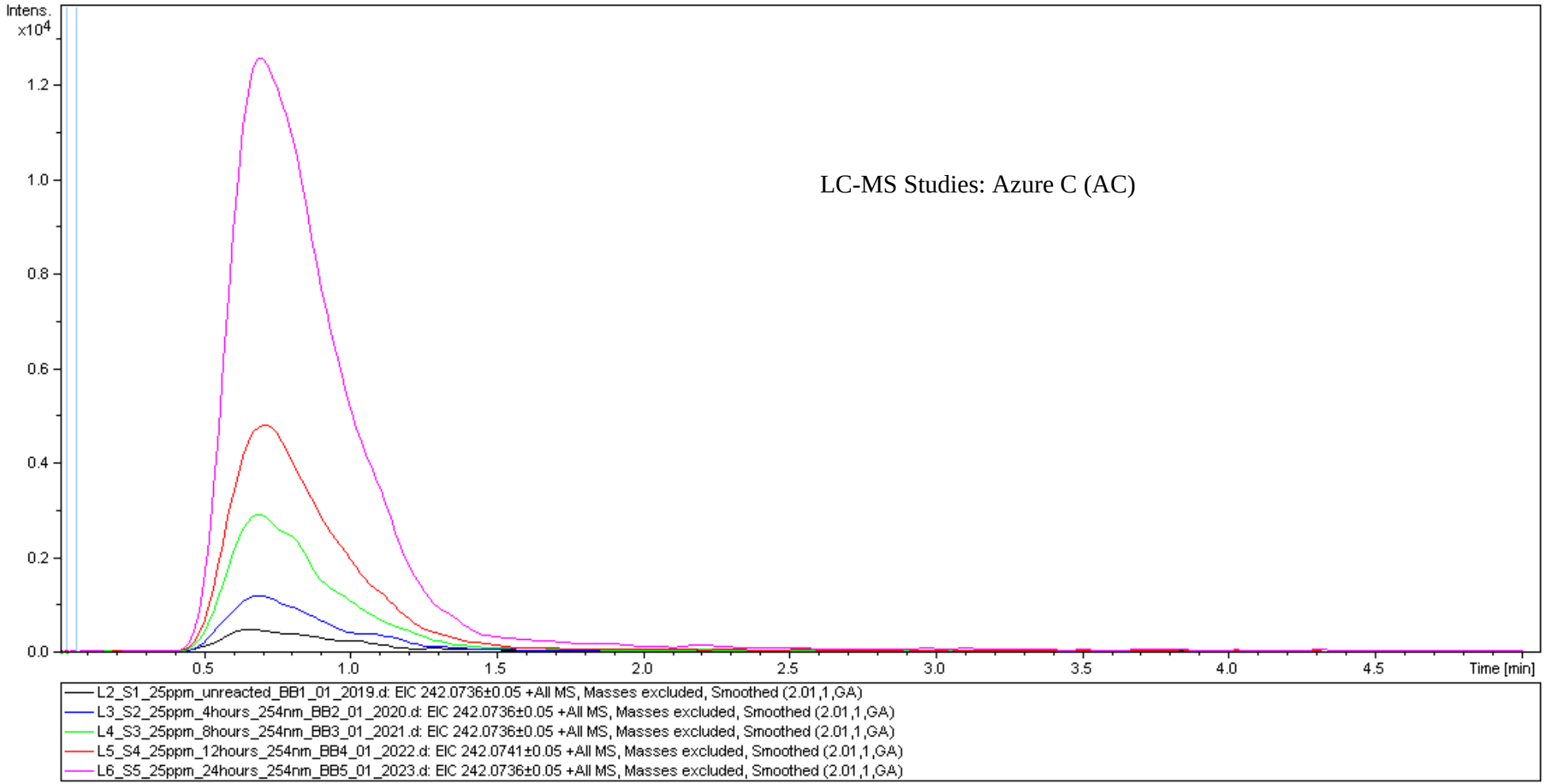
Intens.
x10^4
1.2
1.0
0.8
0.6
0.4
0.2
0.0
0.5
1.0
1.5
2.0
2.5
3.0
3.5
4.0
4.5
Time [min]
LC-MS Studies: Azure C (AC)
L2_S1_25ppm_unreacted_BB1_01_2019.d: EIC 242.0736±0.05 +All MS, Masses excluded, Smoothed (2.01,1,GA)
L3_S2_25ppm_4hours_254nm_BB2_01_2020.d: EIC 242.0736±0.05 +All MS, Masses excluded, Smoothed (2.01,1,GA)
L4_S3_25ppm_8hours_254nm_BB3_01_2021.d: EIC 242.0736±0.05 +All MS, Masses excluded, Smoothed (2.01,1,GA)
L5_S4_25ppm_12hours_254nm_BB4_01_2022.d: EIC 242.0741±0.05 +All MS, Masses excluded, Smoothed (2.01,1,GA)
L6_S5_25ppm_24hours_254nm_BB5_01_2023.d: EIC 242.0736±0.05 +All MS, Masses excluded, Smoothed (2.01,1,GA)

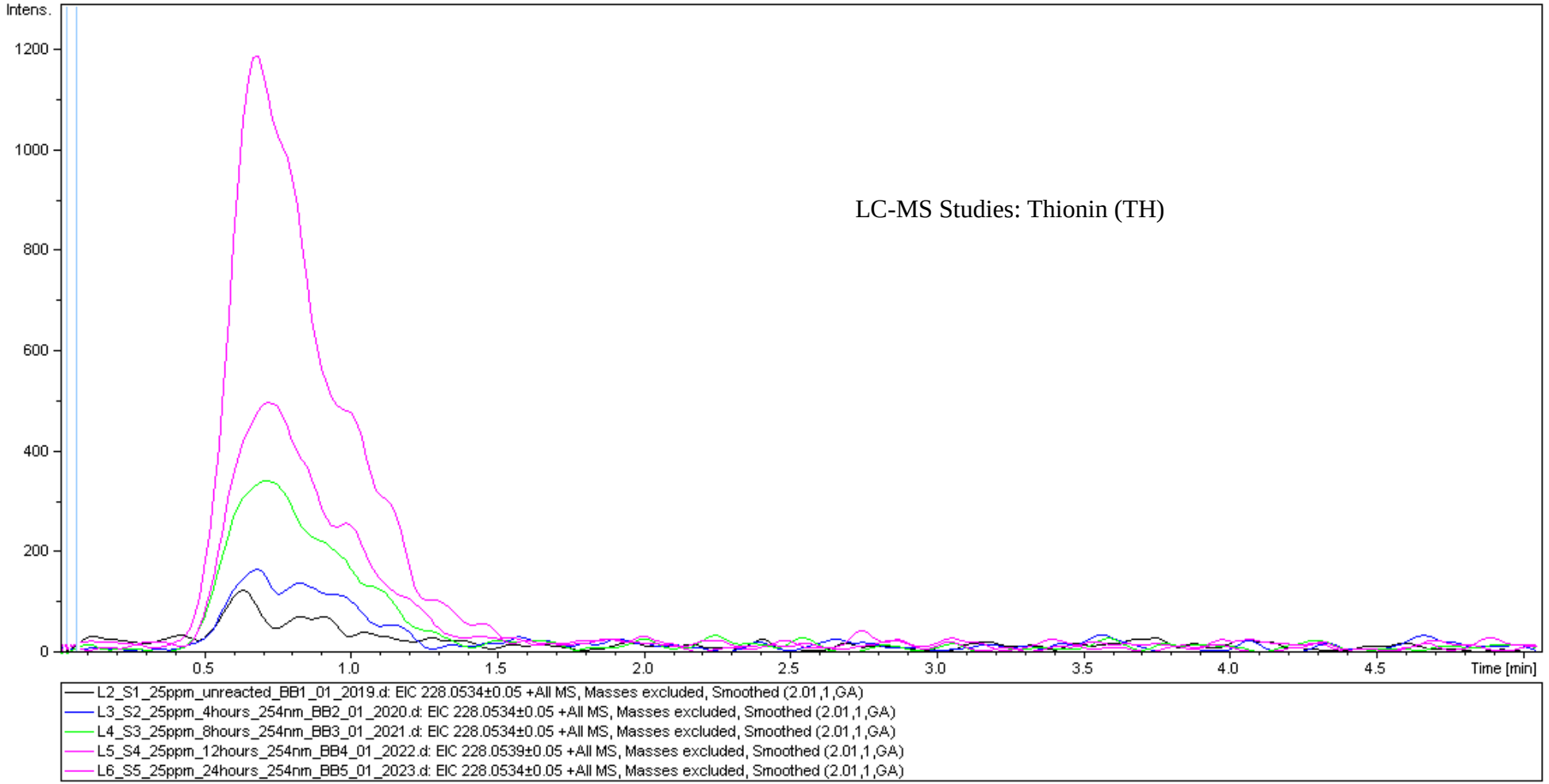

LC-MS Studies: Thionin (TH)

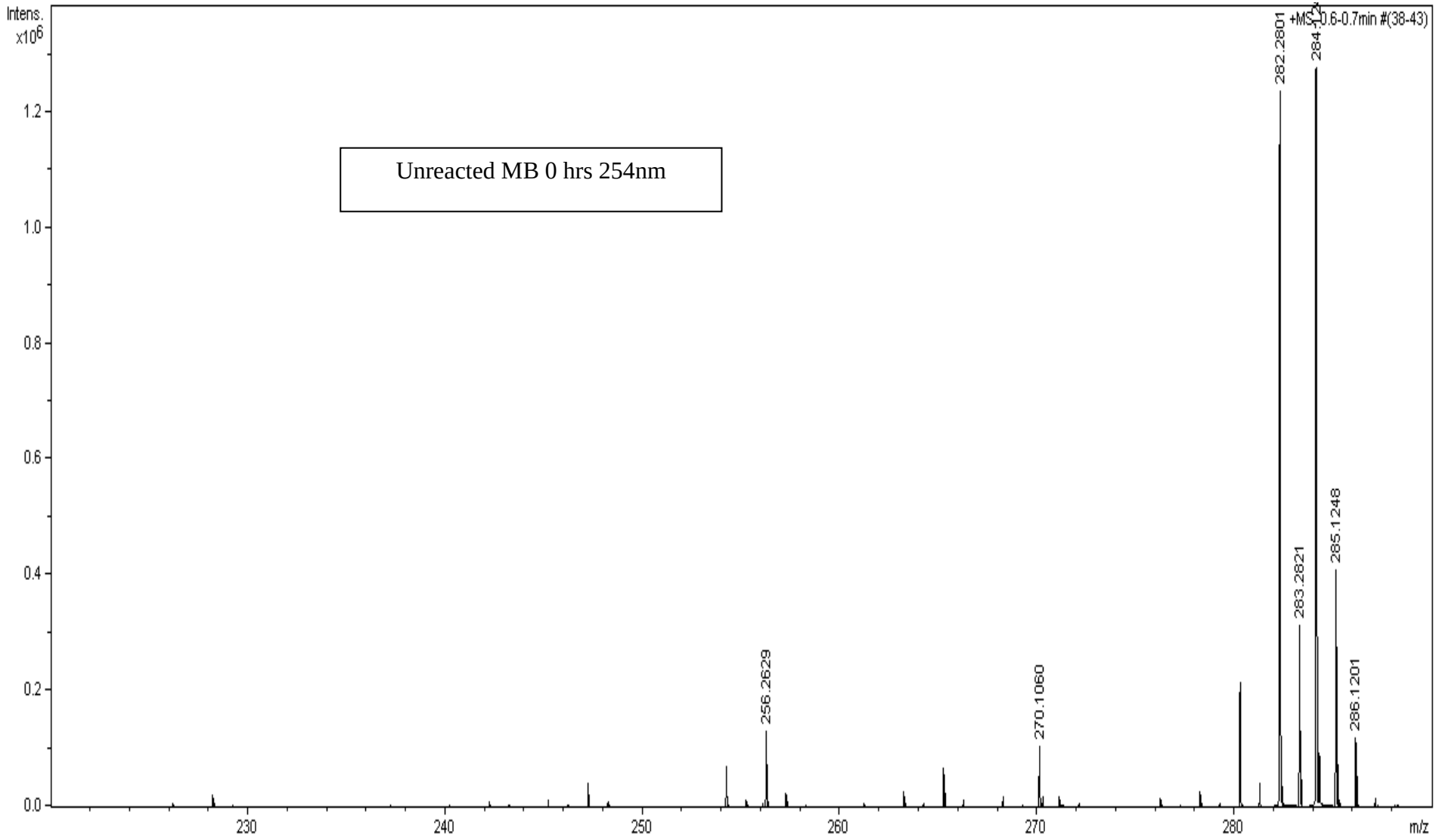
Intens.
x10^6
1.2
1.0
0.8
0.6
0.4
0.2
0.0
Unreacted MB 0 hrs 254nm
282.2801
284.2624
285.1248
283.2821
256.2629
270.1060
286.1201
230
240
250
260
270
280
m/z

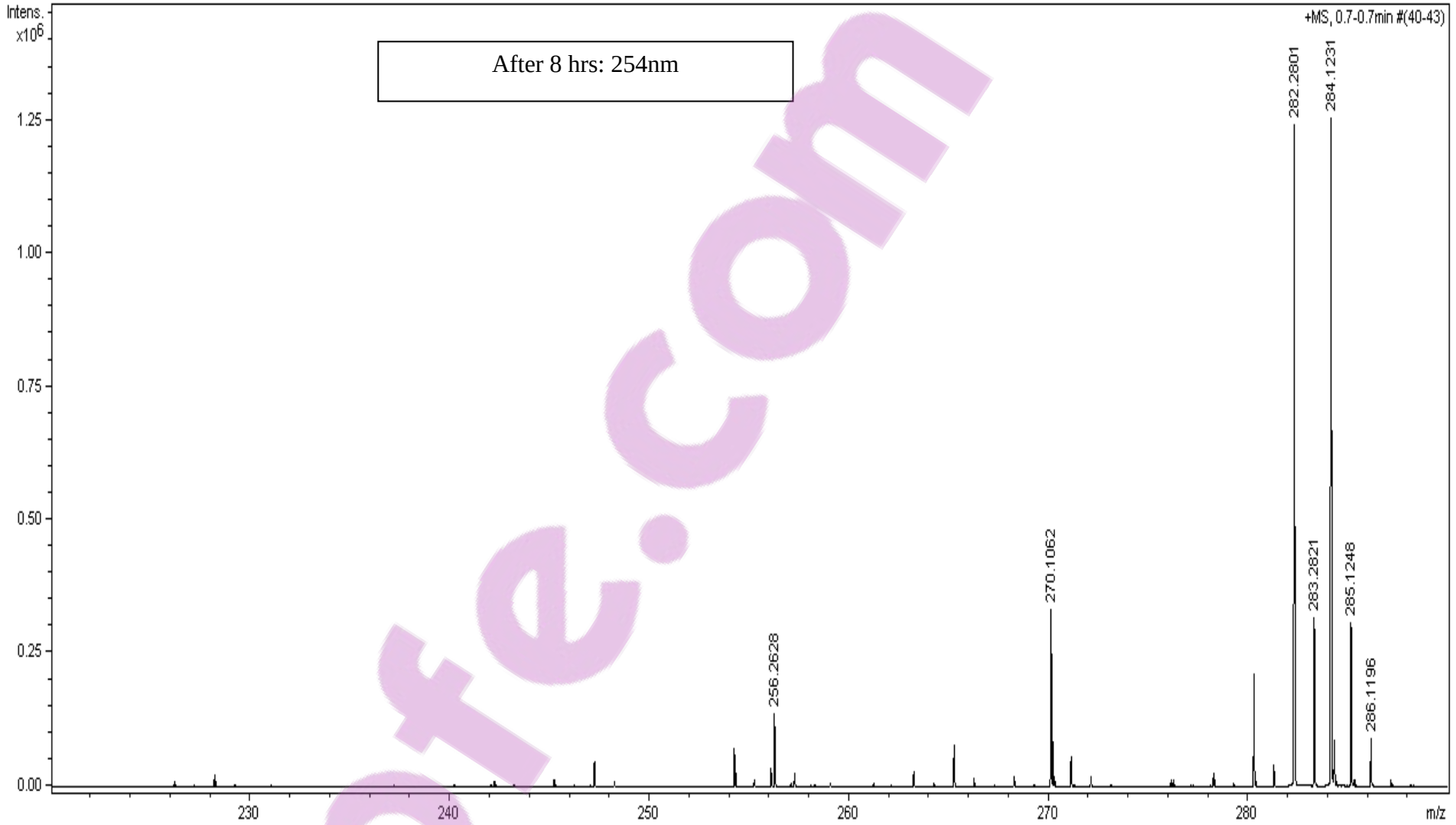
After 8 hrs: 254nm
Intens.
x10^6
+MS, 0.7-0.7min #(40-43)
1.25
1.00
0.75
0.50
0.25
0.00
282.2801
284.1231
270.1062
283.2821
285.1248
256.2628
286.1196
230
240
250
260
270
280
m/z

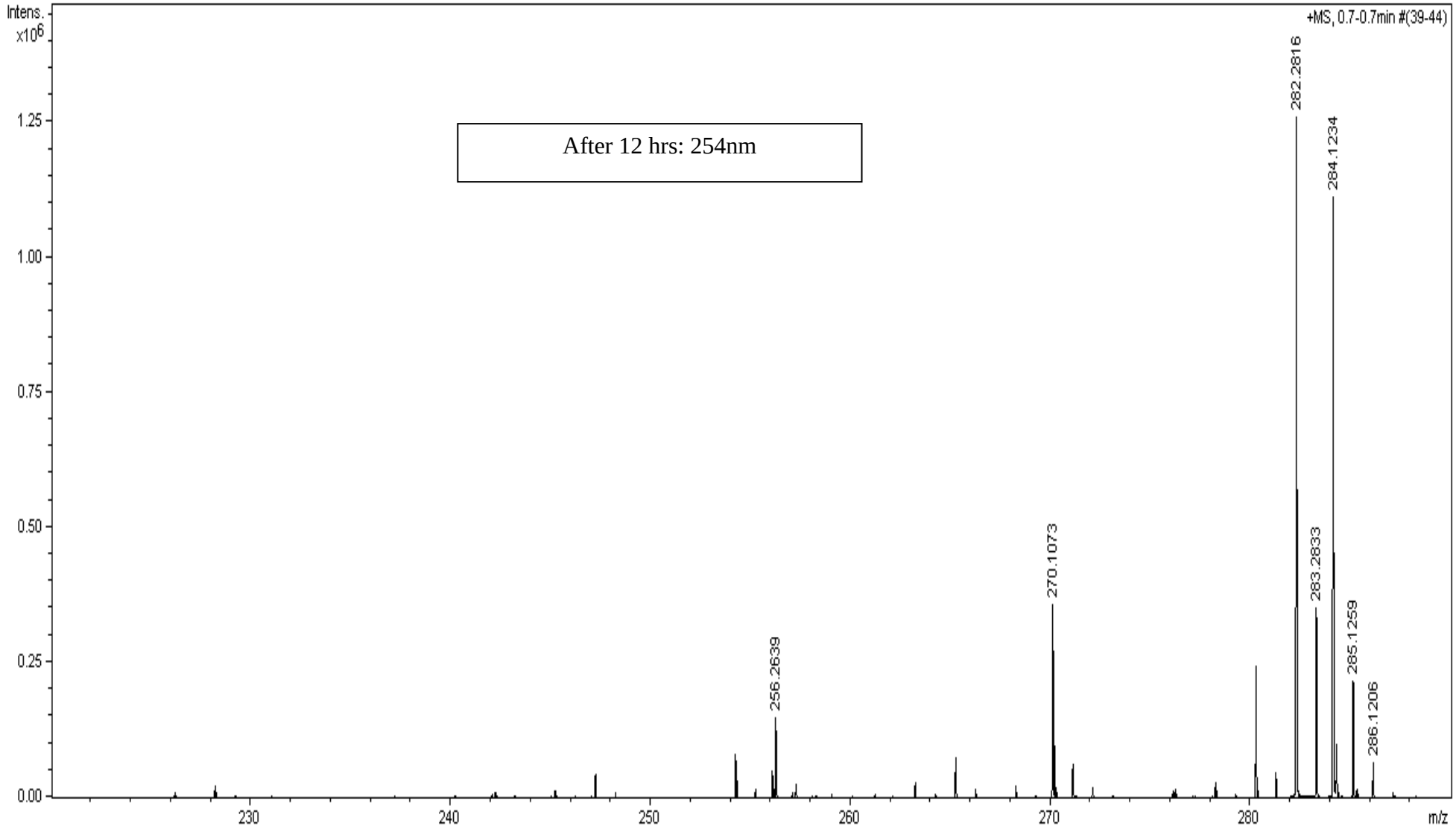
Intens.
x10^6
+MS, 0.7-0.7min #(39-44)
After 12 hrs: 254nm
282.2816
284.1234
270.1073
283.2833
285.1259
256.2639
286.1206
1.25
1.00
0.75
0.50
0.25
0.00
230
240
250
260
270
280
m/z

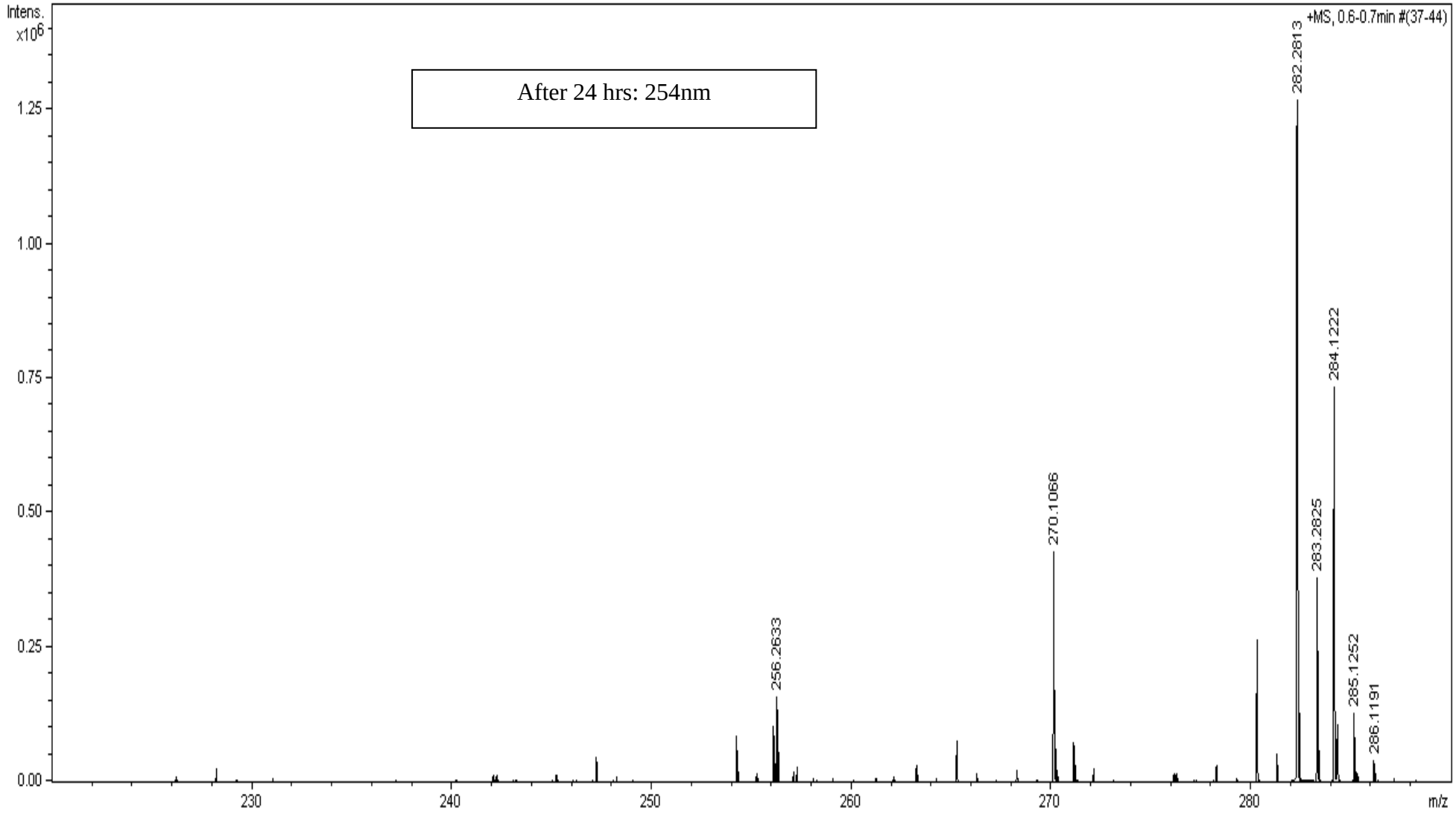
After 24 hrs: 254nm
Intens.
x10^6
1.25
1.00
0.75
0.50
0.25
0.00
+MS, 0.6-0.7min #(37-44)
282.2813
284.1222
270.1066
283.2825
256.2633
285.1252
286.1191
230
240
250
260
270
280
m/z

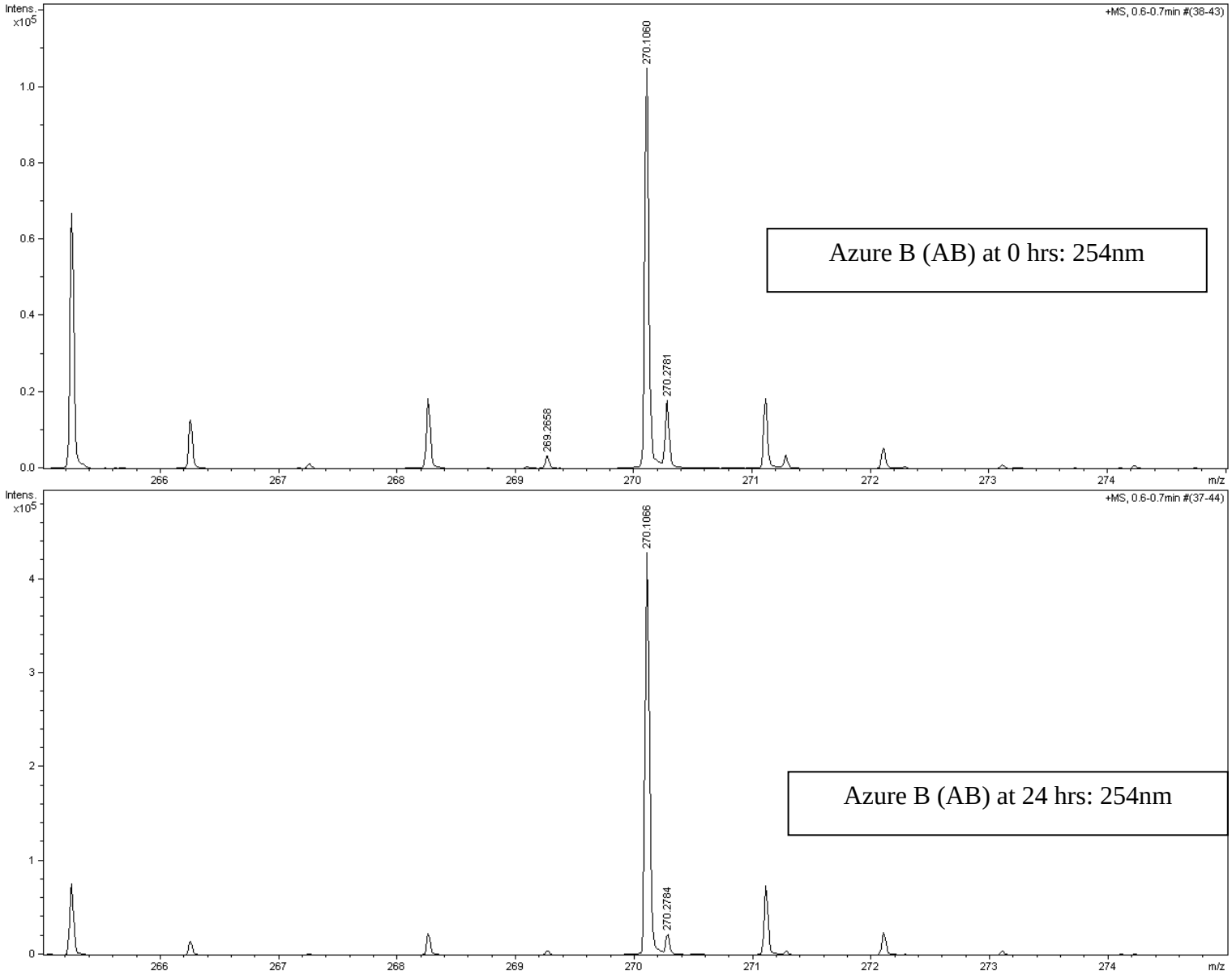
Intens.
x10^5
+MS, 0.6-0.7min #(38-43)
270.1060
269.2658
270.2781
Azure B (AB) at 0 hrs: 254nm
m/z
Intens.
x10^5
+MS, 0.6-0.7min #(37-44)
270.1066
270.2784
Azure B (AB) at 24 hrs: 254nm
m/z

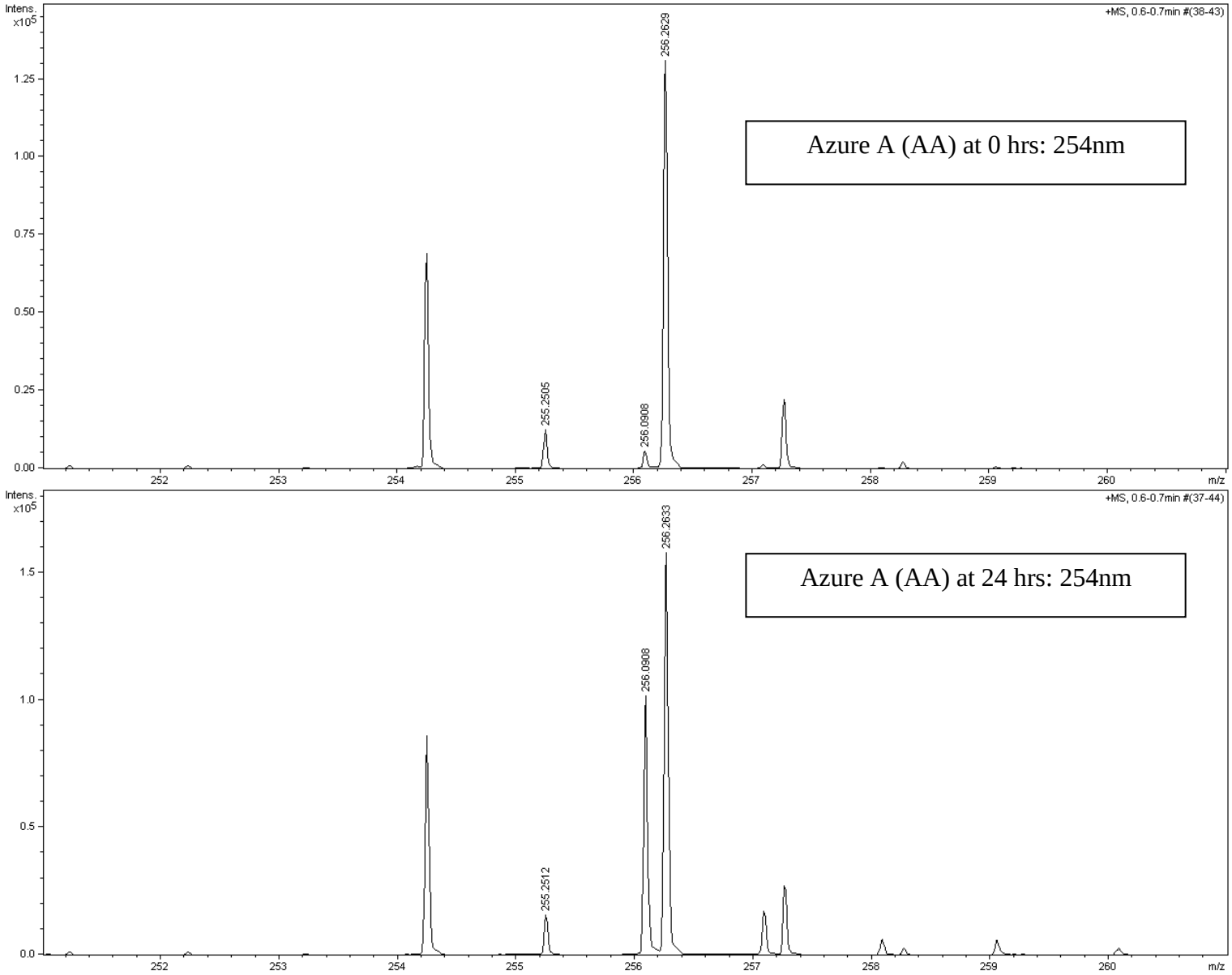
Intens.
x10^5
+MS, 0.6-0.7min #(38-43)
256.2629
255.2505
256.0908
Azure A (AA) at 0 hrs: 254nm
m/z
Intens.
x10^5
+MS, 0.6-0.7min #(37-44)
256.2633
256.0906
255.2512
Azure A (AA) at 24 hrs: 254nm
m/z

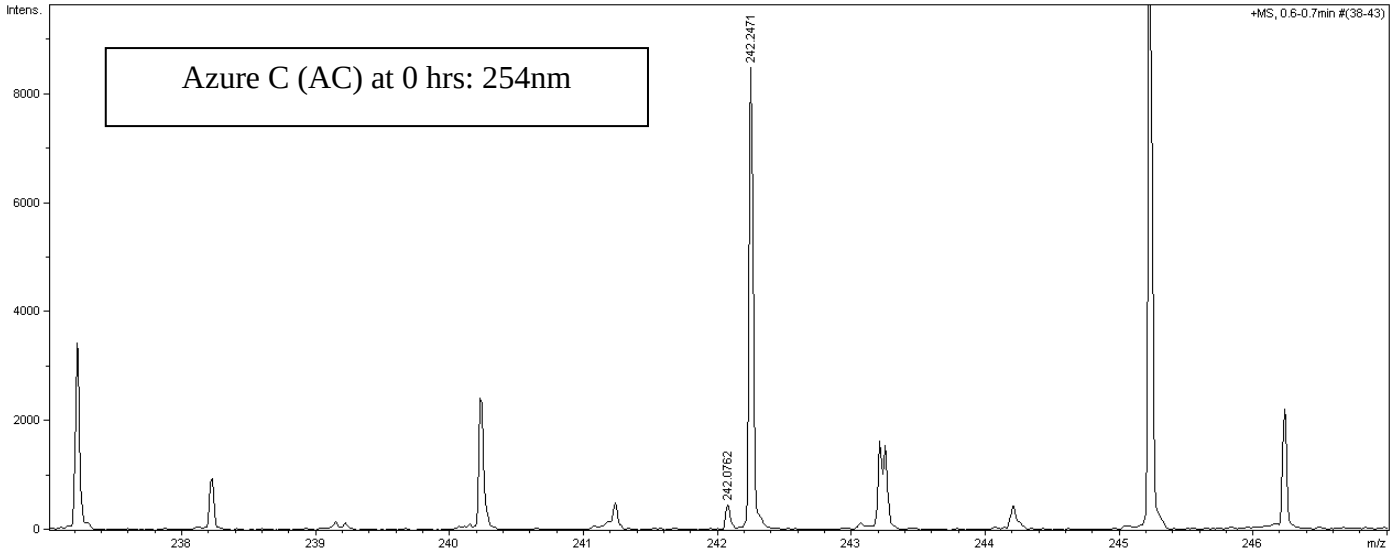
Azure C (AC) at 0 hrs: 254nm
Intens.
+MS, 0.6-0.7min #(38-43)
242.2471
242.0762
8000
6000
4000
2000
0
238
239
240
241
242
243
244
245
246
m/z

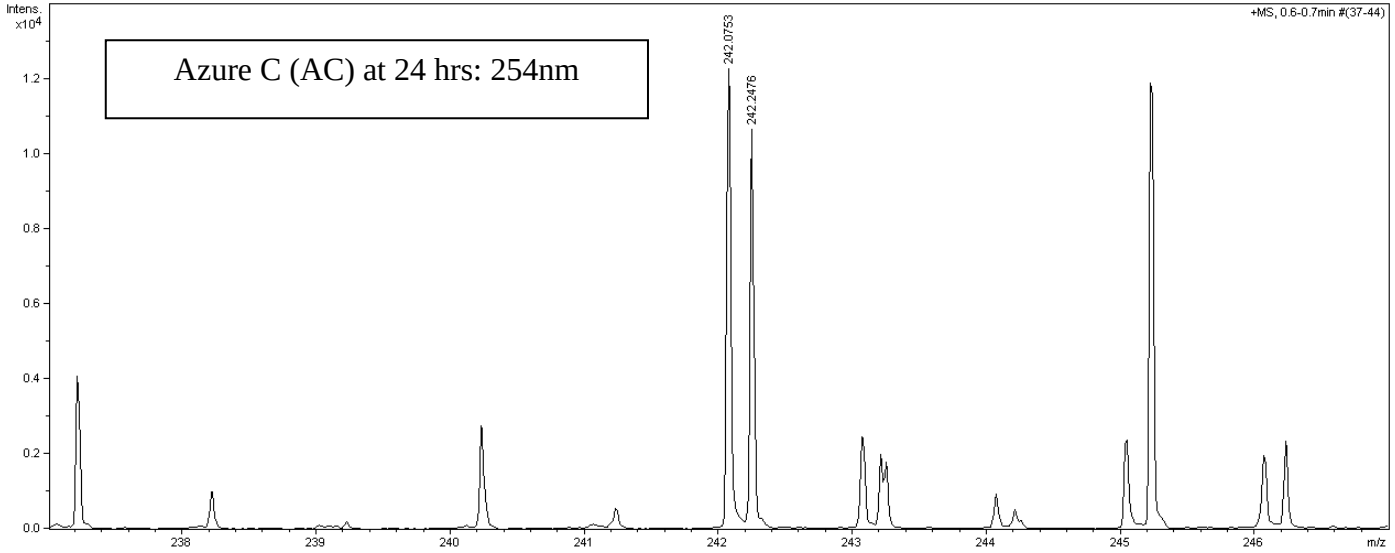
Azure C (AC) at 24 hrs: 254nm
Intens.
x10^4
+MS, 0.6-0.7min #(37-44)
242.0753
242.2476
1.2
1.0
0.8
0.6
0.4
0.2
0.0
238
239
240
241
242
243
244
245
246
m/z

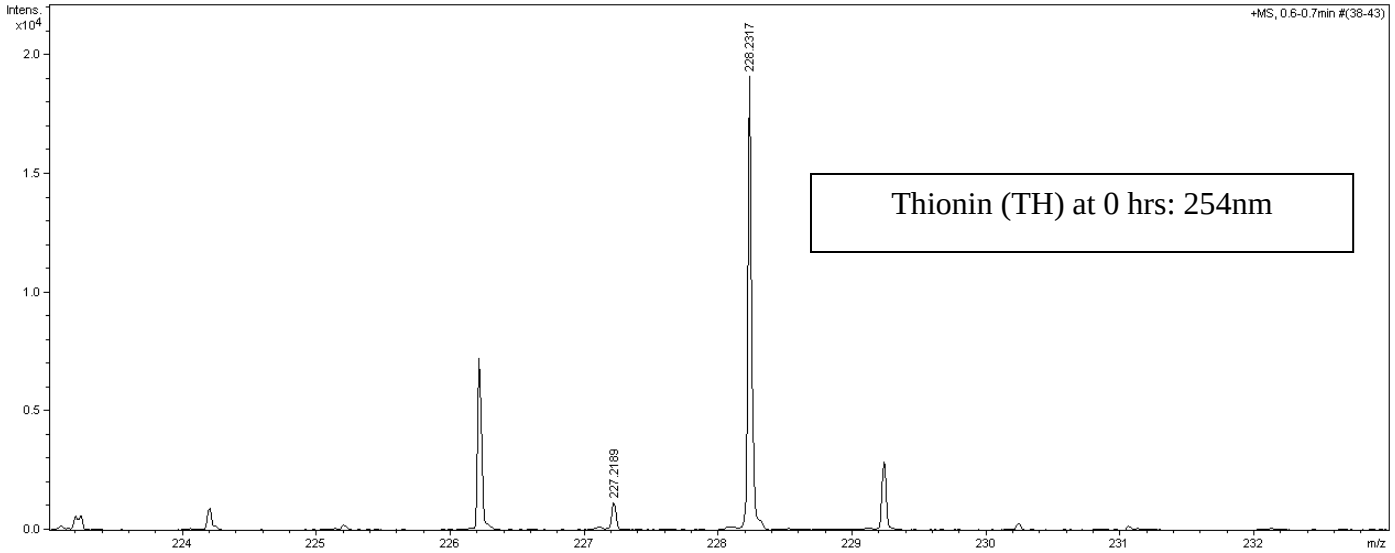
Intens.
x10^4
+MS, 0.6-0.7min #(38-43)
228.2317
227.2189
Thionin (TH) at 0 hrs: 254nm
m/z

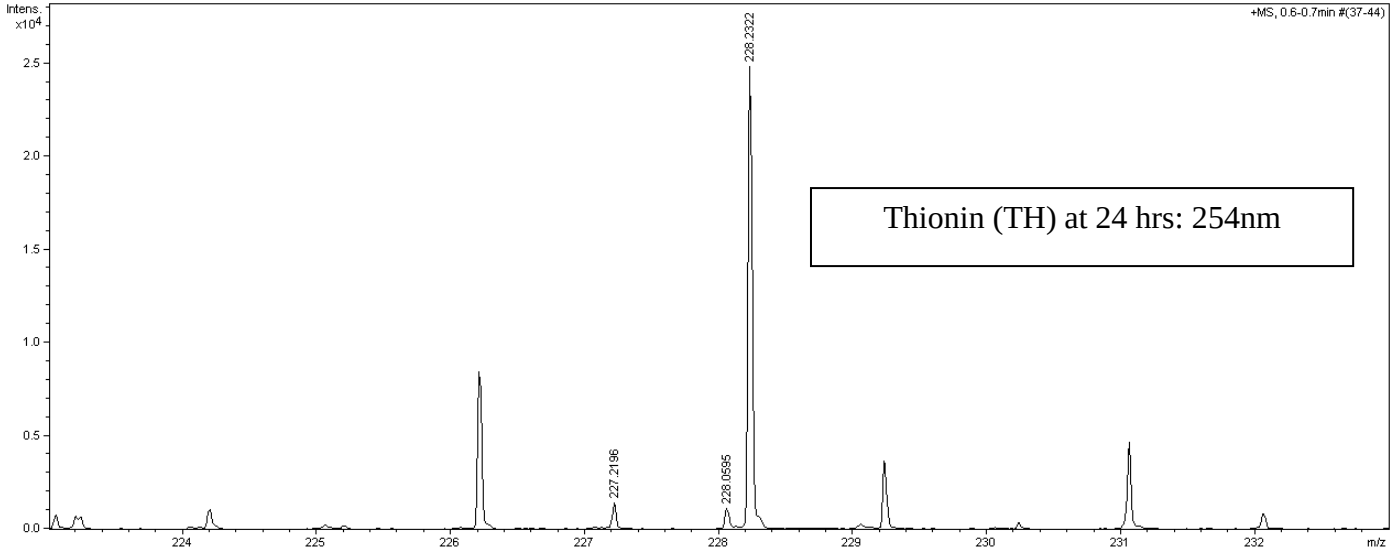
Intens.
x10^4
+MS, 0.6-0.7min #(37-44)
228.2322
227.2196
228.0595
Thionin (TH) at 24 hrs: 254nm
m/z

Appendix D: Band Gap Calculations

The Band Gaps of the undoped and cobalt doped nanostructure ZnO thin films was calculated using the equation below (as describe in [271]).

$$\alpha hv = K\sqrt{(hv - Eg)}$$

Where

α = absorption coefficient

hv= Energy of incident photon

K = constant

$Eg =$ Band gap energy

The results obtained are summarised following:

UV-Vis spectrophotometer was used to measure the absorption at a scanning wavelength range from 300nm-900nm.

Undoped ZnO thin films:

Morphology	Band Gap
S1-MS	3.24 eV
S1-CG	3.21 eV
S2-MS	3.29 eV
S2-CG	3.24 eV

Cobalt doped ZnO thin films:

Morphology Co:S1-MS		Morphology Co:S1-CG	
Co5%:S1-MS	3.23 eV	Co5%:S1-CG	3.20 eV
Co10%:S1-MS	3.21 eV	Co10%:S1-CG	3.22 eV
Co15%:S1-MS	3.23 eV	Co15%:S1-CG	3.21 eV
Co25%:S1-MS	3.24 eV	Co25%:S1-CG	3.20 eV

Morphology Co:S2-MS		**Morphology Co:S2-CG**	
Co5%:S2-MS	3.28 eV	Co5%:S2-CG	3.22 eV
Co10%:S2-MS	3.27 eV	Co10%:S2-CG	3.22 eV
Co15%:S2-MS	3.28 eV	Co15%:S2-CG	3.23 eV
Co25%:S2-MS	3.28 eV		

Appendix E

List of the data discussed in chapter 6 acquired by Nadiah K. Zaman under author's co-supervision are as follows:

- Figure 6.20 A and C
- Figure 6.21 A and C
- Figure 6.28 A-B
- Figure 6.30 A-D
- Figure 6.31 A-D
- Figure 6.32 A-D
- Figure 6.33 A-D
- Figure 6.34 A-D

Appendix F: Band Gap Engineering and Strategy to improve Cobalt incorporation in ZnO lattice

In 1928, Felix Bloch in his PhD thesis "Quantum Theory of Solids" postulated that atoms in solid are arranged in a regular patterns (known as crystal) and if these electrons are free to move then where they would end up. To answer this, he solved the Schrödinger wave equation and ended up with a set of wavelengths of electron (λe) that could propagate or invoke the wave like properties of electrons and end with concept of electrical conductivity. Whilst working on his post - doc he started to formulate the idea of a linear combination of atomic or molecular orbitals.

He concluded that bonding and anti-bonding orbital's (based on Pauli Exclusion Principle: no two orbital's can have the same quantum number) formed when two linearly arranged same atom (A-A) overlap each other to form A2. If A2 further keeps on linearly overlapping with the other same atom (A), let say after N number of atoms, they would end up with a band (set of very closely space orbitals).

Because of the arrangement of sub orbital's in the each atom, two bands may be formed and the energy required to move from the top of valence band to the bottom of the conduction band was given the name 'band gap'.

In photocatalysis, it is essential that the incident photon should have higher energy than the band gap.

Doping to a metal oxide could alter the electronic arrangement that could be useful to induced visible light adsorption for the emission of electron from the top of the valance band to the bottom of conduction band by using visible light. Therefore one has to understand the basics involved in solid state chemistry to understand the mastering in band gap engineering i.e, one has to pay full attention on the overlapping of suborbital of dopant and MO.

Many researchers studied to incorporate of a variety of materials such as metals Fe, Ni, Co, Cu and Cd [272-274] , non metal N, C, and S [103, 146, 171-176, 178-185], metal oxides such as Al_2O_3 and In_2O_3 [275, 276], hetrostructure atom [277-279] are being under vigorous study to manipulate energy levels and sub orbitals to have suitable the band gap. Much work is under study to explore the hidden avenues to improve the existing band gap engineering techniques.

Appendix H: Calculation of lattice oxygen consumption based on Zn Mass Balance

Zinc Balance

Amount of Zn (control)	2197.5	ppb	Amount of Zn (control)	2197.5	ppb
Amount of Zn (Oxygen Limited)	9235.42	ppb	Amount of Zn (Oxygen Rich)	4454.12	ppb
Amount of Zn obtained from ZnO lattice	7037.92	ppb	Amount of Zn obtained from ZnO lattice	2256.62	ppb
	7.03792	ppm		2.25662	ppm
	7.03792	mg/L		2.25662	mg/L
	0.007038	gm/L		0.002257	gm/L
	0.000108	moles/L		3.45E-05	moles/L
	1.08E-04	moles/L		3.45E-05	moles/L
	108	µmol/L		34	µmol/L
Error with AAS analysis	0.2	µmol/L		0.2	µmol/L
Amount of Zn after error	86.4	µmol/L		27.2	µmol/L

$5MB + 12O_2$ -------> $AB + AA + AC + TH + 8CO_2 + 8H_2O$

From equation
5MB -------> 8CO2
1MB -------> 8/5CO2
26.37 MB -------> (8/5) * 26.37 CO_2 which is equal to 42.19 µmol/L of CO_2 produced

Moles of O_2 used for CO_2 is 42.19 µmol/L (1:1 ratio).

Moles of O_2 used for H_2O is 21.09 µmol/L (1:0.5 ratio)

Total moles of O_2 used = 42.19 + 21.09 = 63.28 µmol/L

Under Limited Conditions:

% of O_2 obtained from ZnO lattice = 63.28/86.4 *100 ≈ 74%

Discussion:

1. 74% of oxygen obtained from lattice O_2 is used in the reaction.
2. Remaining 36% could have been disappeared in the form of unstable ZnO
3. The amount of oxygen taken from Zinc lattice is greater than % Zn/Surface area ratio (52%) both under oxygen limited and rich conditions.

Under Oxygen Rich Conditions:

% of O_2 obtained from ZnO lattice = 27.2/86.4 *100 ≈ 31%

Discussion:

1. 31% of oxygen obtained from lattice O_2 is used in the reaction. Remaining 69% should have been supplied by extra source of oxygen
2. The amount of oxygen taken from Zinc lattice is less than % Zn/Surface area ratio (52%) both under oxygen limited and rich conditions.

Appendix I: List of fundamental reasons for selecting cobalt and nitrogen as dopant.

Fundamental Reasons: For Cobalt doping:

1. Metal doping can generate some localized state around conduction band.
2. Availability of its sources such as cobalt nitrate.
3. A low temperature doping method.
4. Co:ZnO nanostructure ≈ Undoped ZnO structure (Wurtzite); leads to possible similar morphology.
5. To see the overall impact of variation in conduction band on photocatalysis.

Fundamental Reasons: For Nitrogen doping:

1. To generate some localized states around the valence band.
2. To study the variation in oxidation power of the photocatalyst.
3. Availability of its sources

Appendix J: Bench Mark Study of S2-MS (ZnO) with Degussa P25 (TiO_2)

Bench mark study of highly efficient nanostructured thin film S2-MS (ZnO) with P25 is summarized below;

Catalyst	k''_{app} ($m^3\ m^{-2}\ s^{-1}$)
P25 *	1.50×10^{-7}
S2-MS (ZnO)	6.27×10^{-4}

Bench mark study showed that morphology S2-MS has higher reaction rate as to that of P25.

*Results for P25 were taken from the study by Irina *et al* [280] under the supervision of Dr. Darrell Patterson.

Appendix K: Surface Area Calculations

Surface area of nanostructured ZnO thin films were estimated by using SEM images (see Page 114, line 1). Detailed calculations are as follws:

Doped Morphologies For Morphology Co15%:S1-MS

Note : All dimension were noted from A4 print of true SEM image
Assumption Same crystal with two different crystal dimensions

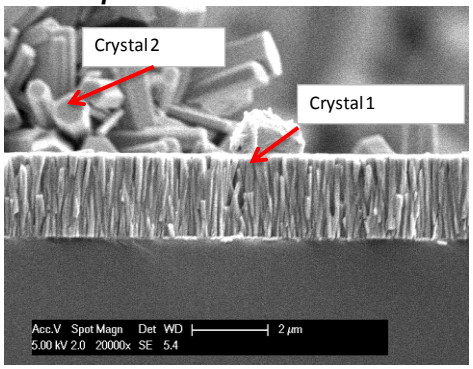

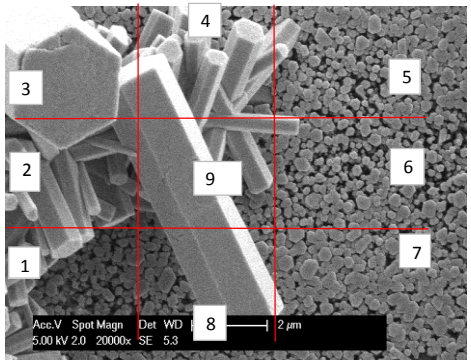

Dimension of crystal 1

Top Surface Area		0.49	cm^2
Side Surface Area		10.7	cm^2
Total Surface Area		11.19	cm^2
Conversion Factor	4.7cm=2µm		*taken from A4 print*
		1cm= 0.42553	µm
Area After Conversion		2.02626E-12	m^2

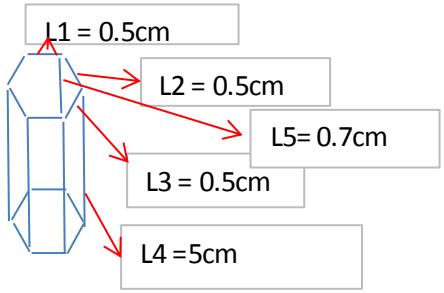

Number of rods:	1st part	2nd part	3rd part	4th part	5th part	6th part	7th part	8th part	9th part
	325	324	325	325	324	302	317	309	321

Total number of rods:	2872	
Total Surface Area	5.81941E-09	m^2

This surface area is from total dimensions of 14.6µm × 8.51µm

Actual Dimensions of the glass substrate		2x1cm^2
or		20×10^{3}µm by 10×10^{3}µm
Hence Total surface area		
14.6µm × 8.51µm		5.8E-09
1		4.7E-11
20×10^{3}µm	by	
10×10^{3}µm		0.00937 m^2
		mm^2
		9367.56

Dimension of crystal 2

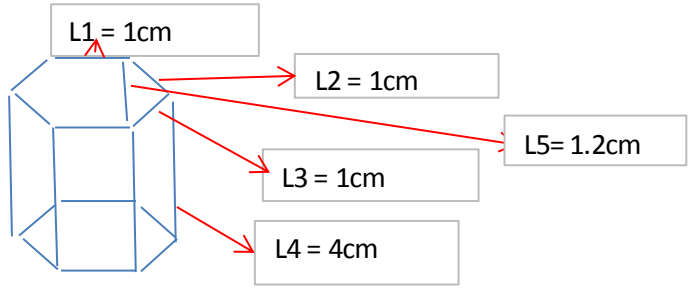

Top Surface Area	2.04	cm^2	
Side Surface Area	24	cm^2	
Total Surface Area	26.04	cm^2	
Conversion Factor	4.7cm=2µm	*taken from A4 print*	
	1cm=	0.425531915	µm
Area After Conversion	4.71526E-12	m^2	

Number of rods:	1st part	2nd part	3rd part	4th part	5th part	6th part	7th part	8th part	9th part
	3	5	1	4	0	0	0	1	3

Total number of rods: 17

Total Surface Area 8.01593E-11 m^2

This surface area is from total dimensions of 14.6µm × 8.51µm

Actual Dimensions of the glass substrate		2x1cm^2
or		20×10^{3}µm by 10×10^{3}µm
Hence Total surface area		
14.6µm × 8.51µm		8.01593E-11
1		6.45166E-13
20×10^{3}µm	by	0.000129033 m^2
10×10^{3}µm		

129.0332858 mm^2

Grand Surface Area

9496.59 mm^2

For Morphology Co15%:S1-CG

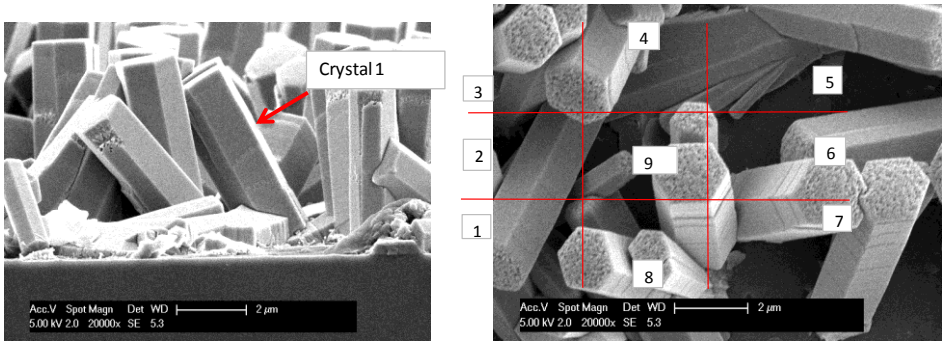

Note : All dimension were noted from A4 print of true SEM image
Assumption Same crystal with almost same crystal dimensions
Dimension of crystal 1

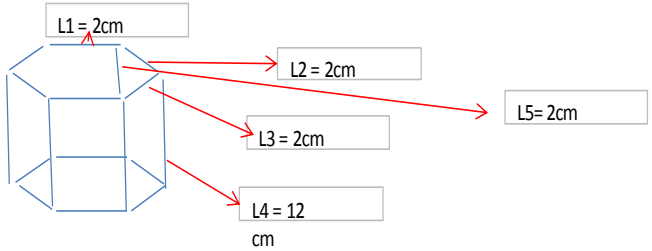

Top Surface Area	7.3	cm^2	
Side Surface Area	144	cm^2	
Total Surface Area	151.3	cm^2	
Conversion Factor	4.7cm=2µm 1cm=	*taken from A4 print* 0.425532 µm	
Area After Conversion	2.7397E-11	m^2	

Number of rods:	1st part	2nd part	3rd part	4th part	5th part	6th part	7th part	8th part	9th part
	3	3	4	1	1	3	1	2	2

Total number of 20

rods:

Total Surface Area	5.4794E-10	m^2

This surface area is from total dimensions of 14.6μm × 8.51μm

Actual Dimensions of the glass substrate		2x1cm^2	
or		20×10^3μm by 10×10^3μm	
Hence Total surface area			
	14.6μm × 8.51μm	5.48E-10	
	1	4.41E-12	
	20×10^3μm by 10×10^3μm	0.000882	m^2
		882.0248	mm^2
	Grand Surface Area		
		882.0248	mm^2

For Morphology Co15%:S2-MS

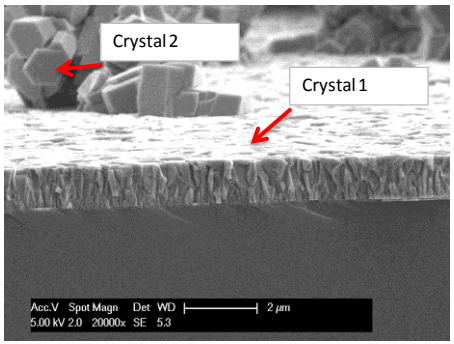

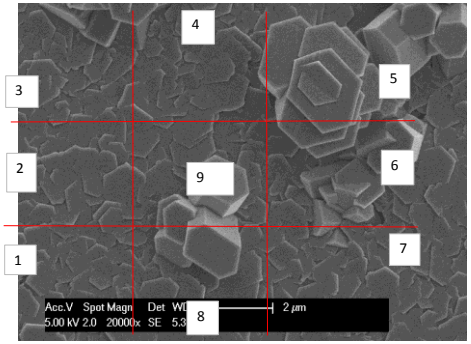

Note : All dimension were noted from A4 print of true SEM image

Assumption Same crystal with two different crystal dimensions

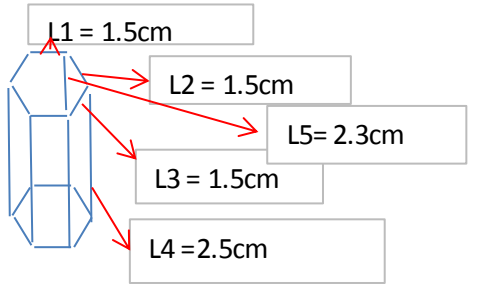

Dimension of crystal 1

Top Surface Area	5.75	cm^2
Side Surface Area	22.5	cm^2
Total Surface Area	28.25	cm^2
Conversion Factor	4.7cm=2µm	*taken from A4 print*
	1cm=	0.425532 µm
Area After Conversion	5.11544E-12	m^2

Number of rods:	1st part	2nd part	3rd part	4th part	5th part	6th part	7th part	8th part	9th part
	35	28	29	28	25	21	35	27	22

Total number of rods: 250

Total Surface Area 1.27886E-09 m^2

This surface area is from total dimensions of 14.6µm × 8.51µm

Actual Dimensions of the glass substrate 2x1cm^2

or 20×10^3µm by 10×10^3µm

Hence Total surface area

14.6µm × 8.51µm	1.28E-09	
1	1.03E-11	
20×10^{3}µm by 10×10^{3}µm	0.002059	m^2
	2058.592	mm^2

Dimension of crystal 2

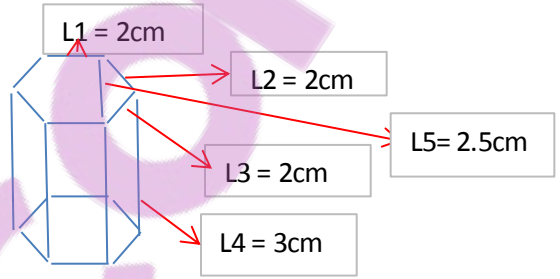

Top Surface Area	7.5	cm^2	
Side Surface Area	36	cm^2	
Total Surface Area	43.5	cm^2	
Conversion Factor	4.7cm=2µm	*taken from A4 print*	
	1cm=	0.425532	µm
Area After Conversion	7.88E-12	m^2	

Number of rods:	1st part	2nd part	3rd part	4th part	5th part	6th part	7th part	8th part	9th part
	0	0	0	1	5	4	0	2	1

Total number of rods: 13

Total Surface Area 1.02E-10 m^2

This surface area is from total dimensions of 14.6µm × 8.51µm

Actual Dimensions of the glass substrate 2x1cm^2

or 20×10^{3}µm by 10×10^{3}µm

Hence Total surface area

14.6µm	×	1.02E-10	
8.51µm			
1		8.24E-13	
20×10^{3}µm	by	0.000165	m^2
10×10^{3}µm			
		164.8331	mm^2

Grand Surface Area

2223.425 mm^2

For Morphology Co15%:S2-CG

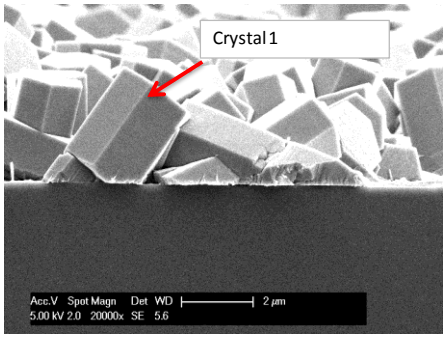

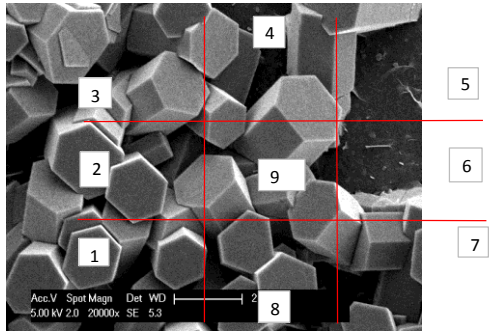

Dimension of crystal 1

Top Surface Area	12.54	cm^2
Side Surface Area	92.46	cm^2
Total Surface Area	105	cm^2
Conversion Factor	4.7cm=2µm	*taken from A4 print*
	1cm=	0.425532 µm
Area After Conversion	1.90131E-11	m^2

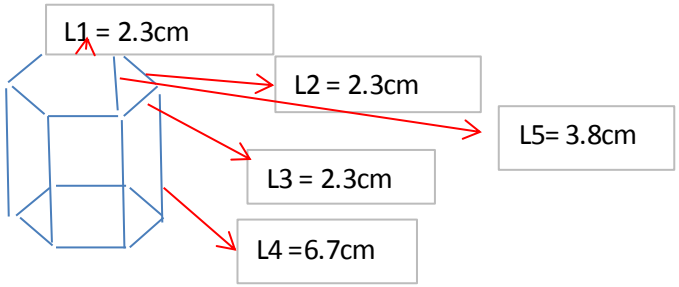

Number of rods:	1st part	2nd part	3rd part	4th part	5th part	6th part	7th part	8th part	9th part
	7	3	8	5	3	2	5	4	5

Total number of rods: 42

Total Surface Area 7.98551E-10 m^2

This surface area is from total dimensions of 14.6µm × 8.51µm

Actual Dimensions of the glass substrate 2x1cm^2

or 20×10^3µm by 10×10^3µm

Hence Total surface area

14.6µm × 8.51µm	7.99E-10	
1	6.43E-12	
20×10^3µm by 10×10^3µm	0.001285	m^2
	1285.436	mm^2

Grand Surface Area

1285.436 mm^2

Undoped Morphologies: S1-MS

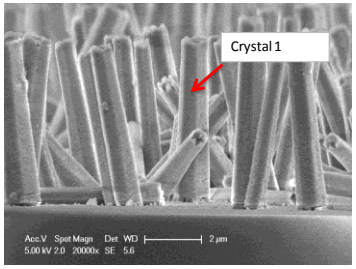

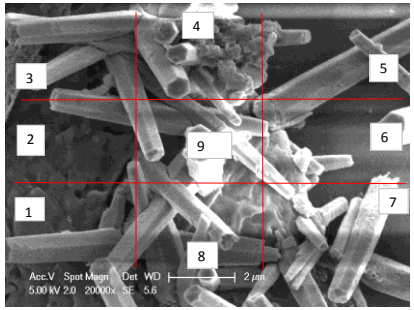

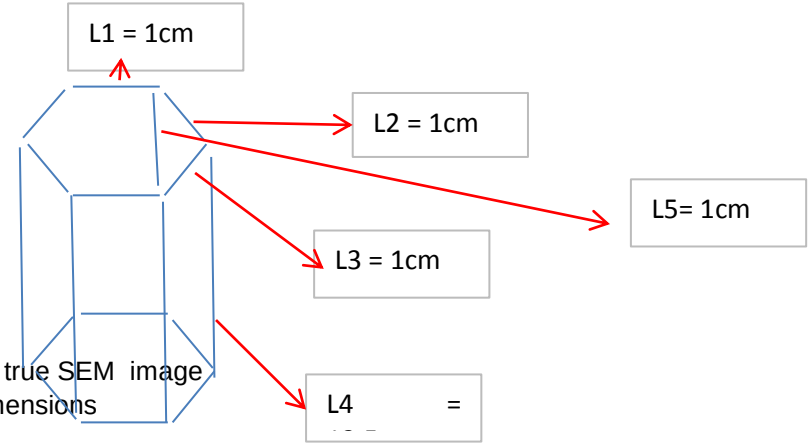

Note : All dimension were noted from A4 print of true SEM image
Assumption Same crystal with two different crystal dimensions

Top Surface Area		1.5	cm^2
Side Surface Area		75	cm^2
Total Surface Area		76.5	cm^2
Conversion Factor	4.7cm=2µm	*taken from A4 print*	
	1cm=	0.425532	µm
Area After Conversion		1.39E-11	m^2

Number of rods:	1st part	2nd part	3rd part	4th part	5th part	6th part	7th part	8th part	9th part
	1	1	4	5	3	2	6	8	4

Total number of rods: 34
Total Surface Area 4.71E-10 m^2

This surface area is from total dimensions of 14.6µm × 8.51µm

Actual Dimensions of the glass substrate		2x1cm^2	
or		20×10^{3}µm by 10×10^{3}µm	
Hence Total surface area			
	14.6µm × 8.51µm	4.71E-10	
	1	3.79E-12	
	20×10^{3}µm by 10×10^{3}µm	0.000758	m^2
		758.1449	mm^2
	Grand Surface Area		
		758.1449	mm^2

Undoped Morphologies: S1-CG

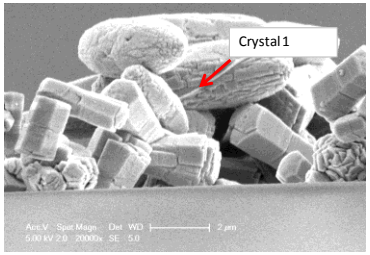

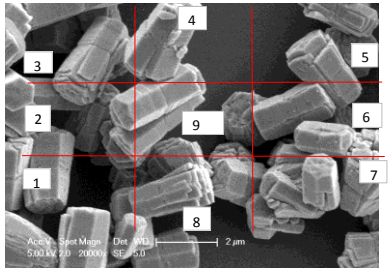

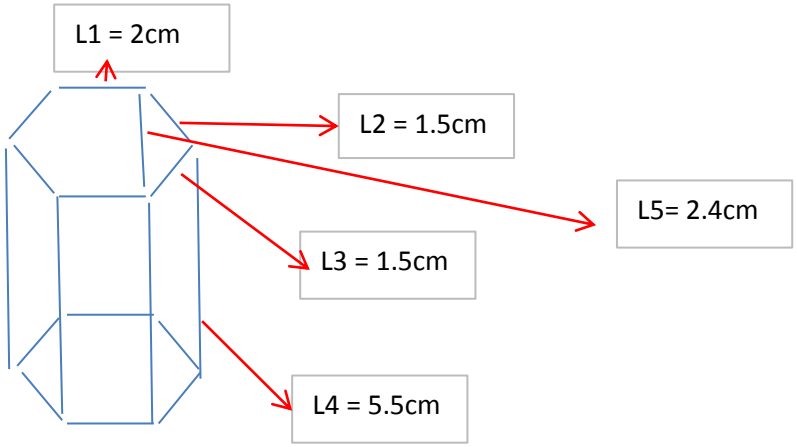

Note : All dimension were noted from A4 print of true SEM image
Assumption Same crystal with almost same crystal dimensions

Top Surface Area		7.2	cm^2
Side Surface Area		55	cm^2
Total Surface Area		62.2	cm^2
Conversion Factor	4.7cm=2μm		*taken from A4 print*
		1cm=	0.425532 μm
Area After Conversion		1.1263E-11	m^2

Number of rods:	1st part	2nd part	3rd part	4th part	5th part	6th part	7th part	8th part	9th part
	5	3	4	1	2	4	6	4	4

Total number of rods:	33	
Total Surface Area	3.71679E-10	m^2

This surface area is from total dimensions of 14.6μm × 8.51μm

Actual Dimensions of the glass substrate	2x1cm^2
or	20×10^3μm by 10×10^3μm

Hence Total surface area

14.6µm × 8.51µm	3.72E-10	
1	2.99E-12	
20×10^3µm by 10×10^3µm	0.000598	m^2
	598.2961	mm^2
Grand Surface Area		
	598.2961	mm^2

Undoped Morphologies: S2-MS

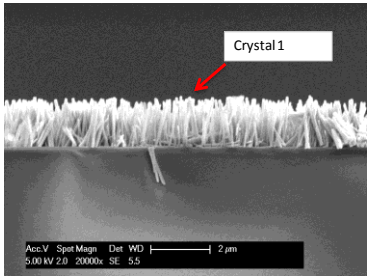

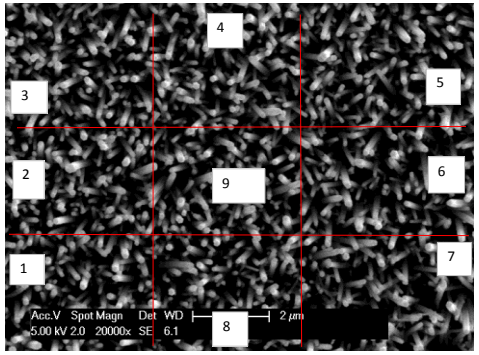

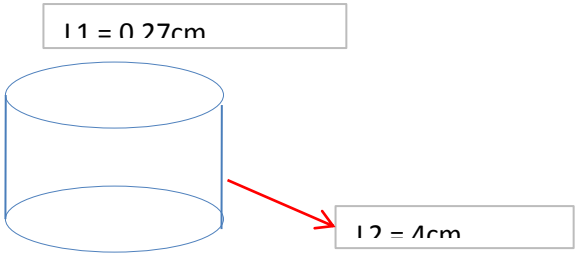

Note :	All dimension were noted from A4 print of true SEM image		
Assumption	Same crystal with two different crystal dimensions		
Top Surface Area	3.3912	cm^2	
Conversion Factor	4.7cm=2μm	*taken from A4 print*	
	1cm=	0.425532	μm
Area After Conversion	6.1407E-13	m^2	

Number of rods:	1st part	2nd part	3rd part	4th part	5th part	6th part	7th part	8th part	9th part
	403	415	425	436	410	427	403	417	455

Total number of rods:	3791	
Total Surface Area	2.32794E-09	m^2

This surface area is from total dimensions of 14.6μm × 8.51μm

Actual Dimensions of the glass substrate	2x1cm^2	
or	20×10^{3}µm by 10×10^{3}µm	

Hence Total surface area

14.6µm × 8.51µm	2.33E-09	
1	1.87E-11	
20×10^{3}µm by 10×10^{3}µm	0.003747	m^2
	3747.305	mm^2
Grand Surface Area		
	3747.305	mm^2

Undoped Morphologies: S2-CG

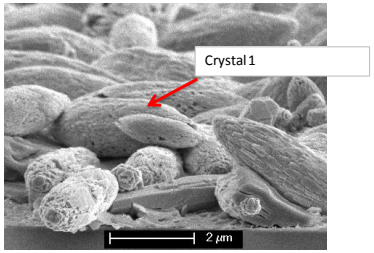

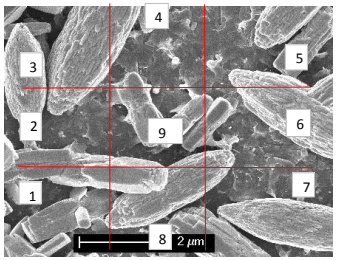

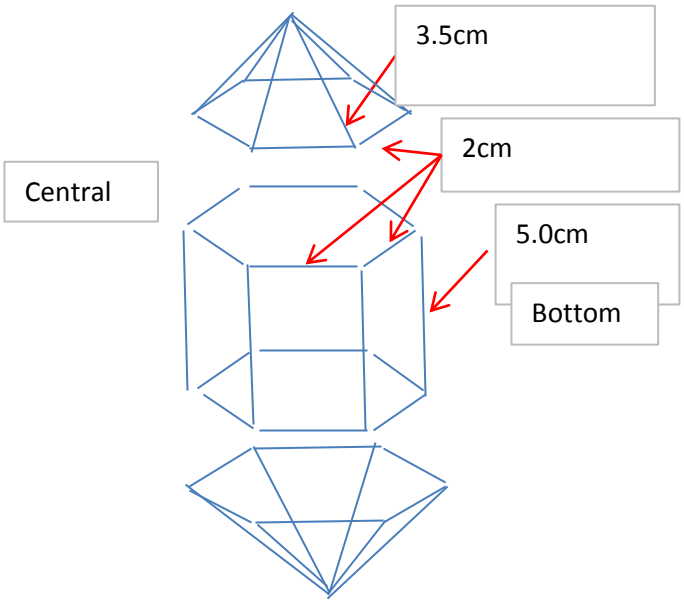

Top Surface Area		30	cm^2
Bottome Surface Area		30	cm^2
Central		60	cm^2
Total Surface Area		120	cm^2
Conversion Factor	4.7cm=2µm		*taken from A4 print*
		1cm=	0.425532 µm
Area After Conversion		2.17293E-11	m^2

Number of rods:	1st part	2nd part	3rd part	4th part	5th part	6th part	7th part	8th part	9th part
	5	3	4	1	2	1	1	3	2

Total number of rods:	22	
Total Surface Area	4.78044E-10	m^2

This surface area is from total dimensions of 14.6µm × 8.51µm

Actual Dimensions of the glass substrate	$2x1cm^2$
or	20×10^3µm by 10×10^3µm

Hence Total surface area

14.6µm × 8.51µm		4.78E-10
1		3.85E-12
20×10^3µm	by	0.00077 m^2

$10\times10^{3}\mu m$

769.5127 mm2

Surface Area Error Calculations

Morphology	***Surface Area (m^2)***			
	Batch I	***Batch II***	***Batch III***	***% Error***
S1-MS 2	7.58×10^{-4}	7.41×10^{-4}	7.21×10^{-4}	±5.0 %
S1-CG 2	5.98×10^{-4}	5.85×10^{-4}	5.77×10^{-4}	±3.0 %
S2-MS 1	3.74×10^{-3}	3.65×10^{-3}	3.61×10^{-3}	±2.8 %
S2-CG 1	7.7×10^{-4}	7.6×10^{-4}	7.4×10^{-4}	±2.0 %

Appendix L: Error in Reaction Rate constants

Errors in the rate constants were calculated by plotting three sets of data collected under the same conditions and determine the rate constant from these. The variation in reaction rate constants is summarised below;

Morphology	***O_2 limited conditions***			***% Error***	***O_2 Rich conditions***			***% Error***
	Run 1	Run 2	Run 3		Run 1	Run 2	Run 3	
	k''_{app} ($m^3\ m^{-2}\ s^{-1}$)	k''_{app} ($m^3\ m^{-2}\ s^{-1}$)	k''_{app} ($m^3\ m^{-2}\ s^{-1}$)		k''_{app} ($m^3\ m^{-2}\ s^{-1}$)	k''_{app} ($m^3\ m^{-2}\ s^{-1}$)	k''_{app} ($m^3\ m^{-2}\ s^{-1}$)	
S1-MS	1.13×10^{-3}	1.11×10^{-3}	1.09×10^{-3}	±3.53 %	1.30×10^{-3}	1.29×10^{-3}	1.28×10^{-3}	±1.53 %
S1-CG	3.27×10^{-4}	3.39×10^{-4}	3.17×10^{-4}	±3.05 %	3.81×10^{-4}	3.49×10^{-4}	3.64×10^{-4}	±4.46 %
S2-MS	6.27×10^{-4}	6.16×10^{-4}	6.29×10^{-4}	±1.75 %	1.11×10^{-3}	1.10×10^{-3}	1.10×10^{-3}	±0.90 %
S2-CG	3.12×10^{-4}	3.07×10^{-4}	3.01×10^{-4}	±3.51 %	3.59×10^{-4}	3.47×10^{-4}	3.62×10^{-4}	±3.52 %

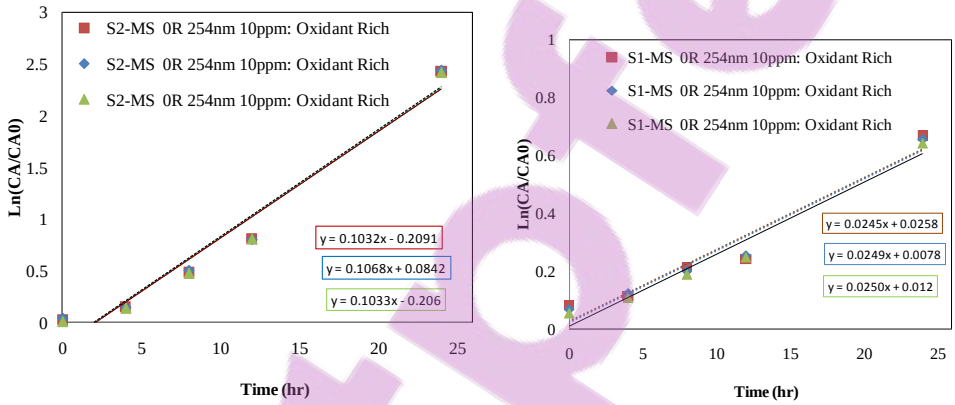

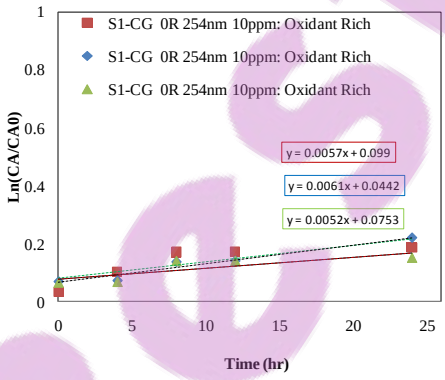

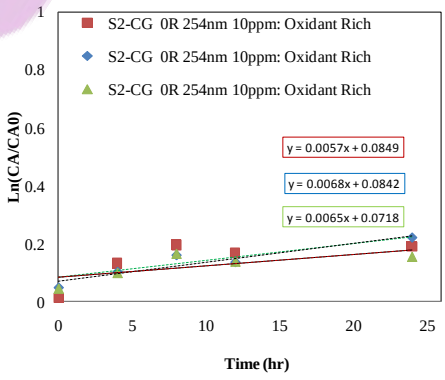

Appendix M: Mass Balance

The equation used to calculate mass balance is

Total number of moles at t_0 (A) = Total number of moles at any time t (B)

Where A = [moles of methylene blue + moles of impurities] at time t=0

B = [moles of methylene blue + moles of reaction intermediates + moles of mineralisation] at any time t

Results are summarised below. Where M_{MB} , M_{AB} , M_{AA} , M_{AC} ,M_{TH} represents the moles of Methylene Blue, Azure B, Azure A, Azure C, Thionin respectively.

<u>Morphology S1-MS</u>

<u>Mole balance after 4 hr reaction time</u>

Moles In (µ mol/L)	Mole Out (µ mol/L)
$M_{MB} + M_{AB} + M_{AA} + M_{AC} + M_{TH}$ 26.68 + 1.94 + 0.34 + 0.058 + 0.044 = 29.062	$M_{MB} + M_{AB} + M_{AA} + M_{AC} + M_{TH}$ 26.00 + 1.95 + 0.35 + 0.063 + 0.052 = 28.415

<u>Mole balance after 8 hr reaction time</u>

Moles In (µ mol/L)	Mole Out (µ mol/L)
$M_{MB} + M_{AB} + M_{AA} + M_{AC} + M_{TH}$ 26.68 + 1.94 + 0.34 + 0.058 + 0.044 = 29.062	$M_{MB} + M_{AB} + M_{AA} + M_{AC} + M_{TH}$ 25.14 + 2.37 + 0.42 + 0.13 + 0.085 = 28.145

<u>Mole balance after 12 hr reaction time</u>

Moles In (µ mol/L)	Mole Out (µ mol/L)
$M_{MB} + M_{AB} + M_{AA} + M_{AC} + M_{TH}$ 26.68 + 1.94 + 0.34 + 0.058 + 0.044 = 29.062	$M_{MB} + M_{AB} + M_{AA} + M_{AC} + M_{TH}$ 24.62 + 2.53 + 0.51 + 0.22 + 0.17 = 28.05

Mole balance after 24 hr reaction time

Mass In (µ mol/L)	Mass Out (µ mol/L)
$M_{MB} + M_{AB} + M_{AA} + M_{AC} + M_{TH}$ 26.68 + 1.94 + 0.34 + 0.058 + 0.044 = 29.062	$M_{MB} + M_{AB} + M_{AA} + M_{AC} + M_{TH}$ 17.99+ 4.63 + 1.083 + 0.60 + 0.53 = 24.86

Morphology S2-MS

Mole balance after 4 hr reaction time

Moles In (µ mol/L)	Mole Out (µ mol/L)
$M_{MB} + M_{AB} + M_{AA} + M_{AC} + M_{TH}$ 26.38 + 1.90 + 0.36 + 0.028 + 0.057 = 28.72	$M_{MB} + M_{AB} + M_{AA} + M_{AC} + M_{TH}$ 15.69 + 3.70 + 1.26 + 0.63 + 0.90 = 22.18

Mole balance after 8 hr reaction time

Moles In (µ mol/L)	Mole Out (µ mol/L)
$M_{MB} + M_{AB} + M_{AA} + M_{AC} + M_{TH}$ 26.38 + 1.90 + 0.36 + 0.028 + 0.057 = 28.72	$M_{MB} + M_{AB} + M_{AA} + M_{AC} + M_{TH}$ 11.65 + 3.54 + 1.82 + 1.16 + 1.64 = 19.81

Mole balance after 12 hr reaction time

Moles In (µ mol/L)	Mole Out (µ mol/L)
$M_{MB} + M_{AB} + M_{AA} + M_{AC} + M_{TH}$ 26.38 + 1.90 + 0.36 + 0.028 + 0.057 = 28.72	$M_{MB} + M_{AB} + M_{AA} + M_{AC} + M_{TH}$ 8.55 + 3.04 + 1.40 + 0.74 + 1.58 = 15.31

Mole balance after 24 hr reaction time

Mass In (µ mol/L)	Mass Out (µ mol/L)
$M_{MB} + M_{AB} + M_{AA} + M_{AC} + M_{TH}$ 26.38 + 1.90 + 0.36 + 0.028 + 0.057 = 28.72	$M_{MB} + M_{AB} + M_{AA} + M_{AC} + M_{TH}$ 6.04+ 0.33+ 0.37 + 0.22 + 0.59 = 7.55

Doped Morphology Co:S1-MS(15%)

Mole balance after 4 hr reaction time

Moles In (µ mol/L)	Mole Out (µ mol/L)
$M_{MB} + M_{AB} + M_{AA} + M_{AC} + M_{TH}$ 26.18 + 2.00 + 0.43 + 0.44 + 0.13 = 29.18	$M_{MB} + M_{AB} + M_{AA} + M_{AC} + M_{TH}$ 25.85 + 2.29 +0.46 + 0.46 +0.16 = 29.22

Mole balance after 8 hr reaction time

Moles In (µ mol/L)	Mole Out (µ mol/L)
$M_{MB} + M_{AB} + M_{AA} + M_{AC} + M_{TH}$ 26.18 + 2.00 + 0.43 + 0.44 + 0.13 = 29.18	$M_{MB} + M_{AB} + M_{AA} + M_{AC} + M_{TH}$ 24.64 +2.18 + 0.44 + 0.44 + 0.11 = 27.81

Mole balance after 12 hr reaction time

Moles In (µ mol/L)	Mole Out (µ mol/L)
$M_{MB} + M_{AB} + M_{AA} + M_{AC} + M_{TH}$ 26.18 + 2.00 + 0.43 + 0.44 + 0.13 = 29.18	$M_{MB} + M_{AB} + M_{AA} + M_{AC} + M_{TH}$ 22.34 +1.96 +0.42 + 0.39 + 0.10 = 25.21

Mole balance after 24 hr reaction time

Mass In (µ mol/L)	Mass Out (µ mol/L)
$M_{MB} + M_{AB} + M_{AA} + M_{AC} + M_{TH}$ 26.18 + 2.00 + 0.43 + 0.44 + 0.13 = 29.18	$M_{MB} + M_{AB} + M_{AA} + M_{AC} + M_{TH}$ 21.50+ 1.98 + 0.39 +0.36 +0.07 = 24.30

Doped Morphology Co:S2-MS(15%)

Mole balance after 4 hr reaction time

Moles In (µ mol/L)	Mole Out (µ mol/L)
$M_{MB} + M_{AB} + M_{AA} + M_{AC} + M_{TH}$ 26.14 + 1.81 + 0.34 + 0.35 +0.11 = 28.75	$M_{MB} + M_{AB} + M_{AA} + M_{AC} + M_{TH}$ 25.09 +2.09 +0.37 + 0.38 +0.10 = 28.03

Mole balance after 8 hr reaction time

Moles In (µ mol/L)	Mole Out (µ mol/L)
$M_{MB} + M_{AB} + M_{AA} + M_{AC} + M_{TH}$ 26.14 + 1.81 + 0.34 + 0.35 +0.11 = 28.75	$M_{MB} + M_{AB} + M_{AA} + M_{AC} + M_{TH}$ 23.78 +2.29 +0.40 +0.40 + 0.10 = 26.97

Mole balance after 12 hr reaction time

Moles In (µ mol/L)	Mole Out (µ mol/L)
$M_{MB} + M_{AB} + M_{AA} + M_{AC} + M_{TH}$ 26.14 + 1.81 + 0.34 + 0.35 +0.11 = 28.75	$M_{MB} + M_{AB} + M_{AA} + M_{AC} + M_{TH}$ 23.82 +1.81 +0.37 +0.31 + 0.08 = 26.39

Mole balance after 24 hr reaction time

Mass In (µ mol/L)	Mass Out (µ mol/L)
$M_{MB} + M_{AB} + M_{AA} + M_{AC} + M_{TH}$ 26.14 + 1.81 + 0.34 + 0.35 +0.11 = 28.75	$M_{MB} + M_{AB} + M_{AA} + M_{AC} + M_{TH}$ 22.18+ 1.67 + 0.35 + 0.29 +0.01 = 25.11

Discussion

The results indicate that total moles at t=0 is not exactly the same as to the number of moles at any time t, especially for the results obtained under morphology S2-MS. This could be because of higher level of mineralisation as it was evident from apparent colour change (dark blue to sky blue). As TOC results were not reliable, therefore the moles of CO_2 and other mineralisation products could be the possible cause of overall error in mass balance. As it can be seen that difference in total moles at t=0 and at any time t is gradually increases that could be the most likely indication of increased level of mineralisation. For morphology S1-MS, almost the mass in ~ mass out, indicated that there is least level of mineralisation of MB, as evident by the lack of degradation of formed reaction intermediates.

The results obtained for doped morphologies such as Co:S1-MS and Co:S2-MS has overall shown less error in moles balance, an indication of the lack of total mineralisation as it was seen for un-doped morphology S2-MS

From above mass balance, in case of un-doped morphologies , apparently it can clearly seen that formed reaction intermediates were clearly further degraded as compared with the results obtained under doped morphologies such as (Co:S1-MS and Co:S2-MS). However, further

work is needed to establish/justify the unaccounted mass present in the reaction vessel and to ensure that presence of cobalt is detrimental to the formation and further degradation of reaction intermediates.

References

1. Gaya, U.I., et al., *Photocatalytic treatment of 4-chlorophenol in aqueous ZnO suspensions: Intermediates, influence of dosage and inorganic anions.* Journal of Hazardous Materials, 2009. **168**(1): p. 57-63.
2. Marci, G., et al., *Preparation Characterization and Photocatalytic Activity of Polycrystalline ZnO/TiO2 Systems. 2. Surface, Bulk Characterization, and 4-Nitrophenol Photodegradation in Liquidâ^'Solid Regime.* The Journal of Physical Chemistry B, 2001. **105**(5): p. 1033-1040.
3. Kamat, P.V., R. Huehn, and R. Nicolaescu, *A "sense and shoot" approach for photocatalytic degradation of organic contaminants in water.* Journal of Physical Chemistry B, 2002. **106**(4): p. 788-794.
4. Yang, J.L., et al., *Photocatalysis using ZnO thin films and nanoneedles grown by metal-organic chemical vapor deposition.* Advanced Materials, 2004. **16**(18): p. 1661-1664.
5. Umar, A., ed. *Metal Oxide Nanostructures and Their Applications*. Vol. 5. 2010 American Scientific Publishers.
6. Lee, S., et al., *Resistive switching characteristics of ZnO thin film grown on stainless steel for flexible nonvolatile memory devices.* Applied Physics Letters, 2009. **95**(26): p. 262113-3.
7. Yan, X., et al., *Template Growth of ZnO Nanorods and Microrods with Controllable Densities.* Crystal Growth & Design, 2008. **8**(7): p. 2406-2410.
8. Li, Z.W., W. Gao, and R.J. Reeves, *Zinc oxide films by thermal oxidation of zinc thin films.* Surface and Coatings Technology, 2005. **198**(1-3): p. 319-323.
9. Guo, M., P. Diao, and S. Cai, *Hydrothermal growth of well-aligned ZnO nanorod arrays: Dependence of morphology and alignment ordering upon preparing conditions.* Journal of Solid State Chemistry, 2005. **178**(6): p. 1864-1873.
10. Gao, W. and Z. Li, *ZnO thin films produced by magnetron sputtering.* Ceramics International, 2004. **30**(7): p. 1155-1159.
11. Ferreira-Leitão, V.S., J.G. da Silva, and E.P.S. Bon, *Methylene blue and azure B oxidation by horseradish peroxidase: a comparative evaluation of class II and class III peroxidases.* Applied Catalysis B: Environmental, 2003. **42**(2): p. 213-221.
12. Calza, P., et al., *Identification of Degradation Products by Adopting GC or HPLC/MS Techniques.* Current Analytical Chemistry, 2005. **1**: p. 267-287.
13. Gogate, P.R. and A.B. Pandit, *A review of imperative technologies for wastewater treatment I: oxidation technologies at ambient conditions.* Advances in Environmental Research, 2004. **8**(3-4): p. 501-551.
14. Akyol, A., H.C. Yatmaz, and M. Bayramoglu, *Photocatalytic decolorization of Remazol Red RR in aqueous ZnO suspensions.* Applied Catalysis B: Environmental, 2004. **54**(1): p. 19-24.
15. Adewuyi, Y.G., *Sonochemistry in Environmental Remediation. 1. Combinative and Hybrid Sonophotochemical Oxidation Processes for the Treatment of Pollutants in Water.* Environmental Science & Technology, 2005. **39**(10): p. 3409-3420.
16. Martinez-Huitle, C.A. and S. Ferro, *Electrochemical oxidation of organic pollutants for the wastewater treatment: direct and indirect processes.* Chemical Society Reviews, 2006. **35**(12): p. 1324-1340.
17. Kawakami, W., et al., *Electron-beam oxidation treatment of a commercial dye by use of a dual-tube bubbling column reactor.* Environmental Science & Technology, 1978. **12**(2): p. 189-194.

18. Mishra, V.S., V.V. Mahajani, and J.B. Joshi, *Wet Air Oxidation.* Industrial & Engineering Chemistry Research, 1995. **34**(1): p. 2-48.
19. Patterson, D.A., et al., *Wet Air Oxidation of Linear Alkylbenzene Sulfonate 1. Effect of Temperature and Pressure.* Industrial & Engineering Chemistry Research, 2001. **40**(23): p. 5507-5516.
20. Castello, G.K., *Handbook of photocatalysts : preparation, structure and applications*: New York : Nova Science Publishers, c2010.
21. Chakravarty, D., *Photocatalytic cleaning of wastewater studied by in situ infrared spectroscopy*, in *Laboratory for surface spectroscopy and nanosciences*2007, Universite de Neuchatel. p. 22.
22. Devilliers, D., *Semiconductor photocatalysis: Still an Active Research Area Despite Barriers to Commercialization*, in *Energia (Center for Applied Energy Research)*2006: UK.
23. Tseng, J.M. and C.P. Huang, Water Sci. Technol., 1991. **23**: p. 377.
24. Kabra, K., R. Chaudhary, and R.L. Sawhney, *Treatment of hazardous organic and inorganic compounds through aqueous-phase photocatalysis: A review.* Industrial and Engineering Chemistry Research, 2004. **43**(24): p. 7683-7696.
25. Davis, R.J., et al., *Photocatalytic Decolorization of Wastewater Dyes.* Water Environment Research, 1994. **66**(1): p. 50-53.
26. Tanaka, K., K. Padermpole, and T. Hisanaga, Water Res., 2000. **34**(1): p. 327.
27. Sakthivel, S., et al., Water Sci. Technol., 2001. **44**(5): p. 211.
28. Arslan, I., I.A. Balcioglu, and D.W. Bahnemann, Water Sci. Technol., 2001. **44**(5): p. 171.
29. Liu, M., et al., *Photocatalytic Water Splitting to Hydrogen over a Visible Light-Driven LaTaON2 Catalyst.* Chinese Journal of Catalysis, 2006. **27**(7): p. 556-558.
30. Gamage, J. and Z. Zhang, *applications of photocatalytic disinfection.* International Journal of Photoenergy, 2010: p. 11.
31. *Pilkington Active Self Cleaning Glass*. Available from: http://www.pilkingtonselfcleaningglass.co.uk/.
32. *ScienceDaily*. . 2010; Available from: http://www.sciencedaily.com/releases/2010/01/100119121539.htm.
33. Chang, H.T., N.-M. Wu, and F. Zhu, *A kinetic model for photocatalytic degradation of organic contaminants in a thin-film TiO2 catalyst.* Water Research, 2000. **34**(2): p. 407-416.
34. Fouad, O.A., et al., *Zinc oxide thin films prepared by thermal evaporation deposition and its photocatalytic activity.* Applied Catalysis B: Environmental, 2006. **62**(1-2): p. 144-149.
35. Zhang, A., et al., *Progress in research on application of photocatalytic oxidation process in pharmaceutical wastewater treatment.* Gongye Yongshui Yu Feishui, 2006. **37**(5): p. 1-6.
36. Kryukov, A.I., et al., *Homogeneous photocatalysis of ethanol reduction of nitrobenzene by titanium complexes.* Theoretical and Experimental Chemistry, 1993. **28**(5): p. 319-321.
37. Zalazar, C.S., et al., *Comparison of H2O2/UV and Heterogeneous Photocatalytic Processes for the Degradation of Dichloroacetic Acid In Water.* Environmental Science & Technology, 2008. **42**(16): p. 6198-6204.
38. Tarr, M.A. and I. NetLibrary, *Chemical degradation methods for wastes and pollutants environmental and industrial applications*2003: New York : M. Dekker, c2003.

39. Tarr, M.A., *Chemical degradation methods for waste pollutants*2003: Marcel Dekker INC.
40. Bussi, J., et al., *Photocatalytic Removal of Hg from Solid Wastes of Chlor-Alkali Plant.* Journal of Environmental Engineering, 2002. **128**(8): p. 733-739.
41. Linsebigler, A.L., G. Lu, and J.T. Yates, *Photocatalysis on TiO2 Surfaces: Principles, Mechanisms, and Selected Results.* Chemical Reviews, 1995. **95**(3): p. 735-758.
42. Daneshvar, N., D. Salari, and A.R. Khataee, *Photocatalytic degradation of azo dye acid red 14 in water on ZnO as an alternative catalyst to TiO2.* Journal of Photochemistry and Photobiology A: Chemistry, 2004. **162**(2-3): p. 317-322.
43. Turchi, C.S. and D.F. Ollis, *Mixed reactant photocatalysis: Intermediates and mutual rate inhibition.* Journal of Catalysis, 1989. **119**(2): p. 483-496.
44. Chen, C.-C., *Degradation pathways of ethyl violet by photocatalytic reaction with ZnO dispersions.* Journal of Molecular Catalysis A: Chemical, 2007. **264**(1-2): p. 82-92.
45. Hoffmann, M.R., et al., *Environmental Applications of Semiconductor Photocatalysis.* Chemical Reviews, 1995. **95**(1): p. 69-96.
46. Turchi, C.S. and D.F. Ollis, *Photocatalytic degradation of organic water contaminants: Mechanisms involving hydroxyl radical attack.* Journal of Catalysis, 1990. **122**(1): p. 178-192.
47. Bhatkhande, D.S., et al., J. Chem. Technol. Biotechnol., 2001. **77**: p. 102.
48. Hodes, G., D. Cahen, and J. Manassen, Nature, 1976. **260**: p. 312.
49. Dhananjay, S.B., G.P. Vishwas, and M.B. Anthony A C *Photocatalytic degradation for environmental applications - a review.* Journal of Chemical Technology & Biotechnology, 2002. **77**(1): p. 102-116.
50. Height, M.J., et al., *Ag-ZnO catalysts for UV-photodegradation of methylene blue.* Applied Catalysis B: Environmental, 2006. **63**(3-4): p. 305-312.
51. Jagadish, C., S.J. Pearton, and ScienceDirect, *Zinc oxide bulk, thin films and nanostructures processing, properties and applications*2006: Amsterdam ; London : Elsevier, 2006.
52. Zhong Lin, W., *Zinc oxide nanostructures: growth, properties and applications.* Journal of Physics: Condensed Matter, 2004. **16**(25): p. R829.
53. Kavitha, R., S. Meghani, and V. Jayaram, *Synthesis of titania films by combustion flame spray pyrolysis technique and its characterization for photocatalysis.* Materials Science and Engineering: B, 2007. **139**(2-3): p. 134-140.
54. Wang, H., et al., *Comparison of dye degradation efficiency using ZnO powders with various size scales.* Journal of Hazardous Materials, 2007. **141**(3): p. 645-652.
55. Sakthivel, S., et al., *Solar photocatalytic degradation of azo dye: comparison of photocatalytic efficiency of ZnO and TiO2.* Solar Energy Materials and Solar Cells, 2003. **77**(1): p. 65-82.
56. Daneshvar, N., et al., *Preparation and investigation of photocatalytic properties of ZnO nanocrystals: effect of operational parameters and kinetic study.(Report).* International Journal of Chemical and Biomolecular Engineering, 2008. **1**(1): p. 24.
57. Chakrabarti, S. and B.K. Dutta, *Dye-sensitised photocatalytic degradation of PVC-ZnO composite film.* International Journal of Environmental Technology and Management, 2008. **9**(1): p. 34-46.
58. Shao, Z.B., et al., *Fabrication of nanometer-sized zinc oxide at low decomposing temperature.* Journal of Materials Processing Technology, 2006. **178**(1-3): p. 247-250.

59. Dindar, B. and S. Iasli, *Unusual photoreactivity of zinc oxide irradiated by concentrated sunlight.* Journal of Photochemistry and Photobiology A: Chemistry, 2001. **140**(3): p. 263-268.
60. Hayat, K., et al., *Kinetic study of laser-induced photocatalytic degradation of dye (alizarin yellow) from wastewater using nanostructured ZnO.* Journal of Environmental Science and Health, Part A: Toxic/Hazardous Substances and Environmental Engineering. **45**(11): p. 1413 - 1420.
61. Behnajady, M.A., N. Modirshahla, and R. Hamzavi, *Kinetic study on photocatalytic degradation of C.I. Acid Yellow 23 by ZnO photocatalyst.* Journal of Hazardous Materials, 2006. **133**(1-3): p. 226-232.
62. Peternel, I.T., et al., *Comparative study of UV/TiO2, UV/ZnO and photo-Fenton processes for the organic reactive dye degradation in aqueous solution.* Journal of Hazardous Materials, 2007. **148**(1-2): p. 477-484.
63. Ullah, R. and J. Dutta. *Photocatalytic activities of ZnO nanoparticles synthesized by wet chemical techniques*. in *Emerging Technologies, 2006. ICET '06. International Conference on*. 2006.
64. Xu, L., et al., *ZnO with Different Morphologies Synthesized by Solvothermal Methods for Enhanced Photocatalytic Activity.* Chemistry of Materials, 2009. **21**(13): p. 2875-2885.
65. Li, X., et al., *Synthesis and characterization of ZnO and TiO2 hollow spheres with enhanced photoreactivity.* Materials Science and Engineering: B, 2009. **158**(1-3): p. 40-47.
66. Kim, S.-J. and D.-W. Park, *Preparation of ZnO nanopowders by thermal plasma and characterization of photo-catalytic property.* Applied Surface Science, 2009. **255**(10): p. 5363-5367.
67. Zhang, D., et al., *Preparation and photocatalytic kinetics of nano-ZnO powders by precipitation stripping process.* Frontiers of Chemical Engineering in China, 2008. **2**(3): p. 319-324.
68. Yu, J. and X. Yu, *Hydrothermal synthesis and photocatalytic activity of zinc oxide hollow spheres.* Environmental Science and Technology, 2008. **42**(13): p. 4902-4907.
69. Rajeshwar, K., et al., *Heterogeneous photocatalytic treatment of organic dyes in air and aqueous media.* J. Photochem. Photobiol., C, 2008. **9**(4): p. 171-192.
70. Chakrabarti, S. and B.K. Dutta, *Photocatalytic degradation of model textile dyes in wastewater using ZnO as semiconductor catalyst.* Journal of Hazardous Materials, 2004. **112**(3): p. 269-278.
71. Park, S., et al., *Photocatalytic ZnO nanopowders prepared by solution combustion method for noble metal recovery.* Journal of Materials Science, 2003. **38**: p. 4493-4497.
72. Anderson, J.V., et al., Sol. Energy Mater., 1991. **24**: p. 538.
73. Rajendra Singh, T., C. Rubina, and S. Chandan, *Fundamentals and applications of the photocatalytic treatment for the removal of industrial organic pollutants and effects of operational parameters: A review.* Journal of Renewable and Sustainable Energy. **2**(4): p. 042701.
74. Lee, S.-K., *Detoxification of water by semiconductor photocatalysis*, in *School of enviornmental Science and Engineering*, Pohang University of Science and Technology: Pohang.
75. Mukherjee, P.S. and A.K. Ray, *Major challenges in the design of a large-scale photocatalytic reactor for water treatment.* Chemical Engineering and Technology, 1999. **22**(3): p. 253-260.

76. Daneshvar, N., et al., *Removal of C.I. Acid Orange 7 from aqueous solution by UV irradiation in the presence of ZnO nanopowder.* Journal of Hazardous Materials, 2007. **143**(1-2): p. 95-101.
77. Evgenidou, E., K. Fytianos, and I. Poulios, *Photocatalytic oxidation of dimethoate in aqueous solutions.* Journal of Photochemistry and Photobiology A: Chemistry, 2005. **175**(1): p. 29-38.
78. *Zn pourbaix diagram*. Available from: http://commons.wikimedia.org/wiki/File:Zn-pourbaix-diagram.svg.
79. Khodja, A.A., et al., *Photocatalytic degradation of 2-phenylphenol on TiO2 and ZnO in aqueous suspensions.* Journal of Photochemistry and Photobiology A: Chemistry, 2001. **141**(2-3): p. 231-239.
80. Parks, G.A., *The Isoelectric Points of Solid Oxides, Solid Hydroxides, and Aqueous Hydroxo Complex Systems.* Chemical Reviews, 1965. **65**(2): p. 177-198.
81. Poulios, I., M. Kositzi, and A. Kouras, *Photocatalytic decomposition of triclopyr over aqueous semiconductor suspensions.* Journal of Photochemistry and Photobiology A: Chemistry, 1998. **115**(2): p. 175-183.
82. Zouaghi, R., et al., *Photocatalytic Degradation of Monolinuron and Linuron in an Aqueous Suspension of Titanium Dioxide Under Simulated Solar Irradiation* Revue des sciences de l'eau / Journal of Water Science, 2007. **20**: p. 163-172.
83. Han, J., W. Qiu, and W. Gao, *Potential dissolution and photo-dissolution of ZnO thin films.* Journal of Hazardous Materials. **178**(1-3): p. 115-122.
84. *Internal Standard ISO 21348:2007E*, 2007, Space Enviornment Technologies.
85. Ollis, D.F., E. Pelizzetti, and N. Serpone, *Photocatalyzed destruction of water contaminants.* Environ. Sci. Technol., 1991. **25**(9): p. 1522-9.
86. Yawalkar, A.A., et al., *Solar-assisted photochemical and photocatalytic degradation of phenol.* Journal of Chemical Technology & Biotechnology, 2001. **76**: p. 363-370.
87. Crittenden, J.C., et al., Water Environ. Res., 1996. **68**: p. 270.
88. Okamoto, K., et al., *Kinetics of heterogeneous photocatalytic decomposition of phenol over anatase titanium dioxide powder.* Bull. Chem. Soc. Jpn., 1985. **58**(7): p. 2023-8.
89. Mark, S.M. and S.T. Craig, *Field testing solar photocatalytic detoxification on TCE-contaminated groundwater.* Environmental Progress, 1993. **12**(3): p. 194-199.
90. Ahmed, S. and D.F. Ollis, *Solar photoassisted catalytic decomposition of the chlorinated hydrocarbons trichloroethylene and trichloromethane.* Solar Energy, 1984. **32**(5): p. 597-601.
91. Li Puma, G. and P.L. Yue, *Effect of the Radiation Wavelength on the Rate of Photocatalytic Oxidation of Organic Pollutants.* Industrial & Engineering Chemistry Research, 2002. **41**(23): p. 5594-5600.
92. Matthews, R.W. and S.R. McEvoy, *A comparison of 254 nm and 350 nm excitation of TiO2 in simple photocatalytic reactors.* Journal of Photochemistry and Photobiology A: Chemistry, 1992. **66**(3): p. 355-366.
93. Hofstadler, K., et al., *New Reactor Design for Photocatalytic Wastewater Treatment with TiO2 Immobilized on Fused-Silica Glass Fibers: Photomineralization of 4-Chlorophenol.* Environmental Science & Technology, 1994. **28**(4): p. 670-674.
94. Li Puma, G. and P.L. Yue, *Comparison of the Effectiveness of Photon-Based Oxidation Processes in a Pilot Falling Film Photoreactor.* Environmental Science & Technology, 1999. **33**(18): p. 3210-3216.
95. Bayarri, B., et al., *Study of the wavelength effect in the photolysis and heterogeneous photocatalysis.* Catalysis Today, 2007. **129**(1-2): p. 231-239.
96. Liu, B., et al., *Photocatalytic mechanism of TiO2-CeO2 films prepared by magnetron sputtering under UV and visible light.* Surface Science, 2005. **595**(1-3): p. 203-211.

97. Tavares, C.J., et al., *Reactive sputtering deposition of photocatalytic TiO2 thin films on glass substrates.* Materials Science and Engineering: B, 2007. **138**(2): p. 139-143.
98. Eufinger, K., et al., *Effect of microstructure and crystallinity on the photocatalytic activity of TiO2 thin films deposited by dc magnetron sputtering.* Journal of Physics D: Applied Physics, 2007(17): p. 5232.
99. Mills, A., et al., *Novel low-temperature photocatalytic titania films produced by plasma-assisted reactive dc magnetron sputtering.* Journal of Photochemistry and Photobiology A: Chemistry, 2007. **187**(2-3): p. 370-376.
100. Han, L., et al., *Comparison of ZnO thin films grown by pulsed laser deposition on sapphire and Si substrates.* Physica E: Low-dimensional Systems and Nanostructures, 2008. **40**(3): p. 699-704.
101. Zhang, W., L. Zou, and L. Wang, *Photocatalytic TiO2/adsorbent nanocomposites prepared via wet chemical impregnation for wastewater treatment: A review.* Appl. Catal., A, 2009. **371**(1-2): p. 1-9.
102. Djouadi, D., et al., *Optical properties of ZnO/silica nanocomposites prepared by sol-gel method and deposited by dip-coating technique.* Physics Procedia, 2009. **2**(3): p. 701-705.
103. Wang, X., et al., *Nitrogen doped ZnO film grown by the plasma-assisted metal-organic chemical vapor deposition.* Journal of Crystal Growth, 2001. **226**(1): p. 123-129.
104. Fabreguette, F., et al., *Conductimetry and impedance spectroscopy study of low pressure metal organic chemical vapor deposition TiNxOy films as a function of the growth temperature: a percolation approach.* Applied Surface Science, 2001. **175-176**: p. 574-578.
105. Park, S.H., et al., *Investigation on the ZnO:N films grown on (0 0 0 1) and (0 0 0 1^{-}) ZnO templates by plasma-assisted molecular beam epitaxy.* Journal of Crystal Growth, 2009. **311**(7): p. 2167-2171.
106. Yamaguchi, Y., et al., *Photocatalytic ZnO films prepared by anodizing.* Journal of Electroanalytical Chemistry, 1998. **442**(1-2): p. 1-3.
107. Rauf, M.A., et al., *Photocatalytic degradation of Methylene Blue using a mixed catalyst and product analysis by LC/MS.* Chemical Engineering Journal. **In Press, Corrected Proof**.
108. Riassetto, D., et al., *Mechanisms involved in the platinization of sol-gel-derived TiO2 thin films.* J. Photochem. Photobiol., A, 2009. **202**(2-3): p. 214-220.
109. Ghosal, S., et al., *Controlling Atomic Layer Deposition of TiO2 in Aerogels through Surface Functionalization.* Chemistry of Materials, 2009. **21**(9): p. 1989-1992.
110. Li, X., et al., *Synthesis and morphology control of ZnO nanostructures in microemulsions.* Journal of Colloid and Interface Science, 2009. **333**(2): p. 465-473.
111. Kato, K., et al., *Crystal structures of TiO2 thin coatings prepared from the alkoxide solution via the dip-coating technique affecting the photocatalytic decomposition of aqueous acetic acid.* Journal of Materials Science, 1994. **29**(22): p. 5911-5915.
112. Gao, W. and Z.-w. Li, *Fabrication of metal oxide films with strong colour emmision,* 2005.
113. Li, D. and H. Haneda, *Morphologies of zinc oxide particles and their effects on photocatalysis.* Chemosphere, 2003. **51**(2): p. 129-137.
114. Wu, P.-Y., et al., *Low-Temperature Synthesis of Zinc Oxide Nanoparticles.* International Journal of Applied Ceramic Technology, 2006. **3**(4): p. 272-278.
115. Tian, Z.R., et al., *Complex and oriented ZnO nanostructures.* Nat Mater, 2003. **2**(12): p. 821-826.

116. Yu, J., et al., *Preparation and photocatalytic activity of mesoporous anatase TiO2 nanofibers by a hydrothermal method.* Journal of Photochemistry and Photobiology A: Chemistry, 2006. **182**(2): p. 121-127.
117. Bakardjieva, S., et al., *Transformation of brookite-type TiO2 nanocrystals to rutile: correlation between microstructure and photoactivity.* Journal of Materials Chemistry, 2006. **16**(18): p. 1709-1716.
118. Wahi, R.K., et al., *Photodegradation of Congo Red catalyzed by nanosized TiO2.* Journal of Molecular Catalysis A: Chemical, 2005. **242**(1-2): p. 48-56.
119. Hariharan, C., *Photocatalytic degradation of organic contaminants in water by ZnO nanoparticles: Revisited.* Applied Catalysis A: General, 2006. **304**: p. 55-61.
120. Du, J., et al., *Control of ZnO morphologies via surfactants assisted route in the subcritical water.* Journal of Crystal Growth, 2005. **280**(1-2): p. 126-134.
121. Jang, Y.J., C. Simer, and T. Ohm, *Comparison of zinc oxide nanoparticles and its nano-crystalline particles on the photocatalytic degradation of methylene blue.* Materials Research Bulletin, 2006. **41**(1): p. 67-77.
122. Moghaddam, F.M. and H. Saeidian, *Controlled microwave-assisted synthesis of ZnO nanopowder and its catalytic activity for O-acylation of alcohol and phenol.* Materials Science and Engineering: B, 2007. **139**(2-3): p. 265-269.
123. Jun, Z., Shao, and X. Le, *Photocatalytic activity of ZnO thin films prepared by two-step thermal oxidation of Zn films*. Vol. 9. 2007, Bucuresti: INOE 2000. 4.
124. Yubuta, K., et al., *Structural characterization of ZnO nano-chains studied by electron microscopy.* Journal of Alloys and Compounds, 2007. **436**(1-2): p. 396-399.
125. Bideau, M., et al., *Diffusional Limitations in Liquid-Phase Photocatalysis.* Prog. React. Kinet, 1994. **19**.
126. Peterson, M.W., J.A. Turner, and A.J. Nozik, *Mechanistic studies of the photocatalytic behavior of titania: particles in a photoelectrochemical slurry cell and the relevance to photodetoxification reactions.* The Journal of Physical Chemistry, 1991. **95**(1): p. 221-225.
127. Shirayama, H., Y. Tohezo, and S. Taguchi, *Photodegradation of chlorinated hydrocarbons in the presence and absence of dissolved oxygen in water.* Water Research, 2001. **35**(8): p. 1941-1950.
128. Wang, Y. and C.-S. Hong, *TiO2-mediated photomineralization of 2-chlorobiphenyl: the role of O2.* Water Research, 2000. **34**(10): p. 2791-2797.
129. Chen, D. and A.K. Ray, *Photodegradation kinetics of 4-nitrophenol in TiO₂ suspension.* Water Research, 1998. **32**(11): p. 3223-3234.
130. Chen, D., F. Li, and A.K. Ray, *External and internal mass transfer effect on photocatalytic degradation.* Catalysis Today, 2001. **66**(2-4): p. 475-485.
131. Goetz, V., et al., *Modeling aqueous heterogeneous photocatalytic degradation of organic pollutants with immobilized TiO2.* Chemical Engineering and Processing: Process Intensification, 2009. **48**(1): p. 532-537.
132. Dijkstra, M.F.J., et al., *Modeling the photocatalytic degradation of formic acid in a reactor with immobilized catalyst.* Chemical Engineering Science. **57**(22-23): p. 4895-4907.
133. Tatterson, G.B., *Scaleup and design of industrial mixing processes (page 109)*2003: Greensboro, N.C. : Gary Tatterson, 2003.
134. Kasper, C., et al., *Bioreactor systems for tissue engineering (page 254)*2008: Berlin ; London : Springer, c2008.
135. Nagata, S., *Mixing : principles and applications (page 256)*1975: Tokyo : Kodansha ; New York : Wiley, 1975.

136. Ulbrecht, J.r.J. and G.K. Patterson, *Mixing of liquids by mechanical agitation (page 145)*1985: New York : Gordon and Breach, c1985.
137. Harnby, N., M.F. Edwards, and A.W. Nienow, *Mixing in the process industries (page 138)*1985: London ; Boston : Butterworths, 1985.
138. De Lasa, H.I., et al., *Photocatalytic reaction engineering*2005: New York : Springer, c2005.
139. Biard, P.-F.o., A. Bouzaza, and D. Wolbert, *Photocatalytic Degradation of Two Volatile Fatty Acids in an Annular Plug-Flow Reactor; Kinetic Modeling and Contribution of Mass Transfer Rate.* Environmental Science & Technology, 2007. **41**(8): p. 2908-2914.
140. Merabet, S., A. Bouzaza, and D. Wolbert, *Photocatalytic degradation of indole in a circulating upflow reactor by UV/TiO2 process--Influence of some operating parameters.* Journal of Hazardous Materials, 2009. **166**(2-3): p. 1244-1249.
141. Ray, A.K. and A.A.C.M. Beenackers, *Novel swirl-flow reactor for kinetic studies of semiconductor photocatalysis.* AIChE Journal, 1997. **43**(10): p. 2571-2578.
142. XiaoWei, H. and G. LieJin, *Numerical investigations of catalyst-liquid slurry flow in the photocatalytic reactor for hydrogen production based on algebraic slip model.* International Journal of Hydrogen Energy. **35**(13): p. 7065-7072.
143. Chen, T., et al., *Study on the Photocatalytic Degradation of Methyl Orange in Water Using Ag/ZnO as Catalyst by Liquid Chromatography Electrospray Ionization Ion-Trap Mass Spectrometry.* Journal of the American Society for Mass Spectrometry, 2008. **19**(7): p. 997-1003.
144. Balcerski, W., S.Y. Ryu, and M.R. Hoffmann, *Visible-Light Photoactivity of Nitrogen-Doped TiO2: Photo-oxidation of HCO2H to CO2 and H2O.* The Journal of Physical Chemistry C, 2007. **111**(42): p. 15357-15362.
145. Colón, G., et al., *Highly photoactive ZnO by amine capping-assisted hydrothermal treatment.* Applied Catalysis B: Environmental, 2008. **83**(1-2): p. 30-38.
146. Shifu, C., et al., *Preparation, characterization and photocatalytic activity of N-containing ZnO powder.* Chemical Engineering Journal, 2009. **148**(2-3): p. 263-269.
147. Rajeshwar, K., *Photoelectrochemistry and the environment.* Journal of Applied Electrochemistry, 1995. **25**(12): p. 1067-1082.
148. Matthews, R.W. and S.R. McEvoy, *Destruction of phenol in water with sun, sand, and photocatalysis.* Solar Energy, 1992. **49**(6): p. 507-513.
149. Matthews, R.W., *Photooxidative degradation of coloured organics in water using supported catalysts. TiO2 on sand.* Water Research, 1991. **25**(10): p. 1169-1176.
150. Thiruvenkatachari, R., S. Vigneswaran, and I. Moon, *A review on UV/TiO2 photocatalytic oxidation process (Journal Review).* Korean Journal of Chemical Engineering, 2008. **25**(1): p. 64-72.
151. Yan, H., et al., *Growth and photocatalytic properties of one-dimensional ZnO nanostructures prepared by thermal evaporation.* Materials Research Bulletin, 2009. **44**(10): p. 1954-1958.
152. Lem, W. and P. Eng, *Scale-up of a medium pressure UV systems for the treatment of N-Nitrosodimethylamine(NDMA) and its advantages over low pressure UV systems*.
153. Zhang, L., et al., *Photocatalytic Degradation of Organic Compounds in Aqueous Solutions by a TiO2-Coated Rotating Drum Reactor Using Solar Light.* Sol. Energy, 2001. **70**(4): p. 331.
154. Xi, W., S.U. Geissen, and A. Vogelpohl, *Solar detoxification of wastewater in a novel aerated cascade photoreactor (ACP)*. Vol. 44. 2001. 237-44.
155. Ray, A.K. and A.A.C.M. Beenackers, *Development of a new photocatalytic reactor for water purification.* Catalysis Today, 1998. **40**(1): p. 73-83.

156. Dionysiou, D.D., et al., *Continuous-mode photocatalytic degradation of chlorinated phenols and pesticides in water using a bench-scale TiO2 rotating disk reactor.* Applied Catalysis B: Environmental, 2000. **24**(3-4): p. 139-155.
157. Daneshvar, N., D. Salari, and A.R. Khataee, *Photocatalytic degradation of azo dye acid red 14 in water: investigation of the effect of operational parameters.* Journal of Photochemistry and Photobiology A: Chemistry, 2003. **157**(1): p. 111-116.
158. Messina, P.V. and P.C. Schulz, *Adsorption of reactive dyes on titania-silica mesoporous materials.* Journal of Colloid and Interface Science, 2006. **299**(1): p. 305-320.
159. Lachheb, H., et al., *Photocatalytic degradation of various types of dyes (Alizarin S, Crocein Orange G, Methyl Red, Congo Red, Methylene Blue) in water by UV-irradiated titania.* Applied Catalysis B: Environmental, 2002. **39**(1): p. 75-90.
160. Borgarello, E., et al., J. Am. Chem. Soc., 1982. **104**: p. 2996.
161. Choi, W., A. Termin, and M.R. Hoffmann, J. Phys. Chem., 1994. **98**: p. 13669.
162. Henderson, M.A., et al., J. Am. Chem. Soc., 2003. **125**: p. 14974.
163. Anpo, M. and M. Takeuchi, Int. J. Photoenergy, 2001. **3**: p. 1.
164. Anpo, M. and M. Takeuchi, J. Catal., 2003. **216**: p. 505.
165. Wang, A., et al., *Nano-structure, magnetic and optical properties of Co-doped ZnO films prepared by a wet chemical method.* Journal of Physics D: Applied Physics, 2008. **41**(21).
166. Xu, C., et al., *Preparation, characterization and photocatalytic activity of Co-doped ZnO powders.* Journal of Alloys and Compounds. **497**(1-2): p. 373-376.
167. Baiqi, W., et al., *Photoluminescence properties of Co-doped ZnO nanorods array fabricated by the solution method.* Physica E: Low-dimensional Systems and Nanostructures, 2009. **41**(3): p. 413-417.
168. Wei, L., Z. Li, and W.F. Zhang, *Influence of Co doping content on its valence state in Zn1-xCoxO (0 <= x <= 0.15) thin films.* Applied Surface Science, 2009. **255**(9): p. 4992-4995.
169. Pandiyarajan, T., et al., *Simple synthesis and spectroscopic studies on cobalt added ZnO nanocrystals.* Spectrochimica Acta Part A: Molecular and Biomolecular Spectroscopy, 2009. **74**(1): p. 84-86.
170. Yang, H. and S. Nie, *Preparation and characterization of Co-doped ZnO nanomaterials.* Materials Chemistry and Physics, 2009. **114**(1): p. 279-282.
171. Kerr, L.L., et al., *Raman analysis of nitrogen doped ZnO.* Thin Solid Films, 2007. **515**(13): p. 5282-5286.
172. Wong, M.-S., H. Pang Chou, and T.-S. Yang, *Reactively sputtered N-doped titanium oxide films as visible-light photocatalyst.* Thin Solid Films, 2006. **494**(1-2): p. 244-249.
173. Sato, S., Chem. Phys. Lett., 1986. **123**: p. 126.
174. Asahi, R., et al., Science, 2001. **293**: p. 269.
175. Sakthivel, S. and H. Kisch, Angew. Chem., Int. Ed., 2003. **42**: p. 4908.
176. Fujishima, A., X. Zhang, and D.A. Tryk, Surf. Sci. Rep., 2008. **63**: p. 515.
177. Mohamed, S.H., et al., *Influence of nitrogen content on properties of direct current sputtered TiO2 films.* physica status solidi (a), 2004. **201**(1): p. 90-102.
178. Wang, J., et al., *Origin of Photocatalytic Activity of Nitrogen-Doped TiO2 Nanobelts.* Journal of the American Chemical Society, 2009. **131**(34): p. 12290-12297.
179. Futsuhara, M., K. Yoshioka, and O. Takai, *Optical properties of zinc oxynitride thin films.* Thin Solid Films, 1998. **317**(1-2): p. 322-325.

180. Li, D. and H. Haneda, *Enhancement of photocatalytic activity of sprayed nitrogen-containing ZnO powders by coupling with metal oxides during the acetaldehyde decomposition.* Chemosphere, 2004. **54**(8): p. 1099-1110.
181. Li, D. and H. Haneda, *Synthesis of nitrogen-containing ZnO powders by spray pyrolysis and their visible-light photocatalysis in gas-phase acetaldehyde decomposition.* Journal of Photochemistry and Photobiology A: Chemistry, 2003. **155**(1-3): p. 171-178.
182. Lindgren, T., et al., *Photoelectrochemical and Optical Properties of Nitrogen Doped Titanium Dioxide Films Prepared by Reactive DC Magnetron Sputtering.* The Journal of Physical Chemistry B, 2003. **107**(24): p. 5709-5716.
183. Rogozin, I.V., *Nitrogen-doped p-type ZnO thin films and ZnO/ZnSe p-n heterojunctions grown on ZnSe substrate by radical beam gettering epitaxy.* Thin Solid Films, 2009. **517**(15): p. 4318-4321.
184. Yang, X., et al., *Nitrogen-Doped ZnO Nanowire Arrays for Photoelectrochemical Water Splitting.* Nano Letters, 2009. **9**(6): p. 2331-2336.
185. Alves, E., et al., *Structural and optical properties of nitrogen doped ZnO films.* Vacuum, 2009. **83**(10): p. 1274-1278.
186. Matsumoto, T., et al., *High visible-light photocatalytic activity of nitrogen-doped titania prepared from layered titania/isostearate nanocomposite.* Catalysis Today, 2007. **120**(2): p. 226-232.
187. Vanheusden, K., et al., *Impact of Pb doping on the optical and electronic properties of ZnO powders.* Applied Physics Letters, 1995. **67**(9): p. 1280-1282.
188. Ullah, R. and J. Dutta, *Photocatalytic degradation of organic dyes with manganese-doped ZnO nanoparticles.* Journal of Hazardous Materials, 2008. **156**(1-3): p. 194-200.
189. Colis, S., et al., *Magnetic properties of Co-doped ZnO diluted magnetic semiconductors prepared by low-temperature mechanosynthesis.* Chemical Physics Letters, 2006. **422**(4-6): p. 529-533.
190. Wang, R., et al., *The characteristics and photocatalytic activities of silver doped ZnO nanocrystallites.* Applied Surface Science, 2004. **227**(1-4): p. 312-317.
191. Serpone, N., *Is the Band Gap of Pristine TiO2 Narrowed by Anion- and Cation-Doping of Titanium Dioxide in Second-Generation Photocatalysts?* The Journal of Physical Chemistry B, 2006. **110**(48): p. 24287-24293.
192. Qiu, X. and C. Burda, *Chemically synthesized nitrogen-doped metal oxide nanoparticles.* Chemical Physics, 2007. **339**(1-3): p. 1-10.
193. J. Hays, *Effect of Co doping on the structural, optical and magnetic properties of ZnO nanoparticles.* Journal of Physics: Condensed Matter, 2007. **19**(26): p. 266203.
194. Jeong, T.S., et al., *Raman scattering and photoluminescence of As ion-implanted ZnO single crystal.* Journal of Applied Physics, 2004. **96**(1): p. 175-179.
195. Chen, S. and U. Nickel, *Controllable exciton bleaching and recovery observed in ZnO-Ag hybrid nanometre-sized particles.* Chemical Communications, 1996(2): p. 133-134.
196. Zheng, M. and J. Wu, *One-step synthesis of nitrogen-doped ZnO nanocrystallites and their properties.* Applied Surface Science, 2009. **255**(11): p. 5656-5661.
197. Liu, J., et al., *Fabrication and characterization of in-doped zinc oxide nanodisks.* Acta Physico - Chimica Sinica, 2006. **22**(1): p. 38-42.
198. Neogi, S.K., et al., *Effects of Co doping on structural, morphological and transport properties of sol-gel AZO thin films.* Journal of Alloys and Compounds, 2009. **487**(1-2): p. 269-273.

199. Kobayashi, K., et al., *Optical and electronic properties of cobalt-doped zinc oxide films prepared by the sputtering method.* Journal of Materials Science, 1992. **27**(21): p. 5953-5957.
200. Li, D., et al., *Transition metal-doped ZnO nanorods synthesized by chemical methods.* Journal of Physics and Chemistry of Solids. **69**(2-3): p. 616-619.
201. Sonnay, L., *Nitrogen Doped Zinc Oxide Thin Films*, 2000.
202. Lin, H.-F., S.-C. Liao, and S.-W. Hung, *The dc thermal plasma synthesis of ZnO nanoparticles for visible-light photocatalyst.* Journal of Photochemistry and Photobiology A: Chemistry, 2005. **174**(1): p. 82-87.
203. Sano, T., et al., *Preparation of a visible light-responsive photocatalyst from a complex of Ti4+ with a nitrogen-containing ligand.* Journal of Materials Chemistry, 2004. **14**(3): p. 380-384.
204. Chen, X.B. and C. Burda, J. Phys. Chem. B, 2004. **108**: p. 15446.
205. Burda, C., et al., *Enhanced Nitrogen Doping in TiO2 Nanoparticles.* Nano Letters, 2003. **3**(8): p. 1049-1051.
206. Bacsa, R., et al., *Preparation, Testing and Characterization of Doped TiO2 Active in the Peroxidation of Biomolecules under Visible Light.* The Journal of Physical Chemistry B, 2005. **109**(12): p. 5994-6003.
207. Chen, X., et al., Nano Lett., 2003. **3**: p. 799.
208. Gole, J.L., et al., J. Phys. Chem. B, 2004. **108**: p. 1230.
209. Prokes, S.M., et al., *Defect-Related Optical Behavior in Surface Modified TiO_{<FONT SIZE='-1'>2</FONT>} Nanostructures.* Advanced Functional Materials, 2005. **15**(1): p. 161-167.
210. Sathish, M., et al., *Synthesis, Characterization, Electronic Structure, and Photocatalytic Activity of Nitrogen-Doped TiO2 Nanocatalyst.* Chemistry of Materials, 2005. **17**(25): p. 6349-6353.
211. Belver, C., et al., *Nitrogen-containing TiO2 photocatalysts: Part 1. Synthesis and solid characterization.* Applied Catalysis B: Environmental, 2006. **65**(3-4): p. 301-308.
212. Nakamura, R., T. Tanaka, and Y. Nakato, *Mechanism for Visible Light Responses in Anodic Photocurrents at N-Doped TiO2 Film Electrodes.* The Journal of Physical Chemistry B, 2004. **108**(30): p. 10617-10620.
213. Sakthivel, S. and H. Kisch, ChemPhysChem, 2003. **4**: p. 487.
214. Mrowetz, M., et al., J. Phys. Chem. B, 2004. **108**: p. 17269.
215. Wang, Z., et al., *Photocatalytic degradation of phenol in aqueous nitrogen-doped TiO2 suspensions with various light sources.* Applied Catalysis B: Environmental, 2005. **57**(3): p. 223-231.
216. Livraghi, S., et al., J. Am. Chem. Soc., 2006. **128**: p. 15666.
217. Liu, Y., et al., *Photocatalytic degradation of azo dyes by nitrogen-doped TiO2 nanocatalysts.* Chemosphere, 2005. **61**(1): p. 11-18.
218. Sakata, Y., et al., Chem. Lett., 1998. **2**: p. 131.
219. Iwasaki, M., et al., J. Colloid Interface Sci., 2000. **224**: p. 202.
220. Okato, T., T. Sakano, and M. Obara, Phys. Rev. B, 2005. **72**: p. 115124.
221. Vayssieres, L., et al., *Purpose-Built Anisotropic Metal Oxide Material: 3D Highly Oriented Microrod Array of ZnO.* The Journal of Physical Chemistry B, 2001. **105**(17): p. 3350-3352.
222. Greene, L., et al., Angew. Chem., Int. Ed., 2003. **42**: p. 3031.
223. Herrmann, J., J. Disdier, and P. Pichat, Catal., 1988. **113**: p. 72.

224. Mozzanega, H., J.M. Herrmann, and P. Plchat, *NH₃ oxidation over UV-irradiated TiO₂ at room temperature.* Journal of Physical Chemistry, 1979. **83**(17): p. 2251-2255.
225. Al-Ekabi, H., et al., Langmuir, 1989. **5**(null): p. 250.
226. Al-Ekabi, H. and P. De Mayo, *Surface photochemistry: CdS photoinduced cis-trans isomerization of olefins.* Journal of Physical Chemistry, 1985. **89**(26): p. 5815-5821.
227. Mohamed, M.M. and M.M. Al-Esaimi, *Characterization, adsorption and photocatalytic activity of vanadium-doped TiO2 and sulfated TiO2 (rutile) catalysts: Degradation of methylene blue dye.* Journal of Molecular Catalysis A: Chemical, 2006. **255**(1-2): p. 53-61.
228. Muruganandham, M. and M. Swaminathan, *Photochemical oxidation of reactive azo dye with UV-H2O2 process.* Dyes and Pigments, 2004. **62**(3): p. 269-275.
229. Konstantinou, I.K. and T.A. Albanis, *TiO2-assisted photocatalytic degradation of azo dyes in aqueous solution: kinetic and mechanistic investigations: A review.* Applied Catalysis B: Environmental, 2004. **49**(1): p. 1-14.
230. Zhang, F., et al., *TiO2-assisted photodegradation of dye pollutants II. Adsorption and degradation kinetics of eosin in TiO2 dispersions under visible light irradiation.* Applied Catalysis B: Environmental, 1998. **15**(1-2): p. 147-156.
231. Serpone, N. and E. Pelizzetti, *Photocatalysis : fundamentals and applications*1989: New York : Wiley, c1989.
232. ; Available from: http://en.wikipedia.org/wiki/Freundlich_equation.
233. Hoffmann, M.R., et al., Chem. Rev., 1995. **95**: p. 69-96.
234. Brandi, R.J., et al., *Photocatalytic reactors: Reaction kinetics in a flat plate solar simulator.* Catalysis Today, 2002. **76**(2-4): p. 161-175.
235. Xiang., Y., et al., *Template Growth of ZnO Nanorods and Microrods with Controllable Densities.* Crystal Grwoth and Design, 2008. **8**(7): p. 2406-2410.
236. Ferreira-Leitão, V.S., M.E.A. de Carvalho, and E.P.S. Bon, *Lignin peroxidase efficiency for methylene blue decolouration: Comparison to reported methods.* Dyes and Pigments, 2007. **74**(1): p. 230-236.
237. Houas, A., et al., *Photocatalytic degradation pathway of methylene blue in water.* Applied Catalysis B: Environmental, 2001. **31**(2): p. 145-157.
238. Byrappa, K., et al., *Photocatalytic degradation of rhodamine B dye using hydrothermally synthesized ZnO.* Bulletin of Materials Science, 2006. **29**(5): p. 433-438.
239. Octave, L. and O. Levenspiel, *Chemical reaction engineering Octave Levenspiel*1999: New York : Wiley, c1999.
240. Ondo-Ndong, R., et al., *Properties of RF magnetron sputtered zinc oxide thin films.* Journal of Crystal Growth, 2003. **255**(1-2): p. 130-135.
241. Ramesh, K., et al., *Re-investigating the CO oxidation mechanism over unsupported MnO, Mn2O3 and MnO2 catalysts.* Catalysis Today, 2008. **131**(1-4): p. 477-482.
242. Lee, G.D. and J.L. Falconer, *Transient measurements of lattice oxygen in photocatalytic decomposition of formic acid on TiO2.* Catalysis Letters, 2000. **70**(3): p. 145-148.
243. Ovesen, C.V., et al., *Kinetic Implications of Dynamical Changes in Catalyst Morphology during Methanol Synthesis over Cu/ZnO Catalysts.* Journal of Catalysis, 1997. **168**(2): p. 133-142.
244. Dindar, B. and S. Içli, *Unusual photoreactivity of zinc oxide irradiated by concentrated sunlight.* Journal of Photochemistry and Photobiology A: Chemistry, 2001. **140**(3): p. 263-268.

245. Li, D., et al., *Morphological reform of ZnO particles induced by coupling with MOx (M=V,W,Ce) and the effects on photocatalytic activity.* Thin Solid Films, 2005. **486**(1-2): p. 20-23.
246. Cross, R.B.M. and M.M.D. Souza, *Investigating the stability of zinc oxide thin film transistors.* Applied Physics Letters, 2006. **89**(26): p. 263513.
247. Tayade, R.J., T.S. Natarajan, and H.C. Bajaj, *Photocatalytic Degradation of Methylene Blue Dye Using Ultraviolet Light Emitting Diodes.* Industrial & Engineering Chemistry Research, 2009. **48**(23): p. 10262-10267.
248. Obee, T.N. and R.T. Brown, *TiO2 Photocatalysis for Indoor Air Applications: Effects of Humidity and Trace Contaminant Levels on the Oxidation Rates of Formaldehyde, Toluene, and 1,3-Butadiene.* Environmental Science & Technology, 1995. **29**(5): p. 1223-1231.
249. Vidal, A., et al., *Heterogeneous photocatalysis: degradation of ethylbenzene in TiO2 aqueous suspensions.* Journal of Photochemistry and Photobiology A: Chemistry, 1994. **79**(3): p. 213-219.
250. Ali, A.M., E.A.C. Emanuelsson, and D.A. Patterson, *Photocatalysis with nanostructured zinc oxide thin films: The relationship between morphology and photocatalytic activity under oxygen limited and oxygen rich conditions and evidence for a Mars Van Krevelen mechanism.* Applied Catalysis B: Environmental. **97**(1-2): p. 168-181.
251. Orendorz, A., C. Ziegler, and H. Gnaser, *Photocatalytic decomposition of methylene blue and 4-chlorophenol on nanocrystalline TiO2 films under UV illumination: A ToF-SIMS study.* Applied Surface Science, 2008. **255**(4): p. 1011-1014.
252. Yogi, C., et al., *Photocatalytic degradation of methylene blue by TiO2 film and Au particles-TiO2 composite film.* Thin Solid Films, 2008. **516**(17): p. 5881-5884.
253. Rauf, M.A., et al., *Photocatalytic degradation of Methylene Blue using a mixed catalyst and product analysis by LC/MS.* Chemical Engineering Journal. **157**(2-3): p. 373-378.
254. Horikiri, S., et al., *Decomposition of methylene blue by new porous photocatalysts and analysis of decomposed products using high-performance liquid chromatography and mass spectrometry.* Bunsekikagaku 2003. **52**(10): p. 881-885.
255. Mcfarlane, C.J., et al., *Optimising Zinc Oxide Nanostructured Thin Films as Photocatalyst for Industrial Wastewaters.* International Journal of Chemical Engineering, 2010. **2**(2): p. 63-79.
256. Kong, J.-Z., et al., *Photo-degradation of methylene blue using Ta-doped ZnO nanoparticle.* Journal of Solid State Chemistry. **183**(6): p. 1359-1364.
257. Kim, K.-K., et al., *The grain size effects on the photoluminescence of ZnO/alpha-Al[sub 2]O[sub 3] grown by radio-frequency magnetron sputtering.* Journal of Applied Physics, 2000. **87**(7): p. 3573-3575.
258. Gaya, U.I. and A.H. Abdullah, *Heterogeneous photocatalytic degradation of organic contaminants over titanium dioxide: A review of fundamentals, progress and problems.* Journal of Photochemistry and Photobiology C: Photochemistry Reviews, 2008. **9**(1): p. 1-12.
259. Richard, C., P. Boule, and J.M. Aubry, *Oxidizing species involved in photocatalytic transformations on zinc oxide.* Journal of Photochemistry and Photobiology A: Chemistry, 1991. **60**(2): p. 235-243.
260. Talebian, N. and M.R. Nilforoushan, *Comparative study of the structural, optical and photocatalytic properties of semiconductor metal oxides toward degradation of methylene blue.* Thin Solid Films. **518**(8): p. 2210-2215.

261. Gnaser, H., et al., *Photocatalytic degradation of methylene blue on nanocrystalline TiO2: Surface mass spectrometry of reaction intermediates.* International Journal of Mass Spectrometry, 2005. **245**(1-3): p. 61-67.
262. Ishibashi, K.-i., et al., *Quantum yields of active oxidative species formed on TiO2 photocatalyst.* Journal of Photochemistry and Photobiology A: Chemistry, 2000. **134**(1-2): p. 139-142.
263. Stafford, U., K.A. Gray, and P.V. Kamat, *Radiolytic and TiO2-Assisted Photocatalytic Degradation of 4-Chlorophenol. A Comparative Study.* The Journal of Physical Chemistry, 1994. **98**(25): p. 6343-6351.
264. Richard, C., *Regioselectivity of oxidation by positive holes (h) in photocatalytic aqueous transformations.* Journal of Photochemistry and Photobiology, A: Chemistry, 1993. **72**(2): p. 179-182.
265. Gohlke, R.S. and F.W. McLafferty, *Mass Spectrometric Analysis. Aliphatic Amines.* Analytical Chemistry, 1962. **34**(10): p. 1281-1287.
266. Choi, W., A. Termin, and M.R. Hoffman, J. Phys. Chem., 1994. **98**: p. 13669.
267. Bhatti, K., V. Malik, and S. Chaudhary, *Cobalt substituted ZnO thin films: a potential candidate for spintronics.* Journal of Materials Science: Materials in Electronics, 2008. **19**(8): p. 849-854.
268. Djerdj, I., et al., *Co-Doped ZnO nanoparticles: Minireview.* Nanoscale. **2**(7): p. 1096-1104.
269. Wang, X.H., et al., *Wavelength-Sensitive Photocatalytic Degradation of Methyl Orange in Aqueous Suspension over Iron(III)-doped TiO2 Nanopowders under UV and Visible Light Irradiation.* The Journal of Physical Chemistry B, 2006. **110**(13): p. 6804-6809.
270. Wong, C.C. and W. Chu, *The direct photolysis and photocatalytic degradation of alachlor at different TiO2 and UV sources.* Chemosphere, 2003. **50**(8): p. 981-987.
271. Gumus, C., et al., *Structural and optical properties of zinc oxide thin films prepared by spray pyrolysis method.* Journal of Optoelectronics and Advanced Materials, 2006. **8**(1): p. 299-303.
272. Zhou, Y.G., et al., *Spin and band-gap engineering in copper-doped BN sheet.* Chemical Physics Letters, 2010. **491**(4-6): p. 203-207.
273. Anandan, S., Y. Ikuma, and K. Niwa, *An Overview of Semi-Conductor Photocatalysis: Modification of TiO2 Nanomaterials.* Solid State Phenomena, 2010: p. 239-260.
274. Anandan, S., N. Ohashi, and M. Miyauchi, *ZnO-based visible-light photocatalyst: Band-gap engineering and multi-electron reduction by co-catalyst.* Applied Catalysis B: Environmental, 2010. **100**(3-4): p. 502-509.
275. Gupta, R.K., et al., *Band gap engineering of ZnO thin films by In2O3 incorporation.* Journal of Crystal Growth, 2008. **310**(12): p. 3019-3023.
276. Barajas-Ledesma, E., et al., *Determination of the band gap of TiO2-Al2O3 films as a function of processing parameters.* Materials Science and Engineering: B, 2010. **174**(1-3): p. 71-73.
277. Liu, G., et al., *Titania-based photocatalysts-crystal growth, doping and heterostructuring.* Journal of Materials Chemistry, 2010. **20**(5): p. 831-843.
278. Venkatachalapathy, V., et al., *Tuning light absorption by band gap engineering in ZnCdO as a function of MOVPE-synthesis conditions and annealing.* Journal of Crystal Growth, 2011. **315**(1): p. 301-304.
279. Gabor, A.M., et al., *Band-gap engineering in Cu(In,Ga) Se2 thin films grown from (In,Ga)2Se3 precursors.* Solar Energy Materials and Solar Cells, 1996. **41-42**: p. 247-260.

280. Boiarkina, I.A., et al., *Preliminary Investigation of Magnetron Sputtered Thin Films as Photocatalysts for Advanced Oxidation.* Chemeca, 2008: p. 680-695.